Imperial College London

Charge separation in low-bandgap polymer/fullerene blends

Elisa Collado Fregoso

Imperial College London

Department of Chemistry

This thesis is submitted to Imperial College London for the degree of Doctor of Philosophy

September 2015

Declaration of originality

Except where specific reference is made to the work of others, this work is original and has not been already submitted either wholly or in part to satisfy any degree requirement at this or any other university.

Elisa Collado Fregoso,

September 2015

The copyright of this thesis rests with the author and is made available under a Creative Commons Attribution Non-Commercial No Derivatives licence. Researchers are free to copy, distribute or transmit the thesis on the condition that they attribute it, that they do not use it for commercial purposes and that they do not alter, transform or build upon it. For any reuse or redistribution, researchers must make clear to others the licence terms of this work.

Abstract

This thesis addresses charge separation and charge recombination in different, mainly low bandgap, polymer/fullerene blend films and their relation to device performance. Charge separation and recombination was studied as a function of variables including the difference in the LUMO levels of the polymer and fullerene, the polymer/fullerene blend ratio, the presence of a fluorine atom on the polymer backbone and the use of a bulky fullerene acceptor (Indene-C60-trisadduct, ICTA). A key focus of the thesis is on the impact of film microstructural differences upon charge generation and recombination kinetics. Charge generation and recombination was studied via transient absorption spectroscopy (TAS) with time resolutions from femtoseconds to microseconds.

In Chapter 1, an introduction to the field is presented. Basic concepts of polymer solar cells and the steps of light-to-electrical energy conversion are included. The chapter focuses on the current discussions on charge generation, separation and recombination and their relationships with other parameters such as material energetics and morphology. In Chapter 2, the experimental methodologies are presented. A description of the materials used, the techniques used to prepare the samples, and the mainly optical techniques used to study them: steady state photoluminescence (PL), TAS (fs and microsecond), X-ray diffraction (XRD) and device characterization.

Chapter 3 to 6 present the results of each project. In Chapter 3, the role of the driving energy for charge separation (ΔE_{CS}) for low bandgap DPP-based polymers is addressed. A μs-TAS characterization of DPP-based polymer/fullerene blends is presented, and the yield of charges correlated with the experimentally obtained ΔE_{CS}. The correlation was then extended to other low-bandgap polymers and the trend compared with that obtained for larger bandgap polymers.

Chapter 4 deals with the effect of DPPTT-T/$PC_{70}BM$ blend ratio upon the film photophysics. With PL quenching and fs-TAS studies, it is demonstrated that the limitations in the performance of DPPTT-T polymer mainly come from an incomplete exciton quenching for all the compositions studied. The study is in agreement with morphology probes including transmission electron and atomic force microscopies, as well as with the changes in crystallinity, as observed by XRD.

Chapter 5 deals with the effect of polymer backbone fluorination on a low-bandgap polymer (PGeDTBT). PL quenching and fs to μs TAS data is presented and correlated with structural analyses and theoretical calculations to compare the properties of non-fluorinated and fluorinated version of the polymers. It was found that charge generation seems to be equally efficient, despite the lower driving energy for charge separation (ΔE_{CS}) in the fluorinated polymer. A four-fold slowing down in non-geminate recombination was also observed upon fluorination, correlated with a larger polymer tendency to aggregate, thus demonstrating its multiple effects on material properties and photovoltaic behaviour.

Chapter 6 deals with the effect of mixed and “flatter” interfaces upon charge separation. XRD data are presented to show the contrast in intercalation between the polymer and the acceptors ($PC_{70}BM$ and ICTA). These results are correlated with fs-TAS data to show the change in the regime of recombination: while the highly intercalated blends present a high predominance of geminate recombination, the blends with ICTA predominantly present non-geminate recombination.

Finally in Chapter 7, the conclusions of every chapter are summarized. A general discussion on the relationship of the conclusions is given and the areas where further research is needed are discussed.

Contents

Publication List

In preparation

Utzat H., Dimitrov S., Wheeler S., **Collado-Fregoso E.**, Tuladhar P.S., Schroeder B., McCulloch I, and Durrant, J. R. "Relationship between Fullerene Aggregation and Charge Photogeneration Dynamics in Intermixed Polymer:$PC_{70}BM$ Photovoltaic Blends"

Submitted - accepted

Collado-Fregoso E, Boufflet P., Fei Z., Gann E., Ashraf S., Li Z., McNeill C.R., Durrant J.R. and Heeney M, "Increased Exciton Dipole Moment Translates into Charge-transfer Excitons in Thiophene-fluorinated Low-bandgap Polymers for Organic Photovoltaic Applications" Submitted to *Chem. Mater.* **2015**.

Published

Wood S., Wade J., Shahid M., **Collado-Fregoso E**., Bradley D.D.C., Durrant J.R., Heeney M. and Kim J.-S, "Understanding the Dominant Optical Transitions in Diketopyrrolopyrrole (DPP)-Based Copolymers and Their Impact on Photostability" Accepted in *Energy. Environ. Sci.* **2015**, DOI: 10.1039/C5EE01974E.

Yue, W., Ashraf R.S., Nielsen C.B., **Collado-Fregoso E**., Niazi M.R., Yousaf S.A., Kirkus M., Chen H.Y., Amassian A., Durrant J.R. and McCulloch I, "A Thieno[3,2-b]benzothiophene Isoindigo building block for additive- and annealing-free high performance polymer solar cells" *Adv. Mat.* **2015**, DOI: 10.1002/adma.201501841.

Holliday, S., Ashraf R.S., Nielsen C.B., Kirkus M., Rohr J.A., Tan C.H., **Collado-Fregoso E**., Knall A.C., Durrant J.R., Nelson J. and McCulloch I, "A rodanine flanked non-fullerene acceptor for solution-processed organic photovoltaics" *J. Am. Chem. Soc.* **2015**, 137, 898-904.

Huang, Z., **Collado-Fregoso E**., Dimitrov S., Tuladhar P.S., Soon Y.W., Bronstein H., Meager I., Zhang W., McCulloch I. and Durrant J.R. "Optimisation of diketopyrroopyrrole:fullerene solar cell performance through control of polymer molecular weight and thermal annealing" *J. Mat Chem A.* **2014**, 2, 19282-19289

Bronstein H., Hurhangee M., Tuladhar P.S., **Collado-Fregoso E**., Soon Y.W., Sohn E., Dimitrov S.D., Ashraf R.S., Kirchartz T., Watkins S.E., Anthopoulous T.D., Durrant J.R., and McCulloch I, "Isostructural, deeper highest occupied molecular orbital analogues of Poly(3-hexylthiophene) for high open circuit voltage organic solar cells " *Chem. Mater.* **2013**, 25 (21) 4239-4249

Bronstein H., **Collado-Fregoso E**., Hadipour A., Soon Y.W., Huang Z., Dimitrov S.D., Ashraf R.S., Rand B.P., Watkins S.E., Tuladhar P.S., Meager I., Durrant J.R., and McCulloch I, "Thieno[3,2-b]thiophene-diketopyrrolopyrrole containing polymers for inverted solar cells devices with high short circuit currents", *Adv. Func. Mat.* **2013**, DOI: 10.1002/adfm.201300287

Zhong H., Zhe L., Deledalle F., **Collado-Fregoso E.**, Munazza S., Fei Z., Nielsen C., Anthopoulous T.D., Durrant J.R. and Henney M., "Fused Dithienogermolodithiophene low bandgap polymers for high performance organic solar cells without processing additives", *J. Am. Chem. Soc*. **2013**, 135, 2040−2043.

Acknowledgements

I gratefully acknowledge my supervisor, James Durrant, for all the support over the course of my PhD and for all the encouragement that he gave at all times. Thank you for not being grumpy at my stubbornness. Thanks to Martin Heeney, for all his support and patience on our collaboration.

Special thanks to all the people at Durrant's group, for help of all sorts, from experimental to personal. Thanks to Stoichko for his help on my thesis and for every time I went to ask for help on TAS. Thanks to Steve, Safa and Yvonne for introducing me to the OPV world, and to Pabitra and Li for being so helpful. To Ching-Hong, for all the laughs! Special thanks to the people of the Solar fuels, for making lunch and drinks always enjoyable: Camilo, Yimeng, Steph, Laia, Ernest, Mike and Rob. You guys make an excellent group!

I greatly thank Paul, my life partner, because he has been with me at every single moment, good and bad believing in me sometimes more than myself and reminding me the meaning of love. Thank you for your proofreading of my thesis too!

Special thanks to my dad Joaquin, for all the math's help and for showing me with actions what I want and what I don't want to be as a researcher and as a person. Special thanks to my mum too, for almost always being my best accomplice, I love talking to you mum! Thank you Beeety, Joaquin and Josué, because without your help and support I certainly would not be doing a PhD. Thanks to María and Angélica for being there for me in the hardest moments. Thanks to all my friends in México who have always encouraged me and with whom I have shared great moments.

Thanks to my *alma mater*, UNAM, for the grounds of my academic life. For the great professors I had and for making me used to work the hardest possible way. Thank you for giving me a reason to be proud of México. UNAM I owe you so much!

Last but not least, I thank CONACyT and the Kernahan Fund, my sponsors, for the economic support without which I could not possibly live in London or study at Imperial College.

Thanks to all for making this dream possible…

Chapter 1. Introduction

This chapter will deal with the motivation, theoretical background, literature review and current discussions in the study of polymer/fullerene bulk heterojunctions (BHJ). Emphasis will be given to the photophysics of charge generation, separation and recombination in active blends, and their relationship to material properties. Definitions that will be used throughout this thesis will be given and discussed. The chapter will first present the current panorama in terms of the interest to develop devices for alternative energy generation. The challenges of energy generation from polymeric solar cells will be presented and a discussion on their potential applications addressed. Next, a brief overview of the functioning of solar cells will be presented, followed by a description of the steps involved in the generation and separation of free charges in organic semiconducting materials. A brief description of the development of new polymeric materials will be presented, followed by a more detailed description of the processes involved in charge generation, charge separation, the formation of bound polaron pairs, and geminate recombination. Onsager-Braun theory will be summarised. Later, non-geminate recombination under the Langevin theory will be discussed, along with its relevance to the organic photovoltaics field. Reference will be given to some of the "hot topics" that will be addressed in more detail in the following results chapters.

1a. Motivation and context

The use of solar energy for its conversion to electrical energy has the potential to be a substantive alternative technology to conventional energy production by fossil fuels. According to NREL, the earth receives in average 5 kWhr/m^2day, measured as direct normal irradiance. This means that if an area of 100,000 km^2 (which is approximately half the UK's territory) were covered with solar panels working at 10% efficiency, they could generate enough energy for the present world's year demand. Moreover, solar technology has the advantages of being abundant, clean, ubiquitous and renewable[1].

In this context, organic solar cells (OSCs) have gained a considerable amount of attention in the scientific community since they have the potential to constitute a low-cost, flexible technology for alternative energy generation. However, despite the fact that they resemble commercial organic light-emitting diodes (OLEDs) in terms of their structure, OSCs remain behind in terms of commercialization. One of the reasons of this delay is that power conversion efficiencies (PCE) for OSCs have yet to be improved. However, the field is moving rapidly, and in fourteen years the performances have quadrupled, from 3% in 2001 to almost 12% certified value obtained by Mitsubishi, as shown in the efficiency chart on *Figure 1.1.* At the moment, the record in non-industrial research laboratories is 10.8%.[1–4] Challenges include stability issues, the use of non-abundant materials and, more recently, the emergence of high-performing perovskite devices, composed by high-dielectric constant inorganic materials. Despite these difficulties, polymer/small organic molecule solar cells are still promising since they present some advantages over their competitors. For example, differently from most inorganic materials, polymer films are flexible and thus can access applications where bending capacity is important.

In order to improve the performance of OSCs it is necessary to have a better understanding of the processes that are relevant and might limit the efficiency of the entire process of energy conversion, from light absorption to charge collection. Many variables can be changed: materials, processing, device architecture (thickness, use of interlayers, doping), which translate in changes in the energetic of the materials, their mobilities, the microstructure or their charge separation and recombination kinetics. In general, compromises are often necessary between two or more of these aspects, and an optimization of the properties usually needs to be done for each type of material. The studies presented in this thesis have the objective of proposing the most general hypotheses possible to explain charge separation and recombination limitations. This can help to construct guidelines for further improvement in the design of more efficient materials and device structures.

It is generally accepted that the processes that are involved in the conversion of light to electricity involve: (1) absorption of light by the donor molecule to generate an exciton, (2) diffusion of the exciton to the interface of the donor and acceptor, (3) electron transfer from the donor to the acceptor to form polaron pairs and finally (4) collection of these polarons by the external circuit.[5–11]

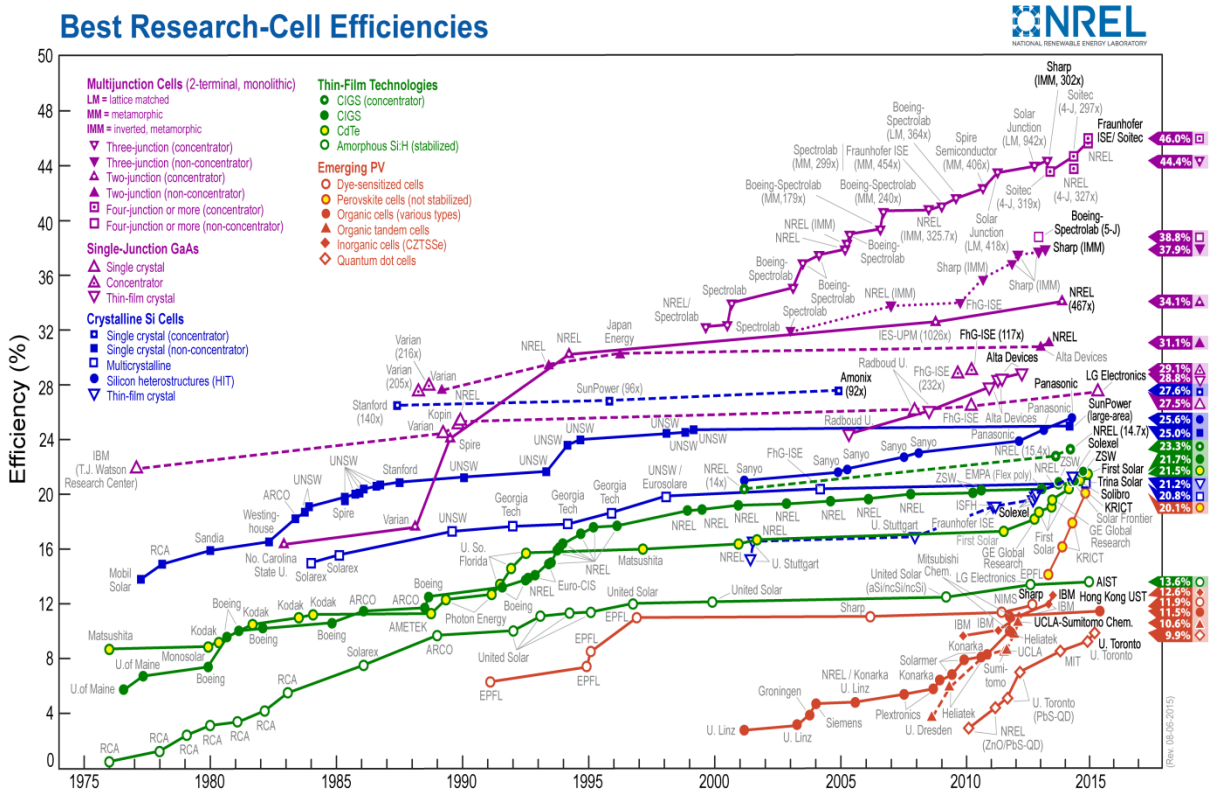

Figure 1.1. National Renewable Laboratory (NREL) chart of certified solar cell efficiencies over time.

1b. General overview and important concepts

1b.1. Excitons, charge separation and the invention of the Bulk Heterojunction (BHJ) cell

Usually organic excitons are classified as strongly bound, spatially localized Frenkel excitons with binding energies of at least 0.2 – 0.3 eV.[12] However, other authors recognise that in some polymers, it might be more adequate to classify excitons as charge transfer (CT) excitons.[13,14] For an exciton to be classified as CT type, a spatial separation of the charges must occur upon excitation, as is found for a fluorinated low-bandgap polymer in Chapter 5. There is no experimental evidence, however, that this results in a lower exciton binding energy, given that the CT character does not necessarily imply a larger delocalization of the wavefunction.[14] Therefore, considering that the binding energy remains relatively unchanged disregarding if the exciton has or not a CT character, the energy

necessary to separate an exciton, is approximately ten times greater than the thermal energy at normal conditions, $\approx 25\ meV$.

It is generally accepted that a first requirement to generate charges in organic semiconductors is to separate the excitons into the charges that compose it, however there are proposals of other ways of charge generation, as will be discussed below. In a breakthrough invention, C.W. Tang[15] realized the need of a heterointerface (or heterojunction) incorporating two materials having donor and acceptor properties, to favour charge separation. In this way, the concept of a bulk heterojunction (BHJ) cell was created. A BHJ therefore is composed by an intimately mixed blend of the two materials, extending throughout the active layer, allowing for nanoscale phase separation between the donor and acceptor.[16] By fabricating devices made of a layer of copper phthalocyanine (CuPc) as a donor and a layer of a perylene derivative as an acceptor, he was capable of measuring a current through the device. This architecture is known as a *bilayer* device and its structure is shown in *Figure 1.5*.

Later it was recognized that a probable factor limiting the efficiency of bilayer devices was an exciton short diffusion length of around 5 - 10 nm[10,17,18], which made it impossible for the device to achieve efficient exciton separation without sacrificing the thickness of the device, and thus loosing efficient light absorption. As such, low efficiencies were ascribed to collection difficulties due to high recombination rates of free charges generated far from the electrodes. To overcome this problem the concept of an interpenetrating network of donor and acceptor materials or bulk heterojunction (BHJ) was created[19], maximizing in this way the donor-acceptor interface in the active layer.

1b.2. Organic semiconductors for solar cell applications

An organic semiconductor is an organic material with semiconducting properties, that is, an electrical conductivity between that of a metal and of an insulator; organic semiconductors can support the existence of delocalised electronic states and can thus function as conductors under certain conditions. The necessary structure for the existence of delocalised electronic states is a structure of conjugated carbon-carbon π-bond, which is exactly the composition of an organic semiconductor. They are materials with sp^2-hybridized orbitals forming a network of alternating (conjugated) double bonds that are susceptible to flow and thus to transport charge when changing their configurations, as shown in *Figure 1.2*.

Additionally, organic materials can absorb and emit visible and near-visible wavelengths of light, therefore their ability to conduct and their responsiveness to the solar spectrum makes them ideal candidates for use in photovoltaics.[20]

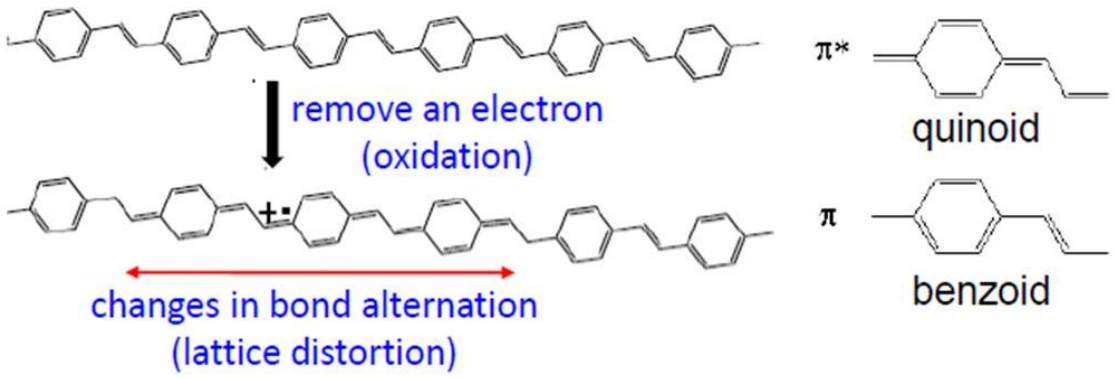

Figure 1.2. Molecular drawings showing how an alternating pattern of double bonds, or conjugation, can result in the transport of polarons along a polymer chain and the alterations they provoke in the lattice. Figure credit to Prof. Ji-Seon Kim.

There are two main differences between organic and inorganic semiconductors that make charge separation a more difficult process in organic as compared to inorganic materials. Firstly, organic materials have in general, considerably lower dielectric permittivities than inorganic materials, resulting in bound excited states (excitons) as widely discussed in the following sections. The second difference is that free electrons cannot be described as fully delocalised in the same sense as electrons in band transport in inorganic semiconductors. Instead they are, to a degree, localised upon atoms within the polymer. As such, charge transport cannot be described using the band approximation, but usually by using a "hopping" model whereby the free charges tunnel from molecular site to molecular site.[20] The result of this difference upon device performance is that charge transport is considerably slower in organic semiconductors than in inorganics, and therefore charge mobilities are reduced.[20] In addition, electrons and holes in organic semiconductors are associated with a significant structural relaxation or 'polarisation' of their surroundings, and are therefore often referred to as 'polarons'. As the charge transport in organic semiconductors is not band-like, and more relevant for this work, the spatial extent of the exciton in organic semiconductors is considerably lower than their inorganic counterpart, it is not correct to use the general terms of conduction and valence band, or even if being strict, to name polarons as *charge carriers* as is typical in the literature. Instead, the nomenclature of HOMO – LUMO energies is often used, although this also includes certain approximations that will be discussed below. In this sense the molecular HOMO and LUMO energy levels are roughly analogous to the valence and conduction

bands of a conventional inorganic semiconductor, respectively; and the bandgap is thus the difference in energy between the HOMO and LUMO levels.[20]

A final characteristic of organic semiconductors that significantly affects the performance of devices fabricated with them is the disordered nature of the material. Organic semiconductors are known to be both morphologically disordered on a range of length-scales, as well as energetically disordered with a distribution of energetic states of the bulk material.[20–22] The physical disorder of organic semiconductors, or the lack of long-range order, results in the existence of a distribution of energetic levels. Therefore instead of the "cartoon" in which only one HOMO and one LUMO energy levels are drawn, more correctly a distribution of HOMOs and LUMOs should be considered, as shown in *Figure 1.3*.

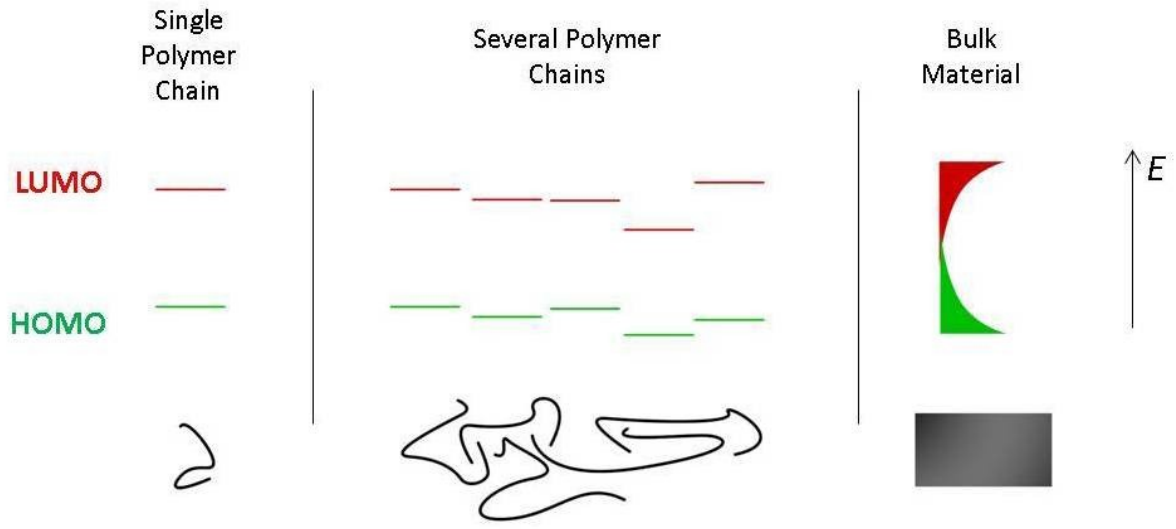

Figure 1.3. Graphical depiction of the energetic effect of disorder when going from, for example, a diluted oligomer solution to a concentrated polymer solution, and finally to the solid bulk material. Figure credit to Dr. George Dibb.[20]

Common materials used in BHJ polymer solar cells

There are a large range of donor polymers that have been used to produce OSCs. Among the initially investigated donors, phenylene vinylene (PPV) derivatives should be highlighted. Although this polymeric family was used in devices with promising efficiencies at the time,[23] later it was recognised that they presented photoxidation problems.[24,25] By far, the most exploited family of compounds used as donors in bulk-heterojunction OSCs are thiophenes and their derivatives, both polymeric and small molecules compounds.[24] Within this family, the most studied polymer is P3HT (poly-3-hexyl-thiophene), which became a benchmark due to the high short circuit currents obtained at the

time in devices with optimized morphologies and balanced mobilities. Most of the donor materials currently investigated, both polymeric and small molecules, are designed in such a way that they have structures with alternating donor-acceptor groups which narrow their bandgaps[8] ("push-pull" effect). This is particularly important since the sun spectrum has high near-IR emission intensity which should be also used for charge photogeneration in optimized solar cells. Narrow bandgaps also enable the minimization of energy losses associated with electron transfer from the donor to the acceptor.[11] Some common groups used as electron rich and deficient units are thiophenes and benzothiadiazoles, respectively. Very recently, materials with efficiencies exceeding 10% PCEs have been fabricated using a 2-D conjugation concept.[3] *Figure 1.4* shows some of the most common materials for polymeric solar cells, including the most efficient materials.[4]

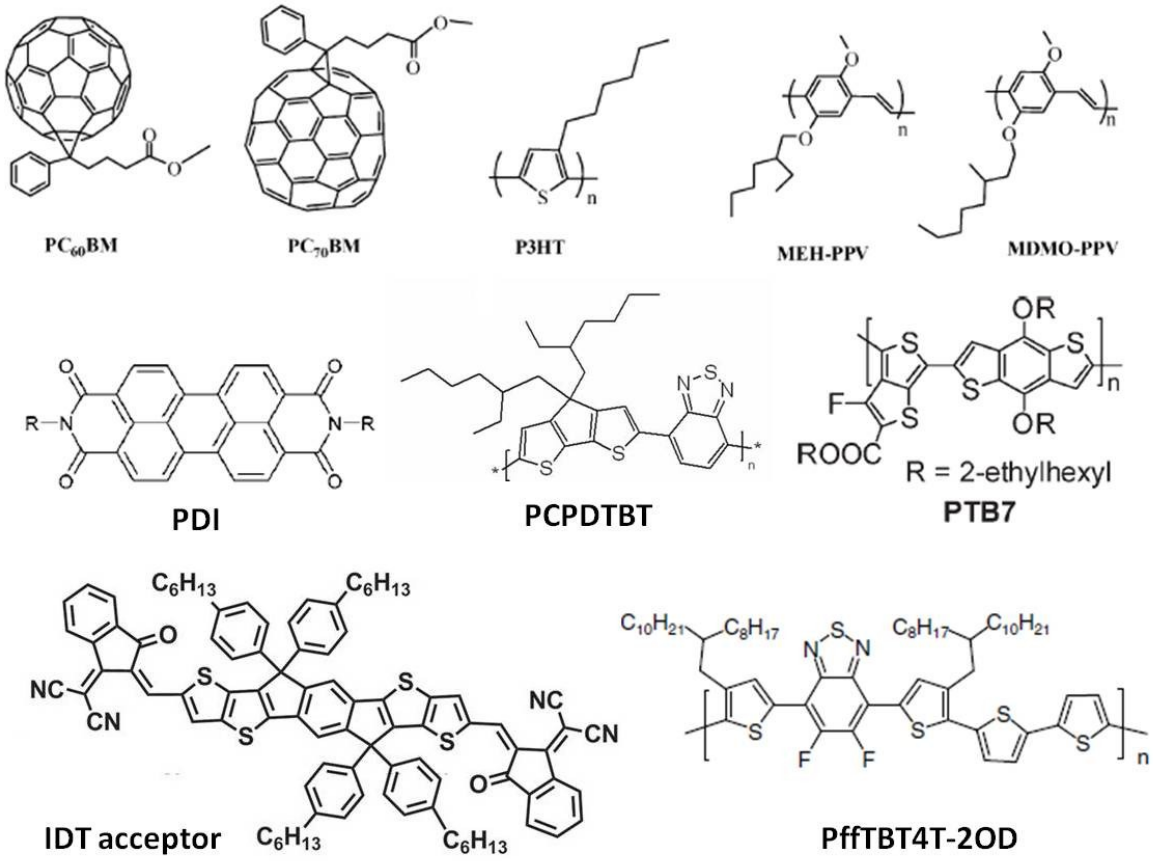

Figure 1.4. Materials that have been used in OSCs. Acceptors (left): fullerene derivatives, PDIs and 6.8% performing fused-ring IDT acceptor.[26] Donors (right): thiophenes, PPVs and polymers that include donor-acceptor moieties: PCPDTBT, PTB7 and the 10.8% performing PffTBT4T-2OD.[4]

Contrasting with the wide variety of compounds used as donors, common acceptors in efficient solar cells are generally limited to soluble derivatives of C_{60} or C_{70} fullerenes such as $PC_{60}BM$ and $PC_{70}BM$

(Figure 1.4). Because of their ability to form semi-crystalline domains when mixed with the appropriate blend ratios and processing conditions, (annealing, use of additives etc.) these materials favour adequate intermixed morphologies required in BHJ devices. Also, due to their large electron affinity and ability to delocalize electrons, they are believed to enhance charge separation.[24] Additionally, due to their high electron mobilities, they enhance the charge transport process after separation.[27] Other acceptors that have been used in OSCs are perylene-diimides (PDI's), cyano derivatives of PPVs, oxidized thiophenes oligomers among others, however, until recently such non-fullerene acceptors had lead to power conversion efficiencies of at most 1% or 2%.[27] For PDIs this has been explained in terms of poor morphology leading to unfavourable charge transport.[28] In the past two years however, there has been an increased interest in the OPV community on the research and design of efficient non-fullerene acceptors, and current PCEs have reached 6.8% for solution-processed devices and 8.4% for vacuum-deposited cells.[26] *Figure 1.4* shows the structure of the best-performing non-fullerene acceptor to date. In this thesis we will focus however, only in systems that comprise polymer donors and fullerene acceptors.

1b.3. Solar cell device architecture and concepts

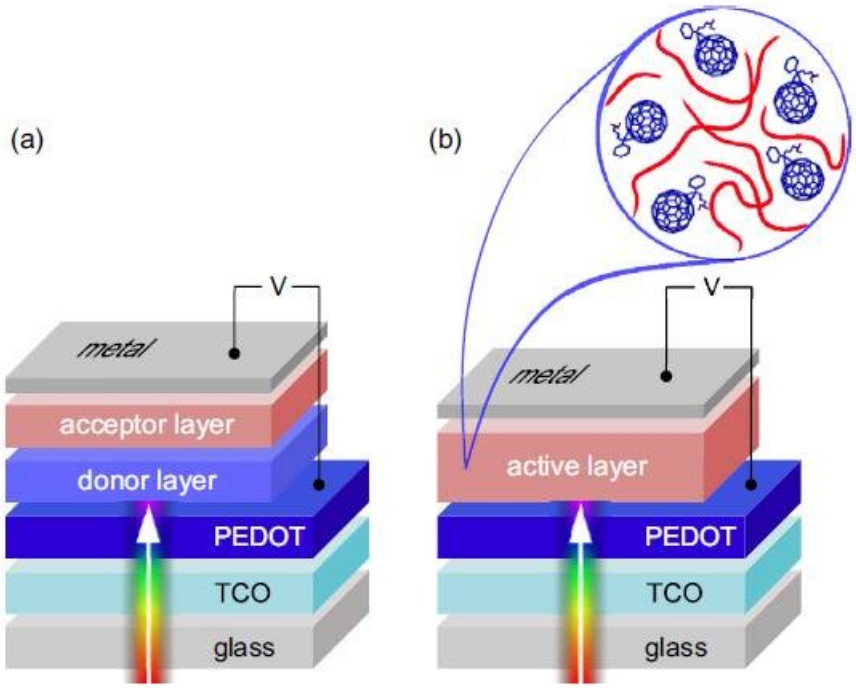

Figure 1.5. Typical device configurations of organic solar cells: (*a*) bilayer device with planar heterojunction, (*b*) bulk heterojunction device consisting of a blend of conjugated polymer with a fullerene derivative. On top of the glass substrate, a transparent conductive oxide (TCO) such as indium tin oxide acts as anode, a poly(3,4-ethylendioxythiophen): polystyrolsulfonate (PEDOT) interlayer helps to avoid local shunts. The active layer consists of either the bilayer or the blend of organic semiconductors. On top, a metallic electrode acts as cathode. Figure credit to Deibel et al.[5]

The general structure of a BHJ solar cells is depicted in *Figure 1.5*, reproduced from Diebel et al.[5] The active layer, which is composed by a donor/acceptor blend of the materials just described, is sandwiched between two electrodes with different workfunctions, which provide the electric field to induce a drift and collect the charges to generate an electric current. The figure also shows the structure of a bilayer device which although it was not used for this thesis, has a value in the proof of concepts such as exciton diffusion, charge separation and geminate recombination.[29]

OSC device performance is normally determined as power conversion efficiency, (PCE, η) which is the main figure of merit for all kinds of solar cells. PCE is defined as the ratio of the maximum power density delivered by the solar cell, $I_{max,out}$, divided by the total incident irradiance, I_{in}. There is a straightforward way to calculate this ratio using lab-measurable variables, as it is shown in *Equation 1.1*.

$$\eta = \frac{I_{max,out}}{I_{in}} = \frac{FF \cdot J_{SC} V_{OC}}{I_{in}} \qquad \text{(Eq. 1.1)}$$

Where J_{SC} stands for short circuit current density, which is the current per unit area measured across the cell at zero voltage and V_{OC} is the open circuit voltage, that is, the voltage present in the cell when no current flows across it. Finally FF stands for fill factor, which is the ratio of the maximum power density delivered by the cell divided by the square described by multiplying J_{SC} times V_{OC}, as shown in *Equation 1.15*. These concepts are described graphically in *Figure 1.6*.

$$FF = \frac{J_{max} V_{max}}{J_{SC} V_{OC}} \qquad \text{(Eq. 1.2)}$$

Another important concept is the external quantum efficiency (EQE) also called incident photon to converted electron ($IPCE$); it is the percentage number of charge carriers collected from the cell per photon shined to the cell, at each photon energy. Normally EQE is reported as a graph of percentage versus wavelength. The short circuit current can be related to EQE if we integrate the contributions at each different wavelength, this is shown in *Equation 1.3*.

$$J_{SC} = q \int b_s(E) \cdot EQE(E) dE \qquad \text{(Eq. 1.3)}$$

Where q is the electronic charge and $b_s(E)$ is the spectrum of the incident source expressed as the number of photons per unit area and per unit time at each differential energy or wavelength change.

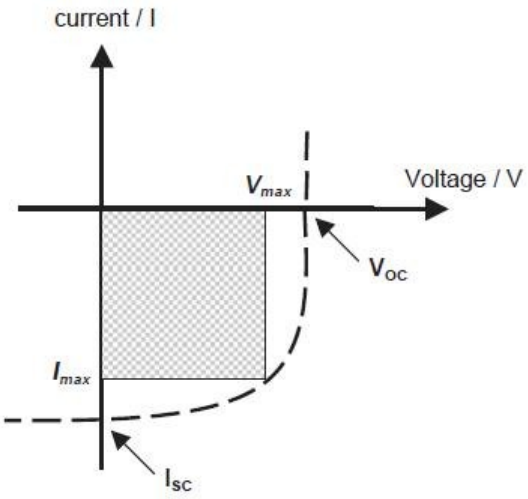

Figure 1.6. Current-voltage (*I-V*) profile of a BHJ solar cell. The main parameters that characterize device performance are pointed out. $\boldsymbol{I_{max}}$ and $\boldsymbol{V_{max}}$ are the current and voltage corresponding to the point of maximum power, $\boldsymbol{P = IV}$. Current *density J* is usually preferred to compare directly the values of current per unit area. Figure taken from reference[25].

1b.4. Photophysics relevant for small molecule and polymers

Organic photovoltaic (OPV) devices use carbon-based semiconductors for the absorption, generation and transport of charges, which are finally collected by one of the electrodes: electrons migrate to a metallic cathode (usually Aluminium) while holes migrate to a transparent ITO anode. The main challenge of using organic materials lies in the fact that the generation of charges compared to the direct free charge generation in their inorganic counterparts. This is because organic semiconductors have relatively low permittivities (dielectric constants) $\varepsilon_r \approx 3$.[10] The low permittivity affect directly the nature of the initial photoexcited species, such that after light absorption, rather than directly forming free charges, as happens in inorganic materials, in organic materials an excited species named *exciton* forms. An *exciton* is an electron-hole pair bound by Coulombic interactions. The exciton forms when an electron is promoted to an upper excited state due to photon absorption and its formation is accompanied by a distortion of the surroundings. Due to this fundamental difference in photophysics of organic semiconductors (as opposed to inorganic materials) light conversion into free charges in organic materials comprises a series of steps each of which needs optimization and corresponds to specific designs of the solar device architecture.

Excitons are neutral quasiparticles, however because they have unpaired electrons, they possess spin. If the spin is paired, the exciton is said to be a *singlet exciton* and is denoted as $S_n, n = 1, 2, \ldots$; 0 is not included since this corresponds to the ground state, which by definition cannot be an

exciton. The symbol S stands for "singlet", with a total spin of zero $S = 0$ and spin quantum number $M_S = 0$. If the spin is unpaired then the exciton is said to be a *triplet exciton* and is denoted as $T_n, n = 1, 2, \ldots$ The symbol T stands for "triplet", with a total spin of one $S = 1$ and spin quantum number with possible values of $M_S = -1, 0, 1$. *Figure 1.7* shows a Jablonski diagram, where these state energies are plotted showing their energy differences. Notice that triplets are lower in energy than singlets, due to the exchange energy term that originates from the requirement of electrons being *fermions*, that is, antisymmetric with respect to particle exchange.[30]

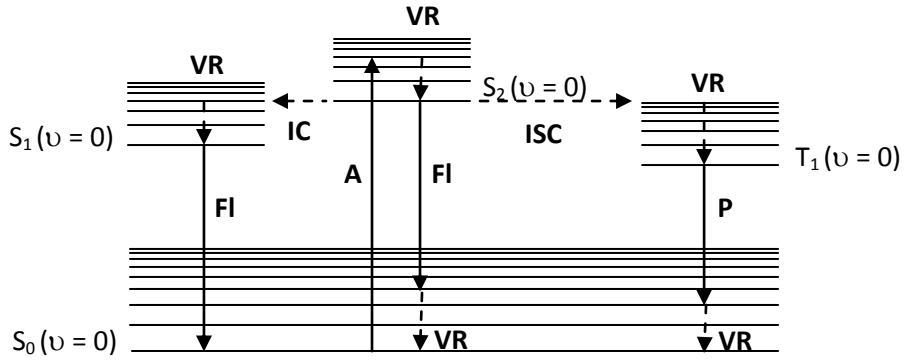

Figure 1.7. State energies Jablonski diagram. **A**: Absorption, **Fl**: Fluorescence, **VR**: Vibrational Relaxation, **IC**: Internal Conversion, **ISC**: Intersystem crossing, **P**: Phosphorescence. Solid and dashed arrows refer to radiative and non-radiative processes respectively.

Figure 1.7, shows a hypothetic situation in which a series of photophysical processes occur. The process start by the absorption of a light photon with energy $E = h\nu$, that places the molecule in an excited state, that in the figure corresponds to $S_2(\upsilon = 4)$ or $S_{2,4}$ where υ corresponds to a vibrationally excited state and thus a *vibronic* excited state (an electronically and vibrationally excited state). According to Kasha's rule, vibration relaxation (VR) is one of the fastest processes of energy dissipation.[14,31] This leaves the molecule in the state $S_2(\upsilon = 0)$. At this stage, the molecule can take three different relaxation pathways. It can emit a photon of energy $E = S_{2,0} - S_{0,3}$ to pass to the vibrationally excited state $S_0(\upsilon = 3)$ and later to dissipate the extra vibrational energy to the surroundings. It can pass to the S_1 states manifold by a process named *internal conversion* (IC), undergo vibrational relaxation and finally emit a photon of energy $= S_{1,0} - S_{0,0}$. The final option depicted in the figure is the molecule accessing the triplet T_1states manifold via a process named *intersystem crossing* (ISC) after which the molecule can also vibrationally relax to the state $T_{1,0}$. This state could phosphoresce, emitting a photon of energy $E = T_{1,0} - S_{0,2}$, and then finally vibrationally relax to the ground state. Vibration relaxation, internal conversion and intersystem crossing are non-radiative processes, since they do not involve the absorption or emission of photons, but rather they

dissipate energy as heat or changing their electronic configuration. There is another process of energy dissipation that is not depicted in *Figure 1.7*, called *vibrational internal redistribution* (VRI) that distributes the energy into different vibrational modes.[31]

1b.5. Excitons and exciton diffusion

The transition from the ground state S_0 to the first excited state S_1 is often approximated as an HOMO → LUMO molecular orbital level transition.[32] This is not strictly true but it is a good enough approximation for the purposes of understanding the steps involved in the generation of free charges. In this sense it can be approximated that after a photon absorption by the donor polymer or small molecule, an electron from its HOMO is promoted to the LUMO leaving a hole at the HOMO. The promoted electron and remaining hole interact to form the singlet exciton. It should also be noted that this process can also occur in the acceptor, especially if it has a relatively high absorption coefficient, as it is the case for example of $PC_{70}BM$[33,34] and some of the newer small-molecule acceptors that will be discussed in the next section.[35] The exciton subsequently thermalizes and induces a series of local deformations of the surroundings.[7,10]

Due to the attraction of its constituent electron and hole, the exciton has energy levels that lie within the electronic bandgap of the material (≈HOMO-LUMO energy). The exciton binding energy, E_{EXC}^{b} is typically estimated as between 0.2 and 0.3 eV, however there is uncertainty in these values and the literature reports energies that range from 0.1 to 0.7 eV.[10,36,37] *Figure 1.8* shows a scheme of the one electron-orbital energies, adapted from Dimitrov et al. and Deibel and co-workers.[37,38] They estimated the value of the exciton binding energy by comparing experimental data of field-dependent photoluminescence quenching. The data was compared to a model based in Onsager-Brown theory, yielding an exciton binding energy of 0.42 eV, they assigned this energy to the transition from excitons to bound polaron pairs as shown in *Figure 1.8* by $\Delta E_{S\rightarrow PP}$. It has to be mentioned however, that the study does not clarify how the initial exciton r_S radius was estimated and what values of the Langevin recombination constant γ and lifetime τ were used and under what conditions they were selected.[37] As such, estimating the exciton binding energy is a difficult task.

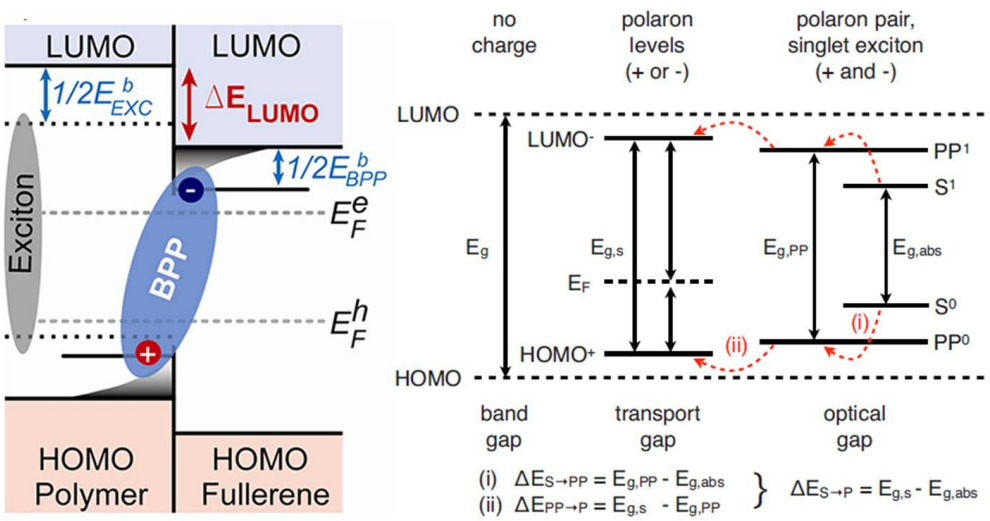

Figure 1.8. Electronic one electron orbital energy diagrams showing HOMO – LUMO energies in a polymer:fullerene donor/acceptor interface during (left) charge generation and bound polaron pair (BPP) formation and (right) light absorption, bound polaron pair formation and free carrier generation. Adapted from references.[37,38]

The previous figure and discussion assumed that the excitons are generated at the interface with the acceptor, now the situation in which the excitons are not generated at the interface, and therefore have to diffuse to reach it is considered. Most commonly, the exciton diffusion length has been measured by relating either photocurrent or photoluminescence data to film thicknesses in donor-acceptor bilayer systems considering a classical hopping mechanism. From these measurements, exciton diffusion lengths ranging from 5 to 14 nm have been obtained.[17] High photoluminescence yields in donor neat films are an indication of long exciton lifetimes and therefore of probably long diffusion lengths.[8,39] Deibel and co-workers also estimated the exciton diffusion length by using Einstein's relation.[37] However, they obtain a low value of 3.5 nm, which appears to be an under-estimation compared to the photoluminescence quenching method.

Exciton migration has also been discussed in terms of different mechanisms of energy transfer.[7] For singlets, it has been proposed that this process follows a Förster resonance energy transfer mechanism which involves a "long range" coulombic coupling of the exciton dipole moments of the donor and the acceptor (in this case these donor-acceptor pairs can be either different units of the same polymer chain or of different polymer chains). The rate constant of this process depends on the distance between the donor and acceptor units. This model predicts that for example, for PPV (poly-phenyl vinylene), the migration is preferred along π-stacked chains with a shorter separation rather than between monomers of the same chain.[7] If this trend was general it would mean that

aggregated π-stacked domains would lead to faster exciton migration compared to for example lamellar aggregated regions.

Results from quantum mechanical calculations in PPV oligomers have shown however, that electrons and holes can delocalize after optical excitation along a single chain. Considering the hole to be located in the middle of a PPV oligomer, the extension of the exciton wavefunction was found to extend with a non-negligible probability amplitude to up to six monomer units away from the monomer in which the hole is located.[40] Considering the size of each PPV monomer to measure transversally ~ 6.5 nm, which means that the spatial separation between the electron and hole could be of ~40 Å, which corresponds to the lowest limit range commonly estimated for the diffusion length for excitons. From this, one can see that at least for this system, there could be a non-negligible exciton population that can dissociate without needing to diffuse to reach the interface from the potential simple extension of the exciton wavefunction within the polymer chain. Evidently, this depends completely on the microstructure of the blend film.

These results are in agreement with recent hypotheses derived from some ultrafast-resolved absorption experiments which claim that charge transfer to the acceptor is ultrafast (≤ 100 fs) and prior to the complete exciton thermalization.[41,42] Heeger and co-workers even claimed that exciton hopping only occurs in blends with low fullerene concentration and poor morphologies such that this process along with the concept of exciton binding energy are less relevant for charge separation.[41] Another theoretical study also supports the idea that charge transfer and exciton migration can occur simultaneously.[43]

The relevance of exciton formation in the process of charge separation has recently been questioned by other groups that have shown experimental evidence for the generation of free charges in a single material domain directly through photon absorption, without ever going through an excitonic state. The work of Burkhard *et al* indicate that photons with sufficient energy can excite free charges in many fullerene derivatives commonly used in OPV devices, as expected since they can support e-h separation.[44] Perhaps more unexpected, from their low dielectric constant and mobility, is the reports that discuss the presence of separated charges in neat polymer films.[45–48] It is unclear whether these contribute significantly to the obtained photocurrent of the device or how long their lifetime will be as the free charges generated in the neat domains are probably likely to encounter an opposite electron or hole and recombine non-geminately. However it shows that the conventional excitonic and polaron pair separation theory of charge generation is not the only plausible model.

As we will see in the following chapters however, in this work, an exciton photoinduced absorption was always detected and electron transfer was observed in the scale of a few picoseconds at low excitation intensity. This supports the exciton/charge separation model on one hand and on the other indicates that not all the exciton population forms charges instantaneously. Rather a more accurate picture would be one in which part of the initial exciton population forms charges instantaneously, another part forms charges in a distribution of times and yet another part of the population decays back to the ground state.

1b.6. Electron transfer and Marcus Theory[49]

We turn now to the description of the electron transfer process under the approximation of weak coupling or non-adiabatic Marcus theory. This approximation implies that the wavefunctions of the donor and acceptor overlap weakly, or analogously, that the probability of electron transfer is low. Marcus theory considers the potential energy of the donor and acceptor as a function of the reaction coordinate –nuclear movements of the donor, acceptor and the surroundings– as two intersecting parabolas (harmonic oscillator approximation). This is shown in *Figure 1.9,* taken from Clarke and Durrant review.[10]

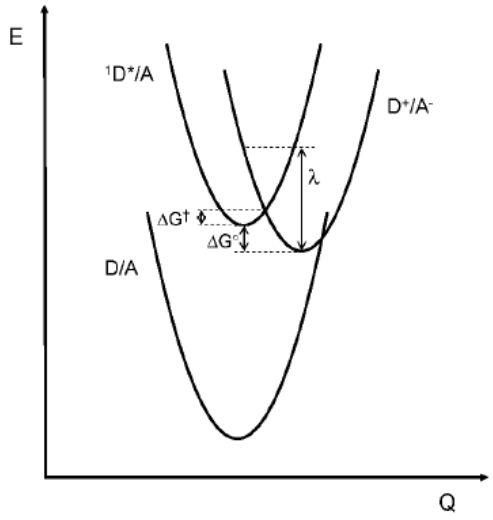

Figure 1.9. Potential energy curves as a function of the reaction coordinate Q for the donor-acceptor system in the ground state D/A, in the excited state (exciton in D) D*/A and after electron transfer D^+/A^-. λ stands for the reorganization energy, see text. Figure credit to Clarke and Durrant review.[10]

For the electron transfer to take place conserving both energy and the Franck-Condon principle, the reactants, including the solvent (or the surroundings) have to follow a series of rearrangements in their geometry such that the crossing point of the parabolas is reached. This is related to the

activation energy of the reaction, $\Delta G^{\dagger}$. Since the products are formed with a non-relaxed geometry, they have to rearrange, along with the surroundings, to their equilibrium position. These geometric rearrangements are characterized by the reorganization energy λ, also interpreted as the energy necessary for the reactants to take the relaxed geometry of the products.

The activation energy of the reaction is related to the reorganization energy and to the total change in Gibbs free energy, by the expression in *Equation 1.4*.

$$\Delta G^{\dagger} = \frac{(\Delta G^{0} + \lambda)^{2}}{4\lambda} \qquad \text{(Eq. 1.4)}$$

Since these expressions were derived under the approximation of weak electronic coupling, an analysis from Fermi's golden rule can be done to determine the rate constant, k_{ET} shown in *Equation 1.5*, where H_{rp} is the matrix element that couples the electronic wave function of the reactant state, ψ_r and the product state ψ_p. Under the weak coupling limit, H_{rp} has an exponential dependence on the distance of the donor and acceptor.[50]

$$k_{ET} = \frac{2\pi}{\hbar\sqrt{4\pi\lambda kT}} H_{rp}^{2} \exp\left(\frac{-\Delta G^{\dagger}}{kT}\right) \qquad \text{(Eq. 1.5)}$$

From *Equations 1.5* and *1.6* one notices that when $\Delta G^{0} = -\lambda$ the reaction is barrierless, and the rate constant takes its maximum value. When the free energy surpasses this limit, that is, $\Delta G^{0} > -\lambda$, the barrier reappears: the reaction enters the so called *inverted region*. In this region the more exergonic the reaction is, the smaller the rate constant. It can be noticed that $\ln k_{ET}$ varies as a downward parabola with ΔG^{0}, with a maximum at the barrierless point.

This type of analysis has been applied by Rumbles and colleagues to donor/acceptor systems similar to the ones used in OSCs.[51] They measured the relative yield of charge generation by performing time-resolved microwave conductivity, as a function of the driving force for charge generation, ΔG^{0}, which was estimated in the same way as done in previous studies.[52–54] In this work they found that the relationship indeed describes a downward parabola, thus observing the inverted region in which further increasing ΔG^{0} leads to a reduction in the relative yield of charge photogeneration. They interpreted the observation of the inverted region as a signature of charge transfer not being limited by diffusion, which would be in agreement with a large fraction of the excitons going through an ultrafast electron transfer.

The reorganization energy is expected to be greater in solids compared to solution due to a larger coupling with the surroundings.[55] However, favouring a constant proximity between the donor and acceptor also increases the rate constant, by increasing the overlap probability H_{rp}^2. Indeed, it has been found that rigid systems in which there is a favoured face-to-face configuration of donor and acceptor have at least one order of magnitude greater rate constants compared to flexible systems,also suggesting an orientation component of the rate constant.

Notice that Marcus theory was originally developed for electron transfer in solution, thus for a correct use of this theory in the description of charge transfer in polymeric solar cells, a density of states (DOS) should be considered in the polymeric donor species.[10] This implies that a series of rate constants with different probabilities would be obtained. It also indicates that the knowledge of the interfacial energetics is extremely important. Regarding this point another complication has been pointed out by Brédas and co-workers[7] who claim that the donor and acceptor HOMO and LUMO levels can be significantly different on the interface compared to isolated compounds, and this difference could also depend on the packing configuration, thus easily changing the description of a systems with different processing conditions are different. Finally, the fact that the process is initiated by light, implies that the "initial reactants" that need to be considered in the Marcus treatment is the vibroelectronically excited donor and acceptor, as previously specified.

1b.7. Bound polaron pairs (BPPs) and charge separation

One proposed mechanism for charge separation in OSC is that it involves the formation of an intermediate state, which in organic photovoltaics is conceived as a coulombically bound polaron pair. Such states are also sometimes associated with reports of observations of interfacial charge transfer (CT) states. The binding energy of relaxed CT states has been considered of at least 0.1 eV,[56] and has normally thought to be less than the binding energy of the exciton due to the increased separation of the electron and hole across the interface.[10]

The degree of relaxation these states undergo before forming charge separated (CS) states (corresponding to free polarons) is still under intense debate. There seems to be evidence that supports charge separation from both "hot" and "cold" CT states. Neher and co-workers have reported the same IQEs and the same field-dependence of free charge generation when they excite upper lying CT states as compare to when they excite relaxed CT states.[57–60] This has supported the idea that charge separation can occur from lowest lying CT states. However, this fundamentally

contradicts the findings of systems with severe geminate recombination and low dielectric constants.

Apparently opposed to this and based on the high charge yields measured in some systems, some authors have concluded that charge separation from a bound pair is impossible or at least highly unlikely, and thus all charge generation must occur through a mechanism that does not involve the formation of a bound pair.[20] One plausible mechanism would be the dissociation of the exciton by the long-range transfer of an electron to the acceptor material even when the exciton is not at an interface. This could occur if the electron component could effectively tunnel across long distances. This has been shown to be possible with the correct material properties through computational modelling studies,[61] however there is little experimental evidence that supports this idea. Also, studies presented in early works in our group[38,52–54] and in Chapter 3 and 6 in this thesis, along with other experimental[62,63,29] and theoretical work, [64,65] have independently shown that charge generation is improved if delocalized and/or higher energy interfacial states are accessible from photogenerated excitons. Chapter 6 gives a more detail description of the state of the field.

It has also been proposed that the relevant variables that determine if CT relaxation or charge separation occurs are the rate constants associated with these events.[7] If the rate constant of internal conversion in CT manifold is greater than the rate constant for charge separation, then the relaxed CT state will form and geminate recombination is likely to occur. Besides, it has been proposed that for some systems geminate recombination losses are the most important losses at short circuit conditions, where non-geminate recombination is believed to contribute less.[53]

An energy model has consistently been used by our group, relating the driving energy for charge separation, as defined by *Equation 1.6, to* the yield of separated charges.[38,52–54] The studies performed by Bakulin and co-workers have proposed that the driving force for charge separation is the energy necessary to reach delocalized band states in the CT manifold,[62,63] which two years later was independently demonstrated by Giebink and co-workers in systems with small molecules.[29]

$$\Delta E_{CS} = E_S - (IP_D - EA_A) \qquad \text{(Eq. 1.6)}$$

Where E_S is the exciton energy, IP_D is the ionization potential of the donor, and EA_A is the electron affinity of the acceptor. Note that with this calculation, the energy of the free charges is estimated to be $(IP_D - EA_A)$. See Chapter 3 for a more in-depth discussion on this topic.

In *Figure 1.10*, taken from reference[7], a summary of the states involved in charge generation based o this model is shown. For simplicity only the pathways that involve electron transfer are shown. After exciton formation, interfacial excited CT states are formed, which depending on the magnitude of the charge separation rate constant can relax or form charge separated states. Notice however, that this figure does not include the distinction made between ΔE_{CS} and ΔG_{CS}, which will be discussed in Chapter 3.

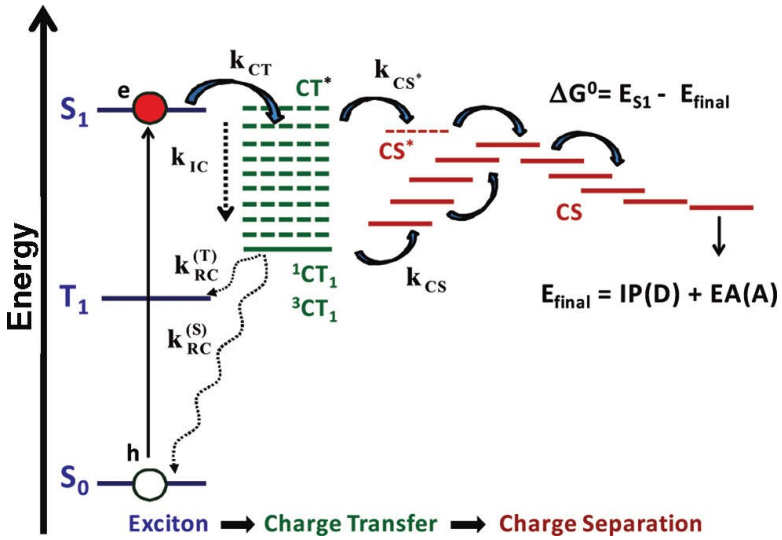

Figure 1.10. Electronic energy states involved in the process of charge separation in an organic solar cell. States in purple are associated with photon absorption and exciton generation (migration not shown). Green states are interfacial intermediate CT states and red states involve charge separated states, that is free positive and negative polarons with energy E_{final}. ΔG^0 for charge separation is also shown. CT* and CS* are vibrationally/electronically excited CT and CS states. Depending on the magnitude of k_{CS^*} CT* states form free charges or relax to further recombine to the ground state or form triplet states through an intersystem crossing pathway. Figure credit to ref[7].

Before moving any further it might be convenient to clarify the difference in the nomenclature that this thesis will use in the terms *charge generation* and *charge separation*, since in the literature these terms are not always clearly distinguished. The first concept will be used to designate exciton dissociation (electron transfer) to generate (bound) polaron pairs, while the second one refers to the formation of the free polarons. The interest will be centred on the factors that determine the *charge separation* efficiency for free polarons as these are the charge carriers able to generate an electrical current in the solar device.

An important consideration that has been so far implicit in our discussion is the spin of the CT states. CT states can intersystem cross to form triplets, ^{3}CT, which can generate triplet excitons in the donor

or acceptor depending on the positioning of their triplet states. However, since intersystem crossing is spin-forbidden and only driven by hyperfine interactions, it is usually *slow* (several tens of nanoseconds[66]). Therefore triplet states might not have enough time to form if charge separation occurs in a faster time scale. Indeed, a recent study proposes that ^{3}CT states might be generated not by the direct formation of CT states but rather from CT state re-forming from non-geminate recombination, that is, by the recombination of two independent free polarons that have uncorrelated spins.[66] In contrast, a study by our own group has reported that observation of intersystem crossing from singlet to triplet CT states, and subsequent triplet exciton formation on the ~ 1 ns timescale.[ref] This process however goes beyond the scope of this thesis and is currently under further investigation in our research group.

Finally, another aspect has to be taken into account for the charge generation and separation processes in organic solar cells: the possibility of an alternative mechanism of charge transfer, named hole transfer. It has been described in two ways. The first process can be described by a mechanism involving an initial energy transfer (also named exciton transfer) from the donor to the acceptor, followed by a back hole transfer to the donor. This process is in effect an hole transfer from the fullerene's HOMO to the polymer's HOMO, and has been observed in some indenofluorene polymers,[39] however, depending on the energetics of the system (energy of HOMO levels and triplet states) it can lead to the formation of triplet states in the donor or the acceptor, which have been correlated with a poor charge generation and device performance, and stability issues.[67] If one were to measure the rate constant for electron transfer in one of these systems, a careful consideration of the energy of the possible states involved (triplets, charge transfer states) should be done. A simpler process is the direct absorption and exciton generation by the acceptor (especially when acceptors with high extinction coefficients are used, such as the $PC_{70}BM$ or the newer small molecule acceptors) followed by a hole transfer from the fullerene to the polymer. It is believed that this process can explain the higher performances usually found when $PC_{70}BM$ is used instead of $PC_{60}BM$, which has lower extinction coefficient. For an improvement to be observed the hole transfer process should operate simultaneously with the electron transfer from the polymer to the fullerene.[33,34] In efficient systems, acceptor absorption and hole transfer can contribute substantially to the short circuit current measured.[68] It has been estimated that if both processes are optimized in a single system with low reorganization energies, PCEs of more than 20% are within reach.[68]

Much of our current understanding of the probability a BPP or interfacial CT state has to dissociate comes from Onsager-Braun theory,[10] which was originally derived for the separation of weak electrolytes in solution. As mentioned, this theory has also been used to estimate satisfactorily the exciton binding energy by Deibel and co-workers.[37] The theory considers that after the photon absorption event, a thermalized hole and an excited electron are formed. The electron however may move a distance a before it thermalizes, this is the thermalization length. It also defines a Coulomb capture radius, r_C by the radius at which the Coulomb attraction is equal to the thermal energy kT. This is shown in *Equation 1.7*, where e is the charge of an electron and ε_0 and ε_r are the vacuum permittivity and the dielectric constant of the material respectively. The model is depicted in *Figure 1.11*, taken from reference.[10]

$$r_C = \frac{e^2}{4\pi\varepsilon_0\varepsilon_r kT} \qquad \text{(Eq. 1.7)}$$

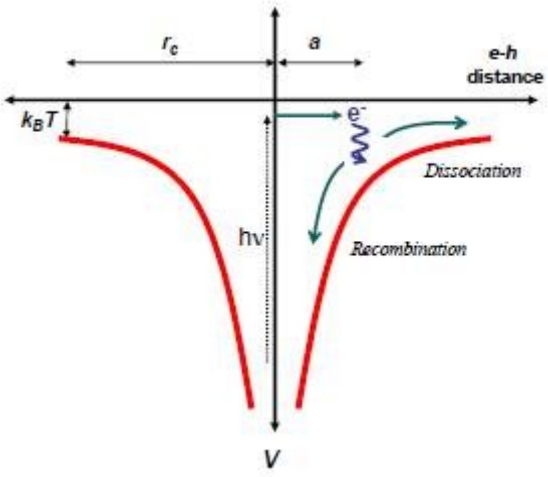

Figure 1.11. A potential energy diagram detailing Onsager's theory of autoionisation. The red curve is the potential as a function of the electron / hole separation distance. Absorption of a photon creates a mobile electron which may thermalise at a given distance from the resulting hole, denoted by distance a. (see text) Figure credit reference[10].

According to the model, if $a > r_C$ the charges separate, however if $a < r_C$ the charges are thermalized within the Coulomb capture radius and separate with a probability $P(E)$ that depends on the presence of a macroscopic electric field. Under Braun's revised model, this probability should take into account the constant rates for dissociation, k_d and geminate recombination, k_r and is defined in *Equation 1.8*, where $\tau(E)$ is the CT state lifetime provided it does not deactivate by other

route, and its dependence on the electric field comes only by the dependence of the dissociation rate constant, k_d. It is thus predicted that the dissociation rate constant will be enhanced in the presence of an electric field.

$$P(E) = \frac{k_d(E)}{k_d\,(E) + k_r} = k_d(E)\tau(E) \qquad \text{(Eq. 1.8)}$$

The process that directly competes with free polaron generation (charge separation) is *geminate recombination*. Geminate recombination is the type of recombination that involves a pair of interacting charges (bound polaron pairs or CT states) that were created from the same exciton. Geminate recombination, then by nature is a fast process and with a time constant which is independent of light intensity (that is, with charge density) since it is a monomolecular process. Chapter 6 will show several different regimes in which geminate recombination is shown for PBTT-T blend films.

Currently, many authors consider that geminate recombination is less important in highly efficient materials constituting morphology-optimized blend films.[69] However, it is still an important limitation to be aware of and conceptually is necessary to understand the relationship between geminate recombination, BPP binding energy and the claims by Neher and others regarding charge separation being possible from cold CT states.

1b.9. Non-geminate charge recombination[20,70]

According to Langevin theory, that considers a simple gas of electrons and holes moving in opposite directions in an electric field, the rate at which the charges meet is dependent upon the speed with which the charges are moving.[20] According to this theory, charge recombination happens when an electron and hole come close to each other (close = within the capture radius r_C). Bimolecular recombination can be expressed using the Langevin formalism, as shown in *Equation 1.9*.[70] In disordered low-mobility organic semiconductors, the probability for a recombination event to occur depends on the likelihood of opposite charges finding each other and hence on charge carrier concentrations (n and p) and the relative mobility at which the opposite charge carriers approach each other. This is expressed through the dependence of the recombination rate prefactor (or the rate constant, in Chemistry nomenclature) on the charge mobility, as shown in *Equation 1.10*. Note that in many instances, the literature uses the Greek letter γ to refer to the recombination rate prefactor.

$$R = knp \quad \text{(Eq. 1.9)}$$

$$k = \frac{e}{\varepsilon_0 \varepsilon_r}(\mu_n + \mu_p) \quad \text{(Eq. 1.10)}$$

Where R is the recombination rate, e is the electron charge, ε_0 is the vacuum permittivity and ε_r is the dielectric constant of the material; μ_n and μ_p are the electron and hole mobilities respectively. Because this model does not consider that recombination in disordered BHJ can only occur in the interface of the separated hole and electron domains, Koster and co-workers proposed that the dependence of the recombination constant on mobility should only consider the slowest-moving charge carrier, as shown in *Equation 1.11*.

$$k = \frac{e}{\varepsilon_0 \varepsilon_r}\langle \mu_n + \mu_p \rangle \cong \frac{e}{\varepsilon_0 \varepsilon_r} \min(\mu_n, \mu_p) \quad \text{(Eq. 1.11)}$$

Even with these modifications, researchers have found that Langevin theory overestimates the value of k by upto several orders of magnitude in polymer/fullerene blends. Therefore, an empirical reduction factor ζ is usually inserted into *Equation 1.11*, as shown in *Equation 1.12.* For P3HT/PC_{60}BM systems, the reduction factor was found to be $\approx 10^{-4}$.[71] The origin of this 'reduced' non-geminate recombination is not known, however it is likely that it is related to the spatial separation that the BHJ structure imposes on the charges.[20] This conclusion is supported by the modelling of experimental results by Hamilton and co-workers.[72]

$$k = \zeta \frac{e}{\varepsilon_0 \varepsilon_r}\langle \mu_n + \mu_p \rangle \quad \text{(Eq. 1.12)}$$

Another important aspect, shown by Durrant's group and others with different experimental techniques is the observation of a dependence of the recombination rate constant on charge density,[73] indicating that the recombination constant is a multivariable function, $k = k(\mu, n)$. The dependence of k on charge density has been found of fractional order, as it will be explained in detail in Chapters 2 and 3. This finding is important, for it results in a fractional, greater than 2, reaction order with respect to charge density. From this, *Equation 1.13* holds. The solution to the differential equation in *Equation 1.13* is presented in Chapter 2 and widely used on Chapter 3.

$$R = k(n)n^2 = k_0 n^{2+\beta} \quad \text{(Eq. 1.13)}$$

Importance of non-geminate recombination in organic photovoltaics

Non-geminate recombination controls to a great extent the *J-V* characteristics of the solar devices; moving from short-circuit to open-circuit conditions, the charge density within the photoactive layer increases, leading to an increase in non-geminate recombination and a decrease in current output of the device.[70] The work of Credgington and Durrant has demonstrated the relation among V_{OC}, J_{SC} and material properties. From their analysis using transient photocurrent (TPC) and photovoltage techniques, they demonstrated that V_{OC} follows the following empirical expression shown *Equation 1.16.*[74]

$$V_{OC} = \frac{1}{e}(IP_D - EA_A) - \frac{n_{id}k_B T}{e}\ln\left(\frac{J_{BI}}{J_{SC}}\right) \quad \text{(Eq. 1.14)}$$

Where IP_D, EA_A, n_{id} and J_{BI} are the ionization potential of the donor, the electron affinity of the acceptor, the ideality factor from the non-ideal diode equation and J_{BI} is the current lost due to non-geminate recombination. For many solar devices, measurements of decay rates and charge densities at different device operation regimes permits to reconstruct the *J-V* curve with good accuracy.

1.b.10 Influence of microstructure upon charge separation and charge recombination[16]

As discussed previously, charge generation and recombination typically occurs at an interface between the donor/acceptor, and not in the bulk of the material. Whilst charge generation is possible in neat materials, this process is not as efficient as in blends and this is one of the factors that reduces the charge generation in bilayers, as many of the excitons fail to find an interface for dissociation.[16] As mentioned before, the BHJ device structure has been used to increase the probability of exciton dissociation, by increasing the surface area between the donor and acceptor materials. In a BHJ, the microstructure of the blend is entirely dependent upon the miscibility of the donor and acceptor phases. The more immiscible the materials are, the greater the tendency to phase separate into –depending on their crystallinity– either amorphous or semicrystalline phases, promoting domain formation.[75] Other materials are more miscible and therefore molecularly mix and form a one-phase microstructure or a co-crystal arrangement, as is the case for PBTTT-T and $PC_{70}BM$, discussed in Chapter 6. The creation of a continuous network of one or both materials

across the active layer leads to a potential electron percolation pathway, which is desirable for charge extraction. However, the increase in the surface area between the two materials also leads to an increase in the recombination of the charges as the probability of the charges reaching another interface to recombine is increased with the increased interfacial area.[16]

An inherent problem of BHJ active films is that typical active layer deposition techniques, such as spin coating from a mixed solution are advantageous due to their ease to commercialise, however they leave little potential for morphological control of the final blend structure which usually leads to problems with its reproducibility. Moreover, the active layer morphology is sensitive to the temperature and solvent. This lack of structural control makes reproducing the blend morphology and the device characteristics a difficult task.[16] Despite this situation, attempts to manipulate the morphology and nanostructure are widespread in the literature and include post-deposition processes including annealing;[76] both thermally[77,78] and with a solvent atmosphere; the addition of a third component, such as an additive or surfactant[79–82] or changing the blend ratio between the donor and acceptor.[75,83–87] Whilst these techniques tend to have an important effect on device performance for some materials systems, there is often little correlation and overlap between processing techniques in different materials systems, with one system responding positively to one technique which is detrimental to device performance in another system. Moreover, many of these advances in device performance do not arise from improvement of the morphology or fine tuning of the electronic properties in well characterised blends, but from the introduction of entirely new donor materials into the blend. This raises interest in not only how the electronic properties are changing between each material system, but how the morphology and structure is changing with each new blend.[16]

Despite the relatively complicated morphology and nanostructure optimization of BHJ active blends, a few groups have successfully incorporated the lessons obtained by the optical and photophysical characterization of the blends into better synthetic recipes, obtaining important advances on the maximum efficiencies that can be obtained from the solar cells, surpassing the 10% PCE.[2–4]

1c. Objectives of the thesis and areas of research addressed

Perhaps one area that was omitted from the theoretical background and literature review just presented is the effect that the microstructure of the active layer has on both properties of the materials and on the actual processes involved in the generation of an electrical current, namely, charge separation, geminate recombination non-geminate recombination. This omission was

deliberate for it will be covered widely in most of the chapters of this thesis. As such, the main objective is the characterization and understanding of the dynamics of charge separation and recombination and the influence of blend microstructure on those processes. The characterization was mainly made via transient absorption spectroscopy (TAS)

Chapter 3 provides an understanding of non-geminate in low-bandgap polymer/fullerene blends and the effect that the driving energy for charge separation, as defined in this chapter, has on the yield of separated polarons and ultimately on the short circuit current in the corresponding devices. Chapter 4 provides an in-depth analysis of the effect the donor/acceptor ratio has upon charge separation and recombination, employing a representative crystalline donor/$PC_{70}BM$ combination, and its relation to other properties including the efficiency of exciton dissociation and the blend crystallinity. Chapter 5 presents the comparison of charge separation and charge recombination upon the fluorination of the backbone of the polymer, including its effect on the blend films microstructure. Finally Chapter 6 provides an in-depth analysis of charge separation and geminate recombination upon the change of the donor/acceptor ratio and the use of bulky acceptors. Chapters 3 to 6 provide detailed morphology studies that include experimental techniques such as wide angle X-ray diffraction, transmission electron microscopy and atomic force microscopy.

1d. References

(1) Xue, J. *Polym. Rev.* **2010**, *50*, 411–419.

(2) Liu, X.; Chen, H.; Tan, S. *Renew. Sustain. Energy Rev.* **2015**, *52*, 1527–1538.

(3) Liu, C.; Yi, C.; Wang, K.; Yang, Y.; Bhatta, R. S.; Tsige, M.; Xiao, S.; Gong, X. *ACS Appl. Mater. Interfaces* **2015**, *7*, 4928–4935.

(4) Liu, Y.; Zhao, J.; Li, Z.; Mu, C.; Ma, W.; Hu, H.; Jiang, K.; Lin, H.; Ade, H.; Yan, H. *Nat. Commun.* **2014**, *5*, 1–8.

(5) Deibel, C.; Dyakonov, V. *Reports Prog. Phys.* **2010**, *73*, 096401.

(6) He, F.; Yu, L. *J. Phys. Chem. Lett.* **2011**, *2*, 3102–3113.

(7) Bredas, J.; Norton, J. E.; Cornil, J.; Veaceslav, C. *Acc. Chem. Res.* **2009**, *42*, 1691–1699.

(8) Ohkita, H.; Ito, S. *Polymer (Guildf).* **2011**, *52*, 4397–4417.

(9) Spectus, C. O. N. *Acc. Chem. Res.* **2010**, *43*, 1227–1236.

(10) Clarke, T. M.; Durrant, J. R. *Chem. Rev.* **2010**, *110*, 6736–6767.

(11) Kroon, R.; Lenes, M.; Hummelen, J. C.; Blom, P. W. M.; de Boer, B. *Polym. Rev.* **2008**, *48*, 531–582.

(12) Riede, M.; Lussem, B.; Leo, K. *Compr. Semicond. Sci. Technol.* **2011**, *4*, 448–507.

(13) Pope, M.; Swenberg, C. E. *Electronic Processes in Organic Crystals and Polymers*; 2nd ed.; Oxford : Oxford University Press, 1999.

(14) Lanzani, G. *The Photophysics behind Photovoltaics and Photonics*; 2012.

(15) Tang, C. W. *Appl. Phys. Lett.* **1986**, *48*, 183.

(16) Jamieson, F. C. Charge Generation in Organic Solar Cells, Imperial College London, 2012.

(17) Markov, D. E.; Amsterdam, E.; Blom, P. W. M.; Sieval, A. B.; Hummelen, J. C. *J. Phys. Chem. A* **2005**, *109*, 5266–5274.

(18) Mikhnenko, O. V.; Azimi, H.; Scharber, M.; Morana, M.; Blom, P. W. M.; Loi, M. A. *Energy Environ. Sci.* **2012**, *5*, 6960–6965.

(19) Yu, G.; Gao, J.; Hummelen, J. C.; Wudl, F.; Heeger, A. J. *Science (80-.).* **1995**, *270*, 1789–1791.

(20) Dibb, G. F. Non-geminate charge recombination in organic solar cells, Imperial College London, 2013.

(21) Brabec, C. J.; Gowrisanker, S.; Halls, J. J. M.; Laird, D.; Jia, S.; Williams, S. P. *Adv. Mater.* **2010**, *22*, 3839–3856.

(22) Blakesley, J.; Neher, D. *Phys. Rev. B* **2011**, *84*, 075210.

(23) Shaheen, S. E.; Brabec, C. J.; Sariciftci, N. S.; Padinger, F.; Fromherz, T.; Hummelen, J. C. *Appl. Phys. Lett.* **2001**, *78*, 841.

(24) Li, Z.; Zhao, X.; Lu, X.; Gao, Z.; Mi, B.; Huang, W. *Sci. China Chem.* **2012**, *55*, 553–578.

(25) Spanggaard, H.; Krebs, F. C. *Sol. Energy Mater. Sol. Cells* **2004**, *83*, 125–146.

(26) Lin, Y.; Zhan, X. *Adv. Energy Mater.* **2015**, n/a – n/a.

(27) Sonar, P.; Fong Lim, J. P.; Chan, K. L. *Energy Environ. Sci.* **2011**, *4*, 1558.

(28) Shoaee, S.; Eng, M. P.; Espíldora, E.; Delgado, J. L.; Campo, B.; Martín, N.; Vanderzande, D.; Durrant, J. R. *Energy Environ. Sci.* **2010**, *3*, 971.

(29) Bernardo, B.; Cheyns, D.; Verreet, B.; Schaller, R. D.; Rand, B. P.; Giebink, N. C. *Nat. Commun.* **2014**, *5*, 3245,DOI: 10.1038/ncomms4245.

(30) Levine, I. N. *Quantum Chemistry*; Fifth.; Prentice-Hall Inc.: New Jersey, USA, 2000.

(31) Requena, A.; Zuniga, J. *Espectroscopia*; Second.; Pearson, Prentice Hall: Madrid, Spain, 2004.

(32) Köhler, A.; Bässler, H. *Electronic Processes in Organic Semiconductors*; Wiley-VCH Verlag & Co. KGaA, 2015.

(33) Dimitrov, S. D.; Nielsen, C. B.; Shoaee, S.; Tuladhar, P. S.; Du, J.; Mcculloch, I.; Durrant, J. R. *J. Phys. Chem. Lett.* **2011**, 140–144.

(34) Dimitrov, S. D.; Huang, Z.; Deledalle, F.; Nielsen, C. B.; Schroeder, B. C.; Ashraf, R. S.; Shoaee, S.; McCulloch, I.; Durrant, J. R. *Energy Environ. Sci.* **2014**, *7*, 1037.

(35) Holliday, S.; Ashraf, R. S.; Nielsen, C. B.; Kirkus, M.; Röhr, J. a.; Tan, C.-H.; Collado-Fregoso, E.; Knall, A.-C.; Durrant, J. R.; Nelson, J.; McCulloch, I. *J. Am. Chem. Soc.* **2015**, *137*, 898–904.

(36) Halls, J. J. M.; Cornil, J.; Silbey, R.; Holmes, A. B.; Bre, J. L.; Friend, R. H. *Phys. Rev. B* **1999**, *60*, 5721–5727.

(37) Deibel, C.; Mack, D.; Gorenflot, J.; Rauh, D.; Dyakonov, V. *Phys. Rev. B* **2010**, *81*, 1–5.

(38) Dimitrov, S. D.; Durrant, J. R. *Chem. Mater.* **2013**, *26*, 616–630.

(39) Soon, Y. W.; Clarke, T. M.; Zhang, W.; Agostinelli, T.; Kirkpatrick, J.; Dyer-Smith, C.; McCulloch, I.; Nelson, J.; Durrant, J. R. *Chem. Sci.* **2011**, *2*, 1111.

(40) Kohler, A.; Dos Santos D.A.; Beljonne, D.; Z., S.; Brédas, J.-L.; Friend, R. H. *Nature* **1998**, *392*, 903–906.

(41) Banerji, N.; Cowan, S.; Leclerc, M.; Vauthey, E.; Heeger, A. J. *J. Am. Chem. Soc.* **2010**, 17459–17470.

(42) Cowan, S. R.; Banerji, N.; Leong, W. L.; Heeger, A. J. *Adv. Funct. Mater.* **2012**, 1–12.

(43) Zhao, Y.; Liang, W. *Chem. Soc. Rev.* **2012**, *41*, 1075–1087.

(44) Burkhard, G. F.; Hoke, E. T.; Beiley, Z. M.; Mcgehee, M. D. *J. Phys. Chem. C* **2012**, *116*, 26674–26678.

(45) Paquin, F.; Latini, G.; Sakowicz, M.; Karsenti, P.-L.; Wang, L.; Beljonne, D.; Stingelin, N.; Silva, C. *Phys. Rev. Lett.* **2011**, *106*, 197401.

(46) Banerji, N. *J. Mater. Chem. C* **2013**, *1*, 3052.

(47) Reid, O. G.; Pensack, R. D.; Song, Y.; Scholes, G. D.; Rumbles, G. *Chem. Mater.* **2014**, *26*, 561–575.

(48) Di Nuzzo, D.; Viola, D.; Fischer, F. S. U.; Cerullo, G.; Ludwigs, S.; Da Como, E. *J. Phys. Chem. Lett.* **2015**, *6*, 1196–1203.

(49) Atkins, P.; Julio, P. *Physical Chemistry*; 2011.

(50) Atkins, P. W.; Paula, J. De. *Atkins' physical chemistry*; Oxford : Oxford University Press, 2006.

(51) Coffey, D. C.; Larson, B. W.; Hains, A. W.; Whitaker, J. B.; Kopidakis, N.; Boltalina, O. V.; Strauss, S. H.; Rumbles, G. *J. Phys. Chem. C* **2012**, *116*, 8916–8923.

(52) Ohkita, H.; Cook, S.; Astuti, Y.; Duffy, W.; Tierney, S.; Zhang, W.; Heeney, M.; McCulloch, I.; Nelson, J.; Bradley, D. D. C.; Durrant, J. R. *J. Am. Chem. Soc.* **2008**, *130*, 3030–3042.

(53) Clarke, T. M.; Ballantyne, A.; Shoaee, S.; Soon, Y. W.; Duffy, W.; Heeney, M.; McCulloch, I.; Nelson, J.; Durrant, J. R. *Adv. Mater.* **2010**, *22*, 5287–5291.

(54) Shoaee, S.; Clarke, T. M.; Huang, C.; Barlow, S.; Marder, S. R.; Heeney, M.; McCulloch, I.; Durrant, J. R. *J. Am. Chem. Soc.* **2010**, *132*, 12919–12926.

(55) Mikkelsen, K. V.; Ratner, M. A. *Chem. Rev.* **1987**, *87*, 113–153.

(56) Lee, J.; Vandewal, K.; Yost, S. R.; Bahlke, M. E.; Goris, L.; Baldo, M. a; Manca, J. V; Van Voorhis, T. *J. Am. Chem. Soc.* **2010**, *132*, 11878–11880.

(57) Vandewal, K.; Albrecht, S.; Hoke, E. T.; Graham, K. R.; Widmer, J.; Douglas, J. D.; Schubert, M.; Mateker, W. R.; Bloking, J. T.; Burkhard, G. F.; Sellinger, A.; Fréchet, J. M. J.; Amassian, A.; Riede, M. K.; McGehee, M. D.; Neher, D.; Salleo, A. *Nat. Mater.* **2014**, *13*, 63–68.

(58) Albrecht, S.; Vandewal, K.; Tumbleston, J. R.; Fischer, F. S. U.; Douglas, J. D.; Fréchet, J. M. J.; Ludwigs, S.; Ade, H.; Salleo, A.; Neher, D. *Adv. Mater.* **2014**, *26*, 2533–2539.

(59) Proctor, C. M.; Albrecht, S.; Kuik, M.; Neher, D.; Nguyen, T. Q. *Adv. Energy Mater.* **2014**, *4*, 1400230.

(60) Zusan, A.; Vandewal, K.; Allendorf, B.; Hansen, N. H.; Pflaum, J.; Salleo, A.; Dyakonov, V.; Deibel, C. *Adv. Energy Mater.* **2014**, *4*, 1400922.

(61) Caruso, D.; Troisi, A. *Proc. Natl. Acad. Sci.* **2012**, *109*, 13498–13502.

(62) Bakulin, A. a; Rao, A.; Pavelyev, V. G.; van Loosdrecht, P. H. M.; Pshenichnikov, M. S.; Niedzialek, D.; Cornil, J.; Beljonne, D.; Friend, R. H. *Science (80-.).* **2012**, *335*, 1340–1344.

(63) Dimitrov, S. D.; Bakulin, A. a; Nielsen, C. B.; Schroeder, B. C.; Du, J.; Bronstein, H.; Mcculloch, I.; Friend, R. H.; Durrant, J. R.; Schroeder, B. C. *J. Am. Chem. Soc.* **2012**, *134*, 18189–18192.

(64) Savoie, B. M.; Rao, A.; Bakulin, A. a.; Gelinas, S.; Movaghar, B.; Friend, R. H.; Marks, T. J.; Ratner, M. a. *J. Am. Chem. Soc.* **2014**, *136*, 2876–2884.

(65) Niedzialek, D.; Duchemin, I.; de Queiroz, T. B.; Osella, S.; Rao, A.; Friend, R.; Blase, X.; Kümmel, S.; Beljonne, D. *Adv. Funct. Mater.* **2015**, *25*, 1972–1984.

(66) Rao, A.; Chow, P. C. Y.; Gélinas, S.; Schlenker, C. W.; Li, C.-Z.; Yip, H.-L.; Jen, A. K.-Y.; Ginger, D. S.; Friend, R. H. *Nature* **2013**, *500*, 435–439.

(67) Soon, Y. W.; Shoaee, S.; Ashraf, R. S.; Bronstein, H.; Schroeder, B. C.; Zhang, W.; Fei, Z.; Heeney, M.; McCulloch, I.; Durrant, J. R. *Adv. Funct. Mater.* **2014**, *24*, 1474–1482.

(68) Koster, L. J. A.; Shaheen, S. E.; Hummelen, J. C. *Adv. Energy Mater.* **2012**, 1–8.

(69) Proctor, C. M.; Kuik, M.; Nguyen, T.-Q. *Prog. Polym. Sci.* **2013**, *38*, 1941–1960.

(70) Lakhwani, G.; Rao, A.; Friend, R. H. *Annu. Rev. Phys. Chem.* **2014**, *65*, 557–581.

(71) Pivrikas, A.; Juška, G.; Mozer, a. J.; Scharber, M.; Arlauskas, K.; Sariciftci, N. S.; Stubb, H.; Österbacka, R. *Phys. Rev. Lett.* **2005**, *94*, 1–4.

(72) Hamilton, R.; Shuttle, C. G.; O'Regan, B.; Hammant, T. C.; Nelson, J.; Durrant, J. R. *J. Phys. Chem. Lett.* **2010**, *1*, 1432–1436.

(73) Shuttle, C.; O'Regan, B.; Ballantyne, A.; Nelson, J.; Bradley, D.; Durrant, J. *Phys. Rev. B* **2008**, *78*.

(74) Credgington, D.; Durrant, J. R. *J. Phys. Chem. Lett.* **2012**, *3*, 1465–1478.

(75) Tumbleston, J. R.; Yang, L.; You, W.; Ade, H. *Polymer (Guildf).* **2014**, *55*, 4884–4889.

(76) Campoy-Quiles, M.; Ferenczi, T.; Agostinelli, T.; Etchegoin, P. G.; Kim, Y.; Anthopoulos, T. D.; Stavrinou, P. N.; Bradley, D. D. C.; Nelson, J. *Nat. Mater.* **2008**, *7*, 158–164.

(77) Clarke, T. M.; Ballantyne, A. M.; Nelson, J.; Bradley, D. D. C.; Durrant, J. R. *Adv. Funct. Mater.* **2008**, *18*, 4029–4035.

(78) Lilliu, S.; Agostinelli, T.; Verploegen, E.; Pires, E.; Hampton, M.; Al-Hashimi, M.; Heeney, M. J.; Toney, M. F.; Nelson, J.; Macdonald, J. E. *Macromol. Rapid Commun.* **2011**, *32*, 1454–1460.

(79) Peet, J.; Kim, J. Y.; Coates, N. E.; Ma, W. L.; Moses, D.; Heeger, A. J.; Bazan, G. C. *Nat. Mater.* **2007**, *6*, 497–500.

(80) Agostinelli, T.; Ferenczi, T. a M.; Pires, E.; Foster, S.; Maurano, A.; Müller, C.; Ballantyne, A.; Hampton, M.; Lilliu, S.; Campoy-Quiles, M.; Azimi, H.; Morana, M.; Bradley, D. D. C.; Durrant, J.; MacDonald, J. E.; Stingelin, N.; Nelson, J. *J. Polym. Sci. Part B Polym. Phys.* **2011**, *49*, 717–724.

(81) Buchaca-Domingo, E.; Ferguson, a. J.; Jamieson, F. C.; McCarthy-Ward, T.; Shoaee, S.; Tumbleston, J. R.; Reid, O. G.; Yu, L.; Madec, M.-B.; Pfannmöller, M.; Hermerschmidt, F.; Schröder, R. R.; Watkins, S. E.; Kopidakis, N.; Portale, G.; Amassian, a.; Heeney, M.; Ade, H.; Rumbles, G.; Durrant, J. R.; Stingelin, N. *Mater. Horizons* **2014**, *1*, 270.

(82) Scarongella, M.; De Jonghe-Risse, J.; Buchaca-Domingo, E.; Causa', M.; Fei, Z.; Heeney, M.; Moser, J.-E.; Stingelin, N.; Banerji, N. *J. Am. Chem. Soc.* **2015**, *137*, 2908–2918.

(83) Kim, Y.; Choulis, S. a.; Nelson, J.; Bradley, D. D. C.; Cook, S.; Durrant, J. R. *J. Mater. Sci.* **2005**, *40*, 1371–1376.

(84) Mihailetchi, V. D.; Koster, L. J. a; Blom, P. W. M.; Melzer, C.; De Boer, B.; Van Duren, J. K. J.; Janssen, R. a J. *Adv. Funct. Mater.* **2005**, *15*, 795–801.

(85) Piersimoni, F.; Chambon, S.; Vandewal, K.; Mens, R.; Boonen, T.; Gadisa, A.; Izquierdo, M.; Filippone, S.; Ruttens, B.; D'haen, J.; Martin, N.; Lutsen, L.; Vanderzande, D.; Adriaensens, P.; Manca, J. V. *J. Phys. Chem. C* **2011**, *115*, 10873–10880.

(86) Guilbert, A. a. Y.; Schmidt, M.; Bruno, A.; Yao, J.; King, S.; Tuladhar, S. M.; Kirchartz, T.; Alonso, M. I.; Goñi, A. R.; Stingelin, N.; Haque, S. a.; Campoy-Quiles, M.; Nelson, J. *Adv. Funct. Mater.* **2014**, n/a – n/a.

(87) Kästner, C.; Egbe, D. a. M.; Hoppe, H. *J. Mater. Chem. A* **2015**, *3*, 395–403.

Chapter 2. Experimental Techniques

In this chapter, the materials used for every chapter are described, as well as the procedures to prepare the samples used. We also describe in detail the main spectroscopy experimental techniques used for our optical characterization studies and finally we describe the models used for the analysis of the data, showing examples illustrating their use. The chapter is organized in the following way:

2a. Materials used in this thesis

All the materials, shown in *Figure 2.1*, were used as received and without further purification. For all the studies except for the second part of Chapter 6, $PC_{70}BM$ was used as the acceptor material. $PC_{70}BM$ was used as acquired from Solenne. In Chapter 3, the DPP-based polymers DPPTT-T (M_n: 35 kDa, M_w: 150 kDa), DPPTT-S (M_n: 32 kDa, M_w: 176 kDa), DPPST-T (M_n: 90 kDa, M_w: 185 kDa) and DPPTT-Tz (M_n: 25 kDa, M_w: 250 kDa) were synthesized in house by Dr. Hugo Bronstein from Prof. Iain McChulloch's group at the Chemistry Department of Imperial College. A further batch of DPPTT-T (M_n: 24 kDa, M_w: 89 kDa) was used for the studies in Chapter 4. Ge-based polymers PGeDTBT (herein F0, M_n: 31 kDa, M_w: 74.4 kDa) and PGeTFDTBT (herein F4, M_n: 34 kDa, M_w: 95.2 kDa) were also synthesized in house by Dr. Zhuping Fei from Prof. Martin Heeney's group. Finally, for Chapter 6, PBTTT (M_n: 30 kDa, M_w: 49 kDa) was synthesized in house by Dr. Bob Schroeder from Prof. Iain McChulloch's group. ICTA was acquired from Solenne.

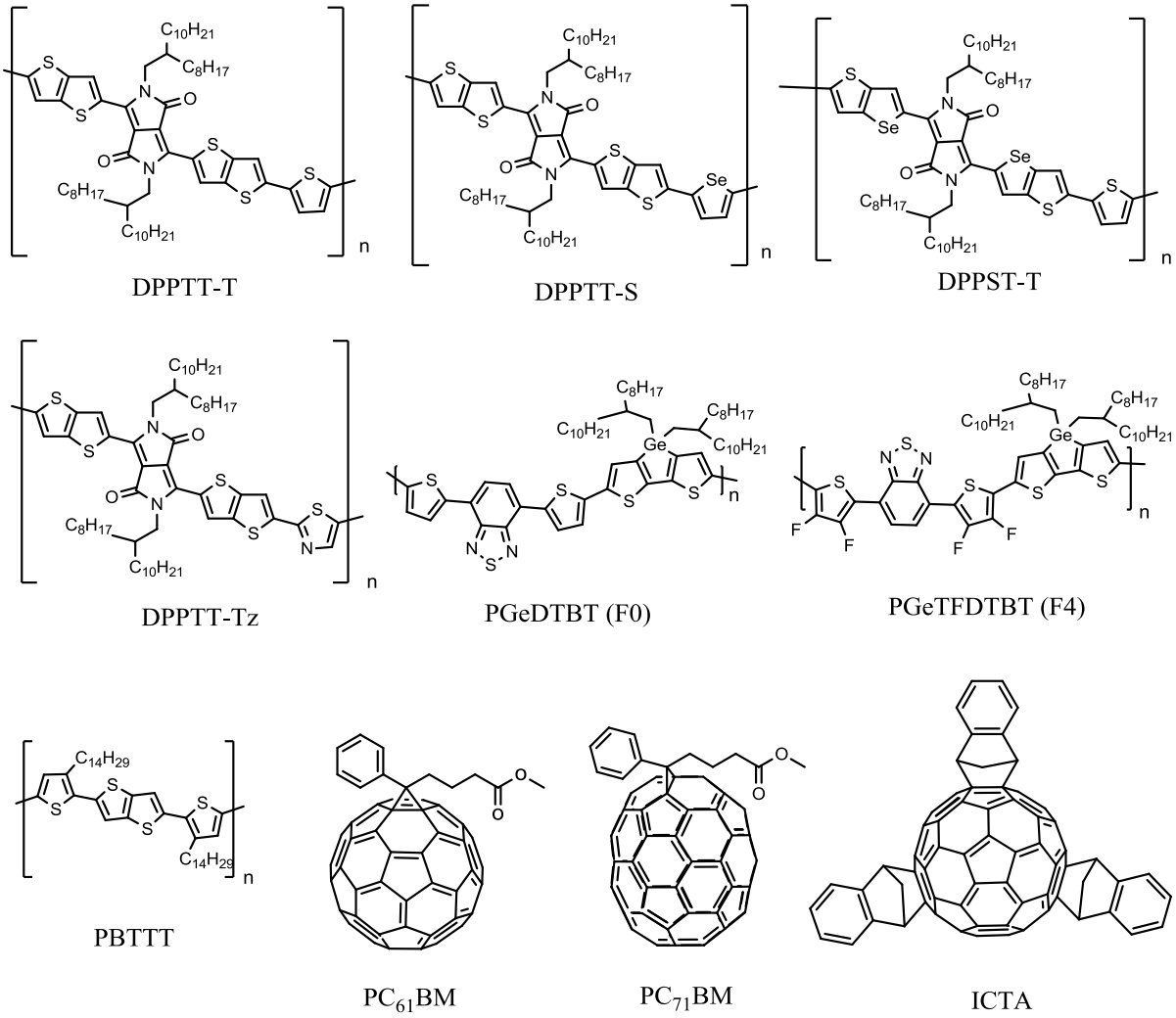

Figure 2.1 Donor polymers and fullerene acceptor materials used in this thesis.

2b. Sample preparation.

All thin films were prepared on glass (VWR) or, for $PC_{70}BM$ neat films, on PEDOT:PSS coated glass. Glass was cut to an approximate 1 cm x 1 cm size, cleaned using 10 min ultrasonication with soap and water followed by acetone, iso-propanol and acetone again, followed by drying with nitrogen.

Polymer solutions were prepared in the appropriate solvent, usually o-dichlorobenzene (Sigma Aldrich, 99% purity), with concentrations between 10 and 30 mg/mL and left stirring overnight (and heating, when necessary) to maximise polymer dissolution. The acceptor solutions were prepared under the same conditions. The films were usually prepared by spin-coating, with a spin coater from Laurell Technologies Corporation, WS400A-6NPP Lite. The same conditions of rate and time as per the optimised method for the working devices was used, usually the coating was done for 1 minute at 1500 to 2500 rpms. In Chapter 4 and 6, non-optimized blends with different blend ratios were prepared to assess the effect of the acceptor concentration within the film on charge generation and charge separation. Drop-casting was used for wide-angle X-ray diffraction (WAXD) samples, covering a glass slide with 2 mg/mL solution and leaving dry overnight. All the sample preparation was carried in air in a fume hood. Films were kept in a glovebox with a positive nitrogen flow before and after usage.

2c. Experimental techniques

2c.1. Steady-state UV-Vis spectroscopy

Steady-state UV-vis is a very essential technique that measures the light absorption in a sample as a function of the wavelength. Absorbance is related to concentration via the Beer-Lambert law in Equation 2.1, therefore it is a useful method to calculate concentrations when the extinction coefficient and the optical length are known.

$$A = \varepsilon l C \qquad \text{(Eq. 2.1)}$$

Where A is the absorbance of the chromophore and C is its concentration in mol/dm^3. ε is the extinction coefficient, in $M^{-1}cm^{-1}$ and l is the optical depth, in cm.

All the films were characterized first by steady state UV-Vis spectroscopy, mainly to correct both the steady state PL and the μs and sub-ps-TAS for the absorption at the excitation wavelength (see below) but also, to gain information on the optical bandgap or the LUMO level of a polymer and

from the vibronic structure of the spectra, to assess changes of packing or crystallinity, as it is the case for PBTTT in Chapter 6 or the aggregation study of DPPTT-T in solution in Chapter 4.

Steady-state absorption spectra were taken in air, scanning from 300 to 1100 nm on a Perkin Elmer Lambda 25 UV-vis spectrometer. All spectra were corrected to 100% T with a glass substrate.

2c.2. Steady-state Photoluminescence (PL) Spectroscopy

In most of our studies, we used photoluminescence spectroscopy to learn about the efficiency of exciton quenching when the maximum PL of the neat polymer films was compared to the PL of a blend. The extent of exciton quenching as observed by this technique can be related to the decrease in the exciton decay time as observed by sub-ps TAS in neat and blend films, as shown in Equation 2.2, provided that the main and fastest quenching process is the electron transfer to the acceptor molecule, which is the case for all the polymers herein studied.

$$\frac{PL_{blend}}{PL_{neat}} \approx \frac{\tau_{ex(blend)}}{\tau_{ex(neat)}} \qquad \text{(Eq. 2.2)}$$

Where PL_{blend} corresponds to the photoluminescence at the maximum for a blend film and PL_{neat} corresponds to the photoluminescence at the maximum for either a polymer or an acceptor neat film. $\tau_{ex(blend)}$ is the exciton quenching characteristic time of a blend film (in the case where the exciton signal can be extracted from the overall spectra) and $\tau_{ex(blend)}$ is the exciton intrinsic decay time in a neat film.

Besides providing information on the efficiency of exciton quenching, the PL technique is very useful and has proven a reliable method to indirectly assess the morphology of the film, more specifically the level of intermixing of the materials within the blend, and therefore can be used as an estimation of the average size of either the polymer or the acceptor domains, as described in ref[1]. A typical way to estimate this is to calculate the PL quenching (PLQ), obtained from *Equation 2.3*. The closer the PLQ is to 100%, the more "amorphous" or intimately intermixed the regions of the materials are, conversely, the further the PLQ is from 95%, the most extended the domains of the material are and possibly the more crystalline the material is.

$$PLQ = 1 - \frac{PL_{blend}}{PL_{neat}} \quad \text{(Eq. 2.3)}$$

The magnitude of the PL quenching *(PLQ)* in blend films can be used to estimate the material domain size by calculating L, the distance that the exciton diffuses before encountering a fullerene molecule. To obtain L, the definition of exciton diffusion length, $L_{ex} = \left(D \cdot \tau_{ex(neat)}\right)^{1/2}$ is used (D corresponds to the diffusivity of the exciton). It is assumed that upon the addition of fullerene, the change in exciton diffusion is only due to the shorter lifetime of the exciton resulting from its quenching by the fullerene. Therefore, L is given by $L = \left(D \cdot \tau_{ex(blend)}\right)^{1/2}$. Substituting *Equation 2.2* and *2.3* into the definitions of L and L_{ex} as described before[1] results in an expression to obtain L in terms of L_{ex} and PLQ, as shown in *Equation 2.4.*

$$L = L_{ex}(1 - PLQ)^{1/2} \quad \text{(Eq. 2.4)}$$

For the polymer exciton, L_{ex} was assumed to be 10 nm, a value typical for narrow a and a few wide bandgap polymers[2,3]. For the PCBM (or $PC_{70}BM$) excitons, L_{ex} was taken to be 5 nm[4]. Note that *Equation 2.4* neglects the finite size of the exciton, and assumes efficient quenching when a polymer exciton reaches fullerene acceptors. As such it gives only an indication of the length scale of exciton diffusion occurring in the blend films.

Steady-state photoluminescence measurements were carried out in air using a Fluorolog FM-32 spectrofluorometer (Horiba Jobin Yvon) using either a visible or a liquid nitrogen-cooled infrared detector, depending on the material bandgap and thus the excitation wavelength. All the signals were corrected for absorbance at the excitation wavelength, to eliminate the dependence of the signal on the amount of absorbed light.

2c.3. μs-resolved Transient absorption spectroscopy (μs-TAS)

Transient absorption spectroscopy is an optical, pump-probe technique used to obtain information on the dynamics of excited and transient species. A scheme of the setup is shown in *Figure 2.2*. It is based in a two-beam system, in which an initial pulse generates a population of excited species that in this case, undergo the processes of exciton migration, electron transfer and charge separation already described in the previous section. The probe white light beam re-excites the sample, and

then it is passed through a monochromator that permits the selection of a single probe wavelength. The change in the intensity of the probe beam as a function of time is taken from the signal before the pump pulse is referenced and thus without excited absorbers, and at a time t after the reference, when the probe is absorbed. The fractional signal is converted to a fractional change in voltage by the photodiode in the detection system and this signal is sent to the oscilloscope. This is shown in *Equation 2.5*, which relates the change in voltage with optical density, ΔOD.

$$\Delta OD(t) = -\log\left(\frac{I_0 - I(t)}{I_0}\right) = -\log\left(1 - \frac{I(t)}{I_0}\right) = -C \cdot \log\left(1 - \frac{V(t)}{V_0}\right) \qquad \text{(Eq. 2.5)}$$

Where I_0 is the intensity of the probe beam before the pump is referenced to the oscilloscope and $I(t)$ is the intensity at a time t. C is a constant that relates the change in intensity with the output voltage and depends on the photodiode of the detector.

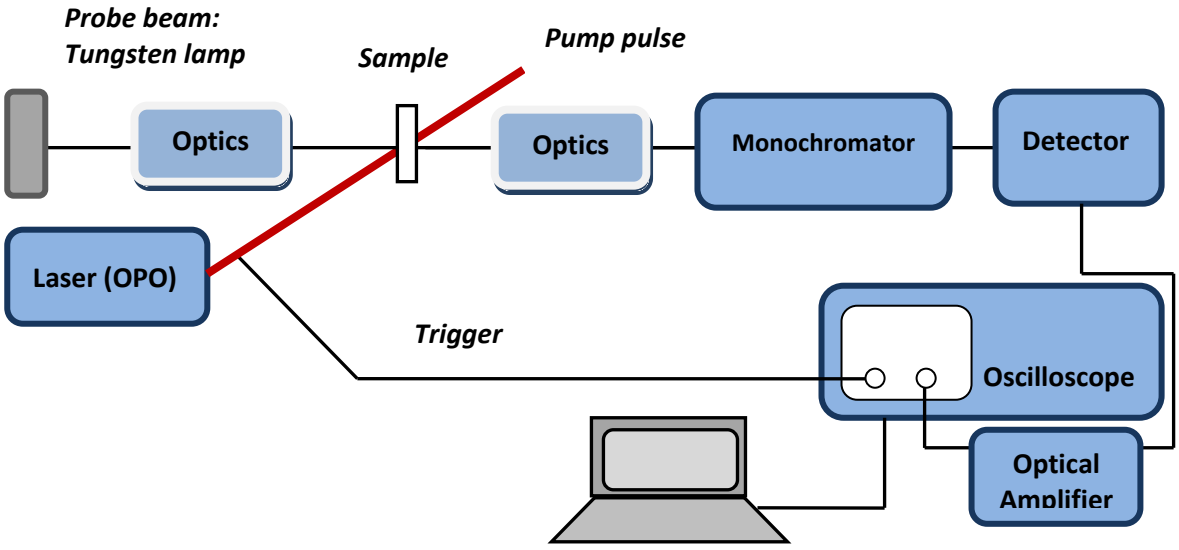

Figure 2.2. Simplified scheme of the μs-resolved TAS setup used in this thesis

In our system the excitation pulse is generated by an optical parametric oscillator (OPO) pumped by a Nd-YAG laser. An OPO is an optical cavity resonator that uses parametric amplification, a non-linear optical phenomenon that generates two beams that cover a wide range of wavelengths. In our system these beams cover energies from near UV to near IR, which is very useful in order to perform experiments with different excitation wavelengths. The width of the pulses is approximately 20 ns and the repetition rate used for the experiments is 20 Hz, which corresponds to a time between

each pulse of 50 ms. This gives us a time window large enough to monitor processes of charge recombination that occur within these timescales. It has also allowed us to estimate the yield of charges by comparing the amplitude of the signal at a certain fixed time delay, as presented in the studies of different DPP-based polymers in Chapter 3.

The probe light comes from a continuous-wave (CV) tungsten lamp, which is then focused into a monochromator that is set to select a particular wavelength. The beam is then focused into either a silicon or an InGaAs detector depending if the probe wavelength is visible-near IR (until ~1000 nm) or if it lies further into the infrared region (until ~1600 nm). The detector converts the optical signal to a voltage difference that is filtered and then passed to a double channel oscilloscope referenced to the pump pulse to set time zero. The oscilloscope is connected to a computer and the data read with LabView program. The instrument response function (IRF) of this system is ~200 ns, taken from the full width at half maximum (FWHM) of a scattering signal. At the end, two types of experiments can be acquired: ΔOD as a function of time at a single pump/probe wavelength or ΔOD as a function of probe wavelength, corresponding to a transient spectrum at a certain time. All films were measured inside quartz cuvettes under a nitrogen atmosphere, unless otherwise indicated.

2c.4. Ultrafast Transient absorption spectroscopy (fs-TAS)

Fs-TAS is an optical, two pulse transient technique, whose main advantage is its high pulse temporal resolution. This permits the user to investigate early (from ~200 fs) excited states dynamics. Therefore, it permits to monitor early aspects of charge generation. Processes such like exciton formation, exciton quenching, polaron generation, polaron relaxation and polaron recombination can be studied. The second advantage is related to the use of white light as probe pulse, along with the use of an imaging spectrometer, which permit to probe an entire spectrum at a time, rather than constructing the spectra from individual decay data at different probing wavelengths.

Sub-ps-TAS measurements were carried out with a commercially available setup which main parts comprise: a) the laser pulse generation by a system comprising a fs laser seeding a regenerative amplifier, b) the excitation pulse tuning by an optical parametric amplifier and c) the transient absorption spectrometer where the sample is measured. Next we will describe briefly the function of each of these parts. These parts are depicted in *Figure 2.3*.

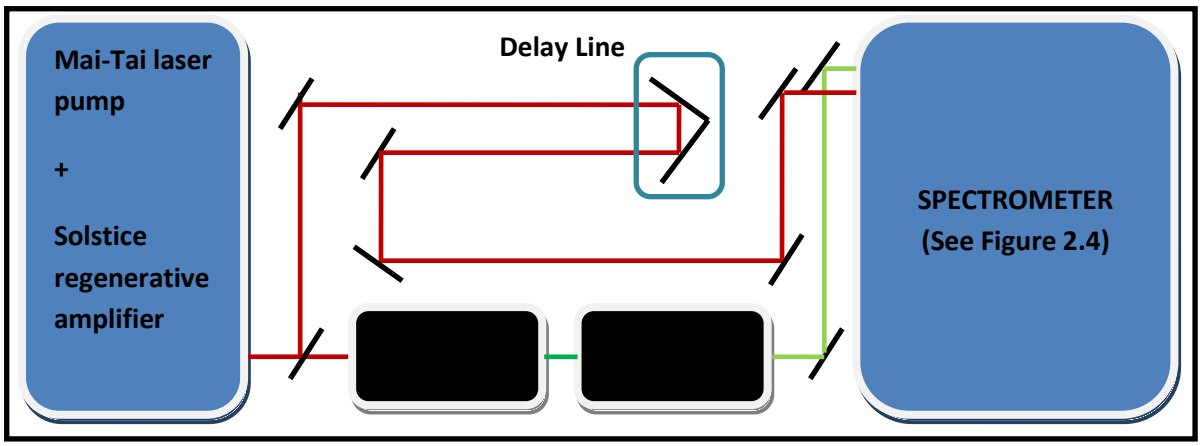

Figure 2.3. Simplified schematics of the sub-ps spectroscopy setup used for the studies presented in this thesis

The Ti: Sapphire regenerative amplifier (Solstice, Spectra Physics) increases the power output of the Ti:Sapphire femtosecond optical cavity (Mai Tai, Spectra Physics) from 17.5 nJ to >2.5 mJ, while maintaining the narrow pulse duration to ~ 100 fs. In order to do this, a series of optical steps need to be carried out. The ultra short pulses cannot be amplified directly, since it could cause damages to the Ti:Sapphire crystal in the regenerative amplifier. The pulses thus, need to be time-stretched, then amplified and finally time-compressed again, this is done within the enclosed Solstice box, which comprises a stretcher, the regenerative amplifier and a compressor. The amplification is particularly important for the generation of white light probing later in the transient spectrometer. The output of the amplified laser is thus, an 800 nm, ~100 fs pulsed beam with a pulse energy of ~2.5 mJ.

Part of the output of the Solstice will be directed to generate the excitation pulse by the OPA and the remaining will be used to generate the time-delayed white light probe pulse later on. The OPA (TOPAS prime, Light conversion) as mentioned before, is an amplifier that uses non-linear optical steps to generate light with different frequencies and polarization; an additional box of frequency mixers is used after the TOPAS to extend the range of possible excitation wavelengths into the UV and IR. The TOPAS is particular useful since it gives the flexibility of being able to tune the excitation pulse to a broad range of possible wavelengths that span from 285 to 1600 nm. In this thesis, we usually used excitation wavelengths between 500 and 850 nm.

The remaining fundamental pulse that is not passed through the TOPAS is directed to the delay line, which is a U shaped series of mirrors attached to a cart that can move with micrometric precision, used to impose a movable distance on the probe pulse that will determine the time delay of this

pulse with respect to the excitation pulse. The delay line permits us to take data spanning to 6 ns. After the probe pulses pass the delay line, they will enter the spectrometer (HELIOS, Ultrafast Systems) area, as shown in *Figure 2.4.* This is a part of the system in which a) white light is generated with the probe pulse, b) the sample is measured and thus the excitation and probe pulses are aligned to hit the sample in the same spot, and c) the change in the intensity of the probe pulse is detected and processed. White light can be generated either in the visible range, from 450 to 750 nm or in the NIR, from 850 to 1450 nm by using different crystals and is accordingly detected either with a CMOS detector for visible light or with an InGsAs, for near IR light. This allows us to have a wide enough wavelength range to probe either ground state bleaching signals (GSB) or excited state absorption signals (ESA) which, in the case of conjugated polymers or their blends with fullerenes, usually appear at longer wavelengths, as discussed in the next section.

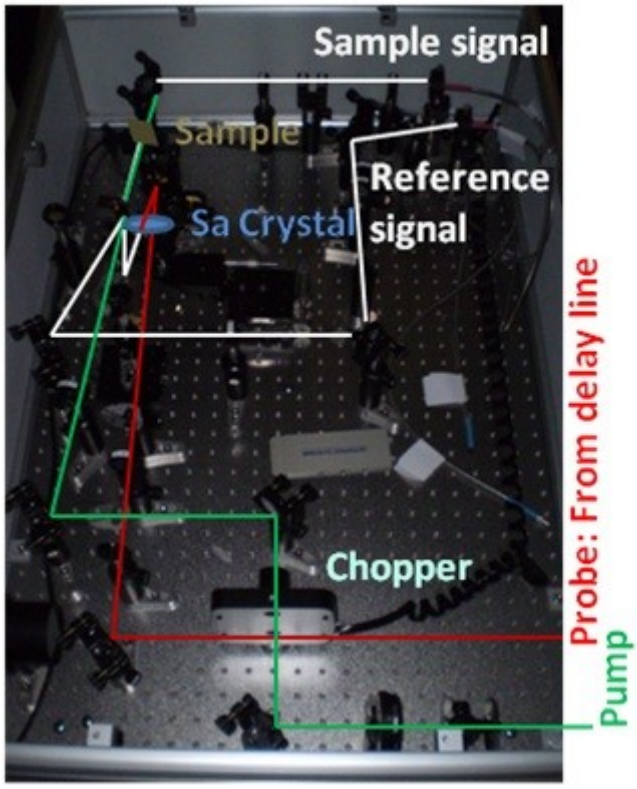

Figure 2.4. Spectrometer area or "experiment" area showing the "chopping" of the pump pulse, the generation of white light in the Sa crystal, the alignment of the pump and probe pulses in the sample and the reference and sample detectors.

The used detectors are imaging spectrometers, that is, they measure the change in intensity at all wavelengths at the same time, and therefore they are much faster in processing large amount of

data, permitting us to have transient spectra (ΔOD vs λ and vs *t*) and not just transients as a function of time, (ΔOD vs *t*) which would be the case if usual monochromators were used. The change in intensity is measured by chopping the pump pulse as shown in *Figure 2.5*. The probe is detected with and without the presence of the excitation pulse, which repetition rate is decreased from 1 KHz to 500 Hz by the chopper, therefore the probe pulses that are frequency-aligned with the pump pulse will be partly absorbed by the excited state, whereas the pulses that are not aligned with a pump pulse will present an absorbance only from the ground state. From the difference in the intensity of this pulses, and with I_0 , ΔOD can be obtained in the same way shown in *Equation 2.5*.

The instrument response function (IRF) of this system is ~200 fs, taken from the full width at half maximum (FWHM) of a scattering signal, well below the characteristic times of the processes herein observed. All films were measured inside quartz cuvettes under a nitrogen atmosphere.

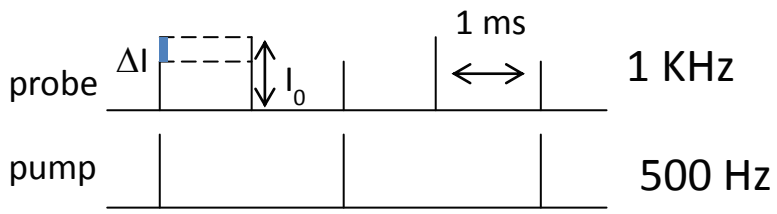

Figure 2.5. Chopping scheme for the pump pulse showing how the difference in pulse intensity is measured.

2c.5. TAS data analysis

a. Signal assignment in μs-TAS

The first step in the data analysis is the assignment of signals. We usually probe at wavelengths between 900 and 1400 nm, where we know the charges are likely to absorb. With the polymer blends and neat films that we have used, we have always observed positive ΔOD signals, which should correspond to an excited state absorption, that is, the absorption of an excited state to an upper excited state, as it is explained in more detail below. At these time scales however, singlet excitons have usually completely decayed, so that the only possible choice of signals is either triplets or polarons, or a combination of both. It is relatively easy to differentiate between triplets and charges. Triplets, when excited with sufficiently low intensity present unimolecular dynamics, (usually non-radiative decays, since the transition $S_0 \leftarrow T_1$ is spin forbidden[5]) and therefore obey the rate-law in *Equation 2.6a* and its integrated form in *Equation 2.6b*.

$$-\frac{d[T]}{dt} = k_{obs}[T] \quad \text{(Eq. 2.6a)}$$

$$[T](t) = [T]_0 e^{-t/\tau_{obs}} \quad \text{(Eq. 2.6b)}$$

Where $[T](t)$ is the triplet concentration at any time, $[T]_0$ is the initial concentration of triplets (at $t = 0$) and τ_{obs} is the characteristic decay time, which considers any possible triplet emission and is defined by $\tau_{obs} = 1/k_{obs}$.

Polarons, as explained in the previous chapter, decay by recombining with the oppositely charged polarons. The charges can recombine either by geminate recombination, in which the still bound polaron-pair recombines before it can form free charges or by non-geminate recombination, which involves the encounter of two already separated charges that have been generated from different polarons. These two regimes have a different kinetic behaviour. Geminate recombination involves a species that comes from the same exciton, therefore obeys the same type of kinetics as triplets, in *Equation 2.6*. It should be noticed that pure exponential decays are hardly observed, and often either multiexponential or streteched exponentials are better models for the experimental data. This is because of the energetic disorder that polymers present. Since excitons of different sizes and with a distribution of energies populate the excited state, exponential decays are "stretched" according to the function that describes the distribution of energies (usually exponential).[6]

Non-geminate recombination involves charges that were generated from different initial excitons, therefore, it would follow a second-order kinetic scheme. Considering that the number of opposite charged charges is balanced (for every free negative charge, there is a free positive charge; $n = p$) then the rate law is described by *Equation 2.7a* and its integrated form in *2.7b*.

$$-\frac{dn}{dt} = kn^2 \quad \text{(Eq. 2.7a)}$$

$$n = \frac{n_0}{1 + n_0 kt} \quad \text{(Eq. 2.7b)}$$

Where n is the charge density in cm^{-3} at any time, and n_0 is the initial charge density after excitation. This is the simplest scenario in which charges recombine non-geminately, which is, however hardly observed in our measurements. This is mainly because, as proposed by Nelson[6], and observed in many other studies that covered charge recombination dynamics[7–10], an exponential

distribution of trap states needs to be considered to describe the observed data, so that k, the non-geminate recombination constant is also a power function of the charge density n, $k(n) = k'n^{\beta}$.

In this case the rate law does not describe simple second order kinetics, but rather a rational dependence on n as depicted in the rate law in *Equation 2.8a* and its integrated form in *Equation 2.8b*. $2 + \beta$ corresponds to the total order of the reaction (not its molecularity). These equations assume that the positive charge and negative charge concentrations are the same ($n = p$). It can also be proved that a power-law is obtained when an exponential distribution of states is present in the system, in which the charges are thermally activated to leave the energy traps.[6]

$$-\frac{dn}{dt} = k'n^{2+\beta} \qquad \text{(Eq. 2.8a)}$$

$$n = \frac{n_0}{(1 + k'\beta' {n_0}^{\beta'} t)^{1/\beta'}} = \frac{n_0}{(1 + at)^{1/\beta'}} \qquad \text{(Eq. 2.8b)}$$

Where $a = k'\beta' {n_0}^{\beta'}$ and $\beta' = \beta + 1$. k' is the recombination constant independent of charge density. Notice that this function tends to n_0 when $t \longrightarrow 0$, thus presenting a plateau at short times. Whenever $1 \ll at$, (or for the effect, $(1/a) \ll t$) the dependency of n with respect to t obeys a power-law as shown in *Equation 2.9*. This is the most used equation to fit data of polaron non-geminate recombination at the microsecond timescale, since it is easy to recognise when it is plotted in a log-log graph, for it should follow a straight line, as shown later in *Figure 2.9*.

$$n \cong n_0 a^{-1/\beta'} \cdot t^{-1/\beta'} = A \cdot t^{-\alpha} \qquad \text{(Eq. 2.9)}$$

Where $A = n_0 a^{-1/\beta'} = (k'\beta')^{-1/\beta'}$ and $\alpha = 1/\beta'$. α is related to the total order of the reaction $2 + \beta$ by using the definitions of α and β': $2 + \beta = 1 + {}^{1}/_{\alpha}$. α is usually a small rational number between 0.25 and 0.9, depending on the scale of energetic disorder, i.e. the amount and distribution of charge trap energies, which varies greatly with processing conditions[10] and with the morphology of the blend. From this, we notice that the reaction orders can deviate greatly from bimolecular recombination.

The condition to make the approximation in *Equation 2.8b*, should be taken carefully, particularly at fast timescales when the approximation might fail. In these cases, a fit of the type described in *Equation 2.10* might be more convenient when plotting in a log-log scale. Careful attention should be given to the meaning of the fitting parameters, as from the logarithm of *Equation 2.8b* (and

defining $y = \log n$) it can be proved that the constants A and α in *Equation 2.9* are not comparable to b and c in *Equation 2.10*.

$$y = a + b * x^c \qquad \text{(Eq. 2.10)}$$

Summarizing, we can see that the distinction between the assignment of triplets and free charges is relatively straightforward if low excitation densities are used and only non-geminate recombination is present if charges are present. If there is a fast, exponential decay that precedes the power-law area of the decay, it could be difficult to make that distinction. In general, another way to determine the presence of triplets, is the use of an oxygen atmosphere to quench the triplets signal, which is specific to the presence of triplets. Energy is transferred from the polymer triplet state to the oxygen ground triplet state, therefore adding one more route of triplet decay and decreasing the triplet lifetime. Therefore, if a monoexponential decay is present at low excitation energy densities and is quenched by the presence of an oxygen atmosphere, then it should correspond to triplets.

For all the studies presented in this thesis in the μs timescale, signals corresponding to charges showed the characteristic power-law decay dynamics corresponding to non-geminate polaron recombination therefore simplifying the signal assignment. *Figure 2.6* shows an example of a signal containing both triplets and charges. The early decay can be fitted to an exponential decay, and could be confused with a geminate recombination phase, however when the measurement is repeated in the presence of oxygen, the early signal is quenched, while the signal of the charges is not. All data was analysed using Origin 8.6.

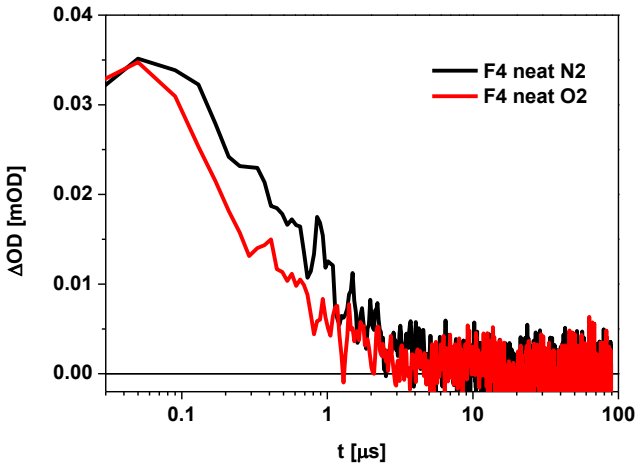

Figure 2.6. Mixed triplet and singlet signal for a low-bandgap neat polymer in nitrogen (black) and oxygen (red) showing a faster decay in the presence of oxygen, indicating the presence of triplets.

b. Signal assignment in sub-ps TAS

Contrary to what we observe at longer timescales, where the assignment is centred on determining whether the signals come from either triplet or polaron absorption, in ultrafast TAS, there are more processes and species that can be observed, since the probe is at least six orders of magnitude faster than our microsecond TAS setup. In general, we can observe three main processes, as depicted in *Figure 2.7*, which shows the possible contributions to the observed transient spectra, marked with a black line. The positive contribution in the black line comes from a superposition of the absorptions of different excited or transient states (ESA). For the materials studied herein it can correspond to a singlet exciton absorption, $S_1 \rightarrow S_n$, a triplet absorption $T_1 \rightarrow T_n$ or a polaron absorption S_0 (P^+) $\rightarrow S_1$ (P^+). In *Figure 2.7,* we illustrate these processes for singlet excitons and polarons in terms of molecular orbital energies. Excitons have the narrowest bandgaps and thus appear at lower energies (higher wavelengths) as we show with grey arrows and a gray line in the transient spectrum. Polarons have slightly wider bandgaps and thus their absorption is slightly blue shifted with respect to excitons, as shown with a green arrow and a green line in the transient spectrum.

The negative contributions to the signals mainly come from two processes. The most common one is named ground state bleaching (GSB, orange line in *Figure 2.7*) which usually appears at the wavelengths where the ground state absorbs and has a distinctive negative feature, since there is a depletion of the population of the ground state that has been excited by the pump pulse (orange, first panel). As the excited state decays back to the ground state, this population builds back and therefore the signal becomes less negative or "recovers". Finally, another possible contribution to the negative signal can come from stimulated emission (SE, red line in Figure 2.7) which is the emission of a photon from the excited state as a result of the interaction with the probe pulse. Because the detector registers a higher light intensity as compared to the reference without the pump (see *Figure 2.4*) the absorption signal is negative. This signal usually appears red shifted to the GSB, frequently close to where the steady state PL emission appears. We notice however that for the studies presented in this study, we did not observe stimulated emission signals, even in neat films. This has also been the case for SE in films prepared with PPV derivatives, and it was assigned to a dominating ESA in the area where SE would appear[11].

In the studies presented herein, the excited state signal is usually complex, containing contributions from both singlet excitons and polarons (both polaron pairs and free polarons), and in some cases, at later times, triplet exciton absorption can be detected as well. In general, it is expected that the earlier signals correspond to singlet exciton absorption, which in the studies presented here and for low-bandgap polymers in the literature[12–15], usually have a maximum photoinduced absorption at

~1300 – 1500 nm. This can be confirmed by comparing the signal of the neat polymer film, expecting it to match with the early signal in the blend. Depending on the extent of exciton quenching, (which is known from the PL quenching studies) and therefore, on the intermixing of the acceptors within the polymer matrix, the exciton decay will be shortened accordingly, as explained in section 2c.2 and Equation 2.2.

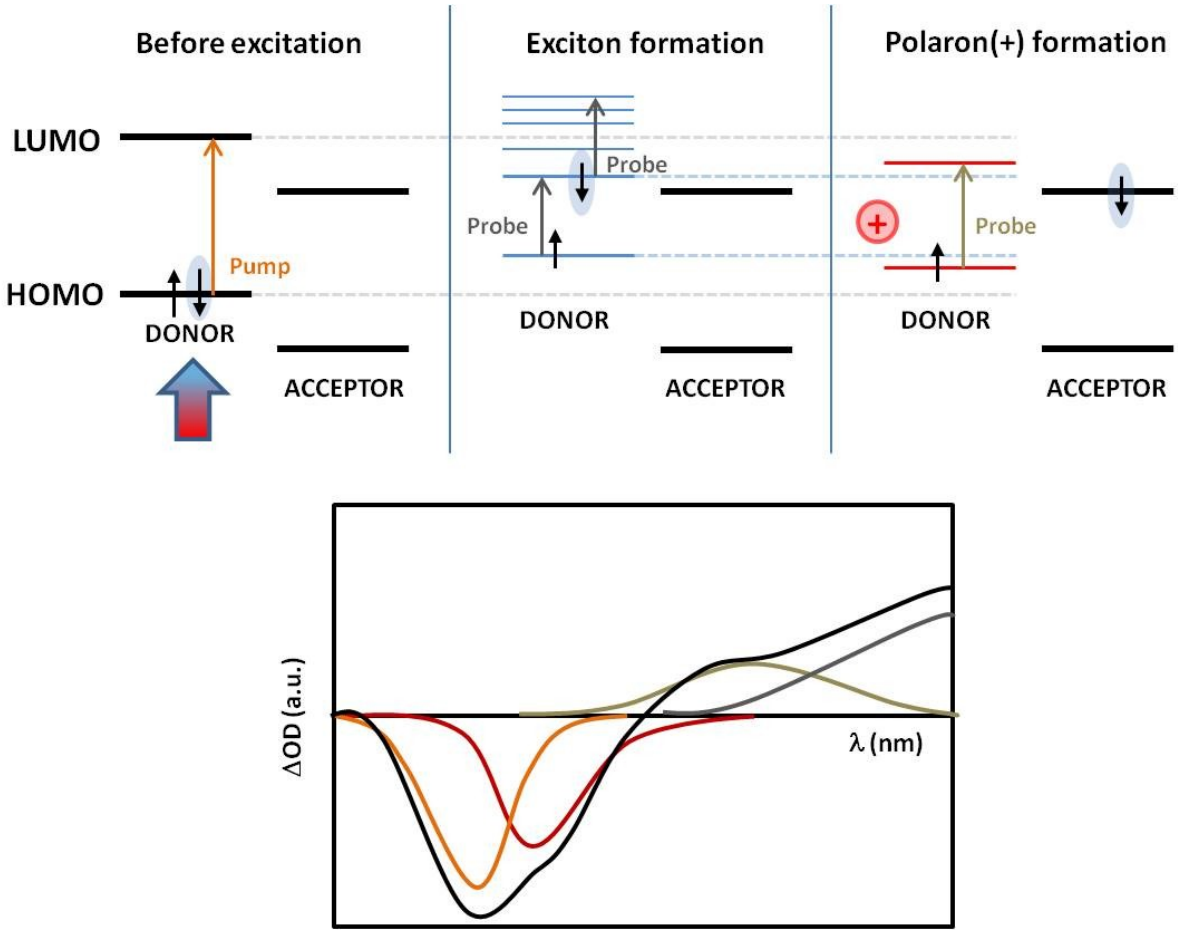

Figure 2.7. Signal components that can be observed after the excitation of an ultrashort pulse, and the species associated with the processes involved in the generation of charges (the formation of bound polaron pairs is omitted for simplicity). The black line corresponds to the resultant observed signal. The green and grey lines correspond to the excited-state absorption contribution, in the case of blend film absorption are usually assigned to excitons (grey) and polarons (green). The orange line corresponds to the ground state bleaching contribution and the red line corresponds to the stimulated emission. See text for more detail.

In Chapter 6, we observed the only case in which the exciton signal has been almost entirely quenched within the time resolution of the setup. Charges on the other hand, tend to have an absorption maximum at ~ 1000 – 1100 nm, and their generation process varies according to the

system. In most of the cases shown in this thesis, there is a proportion of polarons (possibly bound polaron pairs) that are generated faster or within our time resolution (< 200 fs) and another proportion of the polarons that are generated as the singlet excitons are being quenched. Therefore, the initial signal includes contributions of absorption of excitons and bound polaron pairs (or non-relaxed polarons). Once the polarons have relaxed, their spectra can be compared with that taken in the microsecond timescale, helping to confirm the identity of the signal

c. Signals as a function of excitation intensities

In this thesis, we are mainly concerned with the yield and dynamics of polarons. Another important probe to gain more information in the nature of the recombination is comparing the decays at different excitation fluencies. Studying the dynamics as a function of excitation intensity is another way to differentiate between geminate and non-geminate recombination. Because geminate recombination is a unimolecular process, it shows not only a monoexponential decay, but also, the recombination rate constant (and therefore the lifetime) is not expected to vary with the excitation intensity, this means that although the traces show an increment in the initial amplitude, the decay rate should be the same, in other words, the transients should be identical if normalized. In *Figure 2.8* we present an example of this type of behaviour in 1:1 blends of PBTTT/$PC_{70}BM$, showing intensity independent polaron decays assigned to the recombination of bound polaron pairs. This system will be discussed in more detail in Chapter 6.

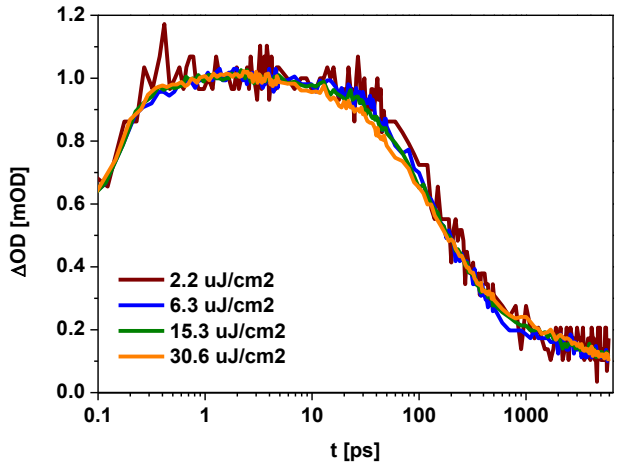

Figure 2.8. Example of intensity independent polaron decays in PBTTT/$PC_{70}BM$ blends assigned to the geminate recombination of bound polaron pairs.

Non-geminate recombination dynamics on the other hand, presents a strong dependence upon charge density, since the characteristic time, τ, is also dependent on charge density, differently from a unimolecular kinetics. There is one main effect in charge recombination dynamics that can be observed when the excitation intensity is increased: the appearance of an early, nanosecond decay; this decay is related with the saturation of the trap states that penetrate into de bandgap[16], therefore entering a regime in which the "trap-exceeding" free charges recombine faster, ideally with a bimolecular decay, followed by a slower recombination of the trapped charges. The observation of a fast phase as the laser intensity is increased is therefore an indication that this signal corresponds to non-geminate recombination rather than a fast, geminate recombination phase. In *Figure 2.9*, we present the effect of increasing the excitation intensity in the recombination dynamics of a polymer/$PC_{70}BM$ blend, showing a clear non-geminate behaviour (the decays are straight lines in a log-log plot). The amplitude of the fast phase is small but it is noticeable that it only appears at high laser intensities. The absence of this fast phase at low-excitation intensities can result in a "plateau" region as observed in *Figure 2.9*. The appearance of this plateau is important since it indicates that charge density variations before ~ 1 μs are negligible, therefore pointing out that processes such as geminate recombination or fast non-geminate recombination due to trap saturation are not taking place. We thus have used this regime as an indication of the intensity in which charge separation yield can be measured. Also noticeable is the increase of the fast phase, before 1 μs, corresponding to the recombination of free polarons or polarons in shallow traps, before the saturation of the slow phase, corresponding to the recombination of polarons in deep traps, corresponding to an incomplete thermalisation of the charges within the trap distribution.

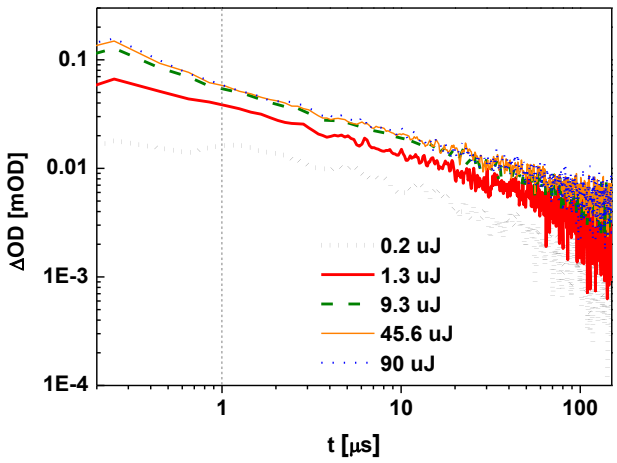

Figure 2.9. Polaron decay dynamics of a Ge-based low bandgap polymer /$PC_{70}BM$ blend showing the appearance of a fast phase at high excitation intensities.

2c.6. Wide angle X-ray diffraction (WAXD)

WAXD is a diffraction technique that provides information on the atomic spacing of ordered structures such as crystals or crystalline powders. It is based on the diffraction fundamentals that come from Bragg's law, in which the interatomic spacing (d) is related to the diffraction angle θ according to *Equation 2.10*, where n is the diffraction order and λ is the wavelength of the monochromatic source. This equation is derived from interference properties of light: constructive interference will only occur when the difference in the paths between the diffracted rays is an integer multiple of the wavelength of the light; this difference is $2d \sin\theta$.

$$n\lambda = 2d \sin\theta \qquad \text{(Eq. 2.10)}$$

Because the materials herein studied are inhomogeneous solid mixtures with semicrystalline components, in general we obtain information on how crystalline the material is as judged by the full width at half max (FWHM) and the height of the peak for a certain film thickness. Most of the polymers studied for OPV present either a lamellar or a hexagonal (or pseudo-hexagonal) packing depending on the molecular structure and the localization of the side chains[17]; the most common arrangement for the polymeric systems herein studied being the lamellar. In general, lamellar packing can take either the edge-on (or out-of-plane), or face-on (or in-plane) direction, as depicted in *Figure 2.10*. The edge-on configuration leads to the lamellar (or alkyl stacking) interaction to lie perpendicular to the substrate plane, whereas the $\pi - \pi$ stacking lies parallel to the substrate plane; conversely, the face-on configuration leads the lamellar interactions to be in the substrate plane, whereas the $\pi - \pi$ stacking is perpendicular to it.

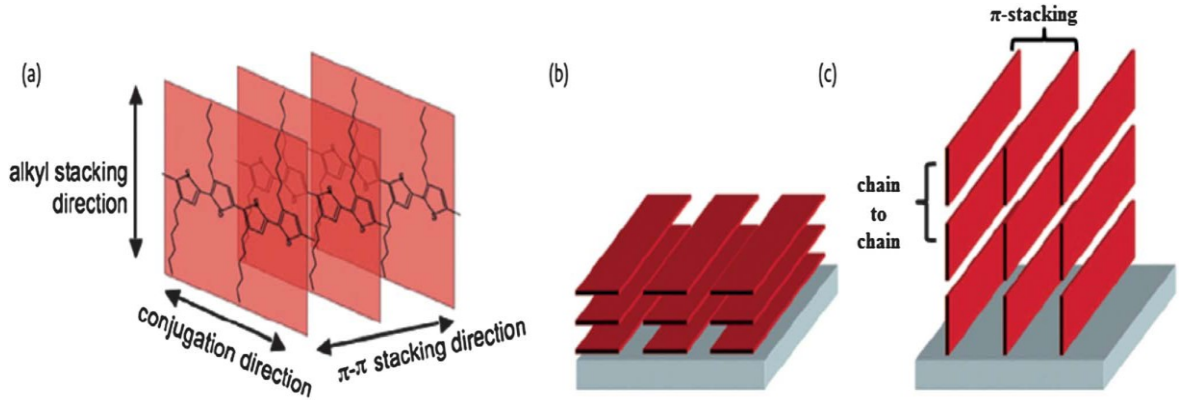

Figure 2.10. a) Crystallite structures in P3HT and the different configurations of lamellar packing, with a) face-on configuration and b) edge-on configuration. Figure taken from[18]

The setup used in this thesis only allows the detection of ordered regions in the out-of-plane direction, thus corresponding to $\pi - \pi$ stacking if the polymer has a face-on configuration and to lamellar or alkyl stacking, if the polymer adopts the edge-on configuration. WAXD measurements were carried out by Dr. Yvonne Soon and Ching-Hong Tan at the Materials Department of Imperial College, with a PANALYTICAL X'PERT-PRO MRD diffractometer equipped with a Nickel-filtered Cu Kα1 beam, with λ = 1.54 Å and an X' CELERATOR detector, using current I = 40 mA and accelerating voltage U = 40 kV. WAXD plots are presented as a function of the wave vector q, defined by Equation 2.9 and can be calculated from the value of the scattering angle 2θ using Equation 2.10 with $n = 1$.

$$q = \frac{2\pi}{d} = \frac{4\pi \sin\theta}{\lambda} \qquad \text{(Eq. 2.11)}$$

2c.7. Solar cell device measurements

The first and most widespread characterization of the performance of a solar cell is its *J-V* curve, as explained in Chapter 1, *J-V* curves are obtained by measuring device current densities as the voltage across the electrodes is varied, while the cell is held at a constant light illumination usually corresponding to 100 mW/cm^2 and with a spectral distribution matching that of the Sun at 48.2°, called 1.5 AM spectrum, this is accomplished by using a solar simulator.

Immediately after device preparation and still in the glovebox, they were placed inside a sample holder and sealed, then the *J-V* curves were taken with a Sciencetech SCI200 solar simulator based on a filtered 300 W xenon lamp. Light intensity (100 mW/cm^2) was calibrated using a Silicon photodiode (Newport UV-818) and the voltage was applied using a Keithley 238 Source Measure Unit, usually between -1 and 1 V. A spectral mismatch correction factor was used to correct J_{SC}, to account for the different spectral response of the photodiode with respect to the solar cell to be measured, as well as for the differences in the spectra of the solar simulator and the standard conditions.

2d. References

(1) Jamieson, F. C.; Domingo, E. B.; McCarthy-Ward, T.; Heeney, M.; Stingelin, N.; Durrant, J. R. *Chem. Sci.* **2012**, *3*, 485.

(2) Mikhnenko, O. V.; Azimi, H.; Scharber, M.; Morana, M.; Blom, P. W. M.; Loi, M. A. *Energy Environ. Sci.* **2012**, *5*, 6960.

(3) Bruno, A.; Reynolds, L. X.; Dyer-Smith, C.; Nelson, J.; Haque, S. A. *J. Phys. Chem. C* **2013**, *117*, 19832.

(4) Cook, S.; Furube, A.; Katoh, R.; Han, L. *Chem. Phys. Lett.* **2009**, *478*, 33.

(5) Klessinger, M.; Michl, J. *Excited states and photochemistry of organic molecules*; 1995.

(6) Nelson, J. *Phys. Rev. B* **2003**, *67*, 1.

(7) Shuttle, C.; O'Regan, B.; Ballantyne, a.; Nelson, J.; Bradley, D.; Durrant, J. *Phys. Rev. B* **2008**, *78*, 1.

(8) Shuttle, C. G.; Hamilton, R.; Regan, B. C. O.; Nelson, J.; Durrant, J. R. *Proc. Natl. Acad. Sci.* **2010**, *107*, 16448.

(9) Maurano, A.; Shuttle, C. G.; Hamilton, R.; Ballantyne, A. M.; Nelson, J.; Zhang, W.; Heeney, M.; Durrant, J. R. *J. Phys. Chem. C.* **2011**, *115*, 5947.

(10) Clarke, T. M.; Jamieson, F. C.; Durrant, J. R. *J. Phys. Chem. C* **2009**, *113*, 20934.

(11) Schwartz, B. J.; Hide, F.; Diaz-Garcia, M. A.; Andersson, M. R.; Heeger, A. J. *Philos. Trans. R. Soc. London A* **1997**, *355*, 775.

(12) Dimitrov, S. D.; Wheeler, S.; Niedzialek, D.; Schroeder, B. C.; Utzat, H.; Frost, J. M.; Yao, J.; Gillett, A.; Tuladhar, P. S.; McCulloch, I.; Nelson, J.; Durrant, J. R. *Nat. Commun.* **2015**, *6*, 6501.

(13) Albert-Seifried, S.; Friend, R. H. *Appl. Phys. Lett.* **2011**, *98*, 223304.

(14) Gehrig, D. W.; Howard, I. a; Kamm, V.; Mangold, H.; Neher, D.; Laquai, F. *J. Phys. Chem. C* **2014**, *118*, 20077.

(15) Yamamoto, S.; Ohkita, H.; Benten, H.; Ito, S. *J. Phys. Chem. C* **2012**, *116*, 14804.

(16) Nogueira, A. F.; Montanari, I.; Nelson, J.; Durrant, J. R.; Winder, C.; Sariciftci, N. S.; Brabec, C. *J. Phys. Chem. B* **2003**, *107*, 1567.

(17) Chabinyc, M. L. *X-ray Scattering from Films of Semiconducting Polymers*; 2008; Vol. 48.

(18) Yao, Y.; Dong, H.; Hu, W. *Polym. Chem.* **2013**, *4*, 5197.

Chapter 3. DPP-based polymers for solar devices. A μs-TAS study.

Due to their red-shifted absorption, the use of narrow-bandgap, donor-acceptor polymers is a common strategy to target low-energy photons that otherwise would not participate in the light-to-energy conversion in solar cell devices. In this study, the concept of a driving energy for charge separation, ΔE_{CS} necessary for charge separation is explored and expanded for low-bandgap, DPP-based polymers according to our previous studies on thiophene-based polymers. A correlation is found between the charge yield in polymer/fullerene blends, as probed by μs-TAS, and ΔE_{CS}. Charge yield is also found to correlate with J_{SC} for the corresponding devices. A further direct correlation between J_{SC} and ΔE_{CS} was obtained, showing that blend energetics does not only impact upon V_{OC} but also upon J_{SC}. This emphasizes energetics importance. A value for ΔS_{TR}, the entropy gained by the charges upon thermalization, was also obtained by computing the values of ΔG_{CS}. In order to corroborate the validity of the correlations just described, two more low-bandgap DPP-based and two more non-DPP based polymers, pDTTGe-TPD and PGeDTBT (the last one analysed in Chapter 5) are presented and added to the correlation.

The introduction presents a literature review concerning DPP-based polymers, their properties and device performance. It also reviews on the correlations between the energetics of polymer/fullerene blends and the yield of free charge formation. Next, the experimental details of sample preparation are described, followed by the results section. The results discussion includes a description of the kinetics of the four DPP-based polymer/fullerene blends as well as of pDTTG-TPD and PGeDTBT. A discussion of the results is then presented, followed by conclusions and references.

3a. Introduction

3a.1. Charge separation and device performance of DPP-based polymers

Diketopyrrolopyrrole (DPP) based polymers have attracted considerable attention because of their low bandgaps, high mobilities and their potential to be used in tandem solar cells with a higher-wavelength absorbing polymers like P3HT.[1–8] Their low bandgaps are a result of relatively low energy LUMO levels due inclusion of the DPP moiety. This results in small $LUMO_D$ – $LUMO_A$ energy offset with $PC_{70}BM$.[1] Their LUMO energy tuning is then likely to be critical for an efficient charge separation. Therefore it is interesting to study the photophysical characteristics of a group of DPP-based polymers with small structural differences which modulate their LUMO level, and relate these material properties to their efficiency of charge separation in blends with $PC_{70}BM$. Two more low-bandgap Ge-based polymers are included in the results of this chapter, pDTTG-TPD[9], and PGeDTBT, analysed in detail in Chapter 5,[10] which for the sake of simplicity will be renamed G1 and F0. *Figure 3.1* shows the structures of the polymers in this chapter.

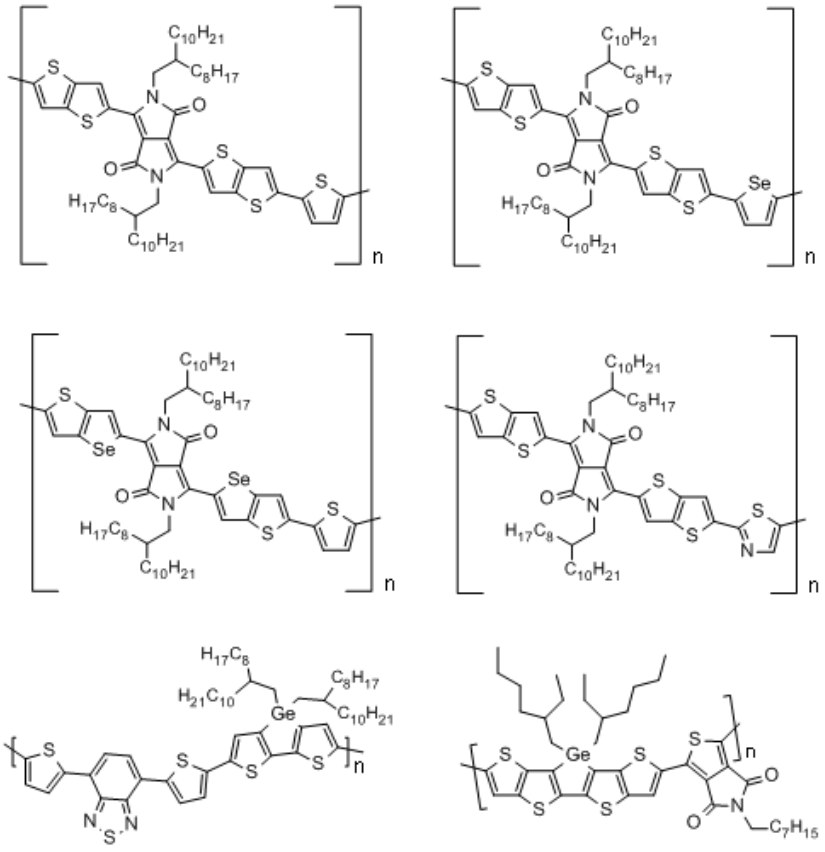

Figure 3.1. Structures of the polymers used for the studies in this chapter. From top to right, left to right: DPPTT-T, DPPTT-S, DPPST-T, DPPTT-Tz, PGeDTBT (herein F0) and pDTTG-TPD (herein G1)

An in-depth study of the device efficiency and morphology of polymer/fullerene blends for the four DPP-based polymers was conducted by Bronstein and co-workers.[1] *J-V* curves and figures of merit of conventional DPP-based polymer/$PC_{70}BM$ are shown in *Figure 3.2.* As can be observed in this figure, J_{SC} values are strongly dependent on the donor polymer employed. All four polymers exhibited similar neat and blend film crystallinity, and nanoscale phase segregation as shown by AFM, but substantially differing LUMO level energies (see below). As such, it was concluded that these polymer series was of particular interest to study the correlation between LUMO level energies, charge separation efficiency, and photocurrent density, as addressed in this chapter.

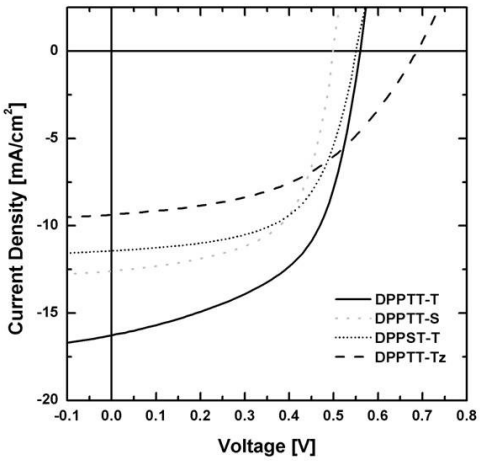

Polymer	Acceptor	V_{OC} [V]	J_{SC} [mA/cm^2]	FF	PCE [%]
DPPTT-T	$PC_{60}BM$	0.57	15.6	60	5.4
	$PC_{70}BM$	0.56	16.2	55	5.0
DPPTT-S	$PC_{60}BM$	0.55	10.8	62	3.7
	$PC_{70}BM$	0.55	11.4	60	3.8
DPPST-T	$PC_{60}BM$	0.50	12.6	61	3.8
	$PC_{70}BM$	0.50	12.6	60	3.8
DPPTT-Tz	$PC_{60}BM$	0.69	8.8	41	2.5
	$PC_{70}BM$	0.68	9.4	48	3.1

Figure 3.2. (Left) Current density vs. voltage characteristics of polymer/$PC_{70}BM$ devices with conventional architecture: ITO/PEDOT:PSS/Active blend/LiF/Al. (Right) Figures of merit of the same devices, measured under constant illumination with 100 mWcm^{-2}, AM1.5 spectrum from a solar simulated light at room temperature. The values of J_{SC} and V_{OC} were used in the analysis presented on the results section.

3a.2. Charge separation, ΔE_{CS} and ΔG_{CS}

At present, predicting an approximate V_{OC} for a working OPV device fabricated by a mixture of organic semiconductors, is relatively easy using experimentally determined material properties provided the device is stable enough.[11–15] Prediction of J_{SC} from material's properties had been more problematic, as discussed in Chapter 1.[16] A belief that an offset of 0.3 eV in the LUMO levels of the donor and acceptor materials is necessary to overcome the exciton binding energy is still widely spread among the OPV community.[17,18] However this model is accompanied by little experimental evidence and is unable to predict reliably the short circuit current of devices. In this chapter,

previous findings[18–21] on the relation between material energetics, the yield of charge separation and J_{SC} will be expanded for low-bandgap polymers.

In terms of one-electron energy levels the energy offset driving charge separation, we focus on, ΔE_{CS} as defined by *Equation 1.8* in Chapter 1, reproduced here.

$$\Delta E_{CS} = E_S - (IP_D - EA_A) \qquad \text{(Eq. 1.8)}$$

Where E_S is the exciton energy, IP_D is the ionization potential of the donor, and EA_A is the electron affinity of the acceptor. In thermodynamic terms, ΔE_{CS} corresponds to the energy released, or lost, in a reaction where an exciton (reactant) separates, due to the presence of a heterojunction, to form a pair of free polarons. It should be noted that there is a difference between ΔE_{CS} and ΔG_{CS}. This concept is illustrated in the state energy diagram in *Figure 3.3,* as well as the potential presence of bound polaron pairs. While the first one measures the energy offset of the polaron pair as $(IP_D - EA_A)$, the second one is defined by the electron and hole quasi-Fermi levels. The splitting of the quasi-Fermi levels by light irradiation determines the voltage output of the device (often referred to, at open circuit, as eV_{OC}, in the absence of other voltage losses) and corresponds to the energy stored by the photogenerated electrons and holes following thermalization within these Fermi levels (CS_{rel} in *Figure 3.3*). The difference in $(IP_D - EA_A)$ and eV_{OC} is given by $\Delta G_{CS} - \Delta E_{CS}$ and is proportional to the increase in entropy of the electrons and holes as they separate from the interface.[18] In this chapter, a calculation of the entropy of thermalization, ΔS_{TR} will be estimated for the series of low-bandgap polymers discussed.

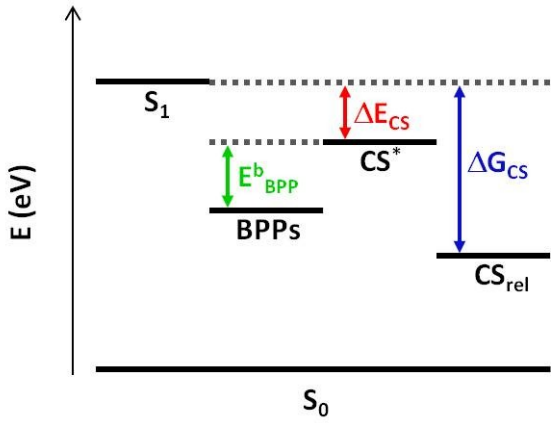

Figure 3.3. State energy diagram, adapted from reference[18]. BPP stands for bound polaron pairs and E^b_{BPP} refers to their binding energy. CS^* refers to the unrelaxed free charges, while ΔE_{CS} refers to the energy released (lost) when unrelaxed free charges are formed from initial excitons with energy S_1. CS_{rel} stands for thermally relaxed free charges, while ΔG_{CS} refers to the free energy lost when thermally relaxed charges are formed from excitons. Energies are referenced to the S_0 ground state.

Other studies have estimated the energy lost to entropy in different ways. Janssen and co-workers for example, have defined the so called *photon energy loss* as the difference between the polymer bandgap and V_{OC}, $E_g - eV_{OC}$.[4] This definition is equivalent to the calculation of ΔG_{CS}, however, because it depends on the magnitude of the splitting of the quasi-Fermi levels, it is sensitive to the light intensity and to non-geminate recombination.[18]

This chapter is primarily focused on testing whether the energy for charge separation as defined in *Equation 1.8*, correlates with the yield of free polarons, as obtained from the absorption amplitude of TAS signals of the positive polymer polarons for a series of low-bandgap polymers. This relationship has already been established for higher bandgap, thiophene-based polymer/fullerene blends[19,20], however in this study, the generalization of this relationship is to be confirmed to lower-bandgap polymers. Further, the chapter determines the extent of the impact of the efficiency of charge separation upon short circuit current in devices with the same active blends. Finally, the author tests whether a direct relation between the material's energetics could determine the short circuit current output of the device.

3b. Experimental section

Material properties such as molecular weight and PDI of the polymers herein analysed are provided in Chapter 2. Synthetic details of the polymers are provided in the supporting information of ref[1]. Glass substrates were cleaned under ultrasound sonication with acetone and isopropanol. Thin films were prepared by spin coating mixed solutions of the corresponding polymer and acceptors on the glass substrates. The conditions for the film preparation corresponded to the optimum device performance conditions. 1:2 blend ratios were used at 15-20 mg/mL and the films were spin coated at 2500 rpm with 1000 rpm/s acceleration rate, unless otherwise specified. Usual solvents used were chlorobenzene, dichlorobenzene and mixtures with chloroform. Solutions were prepared under normal air conditions and stirred overnight.

3c. Results

3c.1. Charge recombination dynamics of DPP-based polymer/fullerene blends

Figure 3.4 shows representative steady-state UV-vis spectra of the DPP-based polymers/$PC_{70}BM$ blend films studied in this chapter. The absorbance of all the blends at all wavelengths lies within similar OD values, (with a dispersion of OD ± 0.15) which is consistent with the films having similar

thicknesses and extinction coefficients. The polymer absorption part of the spectra (> 650 nm, approximately) shows marked vibrational structure, indicating that all of these polymers constitute relatively ordered blends with $PC_{70}BM$. This was also demonstrated via WAXD results of the blends[1]. It is also noticeable that the absorption onset varies from 870 nm for DPPTT-Tz to 930 nm for DPPST-T, indicating that the exciton energy E_S or ($S_0 \rightarrow S_1$) varies between polymer.

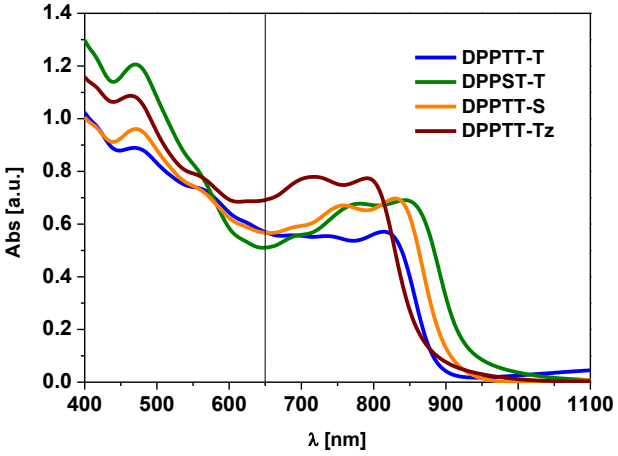

Figure 3.4. Steady state UV-vis absorption of DPP-based blend films with $PC_{70}BM$ at 1:2 blend ratios. The vertical line separates the areas of $PC_{70}BM$ predominant absorption (< 650 nm) and polymer predominant absorption (> 650 nm).

Figure 3.5a shows the transient spectra of DPTT-T and DPPTT-S at 200 ns after excitation at 800 nm and *Figure 3.5b* shows the transient kinetics for the four blends, taken at 1200 nm. These signals were not quenched in the presence of an oxygen atmosphere and thus were assigned to the photoinduced absorption of positive polymer polarons. Additionally, and confirming this assignment, the transients can be fit to power-law decays of the form $\Delta OD(t) = A \cdot t^{-\alpha}$. As explained in Chapters 1 and 2, this model has been proposed to correspond to non-geminate bimolecular recombination in the presence of an exponential density of trap states, whenever the exponent $\alpha < 1$.[18,19,22–27] If the exponent $\alpha = 1$, then pure bimolecular is observed, probably indicative of a physical situation in which no traps are present in the film. For all the blends studied in this chapter, the exponent $\alpha < 1$, as will be discussed below. Such behaviour was observed for early measurements of PPV systems and modelled in detail in terms of charge recombination in the presence of polaron trapping/detrapping[22]; it has been also used successfully to describe a number of polymer/fullerene TAS signals on the microsecond timescale.[18,19,24–27]A second phase at high laser intensities and early times (that can vary from a few hundreds of picoseconds to a few hundreds of

femtoseconds) has been observed in some blends and assigned to bimolecular recombination of untrapped charge carriers present when all the traps are occupied.[23,25]

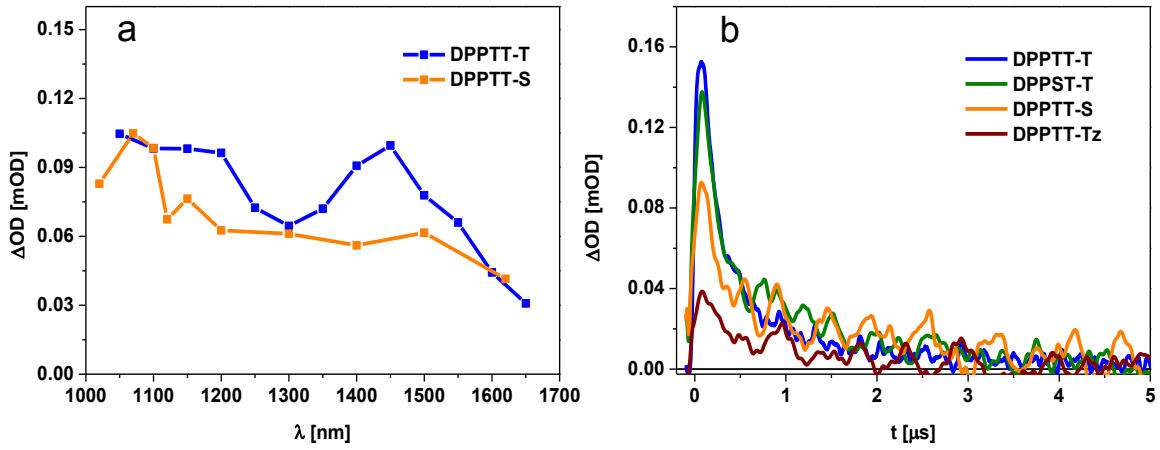

Figure 3.5. Transient absorption spectroscopy signals for 1:2 DPP-based polymer/$PC_{70}BM$ blends after excitation at 800 nm between 1 and 1.8 μJ/cm^2, a) transient spectra of DPPTT-T and DPPTT-S blends at 200 ns, b) polaron dynamics at 1200 nm.

The recombination dynamics for these polymer blends are significantly faster than those we have reported previously for other polymer blends at the same range of charge densities.[24] Such rapid recombination dynamics are consistent with the high carrier mobilities for this class of DPP polymers. This difference will be addressed quantitatively below through calculation of the bimolecular recombination constant k.

The value of α corresponding to the slow phase, has been related with the energetic distribution of the polaron trap states,[22,23,25] a higher α value corresponding to shallower trap states which require a smaller thermal energy to detrap, this is referred as to a *dispersive* recombination.[22] *Figure 3.6* shows two transients representing two blends with different donor polymers. The transients describe a linear behaviour in a log-log plot, in accordance with the explained model. For this polymer series, the slope of the transients is found to be similar for DPPTT-T, DPPTT-S and DPPST-T, but smaller for DPPTT-Tz, whose charge yield is also significantly reduced compared to the other three polymers. This is shown in *Figure 3.6 and Figure 3.7.* The smaller α in DPPTT-Tz is possibly related to the presence of deeper traps that need less thermal activation to detrap. The energetic characteristics of the traps have also been related to the crystallinity of the polymer films so that more crystalline domains would result in shallower traps.[16] However, this will not be considered here, since similar degrees of crystallinity were observed in the 1:2 blends of these polymers.[28] This

indicates that it is unlikely that the differences in charge recombination rate are related to crystallinity aspects of the blends. It can be noted that at the low excitation energy densities used to elaborate *Figure 3.5* and *Figure 3.6* (≈ 1.5 μJ/cm^2), the early fast phase assigned to the filling of traps is not observed, however, upon increasing the excitation intensity, this phase can be observed for DPPST-T, as shown in *Figure 3.7a*. A relatively low excitation intensity, compared to P3HT/fullerene systems,[16] is needed in the DPPST-T blends to observe the fast phase. This confirms that the high charge generation in DPPTT-T and DPPST-T blends could indeed be related to a reduction in the amount of trap states. This behaviour is not observed in DPPTT-S and DPPTT-Tz blends, where higher light intensities are needed to observe the fast decay phase (see *Figure 3.7b)*

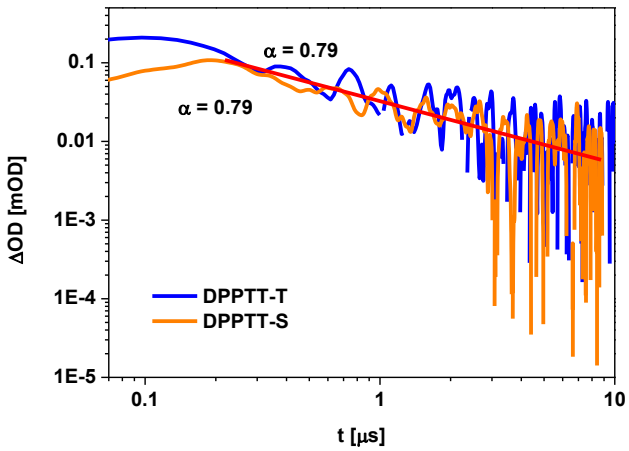

Figure 3.6. Log-log plot version of *Figure 3.5b*. The parameter α is obtained from a power-law fit shown as a red line. Only DPPTT-T and DPPTT-S blends with $PC_{70}BM$ are shown for clarity.

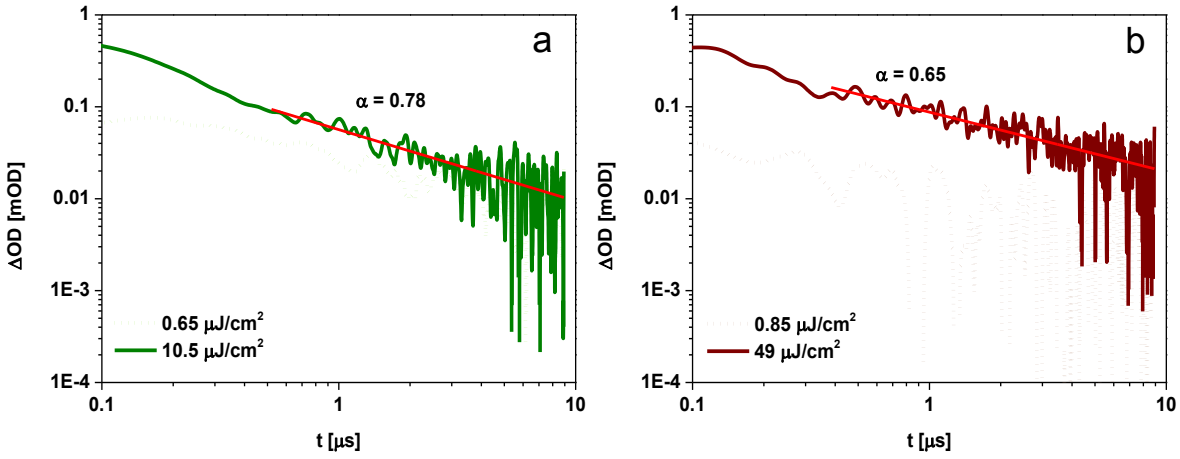

Figure 3.7. Transient absorption decays after excitation at 800 nm at low and high intensities for a) DPPST-T/$PC_{70}BM$ and b) right: DPPTT-Tz/$PC_{70}BM$. Red lines are fits to the slow phase of the decay to power-laws with exponents $-\alpha$ shown in the graph.

The rate constant for trap-limited non-geminate recombination can be obtained if the polaron extinction coefficient and the film thickness are known. The thickness of the films is 80 nm, and the polaron extinction coefficient was assumed to be $\varepsilon = 25{,}000\ M^{-1}cm^{-1}$ in agreement to the one reported for P3HT and a low-bandgap polymer IF-DTBT.[29] An estimate of the variation of the bimolecular rate reaction k as a function of charge density $n, k(n)$ can then be obtained, as previously reported for P3HT[24] and shown in *Figure 3.8* for DPPST-T and DPPTT-Tz. Notice that the slope β in *Figure 3.8* is useful as the reaction rate corresponds to $2 + \beta$, as explained in Chapter 2, and is related to α in *Figure 3.7* by $\beta = (1/\alpha) - 1$.

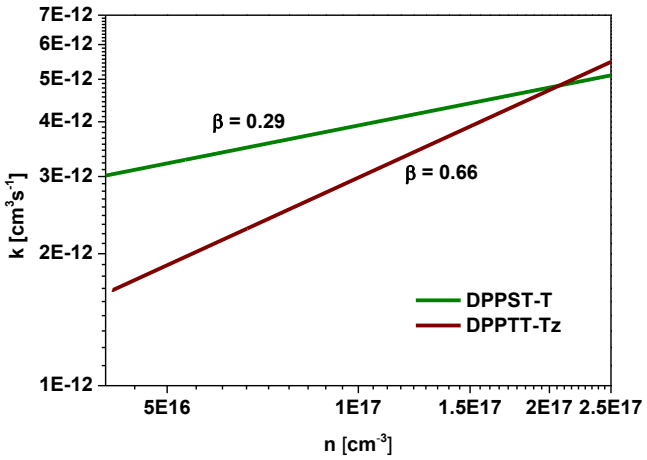

Figure 3.8. Plots of second-order recombination coefficient, k, as a function of carrier concentration, n, calculated from the fits in *Figure 3.4* for DPPST-T/$PC_{70}BM$ and DPPTT-Tz/$PC_{70}BM$ 1:2 blends.

From this analysis it can be observed, that the more "deviated" α is from 1, the more pronounced the dependence $k(n)$ is. It can also be concluded that the blend with DPPST-T has an overall reaction order of 2.3, while DPPTT-Tz has a reaction order of 2.5. As discussed by Dibb,[30] in these systems it is common to observe reaction orders higher than two, attributed to the charge trapping/detrapping processes discussed above. Note however, that obtaining reaction orders higher than 2 does not necessarily mean that the process of recombination is not bimolecular. The bimolecular rate coefficients k plotted in *Figure 3.8* are at least 10 times larger, at the same charge densities, than those reported for P3HT/$PC_{60}BM$ by Shuttle and co-workers.[24]

This faster recombination most probably primarily derives from the faster carrier mobilities reported for these DPP based polymers.[31–33] We note these values for k are still at least 3 times smaller compared to the Langevin predictions[34], consistent with the reported well defined phase segratation for these blends.[1]

Next, the results for two further polymers, pDTTG-TPD and PGeDTBT herein renamed G1 and F0 for simplicity, will be presented. F0 will be analysed in more detail in Chapter 5. These polymers also have a low-bandgap, however they are not DPP-based, as can be observed in *Figure 3.1*. *Figure 3.9a* shows the UV-vis spectra of the 1:2 blends with $PC_{70}BM$ for both of these polymers, while *Figure 3.9b* shows the transient absorption spectra at 150 ns after excitation at the corresponding polymer maximum absorption.

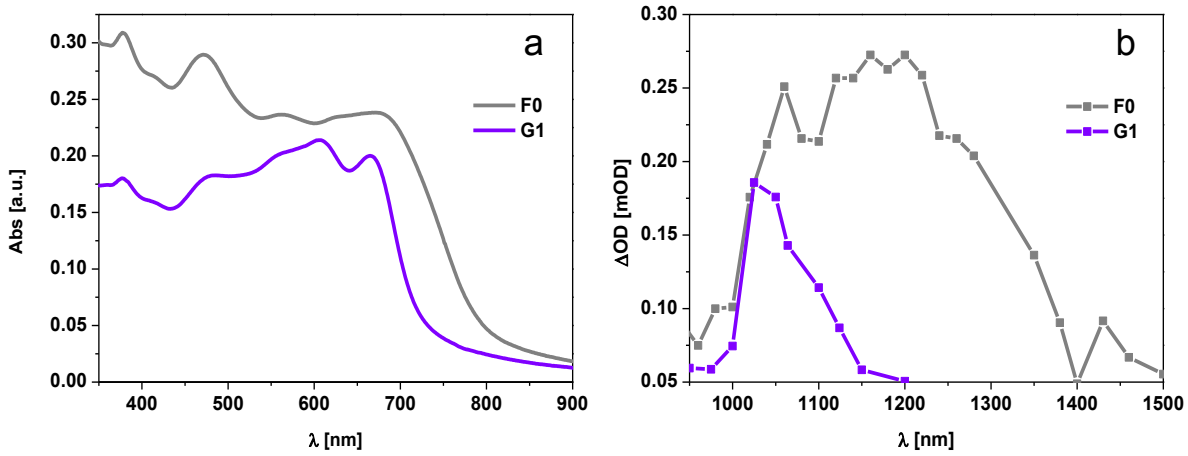

Figure 3.9. a) Left: Steady state UV-vis absorption F0 and G1 1:2 blends with $PC_{70}BM$. b) Right: transient absorption spectra of F0 and G1 at 150 ns after excitation at 660 and 600 nm respectively, with a fluency of 1 μJ/cm^2. The transient spectra were corrected for blend absorption at the excitation wavelength.

These signals, as for the DPP-based polymer/$PC_{70}BM$ blend ones, were not quenched in the presence of an oxygen atmosphere (see Chapter 5 for F0 blend in the presence of oxygen) and thus were assigned to the photoinduced absorption of positive polymer polarons. *Figure 3.10* shows the kinetics of the photoinduced absorption for F0 and G1. As can be observed, they describe power law decays with exponents $\alpha = 0.78$ for F0 and $\alpha = 0.44$ for G1, thus confirming the assignment of these signals to the absorption of positive polymer polarons in the presence of an exponential trap distribution.

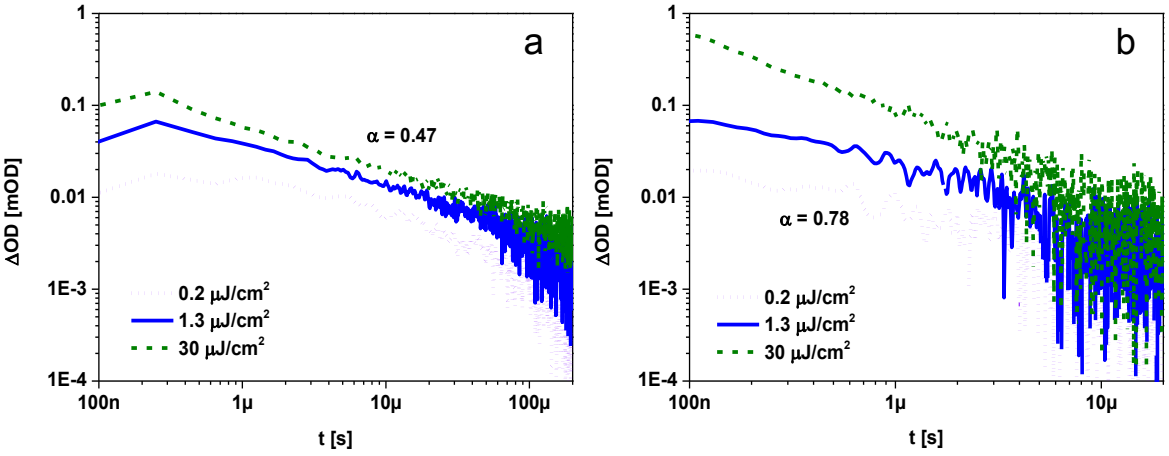

Figure 3.10. Transient absorption decays at different excitation intensities for a) 1:2 G1/$PC_{70}BM$ blend after excitation at 600 nm and probing at 1050 nm and b) 1:2 F0/$PC_{70}BM$ blend after excitation at 660 nm and probing at 1160 nm.

It is interesting however, that despite the similar steady-state absorption of F0 and G1, the absorption of the positive polarons of F0 is much broader as compared to that of G1. It is also noticeable in *Figure 3.10* that their decay dynamics are quite different. G1 presents a much slower and more dispersive decay (lower α) while polarons in F0 decay faster and present an early fast phase at high excitation intensities, indicating a regime of free charge recombination. This phase is barely noticeable for G1, however the decays seem to saturate extremely fast in this blend, as can be confirmed from the change in the initial amplitude when changing the excitation intensity from 1.3 μJ/cm^2 to 30 μJ/cm^2 (corresponding to a more than 20-fold increase in intensity) This is better shown in *Figure 3.11* where the amplitude at 500 ns is plotted at different excitation intensities. As can be observed in that figure, an early, approximately linear region extends within the same limits for both blends (until ≈ 1 - 2 μJ/cm^2). However, while G1 rapidly saturates, ΔOD in F0 seems to not be saturated even at 90 μJ/cm^2, confirming that a fast increasing phase is present only in the F0 blend, while also confirming that the decays correspond to the non-geminate recombination of charges in the presence of an exponential distribution of traps. This is also notably different from the amplitudes of the DPP-based blends which tend to saturate to smaller excitation intensities as compared to F0. The exponents of the power-law fits correspond to reaction orders of ≈ 2.3 for F0 and 3.3 for G1, thus suggesting that the distribution of traps and energetic disorder in both polymers are quite different.

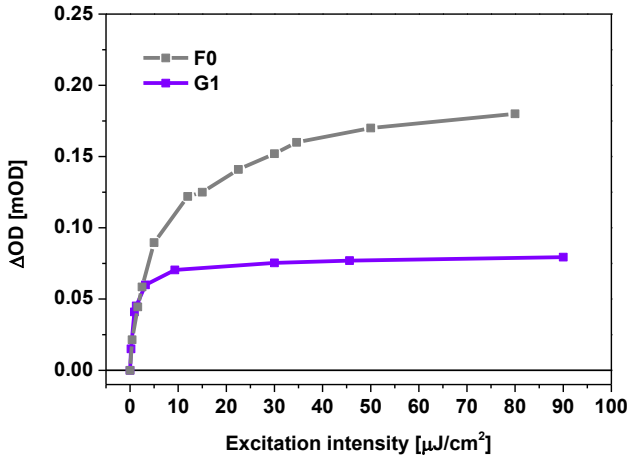

Figure 3.11. Transient absorption amplitudes at 500 ns as a function of excitation intensity for F0 and G1 1:2 blends.

Next, the results that show the calculations of ΔE_{CS} and its correlation with the initial amplitude ΔOD for the polymer/fullerene are shown for the polymers presented along with three additional polymers that were used to increase the ΔE_{CS} range.

3c.2. Driving energy for charge separation, ΔE_{CS} and its relationship with polaron yield in polymer/$PC_{70}BM$ blends and J_{SC} in the corresponding devices.

ΔE_{CS} was calculated according to Equation 1.8 by consistently approximating the ionisation potentials obtained via photoelectron spectroscopy in air (PESA) as the HOMO energies and then adding to this value the energy corresponding to the onset of the UV-vis absorption (considered to be the exciton energy, as discussed in Chapter 1) to obtain the LUMO energy. The value of $PC_{70}BM$ electron affinity (EA) energy was consistently taken as 3.7 eV to be consistent with a number of papers published in our research group[18,19]. The IP, EA, E_S and ΔE_{CS} for the blends herein analysed are included in the *Table 3.1*. Data for three more DPP-based polymers taken from previous literature[1], was included in *Table 3.1* and *Figure 3.12* to expand the ΔE_{CS} range studied.[28]

One of the most controversial issues in this analysis is the way the yield of charges is obtained. Whenever possible the data is taken from the early time plateau region in the ΔOD transients at low excitation densities which can be approximated as the initial charge density n_0 in *Equation 2.7b* in Chapter 2. For the polymers studied in this chapter, this often was not possible, due to the relatively fast non-geminate recombination losses. In these cases, the ΔOD was measured at the earliest time

and lowest excitation density possible, and then normalised to to 1 μJ/cm^2 and 100 ns to allow comparison between polymers. We note this is an approximate treatment, which does not fully eliminate contributions from non-geminate recombination losses prior to 100 ns. Errors associated with this approximation are likely to be a key cause of the 'noise' in the analyses reported below. However we note that these analyses employ a logarithmic scale for ΔOD such that only changes of at least one order of magnitude are notable, which appears to be greater than these errors.

Table 3.1. Ionization potentials (IP), exciton energies (E_S), electron affinities (EA), ΔE_{CS} and positive polaron absorption at 100 ns and 1 μJ/cm^2 for the polymer/$PC_{70}BM$ blends studied in this chapter. J_{SC} refers to the short circuit current of devices fabricated with the same active layer as the characterized films.

Polymer	IP (eV)	E_S[a] (eV)	ΔE_{CS} (eV)	ΔOD[b]	J_{SC} (mA cm^{-2})
F0[35]	5.04	1.57	0.23	3.74 x 10^{-4}	7.5
G1[9]	5.33	1.75	0.12	1.36 x 10^{-4}	13.9
DPPST-T[1]	5.0	1.35	0.05	8.04 x 10^{-5}	12.6
DPPTT-T[1]	5.1	1.40	0.00	1.50 x 10^{-4}	16.2
DPPTT-S[1]	5.1	1.37	-0.03	5.28 x 10^{-5}	11.4
DPPTT-Tz[1]	5.2	1.43	-0.07	1.85 x 10^{-5}	9.4
DTB-DPP[1]	5.3	1.48	-0.12	1.40 x 10^{-5}	5.2
BTT-DPP[36]	5.2	1.35	-0.15	2.40 x 10^{-5}	7.1
DPPT-TT[37,38]	5.4	1.42	-0.28	4.80 x 10^{-6}	6.3

[a] Obtained from the onset of the film UV-vis absorption

[b] ΔOD was taken (or escalated) at 1 μJ/cm^2 and 100 ns, from a plateau region.

It should be noted that uncertainties of ±0.02 eV are expected in the estimation of IP and E_S energies between measurements determined with the same experimental methods; however variations in values between different measurement methods can be much larger. As long as all the values are measured in the same way, these can be used to determine trends in energetics, rather than absolute values.

Figure 3.12a shows a plot of ΔOD vs ΔE_{CS} for the polymer/$PC_{70}BM$ blends energetics characterized in Table 3.1. *Figure 3.12b* shows a plot with additional results from previous measurements of other polymer-families blended with $PC_{70}BM$: thiazolothiazole-based polymers[18] in orange and thiophene-

based polymers in blue[19]. Both graphs were prepared normalizing ΔOD to one for the highest-absorbing polymer blend, which for the polymers analysed herein is F0.

For the four lowest charge generating polymers in the DPP-series, the calculated ΔE_{CS} is predicted to be negative. It should be noted however, that this value largely depends on the fullerene ($PC_{60}BM$ or $PC_{70}BM$) electron affinity. EA for these fullerenes however ranges in literature from 3.7 to 4.3 eV and there is no consensus on the correct value[39]. Aggregation of these fullerenes seems to play a role in the difficulty of the determination of this energy, since, as reported by Jamieson and coworkers,[40] the formation of domains of crystallised fullerene can result in a change in its electron affinity. With such a scenario, researchers have rather opted to determine their own EA consistent with the rest of their energy measurements to make it comparable, usually using CV measurements. For these measurements a $PC_{70}BM$ EA of 3.7 eV was used since this value is consistent with our previous measurements.[18] However, it should be kept in mind that if a $PC_{70}BM$ EA of, for example 4.1 eV had been used in *Table 3.1* and *Figure 3.11*, the whole series would be shifted 0.4 eV to positive values. In this sense, negative ΔE_{CS} should be considered as "very small driving energy for charge separation" rather than an indication of an "up-cascade scenario", that is, a situation in which the LUMO level of $PC_{70}BM$ lies higher in energy than that of the polymer, resulting in a poor electron transfer reaction.

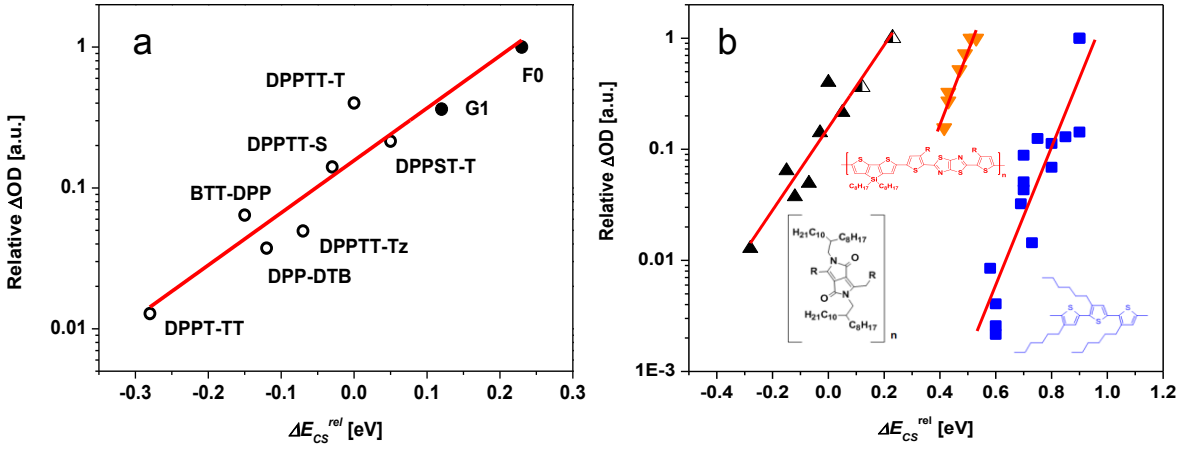

Figure 3.12. Normalized ΔOD amplitudes obtained at low excitation intensities and escalated to 1 μJ/cm^2 at plateau regions when possible, at 100 ns, plotted versus the calculated ΔE_{CS} obtained from Equation 3.1. a) For the polymers analysed in this chapter, plus BTT-DPP[36], DPP-DTB[1] and DPPT-TT[37,38]. b) DPP-series in a) plus two more series, thiazolothiazole-based polymer blends[27] in orange and thiophene-based polymers[19] in blue.

An interesting observation about *Figure 3.12* is that the polymers included were not selected to have any particular microstructure. The relationship thus seems to be general in spite of the polymer's individual morphologic particularities such as polymer domain size, crystallinity, donor/acceptor orientation or number of phases (molecularly intermixed vs pure phases). The blends were also chosen regardless of their processing details including blend ratios, use of solubilising additives or thermal annealing processes. Another aspect to point out is that variations in polaron extinction coefficients are not taken into account and are considered to be a source of scatter in this graph,[20] given that this affects the proportionality between ΔOD and charge density.

An important aspect to clarify is that the ΔOD of the polymer/fullerene blends herein analysed did not include any correction for the magnitude of PLQ. As determined in Chapter 4, this is not the case for DPPTT-T, and the same might true for the rest of the DPP-based polymers in the series, given that most of them present the same crystallinity and phase segregation as DPPTT-T.[1] The differences in ΔOD could then be argued to come from different electron transfer efficiencies. However, even if PLQ is incomplete for these series of polymers, it is likely that the differences in the quenching between the different polymer/$PC_{70}BM$ blends are small enough that, rather than causing the trend itself, they could cause noise in the data points.

The final aspect to discuss in the data presented in *Figure 3.11*, is the observation of almost parallel correlations of ΔOD vs ΔE_{CS} with different *y*-intercepts for the three different families included. While the slopes of the linear regressions in this figure vary only slightly, the *y*-intercepts vary 3 orders of magnitude in a linear scale. The *y*-intercepts in *Figure 3.11*, are proportional to the charge separation efficiency for a blend of the corresponding polymeric family when its $\Delta E_{CS} = 0$. Simultaneously, the *y*-intercept can also be interpreted as the necessary driving energy required to generate a minimum amount of charges. For example, it can be obtained, that to generate 1% of the amount of charges that F0 does (the best polymer within the DPP/low-bandgap series) a small $\Delta E_{CS} = -0.32\ eV$ is needed. This energy however increases to 0.22 eV for the thiazolothiazole series while it significantly increases to 0.64 eV for the thiophene series. The reason for these differences is unknown, but one can speculate that it could be related to a difference in the polymer's dielectric constant which makes charge separation intrinsically more or less demanding in terms of energy.[18] Other possibilities include a higher CT character of the excitons, as found for F4 in Chapter 5 or the orientation of the polymer and fullerene at the interface.[41]

Finally, *Figure 3.12a* presents the correlation between the short circuit current J_{SC} in devices fabricated with the same active layers and processing conditions as the corresponding active blends

and the initial amplitude of polaron absorption, ΔOD for those blends, whilst Figure 3.12b extends this to the correlation between J_{SC} and ΔE_{CS}.

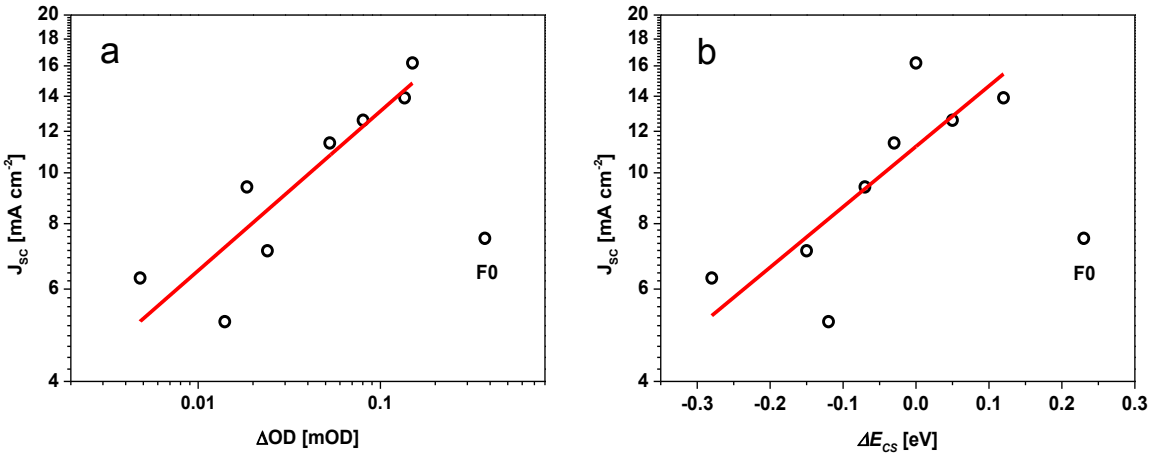

Figure 3.12. Plots using the data in *Figure 3.9a*, of a) log J_{SC} vs log ΔOD and b) log J_{SC} vs ΔE_{CS}. J_{SC} was measured in devices with active layers prepared with the same processing conditions as those of the corresponding blend films analysed in this chapter plus BTT-DPP[36], DPP-DTB[1] and DPPT-TT[37,38]. In red, linear fits of the experimental data excluding F0 for the regression.

As can be observed from this figure, previously reported for thiophene-based polymers[20], a double-logarithmic relationship is observed between the amplitude of the 100 ns polaron absorption and the obtained short circuit current in the corresponding devices. An analogous correlation is observed between ΔE_{CS} and log J_{SC}. This correlation suggests that photocurrent is determined (although certainly not only determined) by the yield of dissociated charges in the blend films.[27] Unlike the linear relationship found by Clarke and co-workers for thiophene-based polymer/fullerene blends,[20] the dependence found in this figure is sub-linear, with a slope $m = 0.30$. Whilst the origin of this behaviour is unclear, it may be related to a trend in optical bandgap, with the low charge separation quantum yields for the lower ΔE_{CS} polymers being partly offset by enhanced light harvesting. A full analysis of this would require optical modelling of the device, beyond the scope of this thesis. The data points for F0 were not considered for both linear regressions. This blend clearly deviates from this trend, most probably due its particularly fast non-geminate recombination dynamics, limiting its J_{SC} consistent the conclusions of Chapter 5.[14]

Figure 3.12b presents the correlation between the calculated ΔE_{CS} and J_{SC} in the corresponding devices. Since a correlation between the charge yield and ΔE_{CS} for low-badgap polymers/fullerene blend films was demonstrated in *Figure 3.11a,* and separately, a correlation between J_{SC} and charge

yield was also found, it was interesting to assess whether ΔE_{CS} could directly impact upon the short circuit current of the devices. Although the scattering is high, one can observe that a clear correlation between ΔE_{CS} and J_{SC} as reflected in the squared Pearson coefficient $r^2 = 0.71$. From this result it can then be concluded, that the driving energy for charge separation directly impacts on J_{SC}, and is indeed its primary determinant, for this series of donor/acceptor polymers. This dependence is indicative of the importance of geminate recombination losses in limiting photocurrent generation in this polymer series, and emphasises the importance of minimising such losses for efficient device performance.

Figure 3.12b presents the correlation between the calculated ΔE_{CS} and J_{SC} in the corresponding devices. Since a correlation between the charge yield and ΔE_{CS} for low-badgap polymers/fullerene blend films was demonstrated in *Figure 3.11a,* and separately, a correlation between J_{SC} and charge yield was also found, it is interesting to assess whether ΔE_{CS} could directly impact upon the short circuit current of the devices. A log-linear relationship between J_{SC} and ΔE_{CS} is expected from *Equation 3.2*. This equation was derived using *Equation 1.16*[14] and the definition of ΔE_{CS} of *Equation 1.8*, and solving for J_{SC}.

$$\ln J_{SC} = A + \frac{\Delta E_{CS}}{B} \qquad \text{(Eq. 3.2)}$$

Where $A = \ln J_{BI} + (eV_{OC} - E_S)/n_{id}k_BT$ and $B = n_{id}k_BT$, J_{BI} is the current lost due to non-geminate recombination and n_{id} is the ideality factor in the non-ideal diode equation. It should be noted that this relationship relies on the assumption that the variables in A and B do not depend upon ΔE_{CS}, which is certainly not the case for J_{BI} or V_{OC} and as such, is just an approximate model.

Although the scattering is high, a linear relationship between $\ln J_{SC}$ and ΔE_{CS} is observed and reflected in the squared Pearson coefficient $r^2 = 0.71$. From this result it can be concluded, that the driving energy for charge separation does directly impact on J_{SC} whenever the blends used are not limited by charge mobility or severe geminate/non-geminate recombination.

3d. Discussion

In this chapter, a thorough characterization of the non-geminate recombination dynamics for a group of low-bandgap polymers, including DPP-based and Ge-thiophene based polymer types was

performed. An analysis similar to the one done by Shuttle and co-workers[24] was included for two representative DPP-based polymers, in which the charge density dependence of the recombination constant k was assessed and the reaction order determined. The magnitude of k at the same charge density was found to be almost 10 times larger compared to that determined by Shuttle for P3HT/PC_{60}BM blends and devices.

The second part of this study demonstrates firstly, the validity of the correlation between the free polaron yield, as assessed via μs-TAS measurements, and the driving energy for charge separation, irrespective of their relative donor-acceptor strength. Further into this discussion, and given the definitions of ΔE_{CS} and ΔG_{CS} in *Figure 3.1,* an estimation of the entropy gained as the charges separate and thermally relax can be estimated if ΔE_{CS} is considered as an enthalpic energy. *Figure 3.13* shows this analysis.

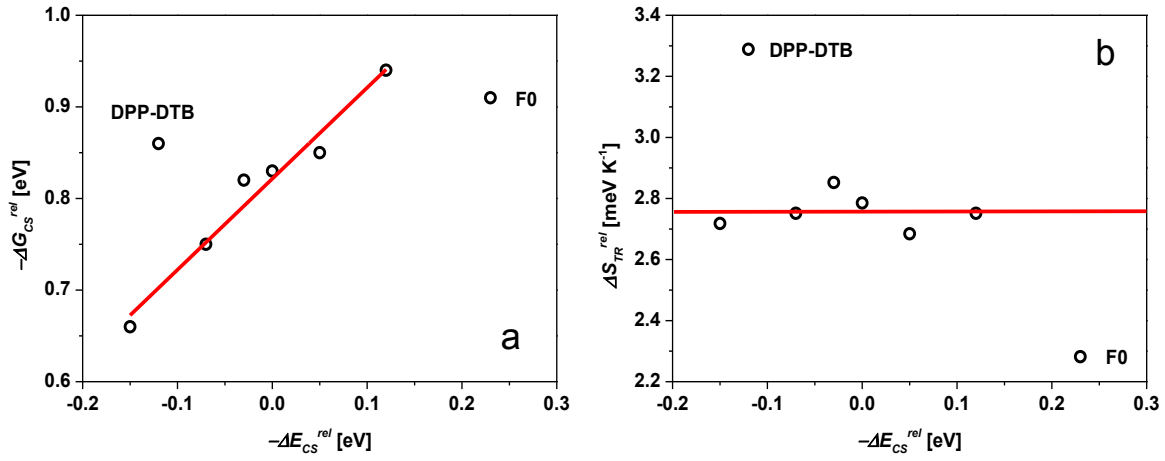

Figure 3.13. a) Linear plot of $-\Delta G_{CS}$ vs $-\Delta E_{CS}$, the red line correspond to a linear fit with slope $m \approx 1$ and b) Calculated ΔS_{TR} vs $-\Delta E_{CS}$, the red line is a constant calculated by a minimum squares procedure.DPP-DTB and F0 were excluded of the regression.

ΔG_{CS} was estimated in the same way as Janssen and co-workers[4] by $-\Delta G_{CS} = E_S - eV_{OC}$. As expected, when plotting $-\Delta G_{CS}$ vs $-\Delta E_{CS}$ a slope very close to 1 was obtained ($m = 0.994 \pm 0.009$) therefore indicating that an estimation of the thermalization entropy, ΔS_{TR} is valid. In order to obtain ΔS_{TR}, the basic equation of thermodynamics, $\Delta G_{CS} = \Delta E_{CS} - T\Delta S_{TR}$ was used. As expected, a constant was obtained when plotting ΔS_{TR} vs $-\Delta E_{CS}$. Using a minimum squares procedure, the value of the thermalization entropy was calculated to be $\Delta S_{TR} = 2.76\, meV \cdot K^{-1}$. This value has the same order of magnitude as those estimated in ref[42].

Secondly, the validity of the correlation between the dissociated polaron yield and the short circuit current in devices with the same active blend is also established for this group of polymers, as it has been done before for other polymer families.[20,38] Even more interesting, a direct correlation was established between the short circuit current of the devices and the driving energy for charge separation in the corresponding blends. While a log-log relationship was found for the dependence of J_{SC} on the charge yield, a log-linear relationship was obtained for these variables, in agreement with the observed logarithmic dependence of charge separation yield upon energy offset. Notice that, ΔE_{CS} is not by any means the only determinant of the magnitude of J_{SC}. Material properties such as microstructure, solubility of the polymer and fullerene, aggregation or presence of pure material phases can extensively affect the yield of charges, as discussed in the following chapters. However these are not the only variables influencing the magnitude of J_{SC}, in working devices other factors must be taken into consideration, such as the $\mu \cdot \tau$ product, the thickness of the device, electrode shunting and so on. Given these considerations, it is particularly striking that a clear correlation is observed between ΔE_{CS} and J_{SC}, indicating that, for this polymer series, the energetics of charge separation are the dominating determinant of photocurrent generation. Although the direct relationship between ΔE_{CS} and J_{SC} had not been demonstrated before, the influence of blend energetics had been discussed before and agrees with the model of charge separation described in earlier contributions.[20,42]

Finally, the issue of the different energy offsets required to generate a fixed yield of charges for the different polymeric families (different *y-intercepts* in the ΔOD vs ΔE_{CS} plot) still needs further investigation, however it seems likely that a combination of higher dielectric constants and higher excitonic CT characters shift the ΔE_{CS} necessary to generate efficiently charges.[18] Although the orientation of the polymer with respect to the fullerene is a hypothesis that has gained attention as a plausible explanation for increased charge separation efficiency,[41] it seems quite difficult to generalize this idea to a family of polymers, even if they present similar crystallinities and morphologies, since the molecular packing is extremely sensitive to minimum structural differences in the polymer backbone, as it will be demonstrated in Chapter 5.

3e. Conclusions

In this study, a characterization of non-geminate recombination dynamics using μs-transient absorption spectroscopy is shown for a group of low-bandgap polymers. The dependence of the recombination constant on charge density is shown as well as a calculation of the order of the

recombination reaction for a couple of DPP-based polymers. A relationship between the yield of charges, as evaluated from the amplitude of the TAS decays at low excitation intensities, and ΔE_{CS} is extended to these low-bandgap polymers however, reaching high yield of charges at lower ΔE_{CS} values compared to other polymeric families. Following the definitions of ΔG_{CS} and ΔE_{CS}, the value of the entropy of charge thermalization, ΔS_{TR} was determined to be $2.76\, meV \cdot K^{-1}$. Finally a relationship was established between the short circuit current of the corresponding devices and the yield of charges, and more interestingly, between the yield of charges and ΔE_{CS}, indicating that the current is largely determined by this energy for this polymeric family.

3f. References

(1) Bronstein, H.; Collado-Fregoso, E.; Hadipour, A.; Soon, Y. W.; Huang, Z.; Dimitrov, S. D.; Ashraf, R. S.; Rand, B. P.; Watkins, S. E.; Tuladhar, P. S.; Meager, I.; Durrant, J. R.; McCulloch, I. *Adv. Funct. Mater.* **2013**, *23*, 5647–5654.

(2) Wienk, M. M.; Turbiez, M.; Gilot, J.; Janssen, R. A. J. *Adv. Mater.* **2008**, *20*, 2556–2560.

(3) Turbiez, M.; Leeuw, D. M. De; Janssen, A. J. **2009**, 16616–16617.

(4) Li, W.; Roelofs, W. S. C.; Wienk, M. M.; Janssen, R. a J. *J. Am. Chem. Soc.* **2012**, *134*, 13787–13795.

(5) Hendriks, K. H.; Heintges, G. H. L.; Gevaerts, V. S.; Wienk, M. M.; Janssen, R. a J. *Angew. Chem. Int. Ed. Engl.* **2013**, *52*, 8341–8344.

(6) Li, W.; Hendriks, K. H.; Furlan, A.; Roelofs, W. S. C.; Wienk, M. M.; Janssen, R. a J. *J. Am. Chem. Soc.* **2013**, *135*, 18942–18948.

(7) Li, W.; Furlan, A.; Hendriks, K. H.; Wienk, M. M.; Janssen, R. A. J. *J. Am. Chem. Soc.* **2013**, *135*, 5529–5532.

(8) Li, W.; Hendriks, K. H.; Furlan, A.; Roelofs, W. S. C.; Meskers, S. C. J.; Wienk, M. M.; Janssen, R. a J. *Adv. Mater.* **2014**, *26*, 1565–1570.

(9) Zhong, H.; Li, Z.; Deledalle, F.; Collado-Fregoso, E.; Shahid, M.; Fei, Z.; Nielsen, C. B.; Yaacobi-Gross, N.; Rossbauer, S.; Anthopoulos, T. D.; Durrant, J. R.; Heeney, M. *J. Am. Chem. Soc.* **2013**, *135*, 2040–2043.

(10) Collado-Fregoso, E.; Boufflet, P.; Fei, Z.; Gann, E.; Ashraf, R. S.; Li, Z.; McNeill, C. R.; Durrant, J. R.; Heeney, M. *Prep.* **2015**.

(11) Scharber, M. C.; Muehlbacher, D.; Koppe, M.; Denk, P.; Waldauf, C.; Heeger, A. J.; Brabec, C. J. *Adv. Mater.* **2006**, *18*, 789–794.

(12) Vandewal, K.; Tvingstedt, K.; Gadisa, A.; Inganäs, O.; Manca, J. V. *Nat. Mater.* **2009**, *8*, 904–909.

(13) Bisquert, J.; Garcia-Belmonte, G. *J. Phys. Chem. Lett.* **2011**, *2*, 1950–1964.

(14) Credgington, D.; Durrant, J. R. *J. Phys. Chem. Lett.* **2012**, *3*, 1465–1478.

(15) Burke, T. M.; Sweetnam, S.; Vandewal, K.; McGehee, M. D. *Adv. Energy Mater.* **2015**, *5*, n/a – n/a.

(16) Clarke, T. M.; Jamieson, F. C.; Durrant, J. R. *J. Phys. Chem. C* **2009**, *113*, 20934–20941.

(17) Halls, J. J. M.; Cornil, J.; Silbey, R.; Holmes, A. B.; Bre, J. L.; Friend, R. H. *Phys. Rev. B* **1999**, *60*, 5721–5727.

(18) Dimitrov, S. D.; Durrant, J. R. *Chem. Mater.* **2013**, *26*, 616–630.

(19) Ohkita, H.; Cook, S.; Astuti, Y.; Duffy, W.; Tierney, S.; Zhang, W.; Heeney, M.; McCulloch, I.; Nelson, J.; Bradley, D. D. C.; Durrant, J. R. *J. Am. Chem. Soc.* **2008**, *130*, 3030–3042.

(20) Clarke, T. M.; Ballantyne, A.; Shoaee, S.; Soon, Y. W.; Duffy, W.; Heeney, M.; McCulloch, I.; Nelson, J.; Durrant, J. R. *Adv. Mater.* **2010**, *22*, 5287–5291.

(21) Shoaee, S.; Clarke, T. M.; Huang, C.; Barlow, S.; Marder, S. R.; Heeney, M.; McCulloch, I.; Durrant, J. R. *J. Am. Chem. Soc.* **2010**, *132*, 12919–12926.

(22) Nelson, J. *Phys. Rev. B* **2003**, *67*, 1–10.

(23) Nogueira, A. F.; Montanari, I.; Nelson, J.; Durrant, J. R.; Brabec, C.; Ag, S.; Electronics, C. T. M. *J. Phys. Chem. B* **2003**, *107*, 1567–1573.

(24) Shuttle, C.; O'Regan, B.; Ballantyne, A.; Nelson, J.; Bradley, D.; Durrant, J. *Phys. Rev. B* **2008**, *78*.

(25) Clarke, T.; Ballantyne, A.; Jamieson, F.; Brabec, C.; Nelson, J.; Durrant, J. *Chem. Commun. (Camb).* **2009**, *7345*, 89–91.

(26) Clarke, T. M.; Ballantyne, A. M.; Tierney, S.; Heeney, M.; Duffy, W.; McCulloch, I.; Nelson, J.; Durrant, J. R. *J. Phys. Chem. C* **2010**, *114*, 8068–8075.

(27) Shoaee, S.; Subramaniyan, S.; Xin, H.; Keiderling, C.; Tuladhar, P. S.; Jamieson, F.; Jenekhe, S. a.; Durrant, J. R. *Adv. Funct. Mater.* **2013**, *23*, 3286–3298.

(28) Bronstein, H.; Collado-Fregoso, E.; Hadipour, A.; Soon, Y. W.; Huang, Z.; Dimitrov, S. D.; Ashraf, R. S.; Rand, B. P.; Watkins, S. E.; Tuladhar, P. S.; Iain Meager; Durrant, J. R.; McCulloch, I. *Adv. Funct. Mater.* **2013**.

(29) Bansal, N.; Reynolds, L. X.; MacLachlan, A.; Lutz, T.; Ashraf, R. S.; Zhang, W.; Nielsen, C. B.; McCulloch, I.; Rebois, D. G.; Kirchartz, T.; Hill, M. S.; Molloy, K. C.; Nelson, J.; Haque, S. a. *Sci. Rep.* **2013**, *3*, 1–8.

(30) Dibb, G. F. Non-geminate charge recombination in organic solar cells, Imperial College London, 2013.

(31) Nielsen, C. B.; Turbiez, M.; McCulloch, I. *Adv. Mater.* **2012**, *25*, 1859–1880.

(32) Zhang, X.; Richter, L. J.; Delongchamp, D. M.; Kline, R. J.; Hammond, M. R.; McCulloch, I.; Heeney, M.; Ashraf, R. S.; Smith, J. N.; Anthopoulos, T. D.; Schroeder, B.; Geerts, Y. H.; Fischer, D. a.; Toney, M. F. *J. Am. Chem. Soc.* **2011**, *133*, 15073–15084.

(33) Bronstein, H.; Chen, Z.; Ashraf, R. S.; Zhang, W.; Du, J.; Durrant, J. R.; Tuladhar, P. S.; Song, K.; Watkins, S. E.; Geerts, Y.; Wienk, M. M.; Janssen, R. a J.; Anthopoulos, T.; Sirringhaus, H.; Heeney, M.; McCulloch, I. *J. Am. Chem. Soc.* **2011**, *133*, 3272–3275.

(34) Lakhwani, G.; Rao, A.; Friend, R. H. *Annu. Rev. Phys. Chem.* **2014**, *65*, 557–581.

(35) Fei, Z.; Shahid, M.; Yaacobi-Gross, N.; Rossbauer, S.; Zhong, H.; Watkins, S. E.; Anthopoulos, T. D.; Heeney, M. *Chem. Commun.* **2012**, *48*, 11130–11132.

(36) Dimitrov, S. D.; Nielsen, C. B.; Shoaee, S.; Tuladhar, P. S.; Du, J.; Mcculloch, I.; Durrant, J. R. *J. Phys. Chem. Lett.* **2011**, 140–144.

(37) Zhang, X.; Richter, L. J.; DeLongchamp, D. M.; Kline, R. J.; Hammond, M. R.; McCulloch, I.; Heeney, M.; Ashraf, R. S.; Smith, J. N.; Anthopoulos, T. D.; Schroeder, B.; Geerts, Y. H.; Fischer, D. a; Toney, M. F. *J. Am. Chem. Soc.* **2011**, *133*, 15073–15084.

(38) Soon, Y. W. Charge Separation, Triplets and Photochemical stability in Polymer/Fullerene Solar Cells, Imperial College London, 2013.

(39) Dennler, G.; Scharber, M. C.; Brabec, C. J. *Adv. Mater.* **2009**, *21*, 1323–1338.

(40) Jamieson, F. C.; Domingo, E. B.; McCarthy-Ward, T.; Heeney, M.; Stingelin, N.; Durrant, J. R. *Chem. Sci.* **2012**, *3*, 485.

(41) Liu, Y.; Zhao, J.; Li, Z.; Mu, C.; Ma, W.; Hu, H.; Jiang, K.; Lin, H.; Ade, H.; Yan, H. *Nat. Commun.* **2014**, *5*, 1–8.

(42) Clarke, T. M.; Durrant, J. R. *Chem. Rev.* **2010**, *110*, 6736–6767.

Chapter 4. Study of DPTT-T/$PC_{70}BM$ blends and devices as a function of fullerene loading

In this chapter, the best performing polymer from the DPP-based polymers studied in Chapter 3, DPPTT-T was studied. The focus of this chapter is the characterization of its photophysical behaviour and its relation with device behaviour as a function of $PC_{70}BM$ loading. DPPTT-T is a relatively stable, low-bandgap polymer that has previously attracted interest in industry projects. Looking towards possible synthetic feedback, the photophysics of exciton quenching, charge separation and recombination as a function of fullerene loading were characterized, correlating the results with the performance of solar cell devices as well as with morphologic assays. From the correlation between photoluminescence quenching, Transient absorption spectroscopy results (TAS) and absorbance-corrected external quantum efficiency, (IQE*) it was concluded that one of the main limitations in the conversion of photons into free charges in DPPTT-T/$PC_{70}BM$ devices is poor exciton harvesting, even with the optimized fullerene loading. After analysis of the morphology assays, it is proposed that such exciton losses are due to a low intermixing of the polymer and $PC_{70}BM$, and it is suggested that this might be a common factor of short circuit current loss in other highly crystalline, DPP-based polymers.

In the introduction, trends in performance data are compared for non-DPP and DPP-based devices and an overview of the current literature on the possible causes for DPP-based devices limitations is presented. Later on, the experimental details of the techniques used to characterize the systems are described. Next, the steady state spectroscopy results are presented, followed by the time-resolved spectroscopy results. Following, a section named *Complementary results* which includes crystallinity and morphology characterization results obtained by collaborators in our group is also discussed. Finally, the relevance of our spectroscopy results and their rationale considering the conclusions from the morphology characterization is discussed.

4a. Introduction

Among low-bandgap polymers, Diketopyrrolopyrrole (DPP)-based polymers are one of the most attractive polymer families. The donor-acceptor synthetic design, with an electron deficient DPP core and electron rich thiophenes, results in a narrow bandgap, capable of absorbing electrons in the near-IR region. Their low bandgaps also make them suitable to be used as low-wavelength co-absorbing material in tandem solar cells. It has been shown that they canconstitute single junction devices with good performances that can reach 8% power conversion efficiency[1]. Moreover, they usually present very high and balanced charge carrier mobilities[2]; this last feature gives them ambipolar characteristics also interesting for applications in transistors[3].

DPP-based polymers usually present a large tendency to aggregate and form crystalline domains, which is related to the high planarity of the DPP core, which in turn enhances π–π interactions and therefore intermolecular overlap. These interactions are so strong with some DPP-based polymers that signatures of aggregation have been detected even in solution[4] as will be shown in this study. The polymer that was analysed in this chapter, DPPTT-T (See *Figure 2.1*, in Chapter 2 for structure) has fused thiophenes as an electron-rich counterpart of the DPP core, which extends the polymer conjugation and thus increases the polymer coplanarity, further enhancing intermolecular interactions[5].

Despite the clear advantages of the use of DPP-based polymers in solar devices, when analysing the best seven single-junction DPP-based conventional devices and some of the best non-DPP conventional recently reported devices, (see *Table 4.1*) it is noticeable that despite DPP-based devices having a significantly higher average J_{SC} (almost 1 mA/cm^2 higher) than that of their non-DPP counterparts, their EQEs are significantly lower in both the blue part of the spectrum, associated with fullerene charge generation and the red, polymer-charge generation wavelengths. It is particularly noticeable in the latter case: while the maximum EQE for DPP systems has an average value of 56%, the same figure for non-DPP devices is ≈ 74%. We rule out systematic absorption limitations in the DPP-based devices since their active blend thickness is similar to those of the non-DPP based devices. Moreover, there is no reason to believe that DPP-based polymers could have lower extinction coefficients compared to their non-DPP based counterparts, quite the opposite, recent studies suggest that at least DPPTT-T, presents a considerably high extinction coefficient[6]. It could be therefore assumed that these figures reflect the intrinsic ability of the polymers to convert photons into photocurrent. This suggests that despite the advantage of DPP-based devices

harvesting low-energy photons and thus contributing to J_{SC}, they have an intrinsic conversion limitation that lowers their EQE values.

Table 4.1. Photovoltaic properties of best DPP-based and some of the best current non-DPP based devices with standard architectures (ITO/PEDOT:PSS/Active blend/Ca (or LiF)/Al) with similar thicknesses and with $PC_{70}BM$ as acceptor.

DPP-based best performing conventional devices (increasing J_{sc})								
Polymer	J_{SC} (mA/cm^2)	V_{OC} (V)	*FF*	EQE_{max} (Polymer)	EQE_{max} ($PC_{70}BM$)	%PCE	Thickness (nm)	LUMO (eV)
PDPP2T-BDT[7]	13.2	0.77	0.68	0.51	0.51	6.9	110	-3.72
PDPPTPT[1]	14	0.8	0.67	0.58	0.52	7.4	115	-3.66
PDPP3T[1]	15.4	0.67	0.69	0.49	0.51	7.1	134	-3.74
PDPP3T*alt*TPT[1]	15.9	0.75	0.67	0.59	0.57	8.0	110	-3.73
PDPP4T[7]	16	0.64	0.69	0.6	0.55	7.1	115	-3.64
DPPTT-T C2[8]	18.6	0.61	0.64	0.61	0.69	7.3	115	-3.7
DPPTT-T C3[8]	18.7	0.6	0.62	0.54	0.65	6.9	115	-3.7
Average	**16.0**	**0.69**	**0.67**	**0.56**	**0.57**	**7.2**	**116**	**-3.70**
Some of the best performing non-DPP-based conventional devices (increasing J_{sc})								
PBDTTPD[9] (2EH/C8)	12.5	0.93	0.65	0.72	0.63	7.5	110	-
PBDTTPD[9] (2EH/C7)	12.6	0.97	0.7	0.73	0.64	8.5	110	-
PBDTT-S-TT[10]	15.3	0.84	0.66	0.70	0.60	8.4	95	-3.27
PTB7[11]	15.75	0.76	0.7	0.75	0.71	8.4	90	-3.31
PBDTDTTT -S-T[12]	16.35	0.69	0.66	0.73	0.51	7.8	110	-3.57
PBDT-TS1[13]	17.4	0.80	0.66	0.72	0.71	9.2	100	-3.52
PBDT-TFQ[14]	17.9	0.76	0.58	0.8	0.85	8	106	-3.30
Average	**15.4**	**0.82**	**0.66**	**0.74**	**0.66**	**8.3**	**103**	**-3.39**

A couple of studies have addressed the EQE limitations, one in DPP polymers with different donor moieties[7] and another one in which the length of the side chains is varied for PDPPTPT[15]. Both studies found that the optimized blend films form fibrillar structures whose widths were inversely correlated with EQE values. The study with PDPPTPT proposed that wide polymer fibrillar structures

prevent an efficient exciton dissociation which impacts on the EQE values for the corresponding devices.

This study takes that hypothesis one step further and aims to investigate how the exciton dissociation, charge separation and charge recombination vary in DPPTT-T in blend films as a function of $PC_{70}BM$ loadings. A key focus is relating these measurements with the morphologies of the blend films and with device parameters.

Surprisingly, there are relatively few studies that address systematically the effect of the polymer/fullerene ratio on charge dynamics and its relation with the changes in morphology and aggregation behaviour for low-bandgap polymers. Composition dependencies have mainly been empirically determined from device optimization in each polymer/fullerene system. Some early papers and a few later ones studied the effect of PCBM loading in P3HT[16–19] and PPV blends[20,21] in films and solar devices. It explained the differences in device performance by a trade-off between light absorption and charge separation as studied by PL quenching. It was also proposed for a PPV-based system[21] that high PCBM concentrations favour not only an increased electron but also a higher hole mobility, which would suggest an improved charge transport in the corresponding devices. Additionally, a transient absorption study on different thiophene-based polymers with 5% and 50% PCBM concluded that the polaron yield is higher for the blends with higher PCBM loadings[22]. High PCBM loadings were associated with a higher polaron pair dissociation efficiency, however little was mentioned on the blend properties that relate with this higher efficiency.

Recently, a few studies that aimed to assess the morphological impact of PCBM concentration have also been reported[23,24]. The current consensus is that as fullerene loading is increased, a trade-off occurs between efficient exciton dissociation, and reduced charge recombination. Exciton dissociation is optimal in intermixed domains, where the proximity between polymer and fullerene directly promotes electron transfer efficiency. Simultaneously, charge separation and collection has been suggested to require an extended, aggregated fullerene network with high electron affinity[25,26], which acts as an energetic drive to spatially separate any initially formed bound polaron pairs. This has been found to be particularly important for amorphous polymers, and less critical if the polymer has a high crystallinity[26]. This idea has been addressed before by Janssen et al[27], who proposed that a high fullerene loading is necessary to drive the separation of bound CT states and increase charge separation efficiency in blends with a fluorene copolymer (PF10TBT). The impact of fullerene aggregation upon charge generation has been further explored and developed in the work by Savoie

et al[28] and others, who proposed that it is the delocalization in the fullerene upper states which controls charge separation efficiency by dissociating charge bound states. Experimentally, using spectroscopy to detect and assign non-emitting bound and separated states has proven a challenge in most of the current, efficient systems, since they usually have indistinguishable absorption features.

Additionally, non-geminate recombination is expected to be slowed down when a network of aggregated fullerene is present, this has been observed in both TPV/TPC studies as a function of acceptor loading[29] and annealing[30] as well as in TAS studies on P3HT as a function of polymer/fullerene composition[18]. It has also been demonstrated for P3HT[17] as well as for low-bandgap polymers[24], that the amount of fullerene necessary to reach the optimum ratio for charge generation and charge collection is related to the miscibility of the fullerene within the polymer matrix. In this sense, polymers with a lower miscibility expel PCBM more easily, as is the case for DPPTT-T[31], and therefore may not need high loadings of the acceptor to form percolating pathways that favour charge collection. In principle, this miscibility is related to the intrinsic ability of the polymer to aggregate and therefore is related to their crystallinity.

It is therefore interesting to determine what processes are related to the EQE limitations for DPPTT-T , studying the polymer aggregation behaviour when we changed the polymer/fullerene loading, as well as charge photogeneration and recombination mechanisms.

4b. Experimental section

5 mg/mL DPPTT-T and 10 mg/mL $PC_{70}BM$ solutions in a mixture of 4:1 Chloroform to ODCB solvents were prepared and stirred overnight to prepare the films with the different $PC_{70}BM$ loadings, whose polymer to fullerene ratio were: 4 to 1 (20% $PC_{70}BM$), 2 to 1 (33% $PC_{70}BM$), 1 to 2 (67% $PC_{70}BM$) and 1 to 4 (80% $PC_{70}BM$). The films were spun on cleaned glass substrates for 1 minute at 2,500 rpms in air, and were then transferred into an inert-atmosphere glovebox until the measurements were performed. These films were used for UV-Vis, PL, sub-ps to μs-TAS and AFM. For XR-D samples, 10 mg/mL DPPTT-T and 20 mg/mL $PC_{70}BM$ solutions were used to prepare drop casted films with the appropriate concentrations ratio on cleaned glass substrates and dried overnight.

In this chapter, Transmission Electron Microscopy (TEM) was used as one of the morphology assays, providing a resolution as high as 1 nm. In brief, TEM operates with the same principle as light microscopes, except that rather than light, it is a beam of electrons that is sent to the sample to obtain an image depending on its degree of deflection, which in turns depends on the electronic density of the part of the sample analysed. Organic molecules do not present enough change in the electron density necessary to detect the changes in inflection, for which the samples are stained with heavy metals. TEM measurements were carried on a JEOL 2010 transmission electron microscope at the Materials Department, Imperial College London by Dr. Safa Shoaee. Samples for TEM were prepared from dilute, 3 mg/mL solutions of the appropriate ratios of DPPTT-T and $PC_{70}BM$. Clean glass was used to spin coat PEDOT:PSS at 3000 rpm and then the dilute solutions were spun on top. The films were retrieved on mesh copper grids and stained with I_2 vapour.

Atomic Force Microscopy (AFM) was also carried out to assess the surface morphology of the blends. AFM operates by bringing into close contact a sharp tip with the surface of the material, then scanning the tip on top of the material. The tip undergoes both attractive and repulsive forces that result in deflections of the tip which are monitored optically by shining a laser on the tip and detecting the changes in its reflection. These deflection patterns are used in a feedback system that adjusts the proximity of the sample to the tip to minimize the deflections and keep the force constant, these patterns are recorded to construct a topography image. The exact operation mechanism though, depends on the operation mode in which AFM is used. For our samples tapping mode was used to avoid surfaces damage. AFM measurements were carried out by Ching Hong Tan at the Materials Department of Imperial College in a Bruker MultiMode 8 setup with a RTESP tip, on blend films prepared in the same way as those used for PL and TAS.

Photovoltaic devices were prepared by Alex Gillett and Dr. Pabitra Shakya Tuladhar. The active layers for devices were prepared in a similar fashion as for blends, except that the substrates had the electrodes deposited. Pre-cleaned, patterned indium tin oxide (ITO) substrates (15 Ω per square) were used. On top of the ITO substrates, PEDOT:PSS was spun at 3000 rpm and dried on a hot plate at 150°C in air for 20 minutes. The active layer was spun on top, in the same fashion as for the films and transferred to a inert-atmosphere glovebox. Following, the counter electrode of LiF (1 nm) and aluminum (100 nm) were deposited by vacuum evaporation at 3×10^{-7} mbar. The active area of the devices was 0.045 cm^2.

4c. Results

4c.1. Steady state UV-vis and Photoluminescence emission spectroscopies: polymer aggregation behaviour in solution and in blend films and exciton quenching.

Figure 4.1a shows representative steady-state UV-vis spectra of the neat DPPTT-T and $PC_{70}BM$ as well as of the DPPTT-T:$PC_{70}BM$ blends as a function of their weight ratio, varying from 4:1 to 1:10 polymer:fullerene. As expected, upon increasing the fullerene ratio, the proportion of $PC_{70}BM$ absorption increases, whereas the 650 – 1000 nm absorption corresponding to the polymer decreases. Interestingly, it is noticeable that upon increasing the $PC_{70}BM$ concentration the shoulder of the polymer $S_0 \rightarrow S_1$ transition band, previously assigned to 0,0 lowest vibronic transition, increases in relative intensity. Additionally, a slight red shift in this 0,0 transition of ~ 0.04 eV is also observed (from 793 nm in the neat polymer to 814 nm in the 1:10 blend). These observations have been argued to originate from an increased order in the polymer packing due to increased π–π stacking[23]. This assignment also agrees with the decrease in the shoulder intensity when a DPPTT-T solution in ODCB solvent is heated, and thus the intermolecular polymer interactions disrupted, as shown in *Figure 4.1b*. It is then surprising that the polymer π–π intermolecular interactions seem to be stronger upon the addition of $PC_{70}BM$. The change in the shoulder intensity has also been observed for DPPTT-T polymers with different branching points in their side chains, both in thin films and solutions[8], and therefore emphasizes that small structural changes in the side chains can have a high impact in DPPTT-T core π–π interactions, thus affecting its packing and crystallinity.

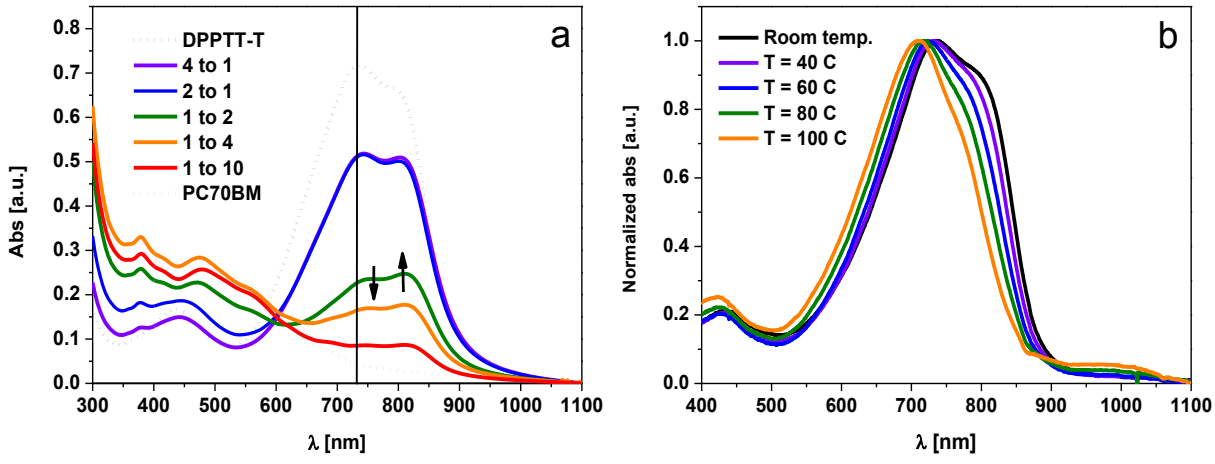

Figure 4.1. a) Steady state UV-vis absorption of neat and blend films of DPPTT-T and $PC_{70}BM$ with different polymer to $PC_{70}BM$ weight ratios. b) Steady state UV-vis absorption of a 5.5 x 10^{-3} mg/mL DPPTT-T ODCB solution at different temperatures, showing the change in intensity of the 0,0 vibronic band of the polymer.

Next, in *Figure 4.3a* and *Figure 4.3b*, the results of both DPPTT-T and $PC_{70}BM$ photoluminescence (PL) emission and their respective quenching in the blend films with varying compositions are presented. This system is convenient to selectively excite and probe, given that the absorption and emission of the polymer and the fullerene are well separated: the emission of the polymer spans from ~850 to 1300 nm and that of the fullerene between ~650 and 800 nm. As expected, the quenching degree increases as the concentration of the complementary component increases; for example, the larger the DPPTT-T concentration, the more quenched the $PC_{70}BM$ emission. However, it is noticeable that whereas the fullerene quenching is complete or close to being complete for the films with high polymer concentration, the polymer emission does not reach complete quenching even with the 1:10 film, an observation that will be discussed shortly.

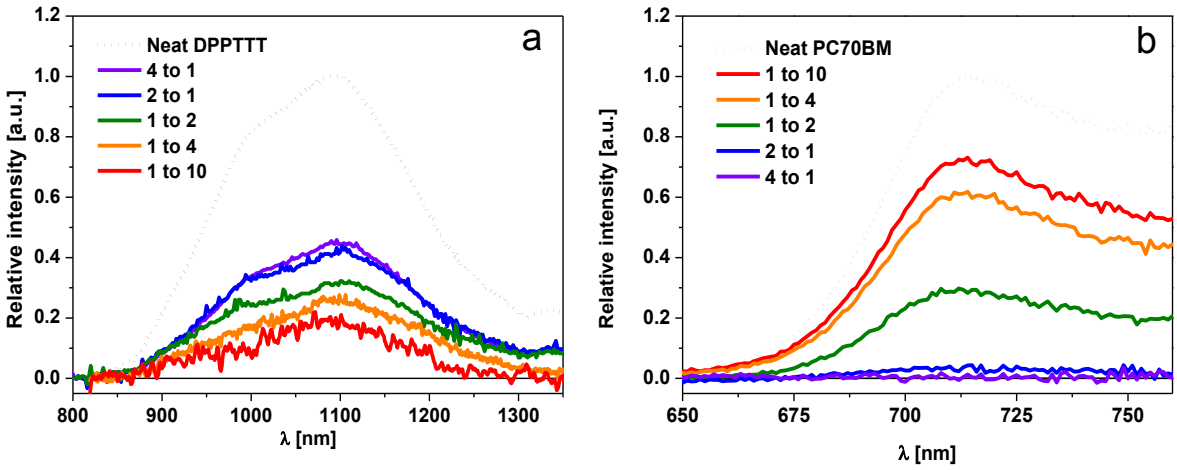

Figure 4.2. a) Steady state PLQ studies of DPPTT-T as a function of $PC_{70}BM$ loading, exciting at 740 nm b) steady state PLQ studies of $PC_{70}BM$ as a function of DPPTT-T loading for the same blend films, exciting at 520 nm, where DPPTT-T has a minimum absorption. PL data was normalized for photon film absorption at the excitation wavelength and then normalized to the neat maximum.

4c.2. Femtosecond to microsecond transient absorption spectroscopy: early photophysics and charge recombination dynamics as a function of fullerene loading.

Following the steady-state characterization, transient absorption data was compared for the samples 4:1, 2:1, 1:2 and 1:4, and neat DPPTT-T measured exciting at 740 nm and an excitation intensity of 25 $\mu J/cm^2$. First the dynamics of the neat DPPTT-T film will be described. In *Figure 4.3a*, and *4.3b* the spectra and decay dynamics of neat DPPTT-T probed at 1000 nm are shown. As can be observed, the photoinduced absorption signals are quite flat and broad, although there appears to be a maximum in the red part of the spectrum, between 1300 and 1400 nm. DPPTT-T signals can be

assigned to the photoinduced absorption of singlet excitons to upper excited states, $S_1 \rightarrow S_n$. As can be observed in *Figure 4.3b*, the signal has completely decayed by 300 – 400 ps, which is incompatible with the presence of triplet states, which usually are at least one order of magnitude longer lived[32]. Additionally, triplet excitons were not observed in oxygen quenching studies in the neat polymer, as detailed in photochemical stability studies[33]. Therefore, it was concluded that no triplets are present formed after photo-excitation, opposite to what has been determined in a recent study of DPP-based polymers[34].

The exciton decay dynamics can be fitted to a monoexponential decay with a time constant τ = 46 ± 3 ps, which was obtained by averaging the time constants obtained at probed wavelengths from 900 to 1300 nm. *Figure 4.3b* shows that this decay is independent of the excitation intensity between 5 and 25 μJ/cm^2, and thus can be assigned to the radiative and non-radiative decay of the singlet exciton. From this data it is also plausible to conclude that no exciton-exciton annihilation processes are observed between these excitation intensities. It is noticeable that this decay time is rather short as compared to other exciton decay times in low-bandgap neat conjugated polymers used in OPV studies, which usually have decay times ranging between 140 – 270 ps[35–39]. This could be the result of increased non-radiative deactivation processes in DPPTT-T due to its small bandgap, as expected from the energy gap law[40–42]. The short exciton decay time might then also prevent the encounter of excitons and thus avoid second order processes including exciton-exciton annihilation.

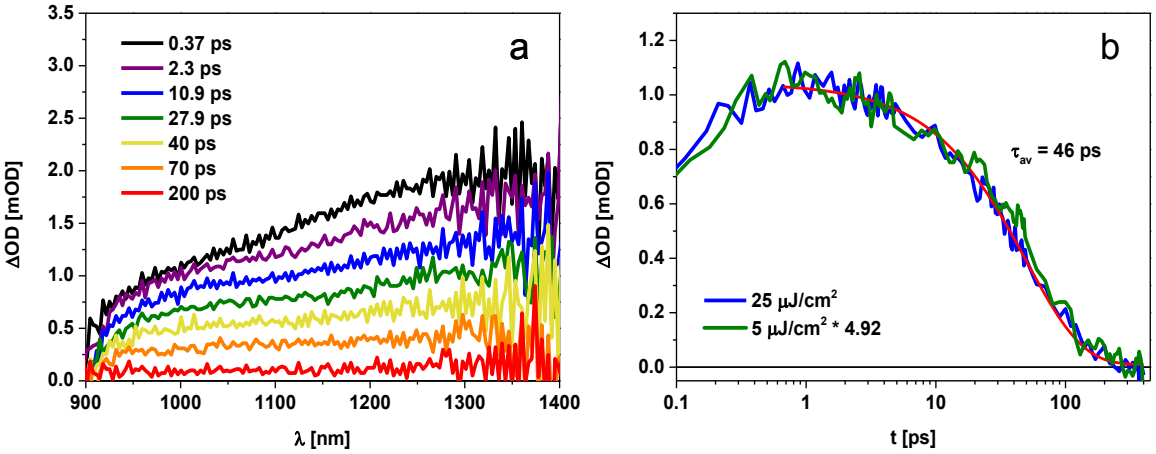

Figure 4.3. Neat DPPTT-T sub-ps transient absorption data in the IR region, excited at 740 nm, in a) transient spectra taken at 25 μJ/cm^2 and b) dynamics averaged between 990 and 1010 nm at 5 and 25 μJ/cm^2. The data was corrected for polymer absorption at the excitation wavelength.

A description of the transient absorption data for the blend films is now presented. Small spectral differences were observed between the four blends analysed (4:1, 2:1 1:2 and 1:4), and thus only

the spectra for 2:1 and 1:2 blend films are shown in *Figure 4.4a* and *4.4b*. In both cases at early times, (≈ 0.4 ps) *ΔOD* increases towards 1400 nm, as well as a positive feature at 950 nm which are likely to come from the initially formed, singlet exciton photoinduced absorption. In other low-bandgap polymers, exciton photoinduced absorption has also been identified in the same wavelength area, which further confirms our assignment[36,40]. This increase in *ΔOD* is slightly different to the photoinduced exciton absorption in the neat film, which could be related to the increased intermolecular interactions in the blend films, as obtained in the UV-vis spectra.

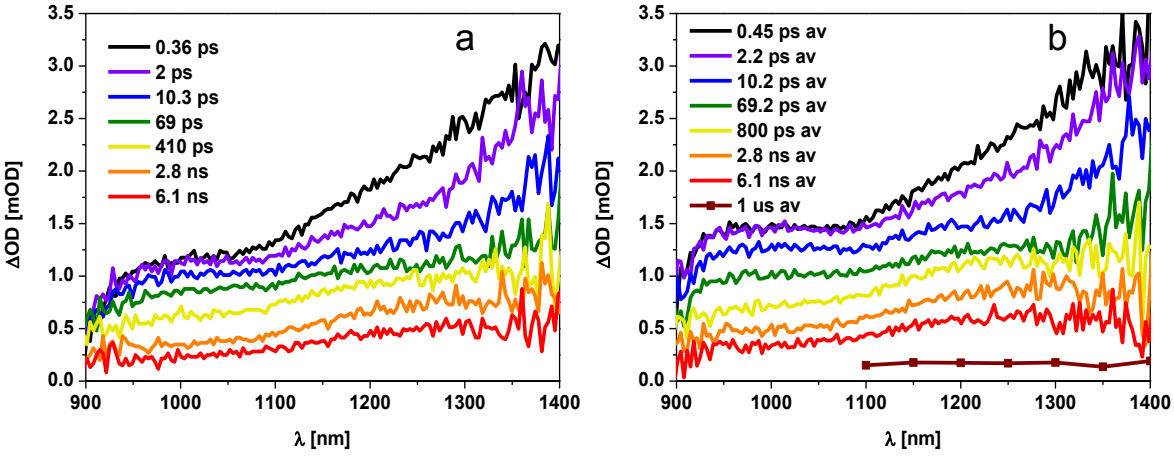

Figure 4.4. Sub-ps transient absorption spectra in the IR region, excited at 740 nm at 25 μJ/cm^2 of a) 2:1 DPPTT-T to $PC_{70}BM$ blend film and b) 1:2 DPPTT-T to $PC_{70}BM$ blend film, including a μs-resolved transient spectra taken under the same excitation conditions. The spectra were corrected for polymer absorption at the excitation wavelength.

Additionally, at late times, (from 400 – 800 ps) the formation of a band centred at ≈ 1300 nm is observed. This band is consistent with the microsecond spectra obtained for the 1:2 blend, and appears at times where the polymer exciton has completely decayed, thus it can be assigned to the photoinduced absorption of positive polymer polarons. Based on the oxygen quenching studies discussed in Chapter 3 we rule out any triplet contribution for the blends.

The shape of the spectra in the blend films being very similar indicates that the changes in morphology and polymer packing upon the incorporation of higher concentrations of $PC_{70}BM$ does not translate into spectrally different excited species. The apparent insensitivity of the blend spectra towards composition is clearly different from the behaviour in other polymer systems, for example PBTTT blend films, where a clear change in the shape of the transient absorption bands upon increasing fullerene concentration was observed, as will be discussed in Chapter 6. Finally it is

noticed that the polaron band does not show a red-shift, previously related to a large energetic disorder and thus a broadening of the density of states[43], which could be an indication of this system not presenting a large amount of deep trap states.

It was interesting to draw a correlation between the exciton emission quenching observed in the PLQ measurements and the exciton dynamics at early times as probed by ultrafast TAS. In order to do this, the decays at 1300 nm were analysed as explained shortly. At this wavelength the exciton is largely predominant at early times, for polaron behaviour is only displayed from ≈ 1 ns. In *Figure 4.5* representative data for the 4:1 and 1:2 blends is shown.

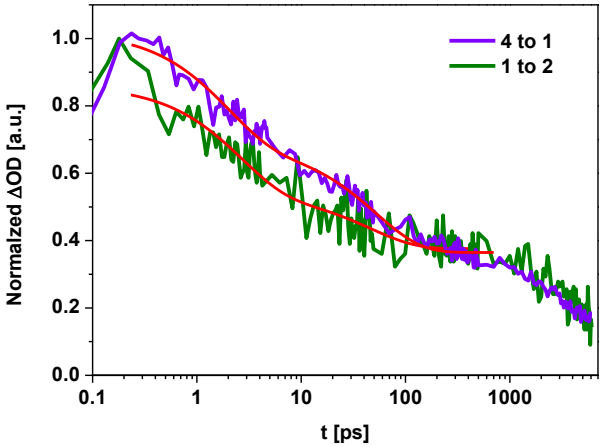

Figure 4.5. Normalized sub-ps transient absorption exciton dynamics exciting at 740 nm with 25 μJ/cm^2 intensity, probed at 1300 nm for 4 to 1 and 1 to 2 blend films. The decays were fitted to a biexponential function plus a constant term (see text).

The data was fitted to a bi-exponential function plus a constant term, as shown in *Equation 4.1.*

$$\Delta OD(t) = A_1 * \exp(-t/\tau_1) + A_2 * \exp(-t/\tau_2) + A_3 \qquad \text{(Eq. 4.1)}$$

The first term was considered to correspond to the decay contribution of polymer excitons that were not quenched, and therefore τ_1 is the intrinsic exciton decay time as obtained from the neat film. From the fits, we obtained values for τ_1 lying between 52 and 44 ps, therefore agreeing with our previous result. The second term corresponds to the contribution of quenched polymer excitons, being τ_2 the decay time of the excitons when they are quenched by the acceptor. To relate with the polymer PLQ values, the percentage of quenched excitons, $\%QE$ was calculated as the relative fraction of the pre-exponential factor A_2, corresponding to the contribution of the quenched excitons, as shown in *Equation 4.2*.

$$\%QE = \frac{A_2}{A_1 + A_2} \times 100 \qquad \text{(Eq. 4.2)}$$

In *Table 4.2* data from the fits for the blends 4 to 1, 2 to 1 and 1 to 2 is shown. Unfortunately the analysis could not be extended to the 1 to 4 blend, since it considers that all of the initial signal comes from excitons. It is likely that upon increasing the fullerene concentration, there is an increasingly large amount of polarons that are formed instantaneously therefore "contaminating" the exciton signal. This is the main reason why the simpler analysis described in section 2c.2 from Chapter 2 was not used in this case. The model also considers that important rearrangements possibly take place in the excitons that are to be quenched, for example the accumulation of electron density in the close vicinity to the fullerene acceptor.

Table 4.2. Comparison between the polymer PLQ values as obtained from steady-state PL and %QE as obtained from sub-ps TAS.

Blend	**% PLQ Polymer**	$\boldsymbol{\tau_1[ps](A_1)}$	$\boldsymbol{\tau_2(A_2)}$	$\boldsymbol{\%QE}$
4 to 1	55	52 (0.32)	1.9 (0.34)	52
2 to 1	57	44 (0.23)	2.0 (0.35)	60
1 to 2	68	46 (0.16)	2.6 (0.32)	66
1 to 4	74	-	-	-

It is noticed that, despite the simplicity of this approach, there is a trend of increasing amount of quenched excitons that is comparable with the results obtained with steady-state PL. Therefore it can be concluded that despite the small differences in the spectra at the sub-ps timescale, the effect of increasing the fullerene concentration can be observed in the exciton dynamics.

The next section addresses the dynamics of the blend films from the sub-ps to the μs timescale. The films were excited at 5 μJ/cm^2 to assure that the lowest possible energy was used without compromising the signal-to-noise ratio. *Figure 4.5* shows the data for the 4:1, 2:1 and 1:2 blend films probing at 980 nm. The blend transients were corrected for absorption at the excitation wavelength and for PL emission, taken at the maximum of each blend. These corrections were made so that the signals represent the polaron yield from the available excitons (quenched excitons), and not a combined measure of exciton dissociation and polaron formation efficiency. As such this yield will be named polaron per quenched exciton (PPQE).

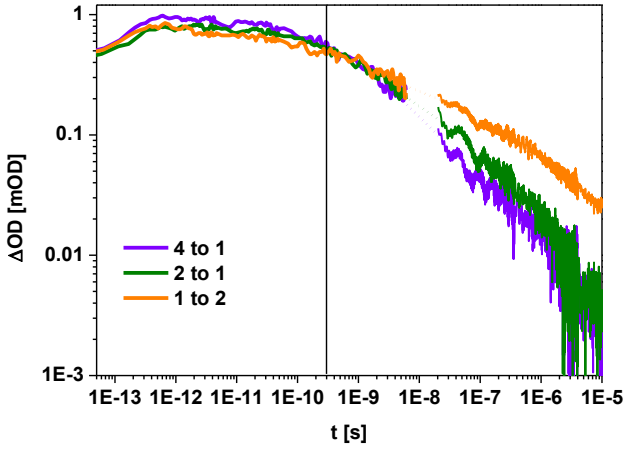

Figure 4.5. Sub-ps to μs transient absorption dynamics of the different blend films, excited at 740 nm at 5 μJ/cm^2 and probed at 980 nm, showing similar polaron yields per quenched exciton, but slower recombination as the fullerene concentration is increased. Data in the nano- to micro-second scale was taken by Hendrik Utzat.

Considering the data from 300 ps (marked with a vertical line) where the contributions to the signal from excitons is negligible, it is quite clear that the changes in the PPQE for the blends with different $PC_{70}BM$ loadings are very small, therefore suggesting that for the DPPTT-T/$PC_{70}BM$ system the efficiency of polaron formation per quenched exciton is independent of the relative $PC_{70}BM$ concentration. However, it can be observed that upon increasing the fullerene loading, charge recombination becomes slower thus indicating the need of high fullerene concentrations to retard recombination.

It is interesting to note that by 1 μs, 88% of the PPQE signal has decayed in the 1:2 blend, while the proportion increases to 95% in the 2:1 blend and 97% in the 4:1 blend. Recombination seems to consume the vast majority of the charges in the three blends in a relatively short time period however, even the low excitation intensity used, (5 μJ/cm^2) corresponds to a much higher power density as compared to the 1 sun irradiation used for device measurements. These decays are then, not directly comparable to the decays of charges recombining in devices at open circuit conditions as in for example, transient photovoltage experiments.

In order to determine whether the recombination behaviour observed here corresponds to non-geminate or geminate charge recombination, measurements with different excitation intensities were performed. These data are shown in *Figure 4.6a* for the 4:1 blend and *Figure 4.6b* for the 1:4 blend, probing at 980 nm. It is noticeable that upon increasing fullerene loading, the recombination behaviour not only becomes slower, but changes from being largely intensity independent to be

intensity dependent. This suggests that as the fullerene concentration is increased, recombination changes from a geminate to a non-geminate nature. This implies that the relative amount of bound polaron pairs decreases as the $PC_{70}BM$ concentration increases, that is, the separation of bound charges into free charges becomes more efficient.

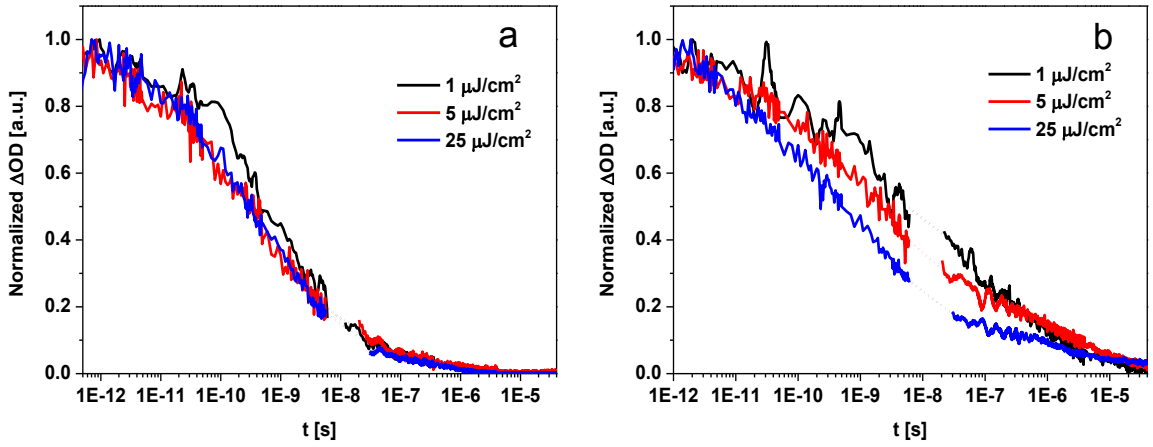

Figure 4.6. Normalized sub-ps to μs transient absorption recombination dynamics pumping at 740 nm and probing at 980 nm and as a function of excitation intensity for a) 4:1 and b) 1:4 blend film. Data in the nano- to micro-second scale was taken by Hendrik Utzat.

Although excitation intensity independent kinetics assigned to the geminate recombination of bound polaron pairs are observed for the 4:1 blend, no spectral features associated with a transient bound state were observed. This seems to be the case of few other studies, in which an excitation intensity independent decay mechanism is identified yet no spectral signatures of bound states are observed[36,43,44], and therefore seems to be an indication that bound electron-hole pairs indeed have similar spectral features to free charges and cannot be distinguished but from their dynamics.

4d. Complementary results[1]

4d.1. Crystallinity and morphology characterization

Wide-angle X-ray diffraction

Wide-angle X-ray diffraction (WAXD) technique was used to assess the change of film microstructure (both polymer and $PC_{70}BM$ domains) upon increasing concentration of $PC_{70}BM$. *Figure 4.8a* shows the data obtained for the 4:1, 2:1, 1:2 and 1:4 blend films, corrected to account for the different thicknesses of the blends. A narrow and intense peak can be observed at q = 0.32 $Å^{-1}$, which is in

[1] All the analysis and graph construction in this section was performed by the author.

good agreement with the peak obtained for a neat DPPTT-T blend at q = 0.3 $Å^{-1}$ [45]. This peak has been assigned to out-of-plane lamellar stacking and thus corresponds to a lamellar spacing of 1.96 nm. Similar signals have been obtained for other crystalline polymers such as P3HT or DPP-T-TT, a very similar polymer to DPPTT-T[33]. Importantly, the lamellar spacing does not change for the different blends, inferring that $PC_{70}BM$ does not intercalate into the polymer chains, as it is the case for PBTTT, discussed in Chapter 6. At the same time, the intensity and width (FWHM) of the blend peaks with high polymer concentration (4 to 1 and 2 to 1) is very close to those of the neat polymer prepared under similar conditions[45], implying that the polymer crystallinity hardly undergoes any change upon addition of small amounts of $PC_{70}BM$. The peaks at q = 0.64 and 1.34 $Å^{-1}$ have been previously assigned to fullerene agglomeration[24,46].

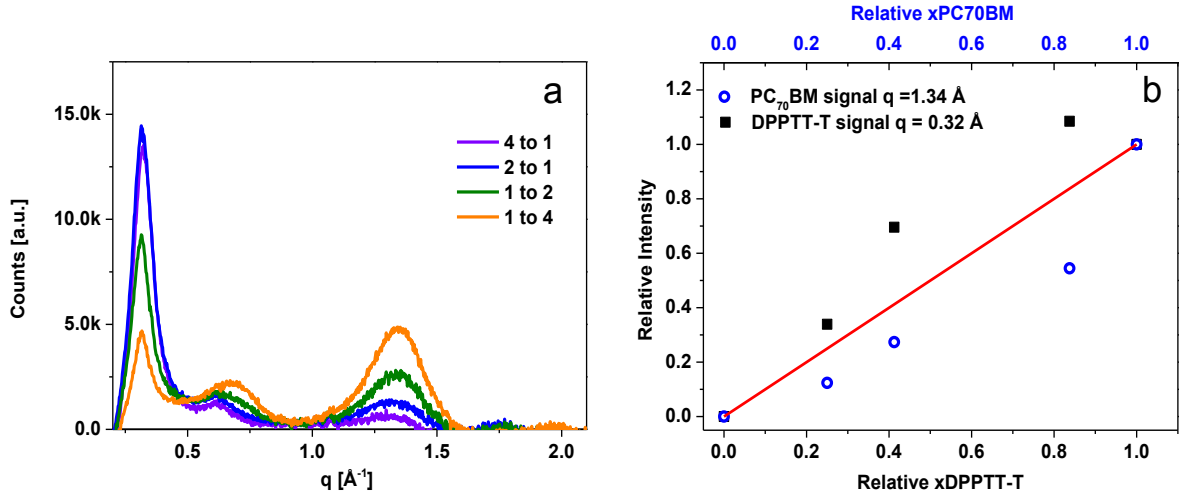

Figure 4.8. a) Wide-angle X-ray diffraction (WAXD) patterns for the different DPPTT-T/$PC_{70}BM$ blends. Data was corrected with a factor that accounts for the differences in film thickness. The scattering vector q is calculated from the scattering angle using the equation $q = (4\pi/\lambda)\sin\theta$ in from section 2c.5 in Chapter 2. b) Relative intensity with respect to the 4 to 1 blend for the polymer lamellar peak (black squares) and with respect to the 1 to 4 blend for the fullerene peak, (blue squares) see text. The red line represents a straight line with $m = 1$ and $b = 0$. A point in (0,0) was added to the data. WAXD data was taken by Ching Hong-Tan.

Further analysis of the peak intensities is discussed next, in relation to *Figure 4.8a*; the analysis assumes that the peak intensities are proportional to the degree of crystallinity of the polymer and fullerene domains. This figure shows the relative intensity with respect to the 4 to 1 blend for the lamellar peak at q = 0.32 Å (4 to 1 blend has a relative intensity = 1) and the relative intensity with respect of the 1 to 4 blend for the fullerene peak at q = 1.34 Å (1 to 4 blend has a relative intensity = 1). As can be observed, the change in the relative peak intensities is close from describing a tendency that is completely due to the change in proportion of the blend components, as described by the straight line in the plot. A few deviations are observed for both the polymer and fullerene

relative peak intensities. Upon fullerene addition, 2 to 1 and 1 to 2 blend relative peak intensities deviate severely from the straight line to higher relative intensity values, implying a relatively higher degree of crystallinity of the polymer domains with respect to the 4 to 1 blend. Simultaneously, the relative degree of crystallinity of the $PC_{70}BM$ domains seems to be lower with respect to the 1 to 4 blend, especially in the 1 to 2 blend, as observed from the negative deviations in the relative peak intensities. As such, it is concluded that the changes observed in peak intensities are largely due to the changes in blend proportions and not in the crystallinity of the polymer or fullerene domains. This is also reflected by noticing that, at least for the case of the DPPTT-T lamellar peak, the peaks do not broaden as their intensities decrease.

Finally, notice that the $\pi - \pi$ stacking peak, reported[24] at q = 1.7 $Å^{-1}$ is barely observed in the results, and thus its trend cannot be related with UV-vis results. This is most likely because the polymer crystallites are oriented edge-on to the substrate and therefore $\pi - \pi$ stacking lies parallel to the plane of the substrate, preventing its detection with this technique.

Transmission electron microscopy (TEM) and Atomic force microscopy (AFM)

Transmission electron microscopy (TEM) and Atomic force microscopy (AFM) were used to further investigate the morphology of the blend films. The TEM micrographs for blends 10:1, 1:1 and 1:4 are presented in *Figure 4.9 (top)*. It appears from the image that as the fullerene concentration is increased, the morphology ranges between essentially undisturbed polymer crystallites in the 10:1 blend, to partial separation of the $PC_{70}BM$ domains in the 1:1 blend and finally growing of the $PC_{70}BM$ domains in the 1:4 blend, similar to those observed by Dimitrov et al.[47]. The observation of fullerene aggregates even in the 1:1 blend is in agreement with the hypothesis that the fullerene solubility within the polymer matrix is low, supporting the WAXD results. It can be observed in the 1:4 micrograph, that the fullerene average domain diameter size is close to 10 nm. For this blend it was obtained from the $PC_{70}BM$ PLQ results that 60% of the fullerene excitons are radiatively lost, therefore, it can be estimated from Equation 2.4 in Chapter 2 that the fullerene excitons have an average diffusion length of 6 – 6.5 nm, which agrees with previous results[48,49]. For this analysis it was assumed that the 10 nm acceptor domains observed in the TEM images correspond to pure domains, which seems a reasonable assumption, considering the relatively low miscibility of DPPTT-T and $PC_{70}BM$, according to the WAXR-D results.

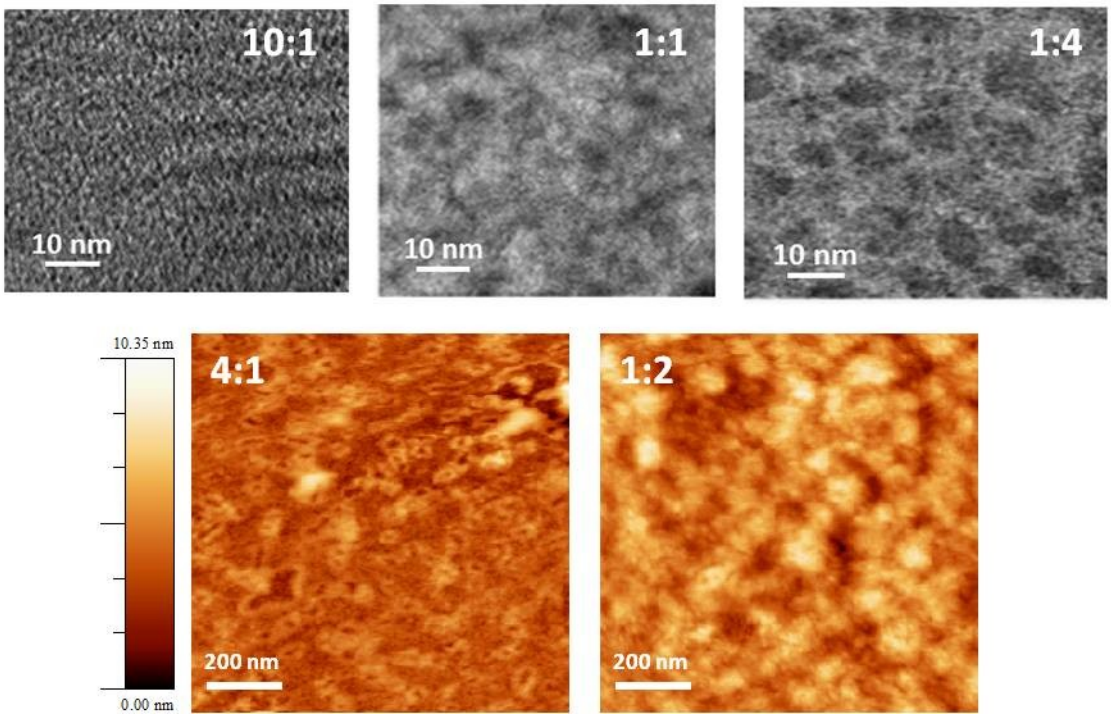

Figure 4.9. (top) TEM micrographs for 10:1, 1:1 and 1:4 DPPTT-T/$PC_{70}BM$ blends, showing the formation of $PC_{70}BM$-rich areas as the fullerene concentration is increased; (bottom) AFM phase images for the 4:1 and 1:2 blend films showing an increased roughness in the 1:2 blend. TEM data was taken by Dr. Safa Shoaee and AFM data was taken by Ching Hong Tan.

In *Figure 4.9 (bottom)* the AFM phase images for the 4:1 and 1:2 blends are shown, demonstrating a higher roughness in the 1:2 blend, and thus supporting the TEM results that show the formation of relatively large $PC_{70}BM$ domains in the blends with high fullerene content. In general, it can be considered that the lighter spots correspond to areas with a higher fullerene concentration, since a vertical fullerene migration towards the air interface has been observed in films deposited on quartz and glass surfaces[50,51]. This actually can be beneficial for electron transport, since it brings the electrons closer to the metallic cathode therefore constituting optimised percolation pathways for charge extraction.

WAXD results have not only confirmed the high crystallinity of DPPTT-T, but have also shown that this crystallinity is not disturbed upon increasing $PC_{70}BM$ concentration. TEM and AFM results confirm the formation of fullerene aggregates, with increasing size which are likely to vertically segregate to the air surface. It is likely that both polymer and fullerene domains are relatively pure, according to their undisturbed degree of crystallinity, according *to Figures 4.8a* and *b*.

The study will now turn to the analysis of device data. A key focus is the EQE changes for the devices fabricated with different polymer/fullerene ratios at different parts of the visible spectrum.

4d.2. Device data: J-V curves and EQE as a function of composition

In *Figure 4.10* the J-V curves for devices fabricated with polymer:fullerene ratios of 4:1, 2:1, 1:2 and 1:4 are shown. The photovoltaic parameters are presented in *Table 4.3*. Notice that for devices with low fullerene concentrations, both the short circuit current and the fill factor are severely limited. The current presents a gradient at low and negative voltages which could be due to voltage-dependent charge separation in competition with geminate recombination, and/or to increased non-geminate recombination at J_{SC}[52,53]. From the excitation intensity TAS results, it seems that an increased relative amount of bound polaron pairs that undergo geminate recombination is present in the blends with low $PC_{70}BM$ thus explaining the gradient in the current at low voltages. However, to confirm this hypothesis transient photovoltage and charge extraction studies are necessary.

Table 4.3. Photovoltaic parameters for the corresponding devices shown in *Fig. 4.9*

	4 to 1	**2 to 1**	**1 to 2**	**1 to 4**
J_{SC} (mAcm^{-2})	1.30	4.80	16.53	11.73
V_{OC} (V)	0.61	0.61	0.61	0.62
Fill Factor	0.29	0.33	0.58	0.65
PCE (%)	0.23	0.97	5.87	4.77

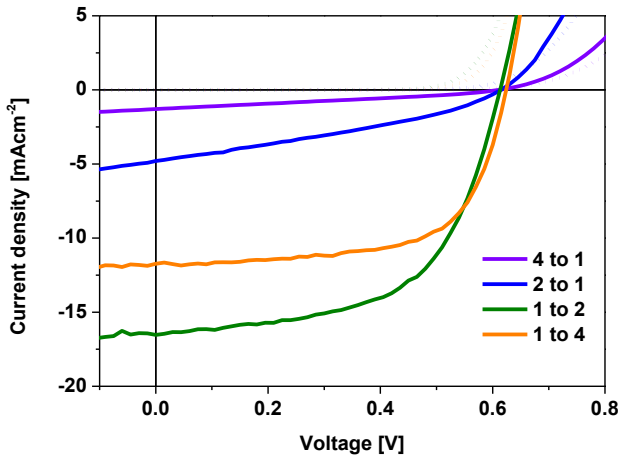

Figure 4.10. *J-V* curves for the best devices fabricated with different DPPTT-T:$PC_{70}BM$ ratios, measured under constant illumination with 100 mWcm^{-2}, AM1.5 spectrum from a solar simulated light at room temperature. Dotted lines correspond to dark current of the respective cells. Devices were fabricated and measured by Alex Gillett and Dr. Pabitra Shakya Tuladhar, and have a standard architecture: ITO/PEDOT:PSS/Active blend/LiF/Al.

Upon the addition of fullerene the current slope is greatly reduced and a much higher J_{SC} is observed. Comparing the 1:2 and 1:4 blends, it is noticeable that the fill factor of the 1:4 blend is considerably higher (see Table 4.3). This indicates that the ≈ 10 nm domains observed by TEM for the 1:4 blend may yield better percolation pathways which slow down non-geminate recombination at J_{SC} and/or suppress any geminate recombination still present in the 1 to 2 device. J_{SC} however, is greatly decreased (-30%) when going from the 1:2 to the 1:4 blend which agrees with the 30% decrease in fullerene PLQ in the same blends as observed in *Figure 4.2b*. Therefore it seems that $PC_{70}BM$ aggregates size increase seems necessary to avoid extensive geminate recombination in blends with low $PC_{70}BM$ loading and to slow down non-geminate recombination in blends with modest $PC_{70}BM$ concentrations. This however, happens at the expense of loosing $PC_{70}BM$ excitons due to their limited diffusion length, which results in a photocurrent reduction.

Next, a more detail analysis of the effect of polymer and fullerene PLQ upon device performance will be presented. EQE was corrected by blend film absorbance as an approximation to IQE, and will be from now on referred as to IQE* (device absorption was not taken due to device degradation problems, and thus our corrected IQEs overlook interference effects due to the electrodes).

IQEs* for the devices with different polymer:fullerene ratios are shown in *Figure 4.11a.* As expected, the highest IQE* was obtained for the best performing 1:2 device, although at higher wavelengths (from ~700 nm) device 1:4 seems to slightly outperform the rest. In order to make clearer these differences IQE* spectra were normalized at 350 nm, (*Figure 4.11b)* to show the changes in the red (polymer absorbing) part of the spectra. IQE* spectra were also normalized at 780 nm (*Figure 4.11c*) to show the changes in the blue (fullerene absorbing) part of the spectra.

It is clear from the figures with normalized IQEs* that devices with higher $PC_{70}BM$ loadings, generate photocurrent more efficiently from absorbed photons in the polymer absorbing areas, whereas devices with higher polymer loadings, generate photocurrent more efficiently in the $PC_{70}BM$ absorbing areas. It is also noticeable in *Figure 4.11b* how device 1:4 only generates photocurrent efficiently in the polymer absorption spectral region, whereas in the fullerene absorption spectral region the conversion is limited, consistent with the previous observations. This suggests that the differences in the IQE* profiles are mainly due to differences in PLQ, since as shown before, polymer excitons, which are generated by excitation in the red part of the spectrum are better quenched with higher $PC_{70}BM$ loadings and conversely, fullerene excitons, which are generated by blue photons are better quenched with higher polymer loadings. In order to make a quantitative correlation as a function of the fullerene fraction (*x*PCBM) *Figure 4.11d* shows the relative PLQ, calculated as the ratio between $PC_{70}BM$ PLQ and DPPTT-T PLQ overlaid upon the relative integrated

IQE*, calculated as the ratio between the area under the curve for the $PC_{70}BM$ absorbing area (considered, as an approximation, from 300 to 560 nm) and the area under the curve for the polymer absorbing area; (considered from 570 to 850 nm), these areas are separated by a dotted line in *Figure 4.11a*. Using relative quantities should in principle cancel out errors associated to the measurements, and therefore is a better way to compare the trends. As is apparent, these two ratios show a clear correlation, thus supporting the hypothesis that incomplete PLQ in the blends has a large impact in current generation in the corresponding devices. In principle then, short circuit currents in device could be even higher if exciton quenching efficiency was higher.

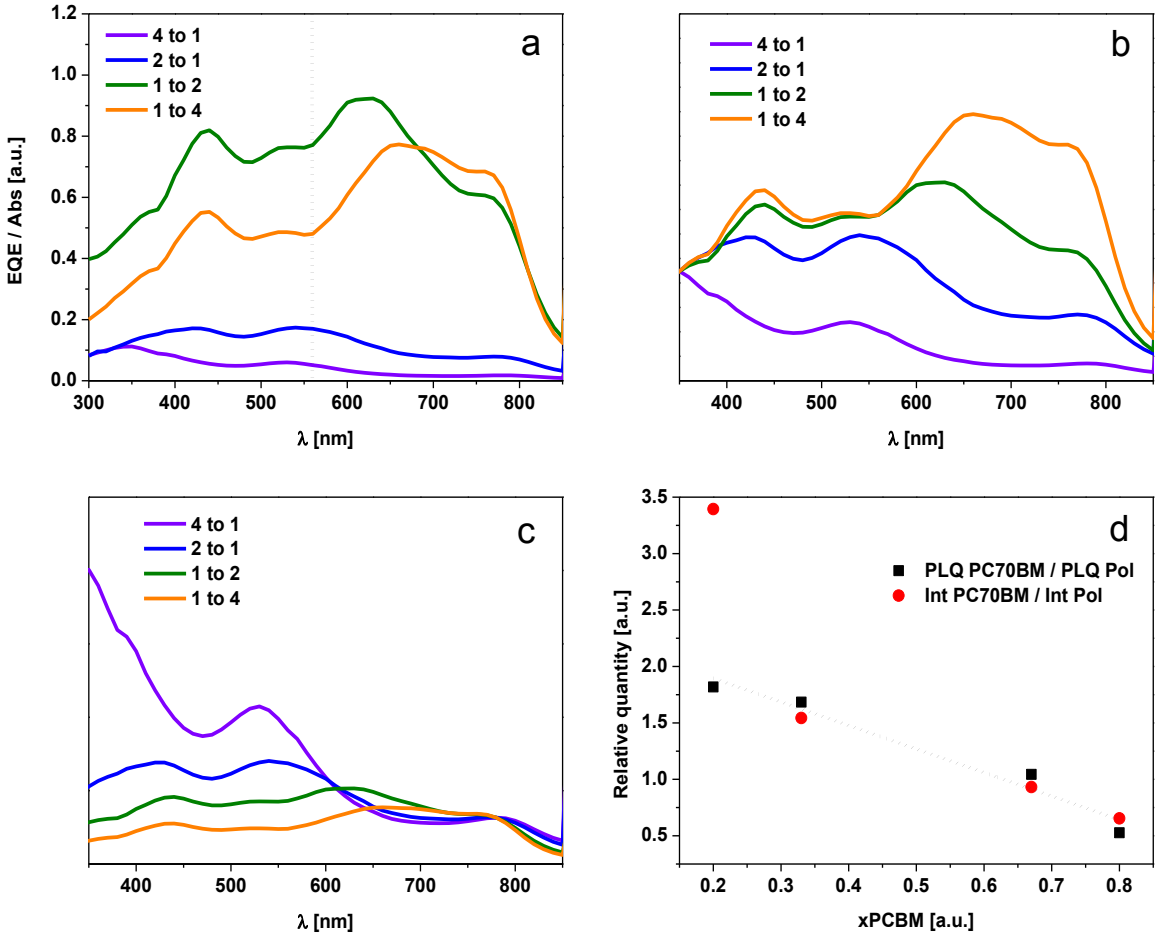

Figure 4.11. a) IQE* for devices fabricated with 4 to 1, 2 to 1, 1 to 2 and 1 to 4 DPPTT-T:$PC_{70}BM$ ratios. The line divides the areas considered for the integration in d), see text. b) IQEs* normalized at the absorption of the 4 to 1 blend at 350 nm. c) IQEs* normalized at the absorption of the 1 to 4 blend at 780 nm. d) $PC_{70}BM$ PLQ divided by DPPTT-T PLQ (black squares) and integrated IQE* in the $PC_{70}BM$ area (Int $PC_{70}BM$) divided by integrated IQE* in the polymer area (red circles) as a function of the fraction amount of $PC_{70}BM$, see text for more details on this relative quantities. Devices were fabricated and measured by Alex Gillett and Dr. Pabitra Shakya Tuladhar.

4e. Discussion

The study herein presented shows interesting trends connecting exciton dissociation, charge separation and recombination, morphology and device performance flor DPPTT-T:$PC_{70}BM$ devices as a function of blend composition. The PLQ results suggest that there is no single composition in which PL from both the polymer and the fullerene are completely quenched at the same time. This is a key finding, since it indicates that all devices fabricated with different polymer/fullerene ratios present intrinsic limitations due to incomplete exciton dissociation. Even in the 1:2 blend, which corresponds to the composition for the optimal device performance, losses are close to 30% for both DPPTT-T and $PC_{70}BM$ excitons, emphasizing the large effect that the conversion of these excitons into charges could have in the short circuit current of the corresponding device.

From the WAXD analysis, it was obtained that the crystallinity of the polymer is largely undisturbed upon fullerene increasing loading. UV-vis results suggest that the $\pi - \pi$ interactions within the polymer even increase upon fullerene loading. On the other hand, $PC_{70}BM$ agglomerates remain relatively undisturbed upon polymer loading. It is likely however, that at low fullerene concentrations, $PC_{70}BM$ molecularly intermixes within the crystalline polymer phase, as suggested from its complete exciton quenching in the 4 to 1 blend and its very high exciton quenching in the 2 to 1 blends. These findings suggest that both components form rather aggregated domains at all blend compositions in which only the relative size changes. While the change in relative size is substantial for $PC_{70}BM$, which shows essentially no domains in the 4 to 1 blend, the high crystallinity of DPPTT-T in all blends appears to result in its domains being relatively large even in the blends with high fullerene loading. Additionally, the fast exciton decay found in the DPPTT-T blend also suggests that its exciton diffusion length might be at least a few nanometers shorter than the average for other low bandgap polymers. This has also been found in another DPP-based polymer study[40]. These morphological and photophysical considerations would explain the asymmetry observed in the polymer compared to the fullerene emission quenching.

The asymmetry in the polymer and fullerene emission quenching can also be explained by energetic arguments. From the DPPTT-T and $PC_{70}BM$ HOMO-LUMO energy levels shown in Chapter 3, one can observe a more favoured HOMO – HOMO energy difference of 0.8 eV as compared to the LUMO – LUMO energy difference of 0 eV, taking $PC_{70}BM$ LUMO level to be -3.7 eV. Assuming that in all blends the reorganization energy is the same, this comparison would suggest that the hole transfer process is a much more efficient process than the electron transfer, which could also explain the residual polymer emission in the 1 to 10 blend.

Whether the incomplete exciton quenching in DPPTT-T is explained by an energetic or a morphological argument is a difficult matter and it is likely that both effects operate simultaneously. However, there is some evidence that the morphology explanation might be more adequate. At least three DPP-based polymers similar to DPPTT-T have been used in conventional devices and have reported to show[7,15] equal or higher EQEs in the polymer area $\left(EQE_{max}^{Pol}\right)$ than DPPTT-T/$PC_{70}BM$ devices, associated with higher polymer PL quenching[15]. These polymers, present lower driving energies for charge separation (ΔE_{CS}) compared to DPPTT-T, indicating that the low ΔE_{CS} is not a limitation for exciton dissociation.

This study shows that the amount of photoluminescence quenching impacts directly upon IQE*. The blends with higher polymer concentrations were more efficient in generating photocurrent from excitons generated in the fullerene domains. Conversely, the blends with higher fullerene concentrations generate photocurrent more efficiently from the polymer domains. This is likely to be a result of the high polymer crystallinity and the relative size of the fullerene domains. If these are too small, as in the 4 to 1 blend, spatially confined polaron are formed and recombine with a half-lifetime of 0.5 ns, independently of the laser excitation intensity. If the fullerene domains are large enough to form percolating pathways (which is likely to happen in blends between 2 to 1 and 1 to 2 loading) polarons separate more efficiently and recombine non-geminately with a half-lifetime of 8.8 ns at the lowest excitation intensity (1 $\mu J/cm^2$). This also impacts on the shape of the J-V curves of the corresponding devices. Blends with low fullerene loadings show not only a low J_{SC} (resulting from the polymer exciton quenching losses) but also a bias-dependent current close to J_{SC} and thus a low fill factor possibly resulting from the aforementioned geminate losses. It is necessary to remark that a charge extraction and transient photovoltage analysis would be required to confirm that the geminate losses indeed are shaping the fill factor of the devices with low $PC_{70}BM$ concentration. As expected, fill factor progressively increases upon the addition of fullerene, even from device 1:2 to 1:4, when current is being sacrificed due to the $PC_{70}BM$ exciton quenching losses. This is likely to be a result of slower non-geminate recombination.

Janssen et al. found that DPP-based polymer crystallite sizes in DPP/$PC_{70}BM$ blend films correlate with EQE in the polymer area.[7,15] From these findings , along with the fast exciton decays obtained herein and elsewhere[40], it seems that the limitations due to efficient exciton dissociation are rather general for DPP-based polymer/fullerene blends and thus, careful morphology optimization such as the addition of processing additives should be considered. This chapter also demonstrates that the spatial confinement of polarons can enhance the formation of polaron pairs and result in geminate recombination.

4f. Conclusions

Summarizing, in this chapter we have studied the correlation between charge photogeneration and charge recombination with blend microstructure and morphology for blends with different DPPTT-T/$PC_{70}BM$ ratios. From the results, it can be concluded that there is a trade off between the optimum composition for exciton dissociation and for geminate recombination suppression and non-geminate recombination retardation. The high crystallinity of DPPTT-T impedes a complete intermixing with $PC_{70}BM$, resulting in intrinsic polymer exciton quenching limitations and formation of a relatively high amount of bound polaron pairs in the blends with low fullerene loadings. Although increasing the fullerene concentration helps to improve polymer exciton quenching, suppresses geminate recombination of bound polaron pairs, and slows down polaron non-geminate recombination, it also incurs in fullerene exciton decay losses. These intrinsic limitations are likely to result in EQE limitations for DPPTT-T. There is evidence that suggests that this might be also the case for others DPP-based devices.

4e. References

(1) Hendriks, K. H.; Heintges, G. H. L.; Gevaerts, V. S.; Wienk, M. M.; Janssen, R. a J. *Angew. Chem. Int. Ed. Engl.* **2013**, *52*, 8341–8344.

(2) Bronstein, H.; Collado-Fregoso, E.; Hadipour, A.; Soon, Y. W.; Huang, Z.; Dimitrov, S. D.; Ashraf, R. S.; Rand, B. P.; Watkins, S. E.; Tuladhar, P. S.; Iain Meager; Durrant, J. R.; McCulloch, I. *Adv. Funct. Mater.* **2013**.

(3) Chen, Z.; Lee, M. J.; Shahid Ashraf, R.; Gu, Y.; Albert-Seifried, S.; Meedom Nielsen, M.; Schroeder, B.; Anthopoulos, T. D.; Heeney, M.; McCulloch, I.; Sirringhaus, H. *Adv. Mater.* **2012**, *24*, 647–652.

(4) Wienk, M. M.; Turbiez, M.; Gilot, J.; Janssen, R. A. J. *Adv. Mater.* **2008**, *20*, 2556–2560.

(5) Bronstein, H.; Chen, Z.; Ashraf, R. S.; Zhang, W.; Du, J.; Durrant, J. R.; Tuladhar, P. S.; Song, K.; Watkins, S. E.; Geerts, Y.; Wienk, M. M.; Janssen, R. a J.; Anthopoulos, T.; Sirringhaus, H.; Heeney, M.; McCulloch, I. *J. Am. Chem. Soc.* **2011**, *133*, 3272–3275.

(6) Vezie, M. S.; Few, S.; Meager, I.; Pieridou, G.; Dorling, B.; Shahid Ashraf, R.; Goni, A. R.; Hayes, S. C.; Campoy-Quiles, M.; Nelson, J. **2015**.

(7) Li, W.; Hendriks, K. H.; Furlan, A.; Roelofs, W. S. C.; Wienk, M. M.; Janssen, R. a J. *J. Am. Chem. Soc.* **2013**, *135*, 18942–18948.

(8) Meager, I.; Ashraf, R. S.; Mollinger, S.; Schroeder, B. C.; Bronstein, H.; Beatrup, D.; Vezie, M. S.; Kirchartz, T.; Salleo, A.; Nelson, J.; McCulloch, I. *J. Am. Chem. Soc.* **2013**, *135*, 11537–11540.

(9) Cabanetos, C.; Labban, A. El; Bartelt, J. A.; Douglas, J. D.; Mateker, W. R.; Frechet, J. M. J.; McGehee, M. D.; Beaujuge, P. M. *J. Am. Chem. Soc.* **2013**, *135*, 4656–4659.

(10) Cui, C.; Wong, W.-Y.; Li, Y. *Energy Environ. Sci.* **2014**, *7*, 2276.

(11) He, Z.; Zhong, C.; Huang, X.; Wong, W.-Y.; Wu, H.; Chen, L.; Su, S.; Cao, Y. *Adv. Mater.* **2011**, *23*, 4636–4643.

(12) Huang, Y.; Guo, X.; Liu, F.; Huo, L.; Chen, Y.; Russell, T. P.; Han, C. C.; Li, Y.; Hou, J. *Adv. Mater.* **2012**, *24*, 3383–3389.

(13) Ye, L.; Zhang, S.; Zhao, W.; Yao, H.; Hou, J. *Chem. Mater.* **2014**, *26*, 3603–3605.

(14) Chen, H. C.; Chen, Y. H.; Liu, C. C.; Chien, Y. C.; Chou, S. W.; Chou, P. T. *Chem. Mater.* **2012**, *24*, 4766–4772.

(15) Li, W.; Hendriks, K. H.; Furlan, A.; Roelofs, W. S. C.; Meskers, S. C. J.; Wienk, M. M.; Janssen, R. a J. *Adv. Mater.* **2014**, *26*, 1565–1570.

(16) Kim, Y.; Choulis, S. a.; Nelson, J.; Bradley, D. D. C.; Cook, S.; Durrant, J. R. *J. Mater. Sci.* **2005**, *40*, 1371–1376.

(17) Müller, C.; Ferenczi, T. a M.; Campoy-Quiles, M.; Frost, J. M.; Bradley, D. D. C.; Smith, P.; Stingelin-Stutzmann, N.; Nelson, J. *Adv. Mater.* **2008**, *20*, 3510–3515.

(18) Keivanidis, P. E.; Clarke, T. M.; Lilliu, S.; Agostinelli, T.; MacDonald, J. E.; Durrant, J. R.; Bradley, D. D. C.; Nelson, J. *J. Phys. Chem. Lett.* **2010**, *1*, 734–738.

(19) Guilbert, A. a. Y.; Schmidt, M.; Bruno, A.; Yao, J.; King, S.; Tuladhar, S. M.; Kirchartz, T.; Alonso, M. I.; Goñi, A. R.; Stingelin, N.; Haque, S. a.; Campoy-Quiles, M.; Nelson, J. *Adv. Funct. Mater.* **2014**, n/a – n/a.

(20) van Duren, J. K. J.; Yang, X.; Loos, J.; Bulle-Lieuwma, C. W. T.; Sieval, A. B.; Hummelen, J. C.; Janssen, R. A. J. *Adv. Funct. Mater.* **2004**, *14*, 425–434.

(21) Mihailetchi, V. D.; Koster, L. J. a; Blom, P. W. M.; Melzer, C.; De Boer, B.; Van Duren, J. K. J.; Janssen, R. a J. *Adv. Funct. Mater.* **2005**, *15*, 795–801.

(22) Clarke, T. M.; Ballantyne, A. M.; Tierney, S.; Heeney, M.; Duffy, W.; McCulloch, I.; Nelson, J.; Durrant, J. R. *J. Phys. Chem. C* **2010**, *114*, 8068–8075.

(23) Kästner, C.; Egbe, D. a. M.; Hoppe, H. *J. Mater. Chem. A* **2015**, *3*, 395–403.

(24) Tumbleston, J. R.; Yang, L.; You, W.; Ade, H. *Polymer (Guildf).* **2014**, *55*, 4884–4889.

(25) Jamieson, F. C.; Domingo, E. B.; McCarthy-Ward, T.; Heeney, M.; Stingelin, N.; Durrant, J. R. *Chem. Sci.* **2012**, *3*, 485.

(26) Shoaee, S.; Subramaniyan, S.; Xin, H.; Keiderling, C.; Tuladhar, P. S.; Jamieson, F.; Jenekhe, S. a.; Durrant, J. R. *Adv. Funct. Mater.* **2013**, *23*, 3286–3298.

(27) Veldman, D.; Ipek, O.; Meskers, S. C. J.; Sweelssen, J.; Koetse, M. M.; Veenstra, S. C.; Kroon, J. M.; van Bavel, S. S.; Loos, J.; Janssen, R. a J. *J. Am. Chem. Soc.* **2008**, *130*, 7721–7735.

(28) Savoie, B. M.; Rao, A.; Bakulin, A. a.; Gelinas, S.; Movaghar, B.; Friend, R. H.; Marks, T. J.; Ratner, M. a. *J. Am. Chem. Soc.* **2014**, *136*, 2876–2884.

(29) Hawks, S. a.; Deledalle, F.; Yao, J.; Rebois, D. G.; Li, G.; Nelson, J.; Yang, Y.; Kirchartz, T.; Durrant, J. R. *Adv. Energy Mater.* **2013**, *3*, 1201–1209.

(30) Hamilton, R.; Shuttle, C. G.; O'Regan, B.; Hammant, T. C.; Nelson, J.; Durrant, J. R. *J. Phys. Chem. Lett.* **2010**, *1*, 1432–1436.

(31) Tsoi, W. C.; Zhang, W.; Razzell Hollis, J.; Suh, M.; Heeney, M.; McCulloch, I.; Kim, J.-S. *Appl. Phys. Lett.* **2013**, *102*, 173302.

(32) Monkman, A.; Burrows, H. D. *Synth. Met.* **2003**, *141*, 81–86.

(33) Soon, Y. W.; Shoaee, S.; Ashraf, R. S.; Bronstein, H.; Schroeder, B. C.; Zhang, W.; Fei, Z.; Heeney, M.; McCulloch, I.; Durrant, J. R. *Adv. Funct. Mater.* **2014**, *24*, 1474–1482.

(34) Ochsmann, J. R.; Chandran, D.; Gehrig, D. W.; Anwar, H.; Madathil, P. K.; Lee, K.; Laquai, F. *Macromol. Rapid Commun.* **2015**, *36*, 1122–1128.

(35) Dimitrov, S. D.; Wheeler, S.; Niedzialek, D.; Schroeder, B. C.; Utzat, H.; Frost, J. M.; Yao, J.; Gillett, A.; Tuladhar, P. S.; McCulloch, I.; Nelson, J.; Durrant, J. R. *Nat. Commun.* **2015**, *6*, 6501.

(36) Yamamoto, S.; Ohkita, H.; Benten, H.; Ito, S. *J. Phys. Chem. C* **2012**, *116*, 14804–14810.

(37) Scarongella, M.; Laktionov, A.; Rothlisberger, U.; Banerji, N. *J. Mater. Chem. C* **2013**, *1*, 2308.

(38) Gehrig, D. W.; Howard, I. a; Kamm, V.; Mangold, H.; Neher, D.; Laquai, F. *J. Phys. Chem. C* **2014**, *118*, 20077–20085.

(39) Paraecattil, A. A.; Beaupré, S.; Leclerc, M.; Moser, J. E.; Banerji, N. *J. Phys. Chem. Lett.* **2012**, *3*, 2952–2958.

(40) Albert-Seifried, S.; Ko, D.-H.; Hüttner, S.; Kanimozhi, C.; Patil, S.; Friend, R. H. *Phys. Chem. Chem. Phys.* **2014**, *16*, 6743–6752.

(41) Lanzani, G. *The Photophysics behind Photovoltaics and Photonics*; 2012.

(42) Köhler, A.; Bässler, H. *Electronic Processes in Organic Semiconductors*; Wiley-VCH Verlag & Co. KGaA, 2015.

(43) Etzold, F.; Howard, I. a; Mauer, R.; Meister, M.; Kim, T.-D.; Lee, K.-S.; Baek, N. S.; Laquai, F. *J. Am. Chem. Soc.* **2011**, *133*, 9469–9479.

(44) Scarongella, M.; De Jonghe-Risse, J.; Buchaca-Domingo, E.; Causa', M.; Fei, Z.; Heeney, M.; Moser, J.-E.; Stingelin, N.; Banerji, N. *J. Am. Chem. Soc.* **2015**, *137*, 2908–2918.

(45) Huang, Z.; Fregoso, E. C.; Dimitrov, S.; Tuladhar, P. S.; Soon, Y. W.; Bronstein, H.; Meager, I.; Zhang, W.; McCulloch, I.; Durrant, J. R. *J. Mater. Chem. A* **2014**, *2*, 19282–19289.

(46) Piersimoni, F.; Chambon, S.; Vandewal, K.; Mens, R.; Boonen, T.; Gadisa, A.; Izquierdo, M.; Filippone, S.; Ruttens, B.; D'haen, J.; Martin, N.; Lutsen, L.; Vanderzande, D.; Adriaensens, P.; Manca, J. V. *J. Phys. Chem. C* **2011**, *115*, 10873–10880.

(47) Dimitrov, S. D.; Nielsen, C. B.; Shoaee, S.; Tuladhar, P. S.; Du, J.; Mcculloch, I.; Durrant, J. R. *J. Phys. Chem. Lett.* **2011**, 140–144.

(48) Dimitrov, S. D.; Huang, Z.; Deledalle, F.; Nielsen, C. B.; Schroeder, B. C.; Ashraf, R. S.; Shoaee, S.; McCulloch, I.; Durrant, J. R. *Energy Environ. Sci.* **2014**, *7*, 1037.

(49) Cook, S.; Furube, A.; Katoh, R.; Han, L. *Chem. Phys. Lett.* **2009**, *478*, 33–36.

(50) Campoy-Quiles, M.; Ferenczi, T.; Agostinelli, T.; Etchegoin, P. G.; Kim, Y.; Anthopoulos, T. D.; Stavrinou, P. N.; Bradley, D. D. C.; Nelson, J. *Nat. Mater.* **2008**, *7*, 158–164.

(51) Georgiou, D.; Laskarakis, a.; Morana, M.; Karagiannidis, P. G.; Logothetidis, S. *Sol. Energy Mater. Sol. Cells* **2014**, *125*, 190–197.

(52) Dibb, G. F. a.; Jamieson, F. C.; Maurano, A.; Nelson, J.; Durrant, J. R. *J. Phys. Chem. Lett.* **2013**, *4*, 803–808.

(53) Proctor, C. M.; Albrecht, S.; Kuik, M.; Neher, D.; Nguyen, T. Q. *Adv. Energy Mater.* **2014**, *4*, 1400230.

Chapter 5. Effect of fluorination on charge generation and recombination

This chapter presents the comparative study of two low-bandgap polymers whose only difference is the substitution of the flanking thiophenes of the DTBT moiety with two fluorine atoms each. Although it seems like these are small changes, they have a profound effect in the energetics of the polymers and their photophysical behaviour, and result in an improved device performance. The LUMO level of the fluorinated polymer is significantly lower than that of its non-fluorinated counterpart, however their bandgap is conserved. As a result, ΔE_{CS} is significantly lower for the fluorinated polymer. From the studies presented in Chapter 3, a negative result in terms of J_{SC} could be predicted upon fluorination if the main drive was energetic. However, it was found that the efficiency is increased and the J_{SC} has an almost double-fold improvement.

In view of these findings, it was interesting to determine whether the correlation between J_{SC} and ΔOD in blends holds, and in that case, to understand which properties are modified upon fluorination and the reasons explaining their opposing effect to the driving energy for charge separation. Ultimately, the objective was to understand the main reasons behind the almost double-fold improvement in J_{SC} in the F4 blend as compared to the F0 blend.

The introduction presents the current literature that addresses the effects of fluorination on intrinsic properties of the polymers such as their energy levels and bandgap, absorption coefficient and crystallinity, and their effects on blend microstructure and ultimately upon device performance. Next, the experimental details of the techniques used to characterize the systems are described. Then the steady-state spectroscopy results are presented, followed by the time-resolved spectroscopy results. In the same way as for Chpater 4, in the section *Complementary Results*, the results obtained by Colleagues at the Chemistry Department at Imperial College are presented. Finally the results are discussed and referenced to the differences in device performance. The conclusions and references are presented at the end.

5a. Introduction

The design of copolymers with donor-acceptor character has been widely used for OPV applications with very positive results, so that most of the devices with champion efficiencies use polymers that were developed using this approach[1–3]. One way to induce a gradient in monomer electron density is through the introduction of strong electron-withdrawing atoms such as fluorine, which has resulted in efficiencies as high as 9.4%[4], close to the best performing single-junction devices.

Fluorinated polymers have often been shown to exhibit improved power conversion efficiencies over their non-fluorinated counterparts; however different reasons behind these variations have been evoked for the different systems studied[5–15]. Most of the studies showed a V_{OC} enhancement upon fluorination, explained by the stabilization of the HOMO level of the polymer. This stabilization is induced by the electron withdrawing nature of fluorine atoms, usually added to the acceptor part of the polymer, conferring it with a stronger acceptor nature. In most cases the LUMO level is also lowered upon fluorination, so that the bandgap of the fluorinated and non-fluorinated polymer versions are similar. Moreover, the majority of the studies show an improved hole mobility upon fluorination, which a few research groups have proposed to improve J_{SC}[7,12] and more recently, to cause an improvement in the fill factor of different devices prepared with polymers with varying amount of fluorination[13]. We remark than in our group, we have not found any relationship between the yield of positive polarons in the polymers and the hole mobility of the polymers[16].

Molecular modeling studies have indicated that partial fluorination of the acceptor unit of the polymer can induce a larger polarization of the polymer excited state, corresponding to an increase in the change in dipole from the ground to the excited state ($\Delta\mu_{ge}$) which could have a direct impact in the charge separation efficiency[6,11,17]. Yu and coworkers[18] recently suggested a linear correlation between PCE and $\Delta\mu_{ge}$ as a guideline for material design. The hypothesis behind this relationship is that the increased polarisation of excitons generated in polymers with a large $\Delta\mu_{ge}$ facilitates charge separation, by decreasing the exciton binding energy, which ultimately results in an increased J_{sc}. However, this relationship was found to break down at higher $\Delta\mu_{ge}$ values, where the acceptor unit is too strong, presumably because of an excessive electron-withdrawing nature of the polymer's acceptor units, which lowers the polymer LUMO level thus reducing the energetic driving force for charge separation[18]. In addition, this study did not provide any direct evidence for a lowered exciton binding energy with fluorination. Another study has proposed that it is not charge separation what is responsible for device PCE improvement upon fluorination, but rather, that the increasing amount of

fluorine in the polymer backbone results in an improved hole mobility that is capable of explaining the significant improvements in fill factor and small improvements they observed in J_{SC}[13].

Fluorination has profound effects on the blend microstructure. Even replacing a single hydrogen atom on the backbone repeating unit with a fluorine atom can enhance polymer aggregation, usually resulting in larger domain sizes, with purer polymer-rich phases than in their non-fluorinated counterparts[9–12]. According to Neher and collaborators[10], high domain purity can produce a reduction in both geminate and non-geminate recombination, as observed with time-delayed collection field measurements on a fluorinated version of PCPDTBT. This facilitates the collection of charge-carriers; however large domain sizes and increased purity can also hamper exciton dissociation by increasing the effective distance the exciton has to travel before reaching the nearest acceptor molecule, as observed in Chapter 4. In some cases, the increase in aggregation upon fluorination has been found to be excessive, leading to solubility problems which make processing conditions extremely sensitive and can provoke detrimental effects on performance[5,9,19,20].

A more recent study[14] determined, using state-of-art morphology techniques and analysis to study a series of fluorinated and non fluorinated polymer/fullerene blends, that both J_{SC} and *FF* presented a linear correlation with the degree of molecular orientation. The degree of molecular orientation quantifies the average orientation of the polymer sheets with respect to the interface with the fullerene. It was found that the more "face-on" the orientation with respect to the interface with the fullerene, the higher J_{SC} and *FF*. The authors proposed that this orientation could result in improved exciton dissociation or charge transport. Finally, another study emphasized that the fluorine effect can be masked if the molecular weight of the polymer upon fluorination changes drastically, mainly due to the effect that the molecular weight of the polymer has on the fullerene domains size, which was found to correlate with J_{SC}[15].

Despite the amount of work carried out on the backbone fluorination issue, studies to date have not, to the best of our knowledge, included a detailed spectroscopic analysis of charge separation and recombination in blend films comparing the use of fluorinated and non-fluorinated polymers. Particularly, it is interesting to assess whether the predicted increase in polarization in the polymer excited state can be observed if it has a direct impact on charge separation and how this relates with the opposing effect predicted by a lower ΔE_{CS}, resulting from a lower LUMO level in the fluorinated polymer version. With this motivation, two low-bandgap polymers, fluorinated and non-fluorinated were investigated.

Whilst the vast majority of the studies focus on fluorination of the benzothiadiazole (BT) unit, in this study, the fluorinated polymer has the fluorine atoms on the flanking thiophenes (T), resulting in a TFDTBT acceptor unit, as depicted in *Figure 5.1*. Copolymerisation of this unit and its non-fluorinated analogue (DTBT) with an alkylated Ge-based dithieno donor unit resulted in directly comparable polymers PGeDTBT and PGeTFDTBT, which will be referred for simplicity as F0 and F4 respectively. These polymers, previously synthesized and reported by our collaborators[21], exhibited similar molecular weights and polydispersities, thus eliminating the interfering microstructure effects provoked by a change in the molecular weight upon the introduction of the fluorine atoms on the structure of the polymers.

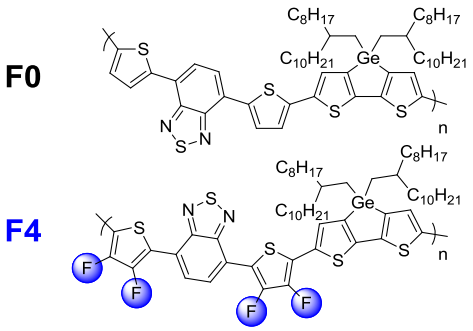

Figure 5.1. Structures of the polymers studied, PGeDTBT (top) and PGeTFDTBT (bottom), referred here as F0 and F4 respectively.

In the investigation of our collaborators[21], it was demonstrated that the effect of fluorination is directly observed with an increased V_{OC}, related to the lowering of the HOMO level in F4, as well as an almost double-fold increment in J_{SC}, corroborated by and improvement of F4's EQE in all the visible area. Device data (J-V curves and EQE) previously obtained for devices fabricated with F0 and F4 are shown in *Figure 5.2*. These changes were correlated with a stronger tendency to aggregate as observed by the vibronic features in the F4 UV-Vis spectrum, along with the formation of a more homogeneous distribution of domains in the blends with $PC_{70}BM$, as observed via AFM.

Further morphological studies were undertaken by our colleagues[22] to assess the change in crystallinity upon fluorination on both neat films and their corresponding 1:2 blends with $PC_{70}BM$. Grazing incidence wide-angle x-ray scattering (GIWAXS) patterns showed that while both polymers are similarly amorphous in pure thin films (weak lamellar diffraction for F4), F4 exhibits some degree of π-stacking when blended with $PC_{70}BM$, whereas F0 shows no significant diffraction features. Although the effect was found to be small, fluorination of the DTBT enhanced the degree of order in the (010) direction, an effect also observed by other groups.[11] A more dramatic change was the enhanced scattering from $PC_{70}BM$ aggregates in the F4 blend compared to the F0 blend. The F0

blend exhibited only weak scattering from $PC_{70}BM$ aggregates whilst the F4 blend exhibited pronounced $PC_{70}BM$ scattering consistent with a significant portion of aggregated $PC_{70}BM$, similar to what was observed in PCDTBT:PCBM[23] and PTB7:PCBM blends[24].

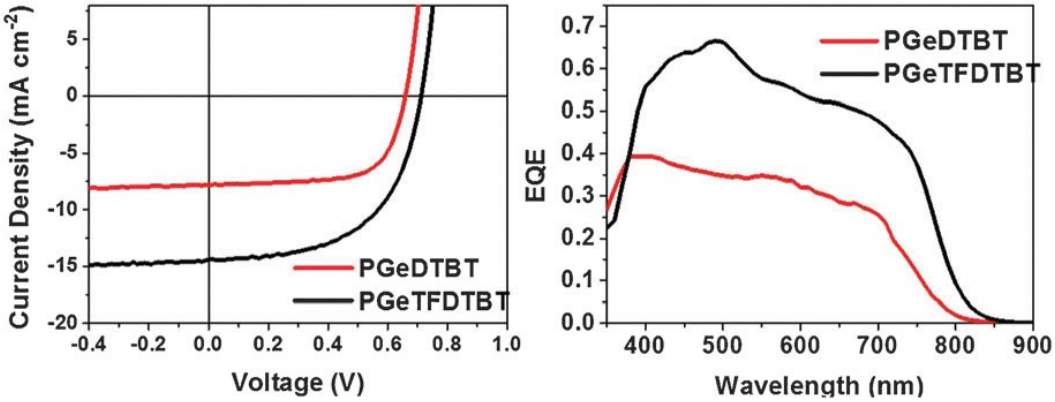

Figure 5.2. J-V curves (left) and EQE (right) curves of polymer solar cells based on 1:2 ratio of polymer:$PC_{70}BM$. Devices have a conventional architecture: ITO/PEDOT:PSS/Polymer:$PC_{70}BM$/LiF/Al. Figure taken from[21].

In this chapter, the influence of thiophene fluorination upon the photophysics and morphology of the neat polymer and polymer/fullerene blend films is assessed, via photoluminescence (PL) quenching and transient absorption spectroscopy (TAS) and compared to the results obtained via GIWAXS. It is shown that the improvement in device performance upon fluorination is likely to be related with two factors: 1) slower charge recombination from the sub-nanosecond timescale, that correlates with a higher induced crystallinity of F4 blends (both in the polymer and $PC_{70}BM$ domains) as obtained by GIWAXS and 2) the appearance of polaron-like charge transfer excitons in the F4 polymer, as observed in ultrafast TAS, which we propose to be related to the equally efficient charge generation observed in F4 blends, despite its lower driving energy for charge generation resulting from a lower-lying LUMO level compared to F0. This effect is attributed to the strong withdrawing nature of the fluorinated DTBT moiety within the polymer resulting in a high excited state polarization, as shown by our TD-DFT calculations.

5b. Experimental section

All blend films were prepared using the same optimized conditions as for active layers of the best performing devices[21], that is, they were spin coated from 12 mg/mL 1:2 polymer to $PC_{70}BM$ solutions

in *o*-dichlorobenzene (ODCB), after heating overnight at 90 °C to ensure full dissolution. Spin coating was performed on substrates at room temperature while solutions were at 60 °C. Neat films were spun from a 15 mg/mL polymer solution. All films were kept under Nitrogen atmosphere unless otherwise stated. PLQ results after exciting $PC_{70}BM$ were corrected to eliminate the contribution from polymer emission, which overlaps with the fullerene emission.

For the computational studies, Density Functional Theory (DFT) theory was used. All DFT calculations were performed using Gaussian 09 Revision C.01[25], at the B3LYP/6.31G(d) level of theory by Pierre Boufflet at the Department of Chemistry of Imperial College.

Alkyl side-chains were replaced by a simple sp^3 methyl group. Energies of the DTBT and TFDTBT units as a function of thiophene-BT dihedral angle were calculated by first optimizing the structure and, using the redundant coordinate editor, running a scan of the dihedral angle in 36 steps of 10° increments. The resulting energies were converted from Hartrees to kilojoules/mol and plotted relative to the respective minima of each structure to give the graph in *Figure 5.12*. The minimum energy conformation was then used to calculate the optimised geometry of the monomer, dimer and trimer molecules of the donor-acceptor unit. Excited-states were calculated using Time-Dependent DFT (TD-DFT), and correspond to the first excited state, before relaxation. HOMO and LUMO levels, as well as $\Delta\mu_{ge}$ values are quoted for trimer units, unless otherwise stated.

5c. Results

5c.1. Steady state UV-vis and Photoluminescence quenching: polymer and $PC_{70}BM$ domains

In order to assess the difference in aggregation behavior upon fluorination both in neat and blend films with $PC_{70}BM$, UV-vis spectra were obtained. Additionally, to gain more insight in the degree of intermixing of $PC_{70}BM$ and the polymers, photoluminescence measurements in both the neat and the blend materials were performed, probing the quenching of both polymer and fullerene photoluminescence (*PLQ*) in the blend films. UV-vis spectra and PL are shown in *Figure 5.3* and *5.4* respectively.

It is apparent from *Figure 5.3* and from the reconstruction of the blend spectra using the spectra of the neat components, that while for the non-fluorinated F0 blend the contribution from the F0 polymer and $PC_{70}BM$ to the blend absorption are similar (approximately 50% each), for the F4 blend, the contribution from $PC_{70}BM$ is much larger, which could suggest an increased aggregation behavior in the fullerene domains resulting in an increased oscillator strength in the F4 blend as compared

with the F0 blend. This aggregation agrees with the observed trends obtained via GIWAX measurements of the blends.

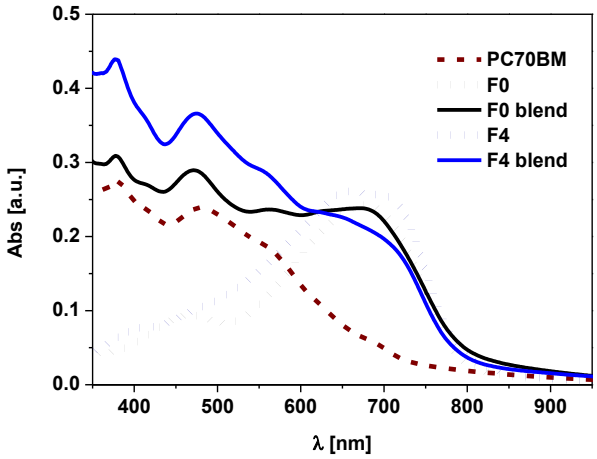

Figure 5.3. Steady state UV-vis absorption of neat and 1:2 blend films of F0 and F4 and $PC_{70}BM$. These films were used for the PL and TAS measurements.

To obtain the polymer PLQ, the blends were excited at 710 nm and detected in the near-IR region. As is noticeable in *Figure 5.4a*, polymer emission from both the F0 and F4 blends is highly quenched (98% for F0 and 95% for F4 compared to their respective neat materials). Analysis of this PLQ using *Equation 2.4* in Chapter 2 and assuming a 10 nm polymer exciton diffusion length, indicates that polymer excitons diffuse only 1 – 2 nm before being quenched by an acceptor fullerene, for both blends. Such short diffusion distances suggest a high level of $PC_{70}BM$ intermixing within the polymer rich domains, and the absence of a significant fraction of large, pure polymer domains. The slightly lower quenching observed in the F4 blend suggests a decrease in the intermixing between the polymer and $PC_{70}BM$; consistent with the increased visible absorption of the fullerene within the blend and the increased scattering from $PC_{70}BM$ aggregates observed by GIWAXS, as discussed later.

For the fullerene PLQ, the blend films were excited at 475 nm and fullerene singlet exciton emission monitored from 650 to 800 nm. As can be observed in *Figure 5.4b*, the quenching relative to neat $PC_{70}BM$ film is noticeably lower as compared to the polymer quenching (69% for F0 and 65% for F4 blend) suggesting the presence of relatively large, pure fullerene domains. Assuming a $PC_{70}BM$ exciton diffusion length of 5 nm,[26] these PLQ data suggest pure fullerene domain diameters on length scales of ≈ 6 nm, slightly larger than the size of the polymer domains, which have diameters between 2 and 4 nm. The low PLQ obtained is indicative of the fullerene exciton diffusion limitations. This would point to an important negative impact upon the efficiency of photocurrent

generation from fullerene excitons, however surprisingly this does not seem to be the case, judging by the rather high EQE at ≈ 450 nm, shown in *Figure 5.2*. The slightly less efficient fullerene exciton separation observed for F4 blends is consistent with the previous findings from GIWAX, in which there is a clear increase in $PC_{70}BM$ scattering corresponding to a higher $PC_{70}BM$ stacking and increased phase separation, as it will be seen shortly. Despite the higher polymer PLQ than the fullerene PLQ, the EQE in the blue spectral region is still higher than that of the red region (see *Figure 5.2*). If it is assumed that the differences in optical interference are negligible for different excitation wavelengths, these results suggest that additional losses, apart from exciton quenching, limit photocurrent generation from polymer excitons, as will be discussed further in the following sections.

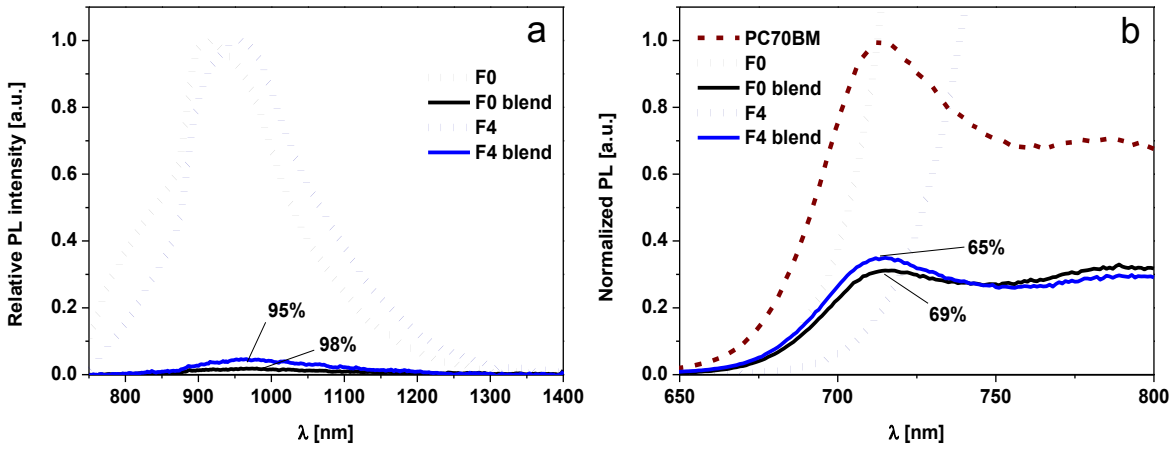

Figure 5.4. Steady-state Photoluminescence (PL) of a) films of neat F0 and F4 and their respective blends with $PC_{70}BM$ after exciting at 710 nm, normalized at the respective neat polymer's signal maxima and b) neat $PC_{70}BM$ film and F0/ $PC_{70}BM$ and F4/ $PC_{70}BM$ blends after exciting the fullerene at 475 nm, normalized at the respective neat fullerene's signal maxima. All signals were corrected for absorbance at their corresponding excitation wavelength.

5c.2. Femtosecond to microsecond transient absorption spectroscopy: photophysics in neat films and charge generation and recombination in blends.

Femtosecond to microsecond-resolved transient absorption spectroscopy (TAS) was used as a probe of exciton and polaron dynamics following polymer excitation in both neat polymer films and blends with $PC_{70}BM$ acceptor. In *Figure 5.5* transient absorption spectra from 200 fs to 6 ns of a) neat non-fluorinated F0 polymer, b) 1:2 F0/$PC_{70}BM$ blend films, c) neat fluorinated F4 polymer and d) 1:2 F4/$PC_{70}BM$ blend is shown. Films were excited at 710 nm with an intensity of 3 $\mu J/cm^2$ and are corrected for differences in absorbance at the excitation wavelength. These conditions assure firstly

that the excitation is selective for the polymer, and secondly, that non-linear processes are minimized, since this excitation intensity produces signals within the linear response region (analogous data taken at lower, ~ 1 µJ /cm^2 excitation intensity show similar results). Neat spectra for both polymers will be presented first, followed by a detailed discussion on exciton generation and decay (*Figure 5.5a* and *5.5c*). Next, charge generation and recombination will be discussed, following from the analysis of F0 and F4 blend spectra in *Figure 5.5b* and *5.5d*.

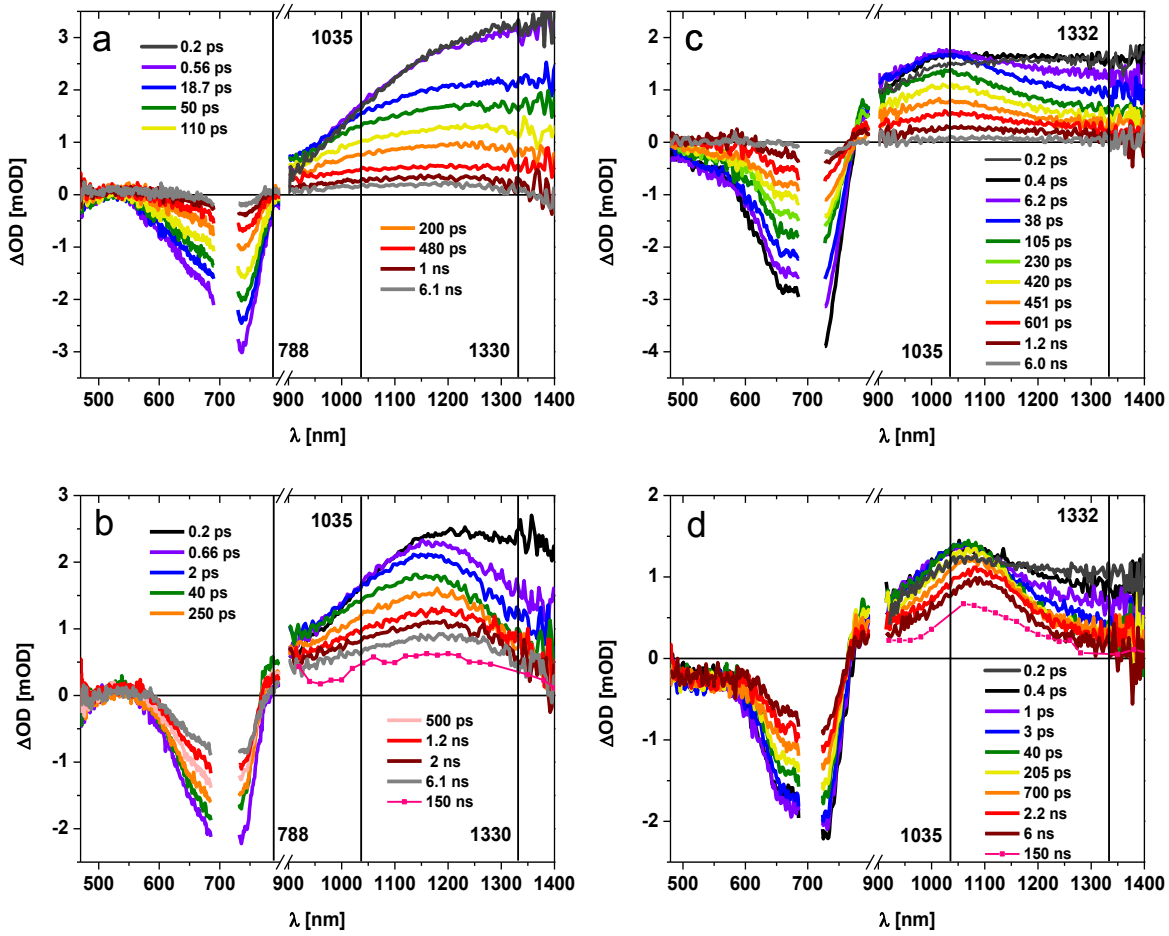

Figure 5.5. Transient absorption spectra after pump excitation at 710 nm, with a beam intensity of 3 µJ/cm^2 for a) F0 neat film, b) 1:2 F0/$PC_{70}BM$ blend, c) F4 neat film, d) 1:2 F4/$PC_{70}BM$ blend. All signals have been corrected for polymer or blend absorbance accordingly. Data with dots was measured in our nanosecond to microsecond setup, 150 ns after exciting at 660 nm and were corrected to match beam intensity.

It can be observed that spectra for both F0 and F4 neat films show two main types of signals. Firstly, a negative feature from ~ 550 to 790 nm for F0 and from ~ 480 to 775 nm for F4. This negative signal corresponds to the polymers ground state bleaching, (GSB) i.e. the depletion of ground state

polymer molecules after the excitation; this signal is probably mixed with the stimulated emission (SE) signal coming from the unrelaxed singlet state S_1. Secondly, a positive photoinduced absorption feature is apparent, extending from ~ 900 to 1400 nm in both polymers. This photoinduced absorption is assigned to $S_1 \rightarrow S_n$ singlet exciton absorption, consistent with literature assignments of analogous data for other low-bandgap semiconducting polymers[27–29]. From the decay times of this positive, photoinduced absorption signal average decay times of the singlet excitons can be extracted, corresponding to $\tau_{F0} \approx 90$ ps for F0 and $\tau_{F4} \approx 180$ ps for F4.

For both polymers, a small, long lived, residual signal is observed at 6 ns. In order to complete the assignment, microsecond-resolved TAS was performed on the neat polymer films in the presence of nitrogen and oxygen atmospheres, as it is shown in *Figure 5.6a* and *5.6b*. In both cases, small but detectable signals under both atmospheres were found, with similar spectra to the residual spectra observed in the ultrafast data at 6 ns. F4 has a larger amplitude compared to F0, but more importantly, a considerably slower decay as compared to F0 when both are measured in nitrogen. ($\tau_{T(F4)} \approx 1.1 \pm 0.07$ μs and $\tau_{T(F0)} \leq 0.7$ μs) F4's microsecond transient absorption signal is strongly quenched when exposed to an oxygen atmosphere, indicating this signal should be assigned to triplet excitons. For F0 film, the shorter lifetime and smaller signal amplitude prevented the observation such oxygen induced quenching, although it appears most likely that this long lived signal also derives from photogenerated polymer triplet states.

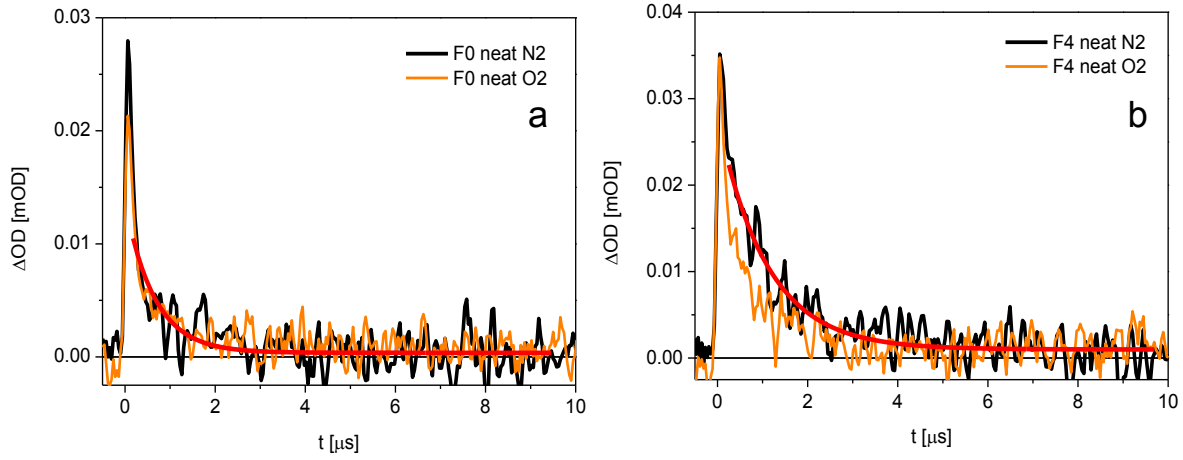

Figure 5.6. Microsecond-resolved transients taken exciting at 660 nm with 5 μJ/cm^2 and probing at 1160 nm for F0 neat film (a) and at 1060 for F4 neat film (b). Red lines correspond to best monoexponential fits, see text.

We now return to the description of the ultrafast transient spectra. It is apparent that the photoinduced absorption of the neat F4 film shows a pronounced, rapid blue shift along with an amplitude increase, such that a band can be observed at 1030 nm from early times. This blue-shifting process exhibits an average time constant of ~ 2.3 ps, as obtained from the fast exponential decays of the transients at different probed wavelengths, as shown in *Figure 5.7*, the data of the fittings is shown in *Table 1*. These decays were fitted to triexponential functions whose characteristic times correspond to a) the blue shift of the signal, b) the intrinsic decay of the excitons and c) the conversion of triplets. The assignment of the blue shift to a rapid intersystem crossing is ruled out, since this would result in an essentially complete quenching of the steady-state PL. Rather, this process was assigned to the slowest characteristic time in *Figure 5.7*. The importance of the blue shift will be discussed below. An analogous, but much weaker blue shift is also observed for F0.

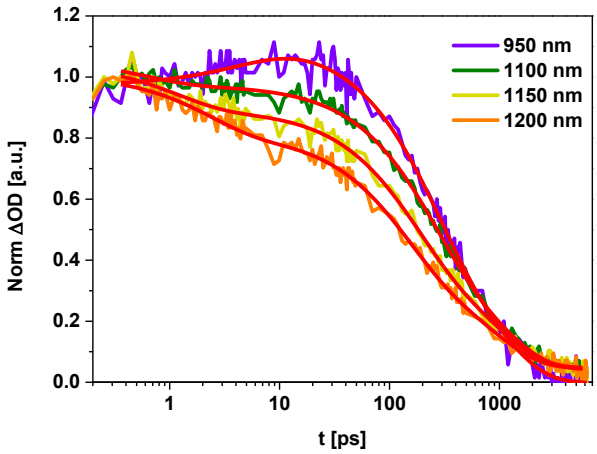

Figure 5.7. Probed-wavelength dependence of the F4 exciton dynamics showing the the blue-shift of the signal in the first 10 ps, after excitation at 710 nm with an intensity of 3 μJ/cm^2. In red, best-triexponential fits.

Table 1. Best tri-exponential fits, $y = y_0 + A_1 e^{-x/\tau_1} + A_2 e^{-x/\tau_2} + A_3 e^{-x/\tau_3}$ to the IR exciton decays for different probed wavelentghts. Values are reported ± standard error.

λ_{prob} (nm)	y_0 (a.u.)	A_1 (a.u.)	τ_1 (ps)	A_2 (a.u.)	τ_2 (ps)	A_3 (a.u.)	τ_3 (ps)
950	0.000±0.008	-0.14±0.01	5.3±1.3	0.62±0.11	227±39	0.40±0.08	961±192
1100	0.042±0.005	0.09±0.03	0.6±0.3	0.53±0.05	217±17	0.40±0.04	1002±112
1150	0.047±0.005	0.15±0.02	1.1±0.2	0.47±0.03	153±13	0.38±0.03	921±101
1200	0.046±0.005	0.19±0.01	2.2±0.2	0.43±0.03	129±11	0.34±0.02	861±96

Following, the description of the spectral dynamics of the F0/$PC_{70}BM$ and F4/$PC_{70}BM$ blend films are presented, as well as a discussion on charge generation and recombination. In *Figure 5.5b* and *5.5d*, broadly similar absorption features as the ones for the neat films can be observed: a negative signal in the visible assigned to GSB and positive photoinduced absorption signal in the NIR. It is apparent that the GSB signal decays much more slowly than the GSB of the neat films. At early times, for both blends, the spectrum of the NIR photoinduced absorption is similar to that observed for the neat films, indicative of the initial formation of polymer singlet excitons. This photoinduced exciton absorption however, is rapidly quenched, and the transient spectra rapidly evolves to a new, blue-shifted absorption signal exhibiting a maximum at ≈ 1150 nm for F0 and ≈ 1100 nm for F4. This blue-shifted signal is still present at 6 ns. It is noticeable that the GSB negative signal has also a larger amplitude at 6 ns compared to the corresponding neat transients, observation that confirms the presence of long-lived species. Additionally, it is apparent that the features corresponding to $PC_{70}BM$ excitons are not observed for either blend films, consistent with our excitation wavelength being selective for polymer excitation. We notice that even when the pump pulse partly excites the fullerene acceptor, previous studies show that fullerene signals are generally not observed since their extinction coefficient is lower[30] with respect to the polymers and tend to be overlapped by the polymer signals.

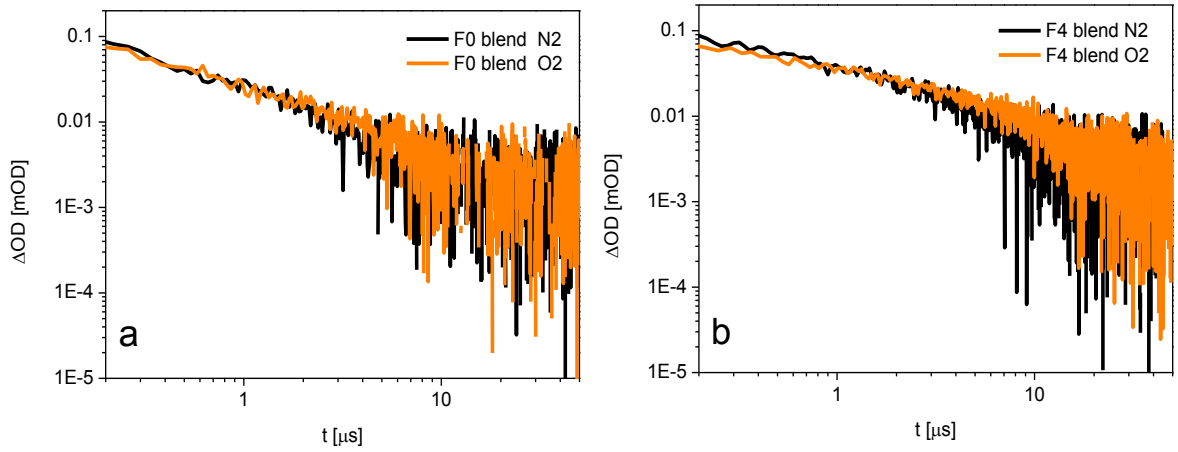

Figure 5.8. Microsecond-resolved transients taken exciting at 660 nm with 5 μJ/cm^2 and probing at 1160 nm for 1:2 F0/$PC_{70}BM$ blend films (a) and at 1060 for 1:2 F4/$PC_{70}BM$ blend films (b).

In order to assign the nature of the long-lived blue-shifted signals, microsecond TAS was used to probe the blend films. As it can be observed in *Figure 5.5b* and *5.5d* the spectra obtained at 150 ns is consistent with the 6 ns spectra. Moreover, the μs-TAS transients in *Figure 5.8*, indicate that both

blends exhibit oxygen-independent, power-law decays that can be assigned to the non-geminate recombination of polymer polarons, as described before for a number of polymer/fullerene systems[31–35]. Therefore, the quenching of the early, 1300 nm polymer exciton absorption and blue-shifting corresponds to the formation of long-lived polymer polarons from the initial polymer excitons. For F4, this blue-shift is observed in both the blend and the neat films, therefore for the neat it is assigned to a partial polaron generation or appeareance of excitons with an increased charge transfer character on the ~ 2 ps timescale.

The decay dynamics in the blends are now addressed in more detail. From the transient data of the blends, shown in *Figure 5.5b* and *5.5d*, a rapid quenching of the exciton absorption can be extracted. The exciton signal quenching was obtained by plotting the decays at ≈ 1300 nm (an area where exciton absoprtion signals dominate) as shown in *Figure 5.9a*.

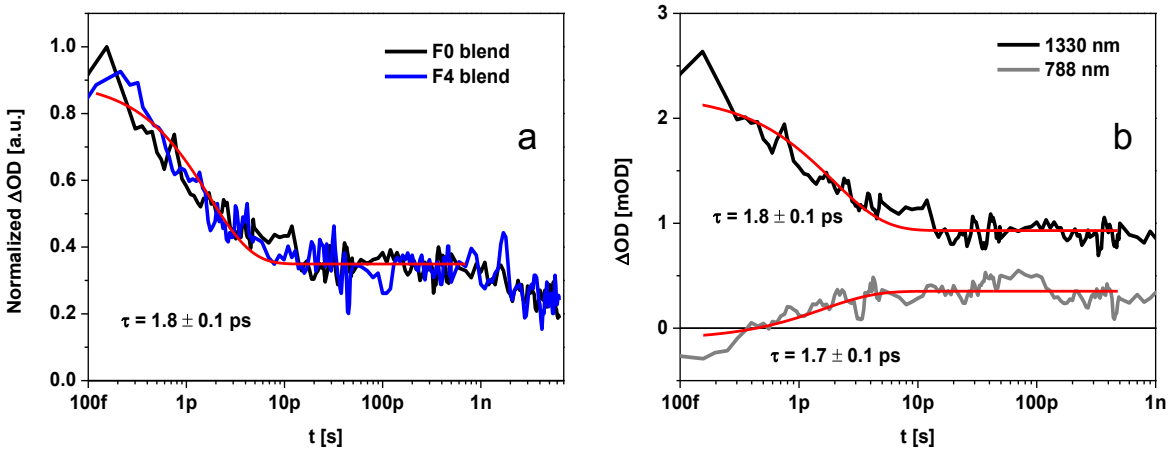

Figure 5.9. a) Normalized transient absorption traces of 1:2 F0 and F4 blends with $PC_{70}BM$ excited at 710 nm and 3 μJ/cm^2, probed at 1330 nm. b) Singlet exciton dynamics at 1330 nm and polaron signal accumulation at 788 nm for the F0/$PC_{70}BM$ 1:2 blend films. Red lines are in both cases monoexponential fits to the data.

It is apparent that both F0 and F4 exciton absorption signals decay with a time constant τ = (1.8 ± 0.1) ps. This is almost two orders of magnitude faster than the corresponding decay dynamics of the neat polymer films. This fast quenching of the polymer singlet exciton in the blend films is in good agreement with the steady-state PLQ results, although it predicts a slightly higher PLQ for F4. For F0 blend films a similar time constant (1.7 ± 0.1 ps) was observed for the rise of polaron absorption at 788 nm, as shown in *Figure 5.9b.* This wavelength was used since it presents little interfering absorption from excitons as observed in *Figure 5.5a*. It is then concluded that exciton separation to

form $F0^+/PC_{70}BM^-$ polaron pairs proceeds in this blend film with a time constant τ = (1.75 ± 0.1) ps. This analysis cannot be carried out for F4 due to the more complex spectra evolution of the neat F4 film spectra, however, we consider 1.8 ps to represent the time constant of the exciton dissociation to form $F4^+/PC_{70}BM^-$ polaron pairs.

It is noticeable in *Figure 5.5b* and *5.5d* that the polymer polaron photoinduced band exhibits a small red shift, of 0.02 eV for F0 blend (from ~1170 to 1190 nm) and 0.03 eV for F4 blend (from 1070 to 1090 nm) from ~ 40 ps. A similar red shift of polymer photoinduced absorption has been reported previously for other donor polymers[17,36] and has been assigned to the energetic relaxation and trapping of the photogenerated polarons. Therefore, to assess polaron decay dynamics, a wavelength at which this red-shift has minimal impact was chosen (1035 nm).

Following the rapid (~1.8 ps) evolution of the photoinduced absorption spectrum from polymer excitons to polarons, the transient polaron absorption in F0 and F4 blend films exhibit a relatively slow decay that initiates at ~ 50 - 100 ps and extends to tens of microseconds, as it is shown in *Figure 5.10a*. It is apparent from this figure, that the polaron decay dynamics, assigned to charge recombination, is approximately four times slower for the F4 blend than the F0 blend. For F0 blend, similar decay dynamics were observed for the recovery of the GSB, as shown in *Figure 5.10b*, consistent with the assignment of this decay to non-geminate charge recombination to the ground state, as it will be discussed next.

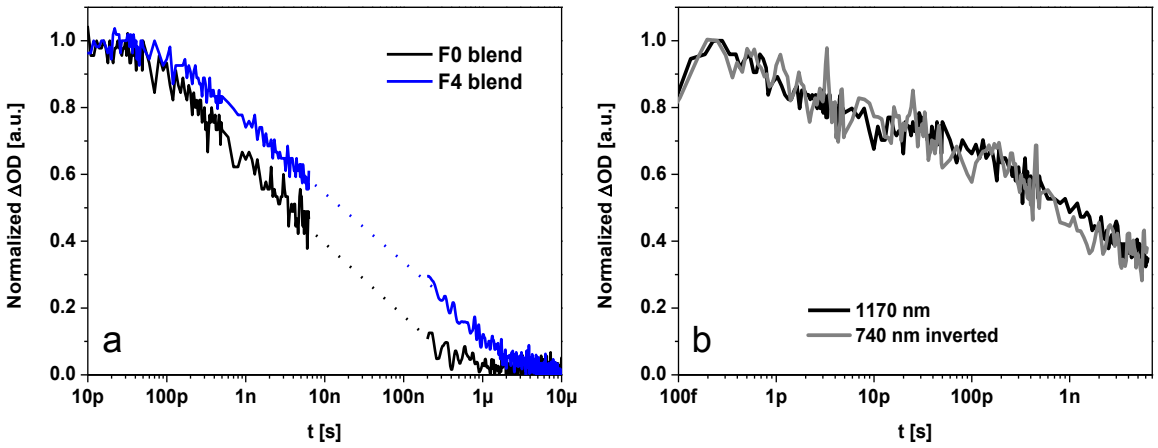

Figure 5.10. a) Normalized transient absorption traces of 1:2 F0 and F4 blends with $PC_{70}BM$ excited at 710 nm and 3 $\mu J/cm^2$ and probed at 1035 nm. b) Normalized polaron trace at 1170 nm and ground state bleach trace (negative) at 740 nm for $F0/PC_{70}BM$ 1:2 blend films, showing matching decay dynamics and therefore non-geminate recombination of polarons back to the ground state.

In order to identify the recombination type observed, the transients were taken as a function of excitation intensity, as observed in *Figure 5.11*. As can be observed, the decays exhibit linear decays on the log-log plots. This type of dynamics is assigned to non-geminate recombination of charges in the presence of an exponential tail of trapped states[31,33]. It is noticeable however, that differently to blends with slower kinetics measured in our group[33,34], these decays do not show an early fast-decaying phase at high intensities, assigned to the recombination of free charges whose density exceed the density of traps in the material.[31,32] This could be related with the relatively high polymer/fullerene mixing in the blends along with the low FET hole mobilities obtained for these polymers: 3 x 10^{-3} and 6 x 10^{-4} cm^2Vs^{-1} for F4 and F0 respectively. The trend in mobilities also indicates that the slower recombination in F4 compared to F0 blends is not a result of its mobility. However, a study on the variation of the non-geminate recombination rate constant with carrier mobilities should be performed with low perturbation measurement and is beyond the scope of this thesis.

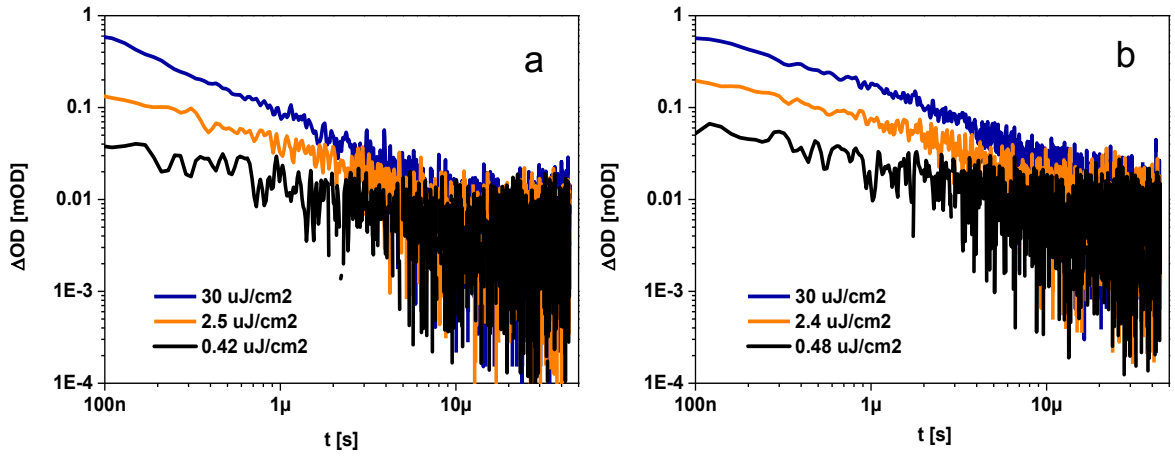

Figure 5.11. Transient absorption spectra in the late nanosecond and microsecond scale, after excitation at 660 nm, for a) 1:2 F0/$PC_{70}BM$ blend, probed at 1160 nm b) 1:2 F4/$PC_{70}BM$ blend, probed at 1060 nm. All signals have been corrected for polymer blend absorbance at the excitation wavelength.

5d. Complementary results

Theoretical Calculations

Computational studies were undertaken to assess the change in dipole moment upon excitation in the non-fluorinated F0 and fluorinated system F4[22]. Density Functional Theory (DFT) was used to

obtain the optimized geometry and conformations in trimer versions of F0 and F4, and then using the optimized geometries, to obtain the energy of the ground state.

Once the optimized geometries, conformations and energy of the ground state were obtained, Time-dependent DFT (TD-DFT) was used to calculate the first excited state energy and the change in magnitude of the dipole moment upon excitation, $\Delta\mu_{ge}$ which was computed for both polymers using *Equation 5.1*[6] and assuming a vertical excitation.

$$\Delta\mu_{ge} = \left[\left(\mu_{x,e} - \mu_{x,g}\right)^2 + \left(\mu_{y,e} - \mu_{y,g}\right)^2 + \left(\mu_{z,e} - \mu_{z,g}\right)^2\right]^{1/2} \qquad \text{(Eq. 5.1)}$$

The conformational analysis is important since the substitution pattern on the flanking thiophenes has been shown[11] to affect the preferred relative orientation of the thiophenes relative to the heteroatomic part of the BT unit, resulting in twisting of the polymer backbone. Evidently, twisting of the polymer chains has a direct impact in the packing of the polymer.

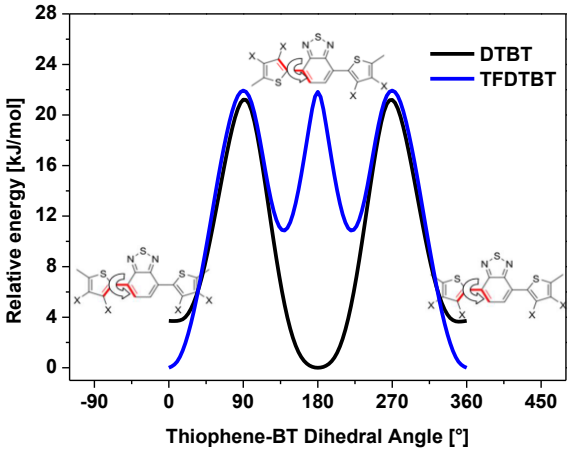

Figure 5.12. Relative energy of DTBT (black) and TFDTBT (blue) units as a function of thiophene-BT dihedral angle. Minimum energy conformations are at 180° for DTBT and 0/360° for TFDTBT. DTBT also exhibits low energy local minima at 10° and 350°. Data calculated by Pierre Boufflet.

The analysis was performed in monomers, before optimizing the geometry in the trimers. Indeed, interesting and relevant results in terms of the microstructure were obtained. While DTBT prefers the conformation where both thiophene units point *anti* to the BT unit (*a*-*a*), the TFDFTBT unit prefers a *syn* relation for thiophene and BT units (*s*-*s*), as depicted in *Figure 5.12*. The results of the DFT calculations closely mirror those of previously reported studies for the DTBT unit[11,12]. Since the

energy difference between the *anti* and *syn* conformations is much smaller for the DTBT moiety as compared to the TFDTBT, it is more likely that the DTBT unit can adopt additional conformations to the lowest (*a*-*a*) conformation, such as (*s*-*s*), (*a*-*s*) or the isomeric (*s*-*a*), therefore leading to twists in the backbone, which could impede aggregation in the F0 polymer. This is in agreement with previous GIWAXS results and explains the differences observed in the PLQ experiments.

The effect of fluorination in the energy levels of the polymers agree qualitatively with the experimental results previously obtained[21] via photo-electron spectroscopy (PESA) and UV-vis and by cyclic voltammetry. *Figure 5.13* shows the comparison between the calculated results and the PESA and UV-vis results for the HOMO and LUMO respectively. The LUMO level is predicted to be stabilized by 0.23 eV by the calculations, which agrees with the 0.23 eV obtained experimentally. However, the change in HOMO is slightly underestimated in the calculations, predicting a stabilization of only 0.17 eV, as compared to the 0.24 eV obtained experimentally. For this reason a slightly smaller bandgap for F4 was predicted for F4. The actual values obtained for the HOMOs, LUMOs and bandgaps of the polymers are quite overestimated by the calculations as can be observed in *Figure 5.13*, however this is unsurprising, as these calculations consider only trimers in the gas phase.

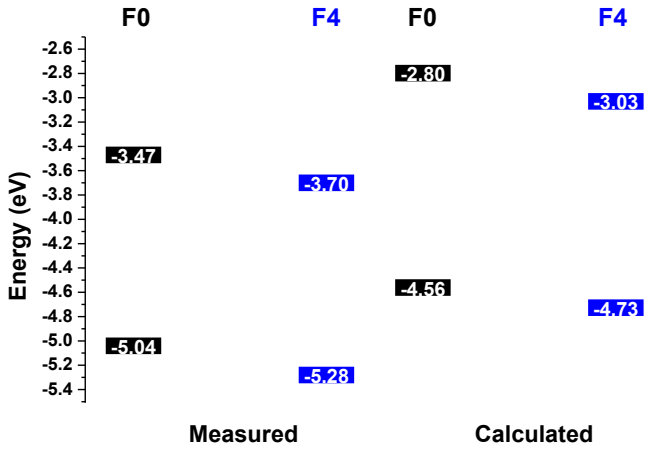

Figure 5.13. HOMO and LUMO energy levels, both measured[21] (PESA and UV-vis) and calculated (trimers, DFT calculations for HOMO and TD-DFT for LUMO levels), for F0 (black) and F4 (blue). Fluorine atoms clearly contribute to the stabilization of both HOMO and LUMO levels. Data calculated by Pierre Boufflet.

The change in dipole moment was obtained for the trimers of F0 and F4 in the most relevant conformations (*a-a*), (*s-s*) and (*s-a*). As *Table 5.2* shows, in all the comparisons, the change in dipole moment magnitude upon excitation is larger for F4 as compared to F0. Considering the preferred conformations for each trimer (shaded in *Table 5.2*), it is obtained that $\Delta\mu_{ge}$ increases from 5.72 D to 7.36 D upon fluorination. According to the correlation obtained by Yu and co-workers[18], this high value of $\Delta\mu_{ge}$ would lead to a decrease in device efficiency due to charge generation deficiencies that impact negatively on J_{SC}, which is clearly not the case in the system presented herein, as demonstrated by the high charge generation efficiency for F4 blends.

Table 5.2. Ground and excited state dipole moments for F0 and F4 trimer units with different conformations. Shaded are the values for the lowest energy conformation. In all cases $\Delta\mu_{ge}$ is larger for F4 than F0. Data calculated by Pierre Boufflet.

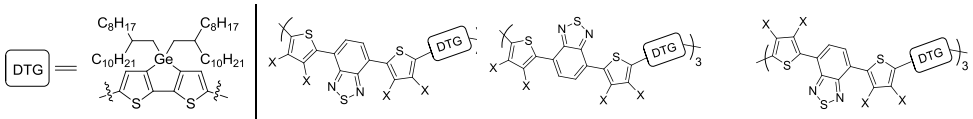

		a-a	***s-s***	***s-a***
F0	μ_g (D)	8.44	1.14	4.38
	μ_e (D)	13.22	3.96	4.96
	$\Delta\mu_{ge}$ (D)	**5.72**	**3.25**	**7.31**
F4	μ_g (D)	17.77	12.67	4.54
	μ_e (D)	23.51	16.05	12.51
	$\Delta\mu_{ge}$ (D)	**7.31**	**7.36**	**10.50**

5e. Discussion

The observations herein presented herein demonstrate that upon fluorination, the photophysics of both the neat and the blend polymers are modified. An important result is the similarity in the early blue shift of the polymer exciton photoinduced absorbance in the F4 neat and blends films. In both cases the processes occur in the 2 ps timescale, with similar energetic changes. (0.27 eV for F4 neat and 0.23 eV for F4 blend) Since in the blend films this blue shift was associated with polaron

formation, in the neat film this blue shift is associated with the formation of excitons with a partial polaron or charge transfer character (CT). The resemblance of these processes indicates that CT excitons in the neat F4 film could be charge precursors that aid to make more efficient the charge generation process in the presence of the fullerene acceptor.

Indeed, the formation of charge transfer excitons is consistent with the increased exciton dipole moment upon the insertion of the fluorine atoms obtained by our colleagues via TD-DFT calculations. This is in agreement with the idea of a larger exciton delocalization, and thus probably a lower exciton binding energy, resulting in a higher polaron character of the excitons. The presence of excitations with a charge character has been reported before for low-bandgap polymers in solution[17,37,38] as well as in PCDTBT and PCPDTBT oligomers in solution[39].

Moreover the backbone fluorination has also a direct effect in the dynamics of the neat polymers. While the decay related to the deactivation of the excitons in F0 occurs in ≈ 90 ps, the decay of the charge transfer excitons in F4 is two times slower (≈ 180 ps). This could indicate that upon fluorination, species with larger charge character are not only more efficiently formed but are also stabilized within the polymer structure. This is also consistent with the larger $\Delta\mu_{ge}$ calculated in the fluorinated polymer. However, there is still a difference of almost two orders of magnitude between the lifetime of F4 charge transfer excitons (≈ 180 ps) in the neat film and charges generated in the blend (≈ 0.5 μs) therefore confirming the assignment to charge transfer excitons rather than polarons.

We turn now to discuss charge generation in blend films. Although a modest contribution of instrument response-limited exciton quenching (charges appearing in less than 100 fs) to the early signal of the blends is not ruled out, the main exciton quenching occurs in ≈ 1.7 – 1.8 ps for these polymers, rather than the ultrafast scale reported before for other donor-acceptor polymers[6,36,40]. This timescale for exciton quenching is consistent with high, but sub-unity, photoluminescence quenching observed for these blend films. Most importantly perhaps, is that the exciton quenching times and concomitant polaron pair generation occurs in the same timescale for both blends, therefore indicating that the efficiency of charge generation is similar in F0 and F4. This shows that for this pair of polymers, the energetic differences are not the main driver for charge separation. The ability of F4 to generate charges efficiently despite its lower energy offset may be related to the higher charge transfer character of F4 polymer excitons, as has been proposed for some studies in organic and dye sensitized solar cells[6,38,41]. It is also possible the increased phase segregation of the F4/PC_{70}BM blend may aid charge separation in this blend.

If the only effect of fluorination was the efficient charge generation in F4, reaching similar charge generation as F0; similar J_{SC} values would be expected, and not an almost double-fold increase in this figure as obtained in the corresponding devices (7.5 mA/cm^2 in F0 blends vs 13.5 mA/cm^2 in F4 blends). It seems then, that additional effects apart from the efficient charge generation observed in F4 blends are responsible for the increase in J_{SC}. When comparing the gradient of the polaron decay dynamics, we obtained that non-geminate recombination of F4 blend polarons is four-fold slower as compared to the decay of F0 blend polarons, as estimated from the half-time in polaron decay in *Figure 5.10a*. Slower non-geminate recombination in F4 blend results in a total higher charge carrier density in the microsecond timescale: with the lowest excitation intensity (0.4 μJ/cm^2) F4 blends present in average, a ≈ 60% higher charge density between 200 ns and 1.2 μs, a timescale relevant for charge collection in devices. This finding is similar to what it was observed for a series of PTB-based polymers[6], where the signal of the best performing polymer, PTB7, assigned to the charge separated state has the slowest recombination time compared to other non-fluorinated and differently structured fluorine-substituted polymers, however, in this study, the slower charge recombination in PTB7 was explained only in terms of the largest dipole moment.

It is noticeable that the slower non-geminate recombination dynamics observed for F4/$PC_{70}BM$ blends do not appear to result from slower charge carrier mobilities. FET hole mobilities obtained for these polymers are 3 x 10^{-3} and 6 x 10^{-4} cm^{2}Vs^{-1} for F4 and F0 respectively.[21] This suggests that an additional factor, such as an improved microstructure in the fluorinated F4 polymer blend favors a spatial separation of holes and electrons and thus slows down non-geminate recombination. Indeed, for the F4 blends studied herein, it is likely that the slower non-geminate recombination is a consequence of a microstructure improvement upon fluorination. F4 blend shows a lower content of fullerene molecules intermixed within the polymer domains, as observed in the polymer PL. This result is consistent with our observation of an increased polymer and $PC_{70}BM$ crystallinity in the F4 blends compared to F0 blends via GIWAX measurements; the origins of the increased crystallinity in the polymer can be explained by our conformer energetic analysis via DFT calculations. The results of our calculations indicate that the planar *s-s* conformation is largely preferred by polymer F4, whereas F0 might well admit *a-s* and *s-a* conformations which would result in a slight twist in the backbone, impeding aggregation. Additionally, the increased $PC_{70}BM$ emission and crystallinity in F4 blends suggests that the more planar, and thus crystallized, polymer backbone also results in the expelling of fullerene molecules which also contributes to spatially separate the electrons and holes and thus result in the slower non-geminate recombination observed. This slower recombination is likely to be responsible, at least in part, of the enhanced device efficiency for the F4 polymer compared to F0.

5f. Conclusions

In this study, it is shown that the effect of polymer backbone fluorination impacts not only in the microstructure, but also in charge generation and charge recombination. Direct evidence of the increase in the polymer polarization, or change in dipole moment, $\Delta\mu_{ge}$ was observed by an ultrafast formation of charge-transfer excitons in the neat fluorinated film. It is proposed that these polaron-like excitons also form in the blend films and aid charge separation, counteracting the effect of a lower driving force for charge generation in the F4 system. The longer lifetimes of these charge transfer excitons in the neat fluorinated film could also be related with a stabilization of the charges in the fluorinated polymer blends.

Evidence of slower non-geminate recombination in the fluorinated polymer blend is presented, which is proposed to be related with the slight increase in polymer crystallinity and $PC_{70}BM$ aggregation, as obtained by GIWAS measurements and corroborated by the PLQ results. The increased crystallinity in F4 also agrees with the planar *s-s* conformation preferred by this polymer, compared to the less planar *a-s* conformation preferred by F0, as obtained previously by the TD-DFT calculations.

The improved charge generation in the F4 blend, along with its slower non-geminate charge recombination are key factors that directly impact upon device performance, thus explaining its almost double-fold increase in short circuit current. The evidence herein presented points out that the impact of fluorination on the short circuit current is explained by the effects on film microstructure and the intrinsic photophysic properties of its excited states.

5g. References

(1) Etxebarria, I.; Ajuria, J.; Pacios, R. *J. Photonics Energy* **2015**, *5*, 057214.

(2) Liu, C.; Yi, C.; Wang, K.; Yang, Y.; Bhatta, R. S.; Tsige, M.; Xiao, S.; Gong, X. *ACS Appl. Mater. Interfaces* **2015**, *7*, 4928.

(3) Ye, L.; Zhang, S.; Zhao, W.; Yao, H.; Hou, J. *Chem. Mater.* **2014**, *26*, 3603.

(4) Nguyen, T. L.; Choi, H.; Ko, S.-J.; Uddin, M. a.; Walker, B.; Yum, S.; Jeong, J.-E.; Yun, M. H.; Shin, T. J.; Hwang, S.; Kim, J. Y.; Woo, H. Y. *Energy Environ. Sci.* **2014**, *7*, 3040.

(5) Son, H. J.; Wang, W.; Xu, T.; Liang, Y.; Wu, Y.; Li, G.; Yu, L. *J. Am. Chem. Soc.* **2011**, *133*, 1885.

(6) Carsten, B.; Szarko, J. M.; Son, H. J.; Wang, W.; Lu, L.; He, F.; Rolczynski, B. S.; Lou, S. J.; Chen, L. X.; Yu, L. *J. Am. Chem. Soc.* **2011**, *133*, 20468.

(7) Price, S. C.; Stuart, a. C.; Yang, L. G.; Zhou, H. X.; You, W. *J. Am. Chem. Soc.* **2011**, *133*, 4625.

(8) Iyer, A.; Bjorgaard, J.; Anderson, T.; Kose, M. E. *Macromolecules* **2012**, *45*, 6380.

(9) Schroeder, B. C.; Huang, Z.; Ashraf, R. S.; Smith, J.; D'Angelo, P.; Watkins, S. E.; Anthopoulos, T. D.; Durrant, J. R.; McCulloch, I. *Adv. Funct. Mater.* **2012**, *22*, 1663.

(10) Albrecht, S.; Janietz, S.; Schindler, W.; Frisch, J.; Kurpiers, J.; Kniepert, J.; Inal, S.; Pingel, P.; Fostiropoulos, K.; Koch, N.; Neher, D. *J. Am. Chem. Soc.* **2012**, *134*, 14932.

(11) Stuart, A. C.; Tumbleston, J. R.; Zhou, H.; Li, W.; Liu, S.; Ade, H.; You, W. *J. Am. Chem. Soc.* **2013**, *135*, 1806.

(12) Yang, L.; Tumbleston, J.; Zhou, H.; Ade, H.; You, W. *Energy Environ. Sci.* **2013**, *6*, 316.

(13) Li, W.; Albrecht, S.; Yang, L.; Roland, S.; Tumbleston, J. R.; McAfee, T.; Yan, L.; Kelly, M. A.; Ade, H.; Neher, D.; You, W. *J. Am. Chem. Soc.* **2014**, *136*, 15566.

(14) Tumbleston, J. R.; Collins, B. a.; Yang, L.; Stuart, A. C.; Gann, E.; Ma, W.; You, W.; Ade, H. *Nat. Photonics* **2014**, *8*, 385.

(15) He, X.; Mukherjee, S.; Watkins, S.; Chen, M.; Qin, T.; Thomsen, L.; Ade, H.; McNeill, C. R. *J. Phys. Chem. C* **2014**, *118*, 9918.

(16) Ohkita, H.; Cook, S.; Astuti, Y.; Duffy, W.; Tierney, S.; Zhang, W.; Heeney, M.; McCulloch, I.; Nelson, J.; Bradley, D. D. C.; Durrant, J. R. *J. Am. Chem. Soc.* **2008**, *130*, 3030.

(17) Rolczynski, B. S.; Szarko, J. M.; Son, H. J.; Liang, Y.; Yu, L.; Chen, L. X. *J. Am. Chem. Soc.* **2012**, *134*, 4142.

(18) Xu, T.; Lu, L.; Zheng, T.; Szarko, J. M.; Schneider, A.; Chen, L. X.; Yu, L. *Adv. Funct. Mater.* **2014**, DOI: 10.1002/adfm.201303688.

(19) Bronstein, H.; Frost, J. M.; Hadipour, A.; Kim, Y.; Nielsen, C. B.; Ashraf, R. S.; Rand, B. P.; Watkins, S.; McCulloch, I. *Chem. Mater.* **2013**, *25*, 277.

(20) Wang, H.; Yu, X.; Yi, C.; Ren, H.; Liu, C.; Yang, Y.; Xiao, S.; Zheng, J.; Karim, A.; Cheng, S. Z. D.; Gong, X. *J. Phys. Chem. C* **2013**, *117*, 4358.

(21) Fei, Z.; Shahid, M.; Yaacobi-Gross, N.; Rossbauer, S.; Zhong, H.; Watkins, S. E.; Anthopoulos, T. D.; Heeney, M. *Chem. Commun.* **2012**, *48*, 11130.

(22) Collado-Fregoso, E.; Boufflet, P.; Fei, Z.; Gann, E.; Ashraf, R. S.; Li, Z.; McNeill, C. R.; Durrant, J. R.; Heeney, M. *Prep.* **2015**.

(23) Wang, T.; Pearson, A. J.; Dunbar, A. D. F.; Staniec, P. a.; Watters, D. C.; Yi, H.; Ryan, A. J.; Jones, R. a L.; Iraqi, A.; Lidzey, D. G. *Adv. Funct. Mater.* **2012**, *22*, 1399.

(24) Collins, B. a.; Li, Z.; Tumbleston, J. R.; Gann, E.; McNeill, C. R.; Ade, H. *Adv. Energy Mater.* **2013**, *3*, 65.

(25) Frisch, M. J.; Trucks, G. W.; Schlegel, H. B.; Scuseria, G. E.; Robb, M. A.; Cheeseman, J. R.; Scalmani, G.; Barone, V.; Mennucci, B.; Petersson, G. A.; Nakatsuji, H.; Caricato, M.; Li, X.; Hratchian, H. P.; Izmaylov, A. F.; Bloino, J.; Zheng, G.; Sonnenberg, J. L.; Hada, M.; Ehara, M.; Toyota, K.; Fukuda, R.; Hasegawa, J.; Ishida, M.; Nakajima, T.; Honda, Y.; Kitao, O.; Nakai, H.; Vreven, T.; Montgomery, Jr., J. A.; Peralta, J. E.; Ogliaro, F.; Bearpark, M.; Heyd, J. J.; Brothers,

E.; Kudin, K. N.; Staroverov, V. N.; Kobayashi, R.; Normand, J.; Raghavachari, K.; Rendell, A.; Burant, J. C.; Iyengar, S. S.; Tomasi, J.; Cossi, M.; Rega, N.; Millam, J. M.; Klene, M.; Knox, J. E.; Cross, J. B.; Bakken, V.; Adamo, C.; Jaramillo, J.; Gomperts, R.; Stratmann, R. E.; Yazyev, O.; Austin, A. J.; Cammi, R.; Pomelli, C.; Ochterski, J. W.; Martin, R. L.; Morokuma, K.; Zakrzewski, V. G.; Voth, G. A.; Salvador, P.; Dannenberg, J. J.; Dapprich, S.; Daniels, A. D.; Farkas, Ö.; Foresman, J. B.; Ortiz, J. V.; Cioslowski, J.; Fox, D. J. Gaussian 09, Revision C.01, 2009.

(26) Cook, S.; Furube, A.; Katoh, R.; Han, L. *Chem. Phys. Lett.* **2009**, *478*, 33.

(27) Yamamoto, S.; Ohkita, H.; Benten, H.; Ito, S. *J. Phys. Chem. C* **2012**, *116*, 14804.

(28) Albert-Seifried, S.; Ko, D.-H.; Hüttner, S.; Kanimozhi, C.; Patil, S.; Friend, R. H. *Phys. Chem. Chem. Phys.* **2014**, *16*, 6743.

(29) Dimitrov, S. D.; Wheeler, S.; Niedzialek, D.; Schroeder, B. C.; Utzat, H.; Frost, J. M.; Yao, J.; Gillett, A.; Tuladhar, P. S.; McCulloch, I.; Nelson, J.; Durrant, J. R. *Nat. Commun.* **2015**, *6*, 6501.

(30) Ohkita, H.; Ito, S. *Polymer (Guildf).* **2011**, *52*, 4397.

(31) Nelson, J. *Phys. Rev. B* **2003**, *67*, 1.

(32) Nogueira, A. F.; Montanari, I.; Nelson, J.; Durrant, J. R.; Brabec, C.; Ag, S.; Electronics, C. T. M. *J. Phys. Chem. B* **2003**, *107*, 1567.

(33) Clarke, T. M.; Jamieson, F. C.; Durrant, J. R. *J. Phys. Chem. C* **2009**, *113*, 20934.

(34) Clarke, T. M.; Ballantyne, A. M.; Tierney, S.; Heeney, M.; Duffy, W.; McCulloch, I.; Nelson, J.; Durrant, J. R. *J. Phys. Chem. C* **2010**, *114*, 8068.

(35) Shoaee, S.; Subramaniyan, S.; Xin, H.; Keiderling, C.; Tuladhar, P. S.; Jamieson, F.; Jenekhe, S. a.; Durrant, J. R. *Adv. Funct. Mater.* **2013**, *23*, 3286.

(36) Etzold, F.; Howard, I. a; Mauer, R.; Meister, M.; Kim, T.-D.; Lee, K.-S.; Baek, N. S.; Laquai, F. *J. Am. Chem. Soc.* **2011**, *133*, 9469.

(37) Winfield, J. M.; Van Vooren, A.; Park, M.-J.; Hwang, D.-H.; Cornil, J.; Kim, J.-S.; Friend, R. H. *J. Chem. Phys.* **2009**, *131*, 035104.

(38) Hwang, I.; Beaupré, S.; Leclerc, M.; Scholes, G. D. *Chem. Sci.* **2012**, *3*, 2270.

(39) Scarongella, M.; Laktionov, A.; Rothlisberger, U.; Banerji, N. *J. Mater. Chem. C* **2013**, *1*, 2308.

(40) Grancini, G.; Maiuri, M.; Fazzi, D.; Petrozza, a; Egelhaaf, H.-J.; Brida, D.; Cerullo, G.; Lanzani, G. *Nat. Mater.* **2012**, *12*, 29.

(41) Listorti, A.; Regan, B. O.; Durrant, J. R. *Chem. Mater.* **2011**, *23*, 3381.

Chapter 6. Charge recombination studies in PBTT-T blends with different blend ratios and acceptors.

In Chapter 4, a thorough study of charge generation and charge recombination as a function of DPPTT-T/$PC_{70}BM$ ratio was presented. However, due to the very low intermixing between the polymer and the fullerene, the spectral signatures of its blends are rather insensitive to the polymer/fullerene loading. In this chapter a study of PBTT-T/$PC_{70}BM$ blends with different donor/acceptor ratios and with ICTA, (indene-C_{60} trisadduct) a bulky acceptor, are presented. This system has the advantage of having clearly differentiated exciton and polaron signals, whose contribution to the transient spectra are extremely sensitive to the microsctructure of the blend. The microstructure is in turn sensitive to the loading and size of the acceptor. As such, it is a system that can be considered a structural model to study charge separation as a function of morphological changes.

Through a combination of steady-state PLQ studies, fs-TAS and wide angle X-ray diffraction (WAXD), a correlation of charge generation and recombination, and intercalation of the acceptors within the polymer matrix is established. Two main results are obtained. Firstly, upon increasing the $PC_{70}BM$ loading from 9 to 1 to 1 to 4 an increase in exciton dissociation rate is observed, as well as a change in recombination regime from geminate (in the 9 to 1 and 1 to 1 blends) to non-geminate (in the 1 to

4 blend). These results are correlated with an increase in the lamellar d-spacing for PBTT-T upon increasing $PC_{70}BM$ loading, related to the formation of a PBTT-T/$PC_{70}BM$ co-crystal. Secondly, upon changing the acceptor from $PC_{70}BM$ to the bulky ICTA at a fixed 1 to 1 PBTT-T/acceptor blend ratio, a slower exciton dissociation is observed. However, a change in the recombination regime from geminate to non-geminate is also observed. The 1 to 1 blend with ICTA shows a much more modest increase in lamellar d-spacing, suggesting that co-crystals of PBTT-T/ICTA are not formed. This indicates that the formation of a co-crystal results in an almost-instantaneous exciton dissociation, with a concomitant high extent of geminate recombination in the absence of extended acceptor domains.

The introduction presents the current literature concerning the recent discussion on CT states and their involvement in charge separation and geminate charge recombination. A literature review on PBTT-T/acceptor blends charge separation and their relation with film microstructure is also presented. Next, the experimental details of sample preparation are described, followed by the results section, which is divided into three subsections, the first one deals with $PC_{70}BM$ different loadings, the second one presents 1 to 1 blends comparing $PC_{70}BM$ to ICTA, the third one presents the WAXD results. For the first two sub-sections, steady-state spectroscopy results are first presented, followed by time-resolved spectroscopy results. A discussion of the results is then presented, followed by conclusions and references.

6a. Introduction

The mechanism of charge separation in organic photovoltaic blends has long been studied and yet, discrepancies still exist in the proposed mechanisms of free polaron generation. Some of the parameters that have been proposed to influence this yield are the driving energy for charge separation[1] (discussed in detail in Chapter 3), the crystallinity of at least one of the blend components[2,3], the orientation of the donor and acceptor molecules with respect to each other[4], the dielectric constant of the blend[5], and the availability of excited states which support a large electron delocalisation[6–8].

It has been generally accepted, that a trade-off exists between the optimal morphology for efficient exciton dissociation versus that for efficient separation of the charges and their subsequent collection[9]. As explained in Chapter 4, it has been proposed that intermixed regions are optimal for exciton dissociation, while more pure, extended regions of donor or acceptor are necessary for an efficient charge separation and collection[9,10]. The increased extension of acceptor domains has been correlated with an increased blend dielectric constant, but especially, with an availability of high energy CT states with a high polarizability and electron delocalization. In this sense, the involvement of "hot" or high-energy charge transfer (CT) states upon charge separation has been particularly controversial.

Studies by Neher and collaborators have experimentally shown that "cold" or relaxed CT state excitation result in the same IQEs and the same field-dependence of free charge generation as excitation of upper lying CT states[11]. From that evidence, they concluded that charge separation may occur via the lowest-lying, cold CT states[11–13]. However, the origin of different extents of field-dependence of free charge generation (interpreted as the contribution of geminate recombination to device losses[14]) for blends with different performances and CT state energies seems rather unclear. In particular, the notion that relaxed CT states are able to generate free charge carriers seems contradictory given that some of the systems used for their discussion, such as Si-PCPDTBT/ICTA[12] or MEH-PPV/PCBM[11] are clearly limited by geminate recombination.

Opposed to this, studies by a few research groups have independently shown that charge generation is improved if delocalized, high energy CT states are available in the system[5–8]. This has been demonstrated experimentally, with studies that use a pump-push spectroscopic technique[15]. In these experiments, an increase in transient current is measured after an IR-push pulse drives bound polaron pairs in cold CT states to upper CT states. Because "pushing" the bound polaron pairs to upper CT states produces an increase in the measured transient current, the study concluded that

upper CT states must be more delocalized and prone to generate free charge carriers. It was found, that the amplitude of this transient current was smaller for highly efficient devices, thus demonstrating that they present less current losses associated to geminate recombination from cold CT states. The delocalization in high energy CT states has also been confirmed via time-dependent density functional theory calculations[8]. In this study, the existence of hot CT states with increased electron delocalization relatively isoenergetic with the singlet S_1 state was correlated with high charge separation efficiency.

An increased CT state polarizabilty was also observed experimentally, via electroabsorption spectroscopy, upon increasing the loading of C_{60} in small molecule/C_{60} devices[5]. This increased polarizability was attributed to an extended crystallinity of C_{60} in devices with high C_{60} loading, which was proposed to allow an extension of the electron wavefunction delocalization. As such, a clear understanding of the role of hot CT states upon charge separation and geminate recombination of bound polaron pairs is still missing. In particular, their relevance in device performance is still under constant debate.

In this Chapter, the role of geminate recombination as a function of blend microstructure will be discussed for PBTT-T/$PC_{70}BM$ with different $PC_{70}BM$ loadings and for PBTT-T with a bulky acceptor, ICTA. This system was chosen since its morphology is particularly sensitive to the size of the acceptor and its loading, and thus its ability to intercalate within the polymer side chains. The easily tuneable ratio of intermixed and pure phases makes it ideal to study charge separation in these blends. From the fs-TAS results herein presented, it is demonstrated that this morphological sensitivity towards the acceptor size and loading translates into different charge recombination regimes which can be related to the intermixing level of the acceptor.

PBTT-T is a highly studied polymer, due to the rather unique microstructure of its blends. When blended with acceptors such as PCBM or $PC_{70}BM$, the fullerene can intercalate within the polymer side chains forming a co-crystal, (or bimolecular crystal) that is, an ordered intermixed phase, as observed by WAXD and GIWAXS studies of their blends[2,16–18]. Additionally, it has been found that when the acceptor is bulky enough, such as for example ICTA or bis-$PC_{60}BM$, it cannot be accommodated within the PBTT-T side chains and thus the co-crystal is not formed[17,18]. Moreover, it is known that when all the co-crystal sites are fully occupied by small enough fullerene molecules, that is, upon increasing acceptor loading, the fullerene starts to form extended aggregated domains[19]. The presence of the fullerene aggregated phase has been correlated with an increased J_{SC} in the corresponding device[13], therefore suggesting that this phase is necessary to increase charge separation efficiency. *Figure 6.1* shows a depiction of PBTT-T with different $PC_{70}BM$ loadings and

with a bulky acceptor (bis-$PC_{60}BM$) showing the formation of the co-crystal (10:1 polymer:$PC_{70}BM$ blend) the saturation of the co-crystal sites (1:1) and the formation of a fullerene aggregated phase (1:4).

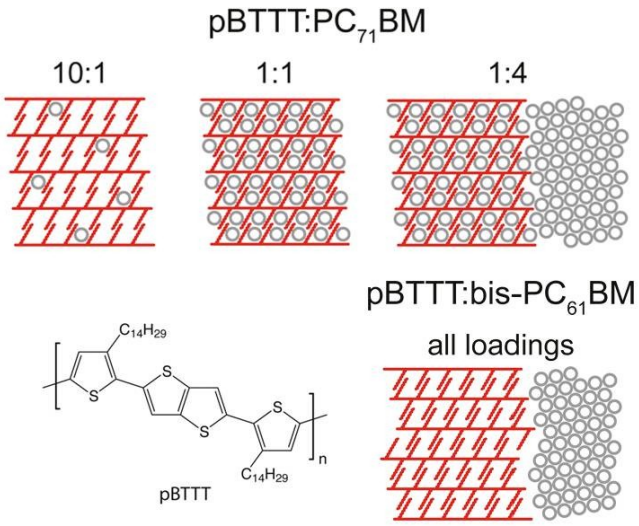

Figure 6.1. Structure of PBTT-T C14 and microstructure arrangements of PBTT-T:$PC_{70}BM$ blends as a function of fullerene loading, and with bis-$PC_{60}BM$, a bulky acceptor that does not intercalate within the lamellar space of PBTT-T. Figure taken from reference[19].

In-depth studies of bias-dependence of charge carrier formation in PBTT-T blends with different loadings of $PC_{60}BM$ and with 1:1 PBTT-T:bis-$PC_{60}BM$ have concluded that increasing the loading of $PC_{60}BM$ results in a reduced field dependence of charge generation, assigned to reduced geminate recombination through cold CT states[13]. Additionally, the authors reported that a 1:1 blend with bis-$PC_{60}BM$ presents reduced geminate recombination similar to that found for the 1:4 blend with $PC_{60}BM$. These findings are opposed to the increased geminate recombination found in Si-PCPDTBT blends when changing the fullerene acceptor from $PC_{60}BM$ to ICTA[12]. However, it should be noted that firstly, Si-PCPDTB blends with fullerenes have not been reported to show intercalated microstructures, thus complicating this comparison[20]. Secondly, given the much lower bandgap of Si-PCPDTBT as compared to that of PBTT-T[21,22], it is likely that the lowest-lying CT state (CT_1) in the Si-PCPDTBT:ICTA system does not allow an efficient electron transfer and thus geminate recombination is predominant in this system. This is not the case for PBTT-T, which S_1 state lays 0.55 eV above the S_1 state of PCPDTBT, thus still allowing efficient electron transfer when blended with bis-$PC_{60}BM$. It is therefore, interesting to compare the recombination regime in PBTT-T blends with ICTA and determine whether the energetic requirements are dominant and how they can be conceived

considering the blend microstructures. *Figure 6.2* shows the HOMO-LUMO energies for PBTT-T, $PC_{70}BM$ and ICTA, as obtained from the literature[22,23]. We notice that experimental methods to determine these energies are not the same in every case (and more extremely, ICTA HOMO was estimated by using the same optical bandgap as that for $PC_{70}BM$, since this value is not reported in the literature) however values consistent with $PC_{70}BM$ and PBTT-T energies were taken.

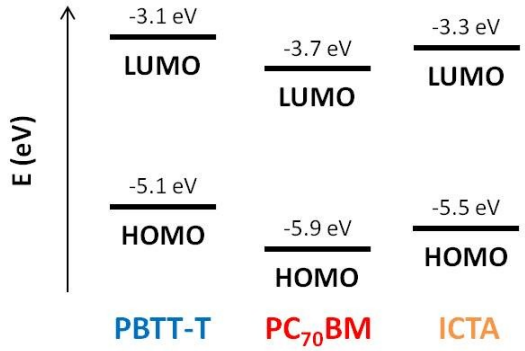

Figure 6.2. HOMO-LUMO energies for the polymer and acceptors used in this chapter. HOMO energy for PBTT-T was obtained by ultraviolet photoelectron spectroscopy (UPS)[23] and its LUMO estimated adding the optical bandgap to the HOMO[22]. HOMO-LUMO energies for $PC_{70}BM$ were used as estimated for $PC_{60}BM$ in ref[24]. ICTA LUMO was taken from the literature, where it was determined using cyclic voltammetry[25] or differential pulse voltammetry[26]. HOMO energy of ICTA was estimated using the same optical bandgap as that of $PC_{70}BM$, consistent with the HOMO-LUMO energies determined by Oh and colleagues[27].

6b. Experimental section

For all measurements (fs-TAS, steady state PL), solutions of PBTT-T and $PC_{70}BM$ (or ICTA) in ODCB were prepared at different concentrations and spin rates so that the visible absorption of the films lied between 0.3 and 0.5 at 540 nm. The composition of the films varied from neat PBTT-T, (1:0) 9:1, 1:1 and 1:4 PBTT-T:$PC_{70}BM$. The neat and 9:1 films were prepared from 20 mg/mL PBTT-T and $PC_{70}BM$ solutions in ODCB, spun at 3000 rpm, whereas 1:1 and 1:4 blends were prepared from 30 mg/mL ODCB solutions at 1500 rpm. The solutions were stirred and heated at 90°C for at least 8 hours to ensure full dissolution. Films with ICTA were prepared under the same conditions as the 1:1 PBTT-T:$PC_{70}BM$ blends. The films were spun on cleaned glass substrates for 1 minute and then transferred into an inert-atmosphere glovebox until the measurements were performed.

For WAXD measurements, films were prepared by drop-casting 30 mg/mL solutions of the neat polymer or the polymer/acceptor mixtures onto clean glass substrates. The thickness of the devices was measured using a Dektak profilometer pre-calibrated using a 100 nm gold film deposited on quartz calibration module. The uncertainty of the films thickness is no more than 10 nm. The thickness was used to correct the WAXD data.

6c. Results

6c.1. PBTT-T:$PC_{70}BM$ blends as a function of $PC_{70}BM$ loading

6c.1a. UV-vis and Photoluminescence steady-state spectra

Figure 6.3a shows representative steady-state UV-vis spectra of the neat PBTT-T and the PBTT-T/$PC_{70}BM$ blends as a function of their weight ratio, varying from 9 to 1 to 1 to 4 polymer:fullerene. It can be observed that as the $PC_{70}BM$ concentration is increased from 9 to 1 to 1 to 1, a vibrational structure appears in the spectra, as well as a small red shift (from 545 to 552 nm) of the absorption maximum corresponding to the 0,1 transition. This is due to an ordering of the polymer chains, most likely related to the formation of the polymer/fullerene co-crystal, as has been reported before[19,28].

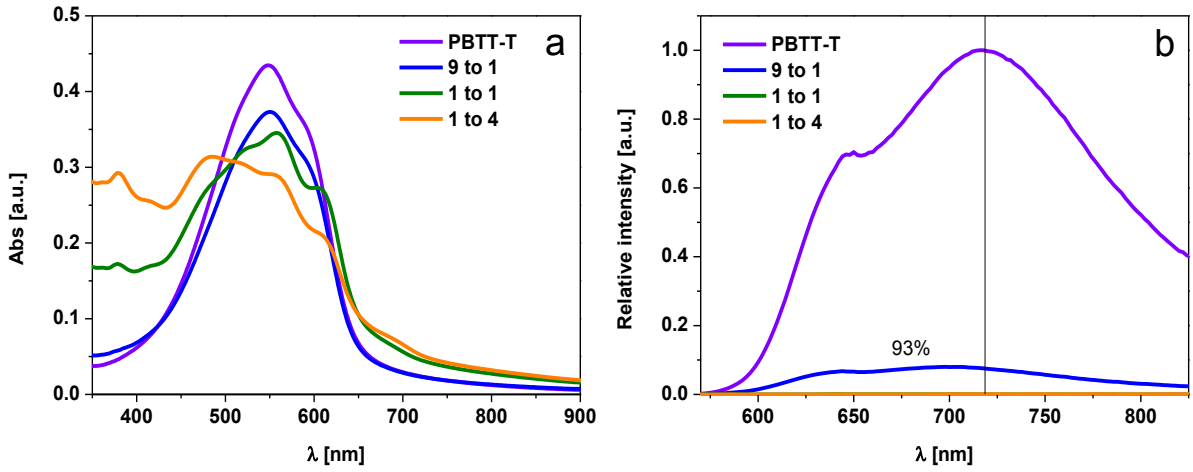

Figure 6.3. a) Steady state UV-vis absorption of neat and blend films of PBTT-T and $PC_{70}BM$ with different polymer to $PC_{70}BM$ weight ratios. b) Steady state PLQ traces of PBTT-T and PBTT-T/ $PC_{70}BM$ blends as a function of $PC_{70}BM$ loading, exciting at 540 nm. The PL traces were corrected for film absorption at 540 nm.

Next, *Figure 6.3b* shows the results for the photoluminescence (PL) emission of the neat PBTT-T film and its quenching upon $PC_{70}BM$ loading. It can be observed that only the 9 to 1 blend film exhibits some weak, 93% quenched, PBTT-T emission. Both 1 to 1 and 1 to 4 blend films are completely

quenched (PLQ >> 99%), showing that $PC_{70}BM$ has completely intermixed within the polymer side chains. These results qualitatively agree with the UV-Vis spectra in *Figure 6.3a* and previous studies on PBTT-T morphology[2,19]. The remaining PL in the 9 to 1 blend is probably due to the low amount of $PC_{70}BM$ not being able to quench all the polymer excitons formed. It is remarkably however, that with only 10% in weight of $PC_{70}BM$, more than 90% of the PBTT-T excitons are quenched. This result is clearly different to the DPPTT-T PLQ results presented in Chapter 4, indicating that the relative intermixing of $PC_{70}BM$ in PBTT-T is much larger, despite this polymer being highly crystalline. This can be explained by the formation of the aforementioned co-crystals. Interestingly, the PBTT-T emission maximum is slightly blue shifted upon blending with $PC_{70}BM$, thus slightly narrowing the Stokes shift between the (0,1) transitions, from 170 nm in the neat PBTT-T film to 152 nm in the 9 to 1 film (≈ 0.05 eV difference). Smaller Stokes shifts have previously been correlated with increased film crystallinity[29] thus implying that the ordering in the polymer chains slightly increases upon $PC_{70}BM$ addition, in agreement with what was found in the UV-vis spectra and WAXD data presented below. This is also consistent with the results of other research groups that use additives to induce a phase separation of the blend[16]

6c.1b. Femtosecond transient absorption spectroscopy: early photophysics and charge recombination dynamics.

Following the steady-state characterization, fs-transient absorption data was compared for the neat PBTT-T and its blends with $PC_{70}BM$ (9:1, 1:1 and 1:4) exciting at 540 nm with different excitation intensities. First, neat PBTT-T spectra and dynamics, shown in *Figure 6.4a* and *Figure 6.4b* will be discussed. As can be observed, the photoinduced absorption spectra of PBTT-T has a rather defined maximum at ≈ 1260 nm from early times (≈ 0.2 ps). This band can be assigned to the photoinduced absorption of PBTT-T excitons from the first excited state S_1 to an upper S_n state. This transition is roughly isoenergetic with that of DPPTT-T (Chapter 4), F0 (Chapter 5) or RR-P3HT[30], which has a similar bandgap and crystallinity compared to PBTT-T. Similar energies for $S_1 \rightarrow S_n$ exciton transitions have also been reported in low-bandgap polymers[31–33]. Our group has found that low or zero triplet yields are observed in polymers with high crystallinity, as determined by oxygen quenching experiments[34]. In particular, PBTT-T microsecond timescale studies under nitrogen and oxygen atmospheres indicated that no triplets are present in both neat and blend films[35]. From this evidence and the dynamics observed at late times (see *Figure 6.5*) it was concluded that the neat film does not present triplet formation.

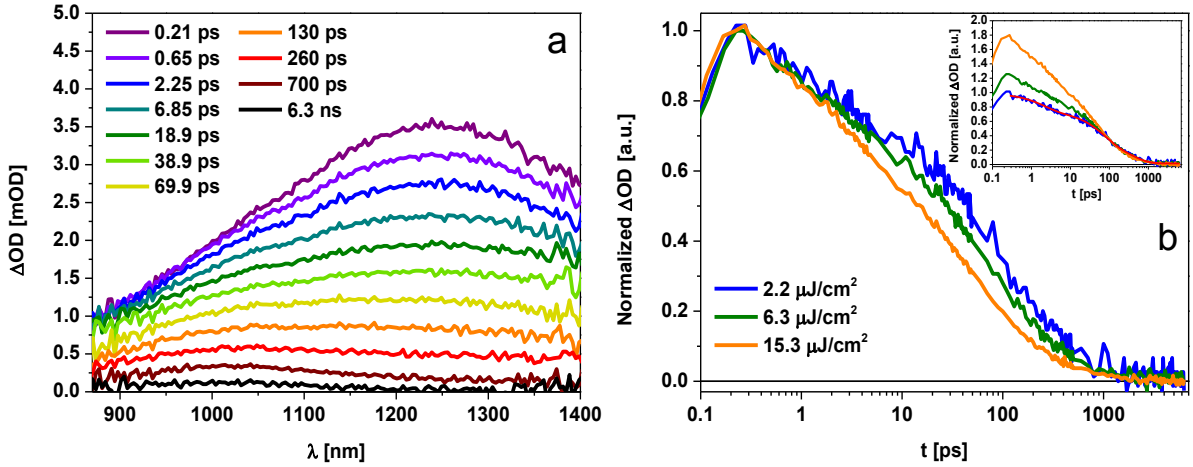

Figure 6.4. Neat PBTT-T sub-ps transient absorption data in the IR region, excited at 540 nm, in a) transient spectra taken at 6.3 μJ/cm^2 and b) normalised dynamics at the exciton maximum absorption at 1260 nm and different excitation intensities. Inset, the same transient data normalised at ≈ 70 ps. All data was corrected for polymer absorption at the excitation wavelength.

Exciton decay dynamics at 1260 nm, shown in *Figure 6.4b* are however very different from the ones observed for DPPTT-T and F0/F4 polymers. An initial fast, intensity-dependent decay is observed until ≈ 70 ps (see *Figure 6.4b* inset) which most likely corresponds to an exciton-exciton annihilation process. The slower component of the decay is intensity independent, and thus can be assigned to the intrinsic exciton decay, which has a time constant τ = 144 ± 20 ps. This is a longer exciton decay time that those found for DPPTT-T, in agreement with slower non-radiative deactivation processes in polymers with larger bandgaps[33,36,37]. Interestingly, PBTT-T transient spectra have a contribution from a long-lived band with a maximum at ≈ 1015 nm from early times. A single value decomposition analysis is precluded since this band presents a blue shift over time. However, when the dynamics at 1015 nm are plotted in a log-log plot, they show linear decays from ≈ 100 ps, thus suggesting the existence of a small amount of dissociated charges in the neat film, as can be observed in *Figure 6.5*. This was also observed by Jamieson in neat PBTT-T films, which presented charge-characteristic decays in the microsecond scale at 980 nm[35]. The assignment of this photoinduced absorption to dissociated charges is also consistent with the polymer positive polaron photoinduced spectra observed in blends with acceptors from the picosecond (as it will be seen shortly) to the microsecond timescale, also shown by Jamieson[35]. Interestingly, a value of $\alpha = 0.5$ was obtained, thus indicating an order of recombination of 3, the highest observed in this thesis. (see section 2c.4.a in Chapter 2). The origin of a third order in the recombination reaction law in the neat film is until present not well understood, however is likely to be related to the energetic

disorder of the film, that is the presence of excitons with different energies, which will likely have different decay times and kinetics, thus reflecting in a general high recombination order.

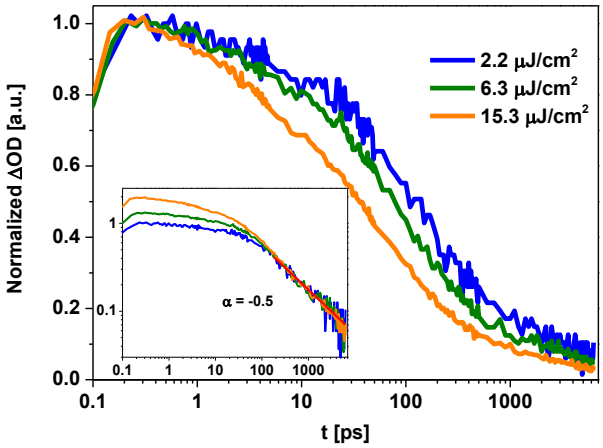

Figure 6.5. Normalised dynamics exciting at 540 nm and probing at ≈ 1015 nm and different excitation intensities. Inset, the same transient data normalised at ≈ 100 ps in a log-log scale, showing the power-law nature of the decays at late times, with an exponent α = -0.5. The data was corrected for polymer absorption at the excitation wavelength.

Next, the description of the transient absorption data for the PBTT-T/$PC_{70}BM$ blend films is presented. Firstly the 9 to 1 PBTT-T/$PC_{70}BM$ blend transient spectra and kinetics, shown in *Figure 6.6a* and *Figure 6.6b* are discussed. *Figure 6.6a* shows two clear distinct contributions to the photoinduced spectra, one with a maximum at ≈ 1250 nm and one at higher energy, whose spectra blue-shifts extremely fast, from 1090 to 950 nm in approximately 5 ps. From the resemblance to the neat spectra, the fast-decaying 1250 nm photoinduced signal can be assigned to the exciton signal being quenched by the presence of the acceptor. In the same way, the signal observed at ≈ 1000 nm can be assigned to the positive polaron photoinduced absorption, and thus the 0.17 eV blue-shifting of its spectrum can correspond to the energetic relaxation of the polarons, as reported before by Laquai and coworkeres.[38] *Figure 6.6b* presents the kinetics of the photoinduced absorption signal at 900 nm, where the contribution of exciton signal is less severe. It can be observed in this graph, that the decay can be largely described by an excitation intensity-independent multiexponential decay, thus suggesting the existence of geminate recombination of bound charges, with an average decay time τ = 209 ± 40 ps, as obtained from the corresponding contributions of the tri-exponential fit. Considering that the change of the extinction coefficient of the polaron absorption is negligible during polaron recombination, it is noticeable that almost 95% of the polarons recombine in 6 ns, an observation which would anticipate a poor device performance for cells fabricated with this

donor/acceptor ratio. Geminate recombination in this blend is expected as the relative amount of $PC_{70}BM$ is only enough to sparsely intercalate within the polymer side chains, as shown in *Figure 6.1*. This results in the formation of bound polaron pairs that are unable to further separate due to the spatial confinement imposed by the small fullerene regions, as has been proposed before[13,19]. From the analysis of the exciton dynamics at 1250 nm, shown in *Figure 6.7*, an average exciton decay time τ = 10.2 ± 0.1 ps could be extracted from the contributions of a tri-exponential fit function. This corresponds to an exciton quenching time of ~93%, in excellent accordance with the steady state PL quenching result shown in *Figure 6.3b*.

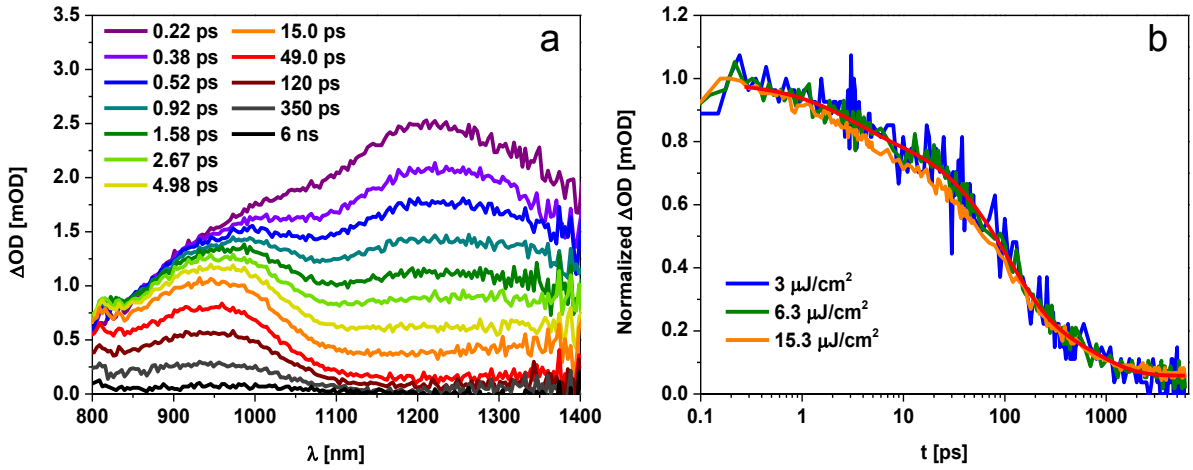

Figure 6.6. 9 to 1 PBTT-T/$PC_{70}BM$ sub-ps transient absorption data in the IR region, excited at 540 nm, in a) transient spectra taken at 6.3 μJ/cm^2 and b) normalised polaron dynamics at 900 nm with different excitation intensities. The red line corresponds to a tri-exponential fit of the data. All data was corrected for blend absorption at the excitation wavelength.

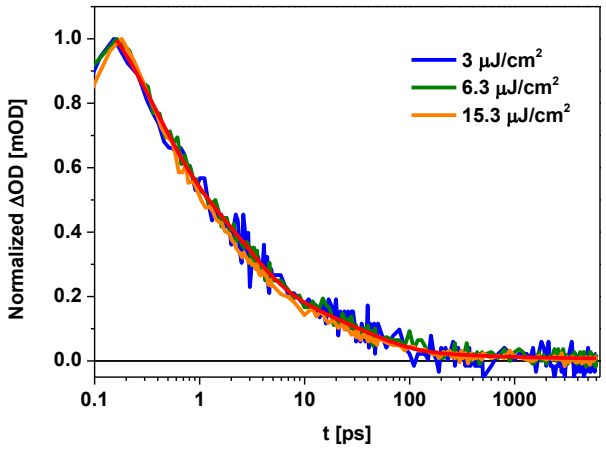

Figure 6.7. Normalised dynamics exciting at 540 nm and probing at 1250 nm at different excitation intensities for the 9 to 1 blend film. The data was fitted to a tri-exponential function (red trace).

Next, the 1 to 1 PBTT-T/$PC_{70}BM$ blend will be discussed. *Figures 6.8a* and *6.8b* show the photoinduced transient spectra and decay dynamics of this blend, respectively. Following the previous assignments, a well defined positive polaron photoinduced absorption band is observed at ≈ 1000 nm. Additionally, a fast-decaying, (see *Figure 6.8*) low OD photoinduced absorption can be observed at ≈ 1250 nm, whose assignment is consistent with that of exciton photoinduced absorption. It is noticeable that only a limited part of the exciton absorption is present in the spectra, since the photoinduced formation of polarons seems to be much faster than in the case of the 9 to 1 blend. This assignment is confirmed by comparing the characteristic exponential decay and accumulation times at 1250 nm and 1000 nm respectively, in the first picosecond, as can be observed in *Figure 6.8b* and *Figure 6.9*. These kinetics have resolution-limited characteristic times $\tau \leq$ 200 fs. It is thus likely that the vast majority of the charges in this system are formed within the time resolution of our fs-TAS setup.

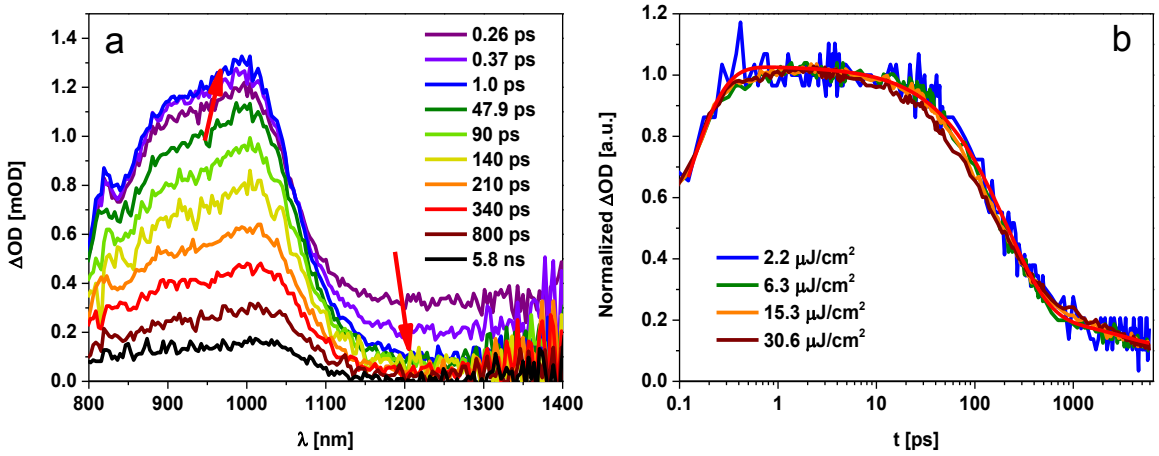

Figure 6.8. 1 to 1 PBTT-T/$PC_{70}BM$ sub-ps transient absorption data in the IR region after excitation at 540 nm, in a) transient spectra taken at 6.3 μJ/cm^2 and b) normalised dynamics at 1000 nm at different excitation intensities. The red line corresponds to a tri-exponential fit of the data plus a power-law decay from ≈ 1 ns. All data was corrected for blend absorption at the excitation wavelength.

In *Figure 6.8b* the complete positive polaron kinetics can be observed. After the initial sub-ps rise, a fast exponential, excitation-independent decay can be observed with a characteristic time τ = 210 ± 10 ps, which can be assigned to the geminate recombination of polaron pairs. This decay accounts for almost 80% of the initial (≈ 2 ps) polaron signal, therefore indicating that geminate recombination in this system is severe. From around 1 ns however, a small contribution from an excitation-dependent phase attributed to the onset of non-geminate recombination of the

"surviving" charges can also be observed. The onset of this phase depends on the excitation intensity also indicating that charge separation is inefficient in this system. *Figure 6.9* also shows a slower exponential, intensity-independent decay from 2 ps, with a characteristic time τ = 260 ± 40 ps which agrees, within the experimental error, with the exponential decay associated to geminate recombination of bound polarons at 1000 nm. This indicates that the polaron band has a small contribution at longer wavelengths, overlapping with the exciton absorption area.

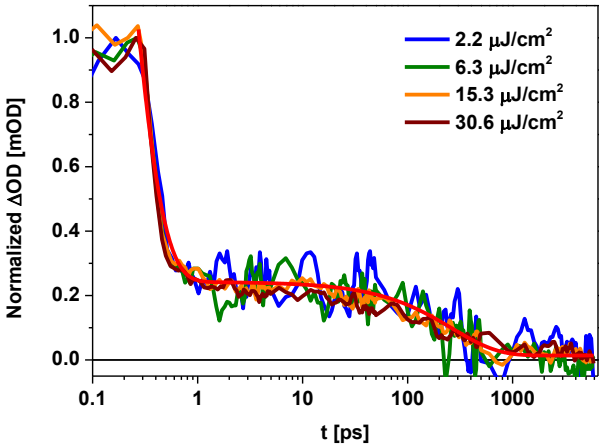

Figure 6.9. Normalised dynamics exciting at 540 nm and probing at 1250 nm at different excitation intensities for the 1 to 1 blend film. Data was corrected for polymer absorption at the excitation wavelength and fitted to a bi-exponential function (red trace).

Finally, the 1 to 4 PBTT-T/$PC_{70}BM$ blend will be discussed. *Figures 6.10a* and *6.10b* show the photoinduced transient spectra and decay dynamics of this blend, respectively. An inspection of *Figure 6.10a* shows that the 1 to 4 blend presents similar spectral features as those observed for the 1 to 1 blend; that is, an early 800 to 1100 nm positive photoinduced absorption assigned to the absorption of the photogenerated positive polarons in PBTT-T. It is noticeable, that both 1 to 1 and 1 to 4 blend films show photoinduced transient spectra with marked vibrational structure, possibly corresponding to different polaron vibronic transitions. Interestingly, this feature is also observed in the steady-state absorption spectra of these blends, a feature that has proposed to be related to a higher polymer structural order[19,28]. This result could suggest that the better polymer ordering is also reflected in the optical transitions of the polarons formed after photoexcitation.

The kinetics of this polaron band, however is completely different from the one of 1 to 1 blend film. As can be observed in *Figure 6.10b,* the decay of the polaron band is not only much slower than in the 1 to 1 blend, but presents a biphasic behaviour. Until $\approx$ 30 ps, an intensity-independent bi-exponential growth with a resolution limited characteristic time ($\tau \leq$ 200 fs) and a much slower

characteristic time $\tau = 7 \pm 2$ ps are observed. The fast growth can be associated to the appearance of polarons from the quenching of the longest-lived excitons, as confirmed by comparing this growth with the decay at 1250 nm *(Figure 6.11*) assigned before to the exciton photoinduced absorption. The slower characteristic growth time is proposed to correspond to the polymer positive polaron formation coming from the quenching of excitons generated in the extended fullerene domains. This is expected from the higher fullerene proportion in this blend, and by the relatively high fullerene absorption at the excitation wavelength. This behaviour was also observed by Dimitrov et.al. in BTT-DPP/$PC_{70}BM$ blends[39] however, in that case the polaron generation from fullerene excitons occurs in the nanosecond timescale. The difference in the fullerene exciton quenching times might originate from smaller and/or more homogeneously distributed fullerene domains in the PBTT-T/$PC_{70}BM$ blends as compared to the BTT-DPP/$PC_{70}BM$ blends, however this requires further investigation.

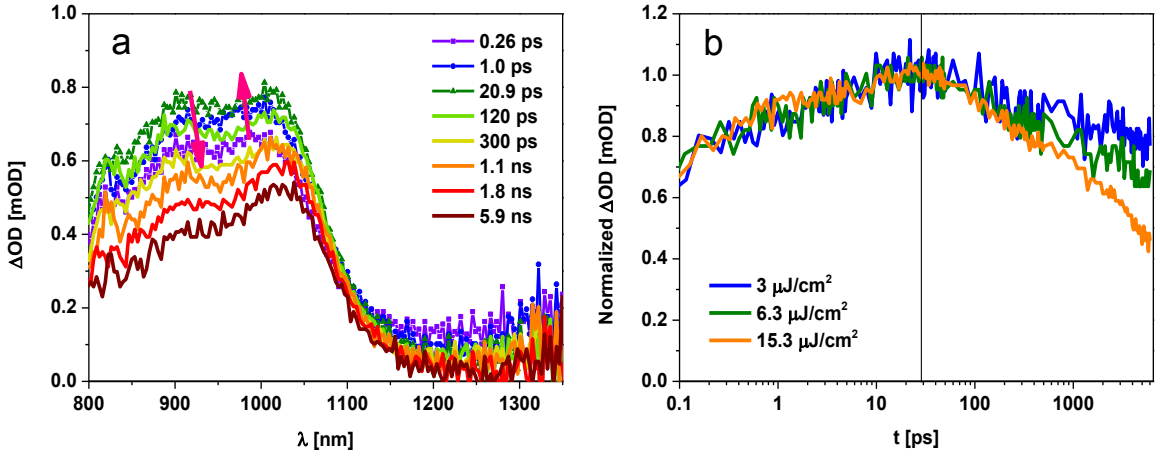

Figure 6.10. 1 to 4 PBTT-T/$PC_{70}BM$ sub-ps transient absorption data in the IR region, excited at 540 nm, in a) transient spectra taken at 6.3 $\mu J/cm^2$ and b) normalised dynamics at the polaron maximum absorption at 1020 nm at different excitation intensities. The data was corrected for blend absorption at the excitation wavelength.

Perhaps more important than the fullerene exciton quenching kinetics is the slow excitation intensity dependent decay observed after ≈ 30 ps in *Figure 6.10b*. Due to the light-intensity dependent nature of the decay, and its linear nature in a log-log plot it is proposed that this decay corresponds to non-geminate polaron recombination. This marks an important difference in the recombination regime compared to the rest of the PBTT-T/$PC_{70}BM$ blend films herein analysed. While both 9 to 1 and 1 to 1 blends presented fast, strictly excitation intensity-independent polaron decays starting at earlier times, (0.2 ps for the 9 to 1 blend and ≈ 10 ps for the 1 to 1 blend) the 1 to 4 blend shows delayed, slower excitation-intensity dependent polaron kinetics that consumes

between 20 and 60% of the charges after 6 ns, depending on the pulse intensity. The change in the recombination regime when increasing the fullerene loading from 1 to 1 to 1 to 4 is in agreement with recent results from Laquai and co-workers[10] (reported whilst this thesis was being written) and is consistent with the improvement obtained in device performance, both resulting from a triple-fold increase in J_{SC} and an almost 20% increase in *FF*.[10] In the discussion section the change in blend crystallinity will be correlated with the change in recombination regime and device performance. Following, the fs-TAS results for the 1:1 blend with ICTA will be presented.

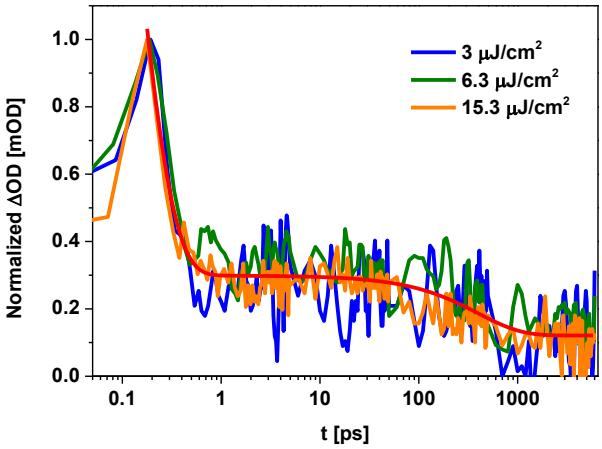

Figure 6.11. Normalised dynamics exciting at 540 nm and probing at 1250 nm at different excitation intensities for the 1 to 4 blend film. The data was corrected for polymer absorption at the excitation wavelength and fitted to a bi-exponential function (red trace).

6c.2. PBTT-T blends with bulky acceptors

6c.2a. UV-vis and Photoluminescence steady-state spectra

Figure 6.12a shows representative steady-state UV-vis spectra of the neat PBTT-T and the 1 to 1 PBTT-T/acceptor blend films. Except for a few nanometers blue-shifting of the polymer absorption maximum, the blend with the bulky acceptor ICTA shows very similar spectra to the neat PBTT-T one. The absence of a vibrational structure in the UV-vis spectra in the ICTA blend is an indication of less structured films and is consistent with the lack of evidence indicating the formation of PBTT-T/acceptor co-crystals, as previously reported.[17–19]

Figure 6.12b shows the results for the photoluminescence (PL) emission of the neat PBTT-T film and PBTT-T emission quenching in the 1 to 1 blends with ICTA and $PC_{70}BM$. It can be observed that differently from the $PC_{70}BM$ 1 to 1 blend, ICTA blend shows incomplete quenching (PLQ < 99%) close to that of the 9 to 1 PBTT-T/$PC_{70}BM$ blend (see *Figure 6.3b*). Using *Equation 2.4* in Chapter 2 and

assuming a PBTT-T exciton diffusion length of 6 - 10 nm,[2] pure domains of PBTT-T in the 1 to 1 blend with ICTA have approximate diameters between 2 and 3 nm. It is important to notice however, that even if these domains seem small, the sizes herein reported corresponds to the average *pure* PBTT-T domain size, and thus suggest that in this blend there are some areas of the polymer in which the fullerene molecules are not intimately intermixed. These results qualitatively agree with the UV-Vis spectra in *Figure 6.12a*. However, it is surprising that given the absence of intercalation of ICTA within the side chains of PBTT-T (as it will be shown in section *6c.3* and has been reported in the literature[17–19]) their PLQ in the 1 to 1 blends is still high. This suggests that some level of intermixing happens in this blend, even though ICTA does not intercalate within the side chains of the polymer. It seems plausible then, that the solubility of the fullerenes with PBTT-T is much higher than in, for example DPPTT-T, despite that both polymers are highly crystalline, as it will be shown in the next section.

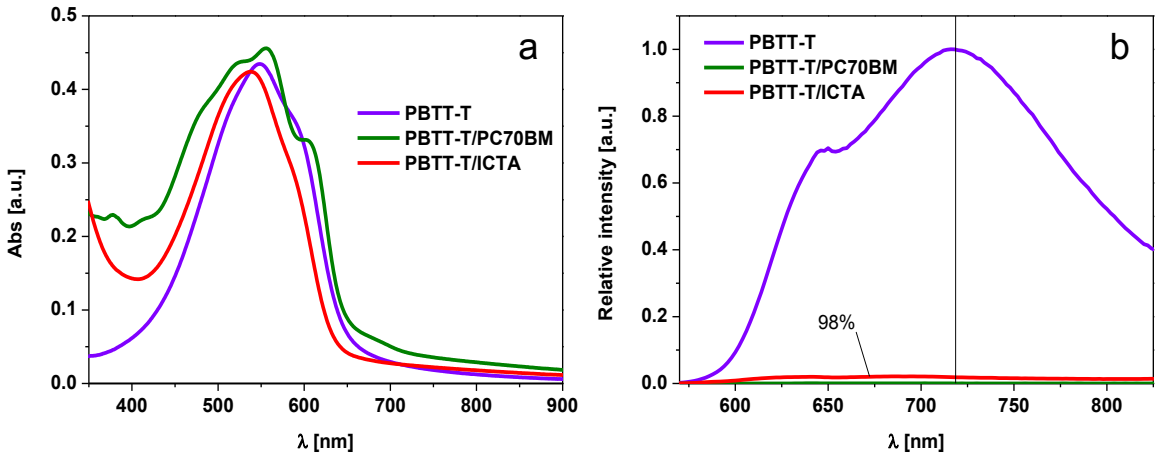

Figure 6.12. a) Steady state UV-vis absorption of neat and blend films of PBTT-T and different acceptors with 1 to 1 PBTT-T/acceptor weight ratios. b) Steady state PLQ traces of PBTT-T and 1 to 1 PBTT-T/acceptor blends after excitation at 540 nm. The PL traces were corrected for film absorption at 540 nm.

6c.2b. Femtosecond transient absorption spectroscopy: early photophysics and charge recombination dynamics.

Figures 6.13a and *6.13b* show the transient spectra and 1250 nm dynamics of PBTT-T/ICTA. Similarly to the 9 to 1 PBTT-T/$PC_{70}BM$ blend, the transient spectra shows features of both excitons, with a maximum at ≈ 1250 nm and polymer positive polarons with a maximum absorption at ≈ 950 nm. The observation of exciton photoinduced absorption signals agrees with the incomplete exciton emission quenching observed in the steady-state PLQ results. Indeed, a comparison of the average neat PBTT-

T exciton lifetime (τ = 144 ± 20 ps) and the average exciton lifetime as obtained by taking into account the contributions from a tri-exponential fit function to the 1250 nm transient in *Figure 6.13b* (τ = 3.5 ± 0.6 ps) predicts a PLQ of 98%, in excellent agreement with the steady-state PLQ results.

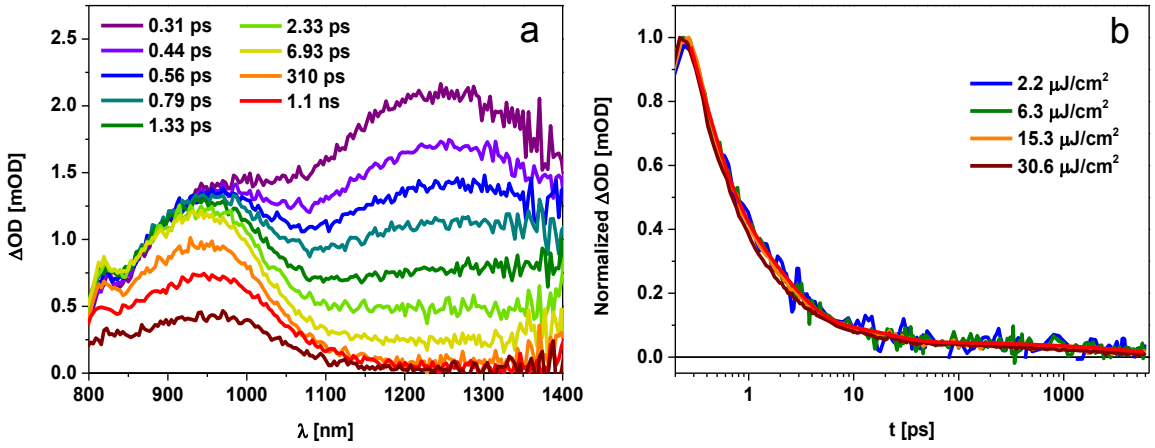

Figure 6.13. 1 to 1 PBTT-T/ICTA sub-ps transient absorption data in the IR region, excited at 540 nm, in a) transient spectra taken at 6.3 μJ/cm^2 and b) normalised dynamics at the exciton maximum absorption at 1250 nm at different excitation intensities; the red trace is a fit to a triexponential function + a power law contribution from 100 ps. The data was corrected for blend absorption at the excitation wavelength.

Figure 6.14 shows the polymer positive polaron kinetics at 910 nm at different laser excitation intensities. A comparison of these signals with signals taken at 1000 nm, where the contribution of the exciton signal is larger, allowed us to identify that polarons contribute dominantly to the 910 nm signal from 4.5 ps, and thus the signal was normalised to a unit value at this time. In this figure, a power-law excitation-intensity dependent polaron decay is observed, suggesting polaron non-geminate recombination that consumes, after 6 ns, between 60 and 80% of the polaron signal depending on the excitation intensity. Charge recombination is not as slow as that observed in the 1 to 4 PBTT-T/$PC_{70}BM$ blend film, however it is approximately 20% slower (at low excitation intensities) than that of the analogous 1 to 1 PBTT-T/$PC_{70}BM$ blend film. Thus, while the 1 to 1 PBTT-T/$PC_{70}BM$ blend film presents predominantly fast ($\tau \approx$ 210 ps) geminate recombination, followed by non-geminate recombination, the 1 to 1 PBTT-T/ICTA blend film presents a fast, non-geminate recombination phase. Depending on the excitation intensity, both recombination types could consume the same relative amount of charges in the corresponding blends by 6 ns. The early onset and fast non-geminate positive polaron recombination in the 1 to 1 PBTT-T/ICTA blend film could be due to an increased mobility in the PBTT-T phase, resulting from the lack of intercalation of ICTA in

the polymer's side chains. An alternative explanation is that the pure domains polymer domains are small, thus spatially confining the polarons which will rapidly non-geminate recombine within this small domains.

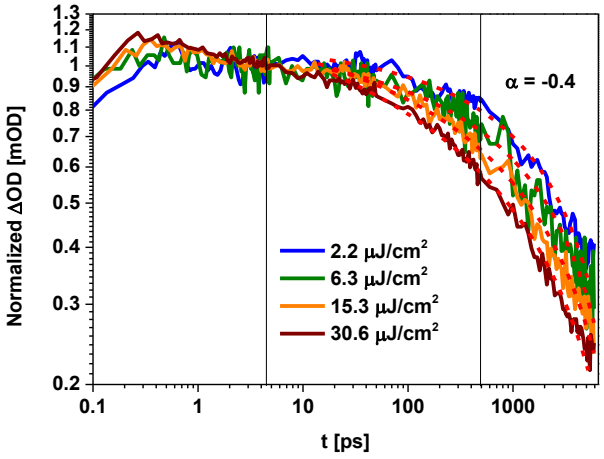

Figure 6.14. Log-log plots of the kinetics at 910 nm after excitation at 540 nm with different intensities normalised at 4.5 ps. The vertical lines show the three main phases in the decay. Red dashed lines are power-law fits of the form $y = a + b * x^c$ as described in Chapter 2. All the transients were corrected for blend absorption at the excitation wavelength.

6c.3. WAXD results

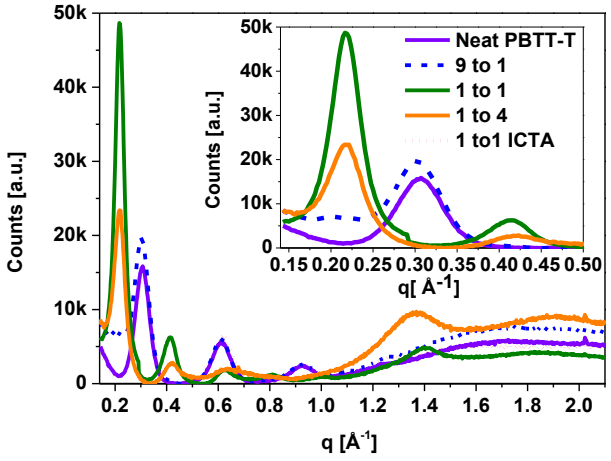

Figure 6.15. a) Wide-angle X-ray diffraction (WAXD) patterns for the different DPPTT-T/$PC_{70}BM$ drop-cast films. Data was corrected with a factor that accounts for the differences in film thickness. The scattering vector q is calculated from the scattering angle using the equation $q = (4\pi/\lambda)\sin\theta$ in from section 2c.5 in Chapter 2. WAXD data was taken by Ching Hong-Tan and Elisa Collado.

Wide-angle X-ray diffraction (WAXD) technique was used to corroborate the intercalation behaviour in these blends. This is done by analysing the change in the lamellar spacing upon increasing concentration of $PC_{70}BM$ and upon the change of acceptor maintaining the 1 to 1 ratio. *Figure 6.15* shows the data obtained for the neat PBTT-T as well as the 9:1, 1:1, 1:4 PBTT-T/$PC_{70}BM$ and the 1:1 PBTT-T/ICTA blend films, corrected to account for the different thicknesses of the blends.

Firstly, it can be observed that from the intensity and narrowness of the peaks, that all the films (both neat and blends with acceptors) have a high crystallinity. Because the method of film preparation is the same as that for the WAXD results of DPPTT-T blends (Chapter 4) and the same equipment was used, the results are comparable. It can then be concluded that PBTT-T blend films are as crystalline as or more crystalline than DPPTT-T blend films.

A narrow peak can be observed in the neat PBTT-T film (purple line) at q = 0.305 $Å^{-1}$, which correspond to a lamellar spacing of 20.6 Å. The lamellar peak was observed at similar q values for the 9:1 PBTT-T/$PC_{70}BM$ and the 1:1 PBTT-T/ICTA: q = 0.302 $Å^{-1}$ and q = 0.309 $Å^{-1}$ respectively, which correspond to lamellar spacing of 20.8 Å and 20.3 Å respectively. The similar values in the lamellar spacing as the neat PBTT-T film indicate that the polymer crystallinity is not altered upon the addition of the fullerene. This is expected for the 9:1 PBTT-T/$PC_{70}BM$ blend since the fullerene proportion is small. Interestingly, this blend presents a small signal at $\approx q$ = 0.2 $Å^{-1}$ which indicates that this film presents an onset signal of intercalation. The peaks at $\approx q$ = 0.6 and 0.9 $Å^{-1}$ observed for these blends correspond to the second and third harmonic of the main lamellar peak.

The 1:1 and 1:4 PBTT-T/$PC_{70}BM$ blend films, on the other hand, present a narrow and intense peak at q = 0.217 $Å^{-1}$ and q = 0.218 $Å^{-1}$ respectively, which correspond to lamellar spacing of 29.0 Å and 28.8 Å respectively. This represents a change in lamellar spacing with respect to the neat PBTT-T film of Δd = 8.4 and 8.2 Å for the 1:1 and 1:4 $PC_{70}BM$ blend films respectively. The change in lamellar spacing takes a small negative value Δd = -0.3 Å for the 1:1 PBTT-T/ICTA blend, indicating that lamellar spacing even becomes slightly smaller upon ICTA addition. The peaks at $\approx q$ = 0.4 and 0.6 $Å^{-1}$ observed for these blends correspond to the second and third harmonic of the main lamellar peak, however in the case of the 1:4 blend, it is possible that the q = 0.6 $Å^{-1}$ is also superimposed to a peak at q = 0.64 $Å^{-1}$, corresponding to $PC_{70}BM$ agglomerates[40,41]. The 1:1 and 1:4 PBTT-T/$PC_{70}BM$ blends also present a broad peak at q = 1.37 $Å^{-1}$ and q = 1.4 $Å^{-1}$ respectively, which most likely also correspond to fullerene agglomeration. This peak is not present in any of the other blends, and it is more prominent in the 1 to 4 blend, confirming that it corresponds to $PC_{70}BM$ domains with some degree of crystallinity[40,41].

The values herein obtained for the PBTT-T lamellar spacings present small variations from those published by McGehee and co-workers[17,18], however variations of 1 to 3 Å have been observed before for these measurements[2,16], especially if the technique used and/or the deposition methods vary.

6d. Discussion

Using a system whose morphology has been extensively investigated; this study demonstrates a clear change in the charge recombination regime, both in terms of spectra and kinetics, upon changing the fullerene loading ($PC_{70}BM$) and replacing $PC_{70}BM$ for ICTA. The results herein presented show that while the 9 to 1 and 1 to 1 PBTT-T/$PC_{70}BM$ blends predominantly show fast (≈ 210 ps in both cases) geminate recombination, the 1 to 4 PBTT-T/$PC_{70}BM$ and the 1 to 1 PBTT-T/ICTA blends show slow and fast non-geminate charge recombination respectively. These results are similar to those recently obtained by Laquai and co-workers[10], however, a comparison with the effect of replacing the acceptor with a bulky one is missing in their work.

From the three $PC_{70}BM$ blends, only the 9 to 1 one shows incomplete PBTT-T exciton emission quenching, however this indicates that the proportion of $PC_{70}BM$ is not enough to achieve a complete quenching. From the WAXD results it can be observed that this blend actually presents a small peak that indicates a small proportion of intercalation of the fullerene within the side chains of the polymer. As such, the polarons formed are likely to remain mainly bound and recombine geminately. It is interesting that the geminate recombination decay constants observed for both 9 to 1 and 1 to 1 PBTT-T/$PC_{70}BM$ blends are so similar. This indicates that increasing the fullerene loading from 10% to 50% in weight actually does not retard or accelerate geminate charge recombination, however it results in faster charge generation, as clearly shown in the exciton decay kinetics. It is also noticeable, in the 1 to 1 $PC_{70}BM$ blend, that after the predominant geminate charge recombination phase, a small non-geminate regime is present from ≈ 900 ps indicating the onset of fullerene aggregation, as can be also inferred from the WAXD results.

Differently from the 9 to 1 $PC_{70}BM$ blend results are the results for the 1 to 1 PBTT-T/ICTA blends. While PBTT-T also presents a small but measurable emission in its blend with ICTA, this does not come from insufficient acceptor. Instead, the WAXD results confirm that ICTA does not intercalate within the side chains of PBTT-T and thus has a partially segregated microstructure. This seemingly small change in morphology has a profound impact on charge separation, for it results in interfaces

that confine less the electron-hole pair and thus permit a higher separation efficiency as compared to the analogous 1 to 1 PBTT-T/$PC_{70}BM$ blend.

The increased charge separation efficiency (i.e. yield of dissociated as opposed to bound charges) in the ICTA blend cannot be attributed to energetic effects since, as can be observed in *Figure 6.1*, ΔE_{CS} is smaller for the PBTT-T/ICTA system as compared to PBTT-T/$PC_{70}BM$.

Similarly, the participation of hot CT states seems not to be the reason for the change in the recombination regime. Consider the following hypothesis. If we approximate the energy gap between a hot, CT_n state and the lowest CT_1 state to have the same energy as the $S_1 \rightarrow S_n$ transitions observed for PBTT-T at ≈ 1 eV (≈ 1250 nm) then it can be observed from *Figure 6.16* that the CT_n state of ICTA lies above the S_n state and thus seems unlike to be able to participate in the process of charge generation and separation. Opposed to this, CT_n state of $PC_{70}BM$ is almost isoenergetic with the S_n level of PBTT-T, which would indicate that this CT state is available to participate in the charge generation and separation process from unrelaxed excitons.

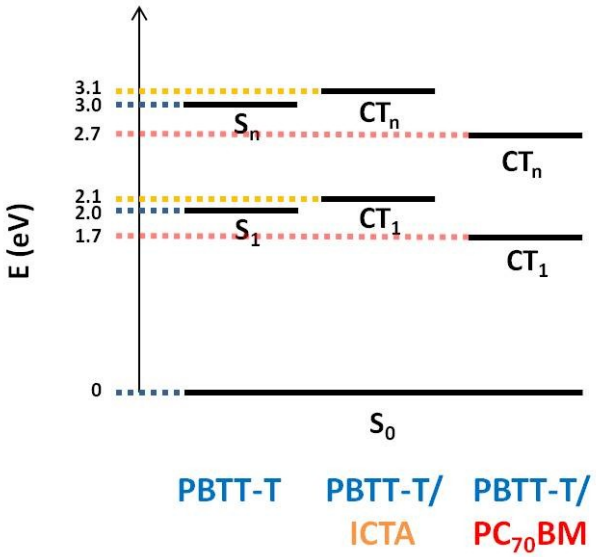

Figure 6.16. Jablonsky state energies diagram. S_1 energy was calculated using the values of HOMO – LUMO of *Figure 6.2* considering that the main contribution of $S_0 \rightarrow S_1$ comes from the HOMO → LUMO transition. Energies of cold CT states E_{CT_1} were estimated using Janssen's approximation[42] $E_{CT_1}(eV) \approx |E_{LUMO} - E_{HOMO}| - 0.29$. The transition $CT_1 \rightarrow CT_n$ was approximated to be isoenergetic with S1 → Sn, whose value was taken from the ultrafast spectra exciton maxima at ≈ 1250 nm.

These results however, show an opposite trend to what it was experimentally obtained in terms of charge separation: while the 1 to 1 PBTT-T/$PC_{70}BM$ blend mainly presents geminate recombination in competition with charge separation, charge separation in the 1 to 1 PBTT-T/ICTA blend film seems

to be more efficient for it shows only non-geminate recombination. One needs to be aware however, that these state energies rely in rather severe approximations and should be considered with care. Even with these limitations, energetic arguments, either regarding the driving energy for charge separation or the participation of hot CT states do not seem to be able to explain the results herein obtained.

If the fullerene in question only exists intercalated with PBTT-T, geminate recombination is observed, as is the case of the 9 to 1 and 1 to 1 $PC_{70}BM$ blends. However, the existence of intercalated phases does not exclusively result in geminate recombination if an extended and rather crystallised acceptor phase is present in the blend, as is the case of the 1 to 4 $PC_{70}BM$ blend, confirmed with the fullerene agglomerate peak observed in the WAXD results. In fact, the 1 to 4 $PC_{70}BM$ blend presents the slowest, (non-geminate) charge recombination of all the blends analysed, such that at the lowest excitation intensities used, less than 20% of the polarons have recombined after 6 ns. This is in agreement with the best performance of PBTT-T/$PC_{70}BM$ found for this blend ratio[10]. Such a dramatic change in both the regime and the rate of charge recombination compared to the 1 to 1 PBTT-T/$PC_{70}BM$ blend is a result of the presence of an aggregated phase of $PC_{70}BM$. This phase complies with two functions, the first one is to provide with relatively pure neighbouring regions, (possibly with a higher electron affinity[2]) such that the bound polaron pairs can separate from the intercalated phases in which they are confined in the absence of this extended fullerene phase. The second function consists in maintaining a domain separation that avoids encounters between positive and negative polarons thus reducing the non-geminate charge recombination rate. Notice that these results are in agreement with those reported by Deibel and co-workers in their TDCF PBTT-T/$PC_{70}BM$ and PBTT-T/bulky acceptor study.[13]

It is likely that non-geminate charge recombination in the 1 to 1 PBTT-T/ICTA blend is much faster than in the 1 to 4 PBTT-T/$PC_{70}BM$ since the segregation in the former blend is not enough to slow down non-geminate recombination. Because pure domains in the 1 to 1 PBTT-T/ICTA blend are small, the polarons are confined and thus are more likely to rapidly non-geminate recombine. The confinement is less severe than that of the 1 to 1 PBTT-T/$PC_{70}BM$ and therefore recombination can be non-geminate in nature, but still fast.

From this discussion it seems very likely that the changes in the charge recombination regimes and rates are largely a result of the different microstructures in the blends, that range from intercalated (in the 9 to 1 and 1 to 1 PBTT-T/$PC_{70}BM$ blends) to intercalated with an aggregated phase (in the 1 to 4 PBTT-T/$PC_{70}BM$ blend) to a partially segregated microstructure (in the PBTT-T/ICTA blend) which

emphasize the importance that microstructure can have in some polymer/acceptor systems as the one herein presented.

6e. Conclusions

In this study, the effect of microstructure on charge generation, separation and recombination are clearly shown. A difference between *intercalation* and *intermixing* can be established based upon the effect of the acceptor addition on the WAXD results, the polymer exciton emission quenching and the blend charge recombination observed. Direct evidence of the drastic effect of $PC_{70}BM$ aggregation upon charge recombination was shown, changing the regime of charge recombination from geminate to non-geminate and largely decreasing the recombination rate. At a fixed 1 to 1 blend ratio, the change to a bulky acceptor (ICTA) unable to intercalate within PBTT-T side chains results in the change from fast geminate recombination in the $PC_{70}BM$ blend to fast non-geminate charge recombination in the ICTA blend film. The fast non-geminate charge recombination in the ICTA blend film is likely to come from a decreased energetic disorder resulting in the reduction of the amount of deep traps which slow down bimolecular recombination. Finally, the improved efficiency of charge separation in the ICTA blend film is unlikely to come from energetic arguments either involving ΔE_{CS} or the participation of hot CT states.

6f. References

(1) Dimitrov, S. D.; Durrant, J. R. *Chem. Mater.* **2013**, *26*, 616–630.

(2) Jamieson, F. C.; Domingo, E. B.; McCarthy-Ward, T.; Heeney, M.; Stingelin, N.; Durrant, J. R. *Chem. Sci.* **2012**, *3*, 485.

(3) Shoaee, S.; Subramaniyan, S.; Xin, H.; Keiderling, C.; Tuladhar, P. S.; Jamieson, F.; Jenekhe, S. a.; Durrant, J. R. *Adv. Funct. Mater.* **2013**, *23*, 3286–3298.

(4) Tumbleston, J. R.; Collins, B. a.; Yang, L.; Stuart, A. C.; Gann, E.; Ma, W.; You, W.; Ade, H. *Nat. Photonics* **2014**, *8*, 385–391.

(5) Bernardo, B.; Cheyns, D.; Verreet, B.; Schaller, R. D.; Rand, B. P.; Giebink, N. C. *Nat. Commun.* **2014**, *5*, 3245,DOI: 10.1038/ncomms4245.

(6) Bakulin, A. a; Rao, A.; Pavelyev, V. G.; van Loosdrecht, P. H. M.; Pshenichnikov, M. S.; Niedzialek, D.; Cornil, J.; Beljonne, D.; Friend, R. H. *Science (80-.).* **2012**, *335*, 1340–1344.

(7) Savoie, B. M.; Rao, A.; Bakulin, A. a.; Gelinas, S.; Movaghar, B.; Friend, R. H.; Marks, T. J.; Ratner, M. a. *J. Am. Chem. Soc.* **2014**, *136*, 2876–2884.

(8) Niedzialek, D.; Duchemin, I.; de Queiroz, T. B.; Osella, S.; Rao, A.; Friend, R.; Blase, X.; Kümmel, S.; Beljonne, D. *Adv. Funct. Mater.* **2015**, *25*, 1972–1984.

(9) Kästner, C.; Egbe, D. a. M.; Hoppe, H. *J. Mater. Chem. A* **2015**, *3*, 395–403.

(10) Gehrig, D. W.; Howard, I. a.; Sweetnam, S.; Burke, T. M.; McGehee, M. D.; Laquai, F. *Macromol. Rapid Commun.* **2015**, *36*, 1054–1060.

(11) Vandewal, K.; Albrecht, S.; Hoke, E. T.; Graham, K. R.; Widmer, J.; Douglas, J. D.; Schubert, M.; Mateker, W. R.; Bloking, J. T.; Burkhard, G. F.; Sellinger, A.; Fréchet, J. M. J.; Amassian, A.; Riede, M. K.; McGehee, M. D.; Neher, D.; Salleo, A. *Nat. Mater.* **2014**, *13*, 63–68.

(12) Albrecht, S.; Vandewal, K.; Tumbleston, J. R.; Fischer, F. S. U.; Douglas, J. D.; Fréchet, J. M. J.; Ludwigs, S.; Ade, H.; Salleo, A.; Neher, D. *Adv. Mater.* **2014**, *26*, 2533–2539.

(13) Zusan, A.; Vandewal, K.; Allendorf, B.; Hansen, N. H.; Pflaum, J.; Salleo, A.; Dyakonov, V.; Deibel, C. *Adv. Energy Mater.* **2014**, *4*, 1400922.

(14) Proctor, C. M.; Albrecht, S.; Kuik, M.; Neher, D.; Nguyen, T. Q. *Adv. Energy Mater.* **2014**, *4*, 1400230.

(15) Dimitrov, S. D.; Bakulin, A. a; Nielsen, C. B.; Schroeder, B. C.; Du, J.; Bronstein, H.; Mcculloch, I.; Friend, R. H.; Durrant, J. R.; Schroeder, B. C. *J. Am. Chem. Soc.* **2012**, *134*, 18189–18192.

(16) Buchaca-Domingo, E.; Ferguson, a. J.; Jamieson, F. C.; McCarthy-Ward, T.; Shoaee, S.; Tumbleston, J. R.; Reid, O. G.; Yu, L.; Madec, M.-B.; Pfannmöller, M.; Hermerschmidt, F.; Schröder, R. R.; Watkins, S. E.; Kopidakis, N.; Portale, G.; Amassian, a.; Heeney, M.; Ade, H.; Rumbles, G.; Durrant, J. R.; Stingelin, N. *Mater. Horizons* **2014**, *1*, 270.

(17) Miller, N. C.; Sweetnam, S.; Hoke, E. T.; Gysel, R.; Miller, C. E.; Bartelt, J. a.; Xie, X.; Toney, M. F.; McGehee, M. D. *Nano Lett.* **2012**, *12*, 1566–1570.

(18) Miller, N. C.; Cho, E.; Gysel, R.; Risko, C.; Coropceanu, V.; Miller, C. E.; Sweetnam, S.; Sellinger, A.; Heeney, M.; McCulloch, I.; Brédas, J.-L.; Toney, M. F.; McGehee, M. D. *Adv. Energy Mater.* **2012**, *2*, 1208–1217.

(19) Rance, W. L.; Ferguson, A. J.; McCarthy-Ward, T.; Heeney, M.; Ginley, D. S.; Olson, D. C.; Rumbles, G.; Kopidakis, N. *ACS Nano* **2011**, *5*, 5635–5646.

(20) Guilbert, A. a Y.; Frost, J. M.; Agostinelli, T.; Pires, E.; Lilliu, S.; MacDonald, J. E.; Nelson, J. *Chem. Mater.* **2014**, *26*, 1226–1233.

(21) Albrecht, S.; Janietz, S.; Schindler, W.; Frisch, J.; Kurpiers, J.; Kniepert, J.; Inal, S.; Pingel, P.; Fostiropoulos, K.; Koch, N.; Neher, D. *J. Am. Chem. Soc.* **2012**, *134*, 14932–14944.

(22) Parmer, J. E.; Mayer, A. C.; Hardin, B. E.; Scully, S. R.; McGehee, M. D.; Heeney, M.; McCulloch, I. *Appl. Phys. Lett.* **2008**, *92*, 113309.

(23) McCulloch, I.; Heeney, M.; Bailey, C.; Genevicius, K.; Macdonald, I.; Shkunov, M.; Sparrowe, D.; Tierney, S.; Wagner, R.; Zhang, W.; Chabinyc, M. L.; Kline, R. J.; McGehee, M. D.; Toney, M. F. *Nat. Mater.* **2006**, *5*, 328–333.

(24) Brabec, C.; Dyakonov, V.; Scherf, U. *Organic Photovoltaics: Materials, Device Physics, and*

Manufacturing Technologies; 2009.

(25) Nardes, A. M.; Ferguson, A. J.; Whitaker, J. B.; Larson, B. W.; Larsen, R. E.; Maturová, K.; Graf, P. a.; Boltalina, O. V.; Strauss, S. H.; Kopidakis, N. *Adv. Funct. Mater.* **2012**, *22*, 4115–4127.

(26) Faist, M. A.; Kirchartz, T.; Gong, W.; Ashraf, R. S.; McCulloch, I.; De Mello, J. C.; Ekins-Daukes, N. J.; Bradley, D. D. C.; Nelson, J. *J. Am. Chem. Soc.* **2012**, *134*, 685–692.

(27) Yu, H.; Cho, H. H.; Cho, C. H.; Kim, K. H.; Kim, D. Y.; Kim, B. J.; Oh, J. H. *ACS Appl. Mater. Interfaces* **2013**, *5*, 4865–4871.

(28) Scarongella, M.; De Jonghe-Risse, J.; Buchaca-Domingo, E.; Causa', M.; Fei, Z.; Heeney, M.; Moser, J.-E.; Stingelin, N.; Banerji, N. *J. Am. Chem. Soc.* **2015**, *137*, 2908–2918.

(29) Soon, Y. W. Charge Separation, Triplets and Photochemical stability in Polymer/Fullerene Solar Cells, Imperial College London, 2013.

(30) Guo, J.; Ohkita, H.; Benten, H.; Ito, S. *J. Am. Chem. Soc.* **2010**, *132*, 6154–6164.

(31) Dimitrov, S. D.; Wheeler, S.; Niedzialek, D.; Schroeder, B. C.; Utzat, H.; Frost, J. M.; Yao, J.; Gillett, A.; Tuladhar, P. S.; McCulloch, I.; Nelson, J.; Durrant, J. R. *Nat. Commun.* **2015**, *6*, 6501.

(32) Yamamoto, S.; Ohkita, H.; Benten, H.; Ito, S. *J. Phys. Chem. C* **2012**, *116*, 14804–14810.

(33) Albert-Seifried, S.; Ko, D.-H.; Hüttner, S.; Kanimozhi, C.; Patil, S.; Friend, R. H. *Phys. Chem. Chem. Phys.* **2014**, *16*, 6743–6752.

(34) Soon, Y. W.; Shoaee, S.; Ashraf, R. S.; Bronstein, H.; Schroeder, B. C.; Zhang, W.; Fei, Z.; Heeney, M.; McCulloch, I.; Durrant, J. R. *Adv. Funct. Mater.* **2014**, *24*, 1474–1482.

(35) Jamieson, F. C. Charge Generation in Organic Solar Cells, Imperial College London, 2012.

(36) Lanzani, G. *The Photophysics behind Photovoltaics and Photonics*; 2012.

(37) Köhler, A.; Bässler, H. *Electronic Processes in Organic Semiconductors*; Wiley-VCH Verlag & Co. KGaA, 2015.

(38) Etzold, F.; Howard, I. a; Mauer, R.; Meister, M.; Kim, T.-D.; Lee, K.-S.; Baek, N. S.; Laquai, F. *J. Am. Chem. Soc.* **2011**, *133*, 9469–9479.

(39) Dimitrov, S. D.; Huang, Z.; Deledalle, F.; Nielsen, C. B.; Schroeder, B. C.; Ashraf, R. S.; Shoaee, S.; McCulloch, I.; Durrant, J. R. *Energy Environ. Sci.* **2014**, *7*, 1037.

(40) Piersimoni, F.; Chambon, S.; Vandewal, K.; Mens, R.; Boonen, T.; Gadisa, A.; Izquierdo, M.; Filippone, S.; Ruttens, B.; D'haen, J.; Martin, N.; Lutsen, L.; Vanderzande, D.; Adriaensens, P.; Manca, J. V. *J. Phys. Chem. C* **2011**, *115*, 10873–10880.

(41) Tumbleston, J. R.; Yang, L.; You, W.; Ade, H. *Polymer (Guildf).* **2014**, *55*, 4884–4889.

(42) Veldman, D.; Meskers, S. C. J.; Janssen, R. a. J. *Adv. Funct. Mater.* **2009**, *19*, 1939–1948.

Chapter 7. General conclusions and further work

This thesis has presented a series of studies that address different aspects of charge separation efficiency and charge recombination in polymer/fullerene blends used to fabricate active layers for solar devices. This work has provided insight into the influence on charge separation and recombination of material properties such as blend energetics, donor/acceptor ratio, polymer backbone modification (fluorination) and interfacial morphology. All these concepts are complex and modify more than one aspect of the spectroscopy and dynamics of the excited species of the blends, however they have helped to build an improved understanding of the process of current generation in these organic semiconductor blends. The study of polymer/fullerene blends is still an important area of solar research. Although recently new materials have attracted attention, organic materials remain an important niche due to their flexible structures. Following the conclusions of each chapter will be summarized and the future of these studies commented.

7a. Conclusions

Throughout this thesis relationships between low-bandgap polymer/fullerene blend characteristics including interface energetics (Chapter 3) and microstructure (Chapter 6), donor/acceptor ratio (Chapter 4) and polymer backbone fluorination (Chapter 5) were related to the charge generation and separation efficiency and charge recombination in systems with. These photochemical aspects were probed via mainly two experimental techniques: photoluminescence quenching and transient absorption spectroscopy from the sub-ps to the millisecond timescales. In all cases a relation with device performance was discussed. A general observed trend, evidenced in Chapter 3, is that the yield of charges correlates with the short circuit current of the device, thus directly impacting on its power conversion efficiency. Charge recombination kinetics is a slightly more complicated to interpret, since it depends on the recombination rate constant, on the charge density and on charge mobility.

Studying a series of DPP-based and Ge-based low-bandgap polymer/fullerene blends, Chapter 3 provided evidence that the driving energy for charge separation does not only impact on the yield of charges, as probed via TAS, but also on the short circuit current of devices. As such not only V_{OC} is a function of interface energetic, but also J_{SC}. Additionally, an estimation of the polaron entropy of thermalization was obtained by comparing the experimentally determined ΔE_{CS} and ΔG_{CS}, estimated as $E_S - eV_{OC}$.

Chapter 4 presented a complete study of the effect that changing the donor/acceptor ratio has upon charge separation and recombination dynamics of DPPTT-T/$PC_{70}BM$ blend films. The main conclusion supports the idea that a main limitation of DPP-based polymers is their inability of dissociate efficiently the excitons from both polymer and fullerene harvested photons. A careful microstructure analysis that included WAXD, TEM and AFM and a comparison with published data on other DPP-based polymers suggest that the main reason for the incomplete exciton dissociation is due to a non-optimized mixing between the polymer and $PC_{70}BM$.

Chapter 5 addresses a detailed study on the effect of fluorination of a Ge-based polymer upon excited state photophysics and photochemistry. It was found that fluorination increases the change of dipole moment upon excitation, which results in the formation of excitons with increased charge transfer character, as obtained via Fs-TAS. Fluorination also has important effects upon $PC_{70}BM$ crystallinity, which results in slower charge recombination which might impact on device performance.

Finally Chapter 6 provides a detailed analysis of the impact of interface microstructure upon charge separation and charge recombination, as probed by Fs-TAS. This chapter shows clear changes in the regime of recombination (from geminate to non-geminate) upon donor/acceptor ratio and upon the use of an acceptor unable to intercalate within the polymer chains. The level of intercalation in the used blend films was clearly shown using WAXD. A clear change from geminate to non-geminate recombination was observed when the acceptor was able to aggregate or when the bulky acceptor was unable to intercalate. It was concluded that the changes in dynamics can be exclusively explained with morphological arguments.

7b. Further work

Both Chapter 3 and Chapter 6 have work relevant to a "hot" discussion at the moment, which is the relevance of hot CT states upon charge separation. Although the counter-arguments of some researchers are not directly disproven with the contributions herein presented, they are an antecedent to further research in this area. Current work carried out at Durrant's group suggests that the intermediates states involved in charge separation as compared to those involved in charge recombination might be different. This would explain the seemingly contradicting results by Neher and co-workers and those of our group. The implication of the existence of bound states needs to be revised as well as the concept of geminate recombination. This work seems extremely exciting and a theory that unifies both viewpoints would be extremely important.